POLYTECHNIQUE MONTRÉAL

affiliée à l'Université de Montréal

Towards Battery-Free Internet of Things (IoT) Sensors: Far-Field Wireless Power Transfer and Harmonic Backscattering

XIAOQIANG GU

Département de génie électrique

Thèse présentée en vue de l'obtention du diplôme de *Philosophiae Doctor*

Génie électrique

Octobre 2020

POLYTECHNIQUE MONTRÉAL

affiliée à l'Université de Montréal

Cette thèse intitulée:

Towards Battery-Free Internet of Things (IoT) Sensors: Far-Field Wireless Power Transfer and Harmonic Backscattering

présentée par: **Xiaoqiang GU**

en vue de l'obtention du diplôme de *Philosophiae Doctor*

a été dûment acceptée par le jury d'examen constitué de :

M. Jean-Jacques LAURIN, président

M. Ke WU, membre et directeur de recherche

M. Simon HEMOUR, membre et codirecteur de recherche

M. Tarek DJERAFI, membre

M. Roni KHAZAKA, membre externe

DEDICATION

To my wife Shuangshuang Xu

To my mother Liuying Huang and my father Xinhua Gu

ACKNOWLEDGEMENTS

RÉSUMÉ

Notre vie tend à être plus agréable, plus facile et plus efficace grâce à l'évolution rapide de la technologie de l'Internet des objets (IoT). La clef de voute de cette technologie repose essentiellement sur la quantité de capteurs IoT interconnectés, que l'on est en mesure de déployer dans notre environnement. Malheureusement, l'électronique conventionnelle fonctionnant sur piles ou relié au réseau électrique ne peut pas constituer une solution durable en raison des aspects de coût, de faisabilité et d'impact environnemental. Pendant ce temps, le changement climatique dû à la consommation excessive de combustibles fossiles continue de s'aggraver. Il devient donc urgent de trouver une solution pour l'alimentation électrique des capteurs IoT géographiquement répartis à grande échelle, afin de simultanément soutenir la mise en œuvre de nombreux capteurs IoT tout en limitant leur poids environnemental.

L'énergie radiofréquence (RF) ambiante, qui sert de support à l'information sans fil, est non seulement capitale pour notre société, mais aussi omniprésente dans les zones urbaines et suburbaines. Elle permet de réaliser des communications et des détections sans fil. Cependant, l'énergie RF ambiante est majoritairement « gaspillée » car seule une toute petite partie de la puissance transmise est effectivement reçu ou « consommée » par le destinataire. C'est pourquoi le recyclage de l'énergie RF ambiante est une solution prometteuse pour alimenter les capteurs IoT. Pour certains capteurs IoT consommant une puissance plus élevée, l'apport d'énergie sans fil pourra similairement se faire par des centrales électriques spécialisées, suivant le même schéma d'alimentation sans fil. Pour utiliser et récupérer cette énergie RF, cette thèse présente deux techniques principales : la récupération/réception de puissance sans fil en champ lointain (wireless power transfer: WPT) et la rétrodiffusion d'harmoniques. Le chapitre 2 aborde les différents mécanismes de conversion de fréquence entre le WPT en champ lointain et la rétrodiffusion d'harmoniques. La récupération de WPT en champ lointain consiste à convertir l'énergie RF en puissance continue. En revanche, la rétrodiffusion d'harmoniques a pour but de convertir l'énergie RF dans une autre fréquence, dans la plupart des cas, la composante harmonique de rang 2. A titre d'étape préliminaire de recherche et d'étude de faisabilité, une cartographie de la densité de l'énergie RF ambiante dans les zones centrales de l'île de Montréal est résumée au chapitre 3. Contrairement aux mesures traditionnelles précédentes effectuées à des endroits fixes, cette mesure dynamique a été réalisée le long des rues, des routes, des avenues et des autoroutes pour couvrir une large zone.

De plus, une mesure stationnaire dans le centre-ville de Montréal permet de révéler si les activités humaines apportent un changement visible aux niveaux d'énergie RF ambiante. Ce travail met en valeur la quantité d'énergie RF ambiante disponible dans l'espace libre et constitue une référence importante pour les chercheurs et les ingénieurs qui conçoivent des circuits/systèmes de collecte de l'énergie RF ambiante pour des applications pratiques.

Après cette étude de faisabilité, cette thèse est ensuite organisée en discutant d'abord de la conception du redresseur WPT en champ lointain puis de la rétrodiffusion d'harmoniques. L'objectif principal est d'améliorer l'efficacité de la conception des circuits et des systèmes pour le WPT en champ lointain et la rétrodiffusion d'harmoniques. Le chapitre 4 présente un modèle analytique pour la prévision des redresseurs de WPT en champ lointain avec une gamme dynamique étendue jusqu'à une région d'environ un milliwatt. En outre, une étude sur les effets de la température des redresseurs à diodes Schottky indique que celle-ci doit être prise en compte lors de la conception car les redresseurs à diodes ont leurs propres températures de fonctionnement optimales pour atteindre un rendement de conversion maximal. En raison de la densité de puissance limitée de la puissance RF ambiante, le chapitre 5 propose d'ajouter l'énergie vibratoire ambiante dans le processus de redressement. Un redresseur hybride est réalisé pour collecter simultanément l'énergie RF ambiante et l'énergie vibratoire. Il est démontré que la puissance de sortie en courant continu de ce redresseur hybride est considérablement augmentée grâce à la synergie des deux puissances d'entrée permettant l'amélioration simultanée du rendement.

La deuxième partie de cette thèse porte sur la rétrodiffusion d'harmoniques, plus précisément sur la conception et l'optimisation des performances des transpondeurs d'harmoniques. Les transpondeurs d'harmoniques reçoivent l'énergie RF à la fréquence fondamentale, qui peut être la puissance RF ambiante ou provenir d'un radar harmonique spécialisé. Après l'avoir convertie en deuxième harmonique, les transpondeurs la renvoient vers des récepteurs ou des radars harmoniques pour l'interprétation des informations. Le chapitre 6 propose ainsi une nouvelle architecture de transpondeur d'harmonique en insérant un duplexeur pour réduire le nombre d'antennes. Un modèle analytique du comportement des diodes dans la conversion de fréquence des transpondeurs harmoniques est développé, permettant de choisir les diodes optimales pour la conception des transpondeurs. Sur la base des résultats mesurés, la perte de conversion du transpondeur d'harmoniques entièrement passif proposé a été réduite en sélectionnant la meilleure

diode (SMS7630) et en optimisant les antennes du transpondeur. Le chapitre 7 présente l'amélioration de la distance de lecture des transpondeurs harmoniques en utilisant la diode SMS7621 et des opérations à basse température. Une analyse théorique, ainsi qu'une vérification des mesures en champ lointain, ont été fournies. Enfin, le chapitre 8 propose une conclusion et une discussion sur les travaux futurs.

ABSTRACT

Our life is becoming more convenient, efficient, and intelligent with the aid of fast-evolving Internet of Things (IoT) technology. One essential foundation of IoT technology is the development of numerous interrelated IoT sensors that are distributed extensively in our environment. However, conventional batteries/cords-based powering solutions are certainly not an acceptable long-term solution, considering the incurred cost, feasibility, most of all, environmental impact. Meanwhile, climate change due to excessive consumption of fossil fuels is worsening day by day. Therefore, a transformative powering solution for such large-scale and geographically scattered IoT sensors is of extreme importance in support of such extensive IoT sensors implementation while simultaneously mitigating its environmental burden.

Serving as a critical information carrier, ambient radiofrequency (RF) energy is pervasive in urban and suburban areas to realize wireless communication and sensing. However, part of ambient RF energy is dissipated due to path loss if not fully consumed by end-users. Hence, recycling the wasted ambient RF energy to power IoT sensors is a promising solution. The concept of harnessing wireless energy for powering IoT sensors requiring a higher power supply is also feasible through the dedicated wireless power delivery from specialized power stations, which can be an effective supplement. To realize the RF power scavenging, this thesis research introduces two mainstream techniques: far-field wireless power transfer (WPT) and harmonic backscattering. Chapter 2 discusses the different frequency conversion mechanisms applied for far-field or ambient WPT harvesting and harmonic backscattering. Far-field WPT harvesting converts RF energy into dc power (zeroth harmonic). In contrast, harmonic backscattering upconverts RF energy into its harmonics, in most cases, the second harmonic component. As a preliminary research step and a feasibility study, a survey of ambient RF energy density in the core areas on Montreal Island is summarized in Chapter 3. Different from the previously published traditional measurements at fixed locations, this dynamic measurement is carried out along streets, roads, avenues, and highways to cover a large area. Also, a stationary measurement in Downtown Montreal is to reveal whether human activities are able to bring visible change to ambient RF energy levels. This work demonstrates how much ambient RF energy is available in free space and acts as a significant reference for researchers and engineers designing ambient RF energy harvesting circuits/systems for practical applications.

After this feasibility study, this thesis first discusses far-field WPT rectifier designs and then addresses harmonic backscattering in the second half. The primary goal is to enhance efficiency performance in circuit/system design for both far-field WPT and harmonic backscattering. Chapter 4 introduces an analytical model for predicting far-field WPT rectifiers with an extended dynamic range up to approximately milliwatts (mW) region. Furthermore, a study on the temperature effects of Schottky diode-based rectifiers indicates that different diode-based rectifiers have their own optimum operating temperatures to achieve peak conversion efficiency. Due to the limited power density of ambient RF power, Chapter 5 further introduces ambient vibration energy into the rectifying process. A hybrid rectifier is realized to collect ambient RF and vibration energy at the same time. Predicted by closed-form analyses and verified by measurements, the power synergy leads to a substantial enhancement of dc output power and conversion efficiency of this hybrid rectifier simultaneously. The second part of this thesis focuses on harmonic backscattering, specifically harmonic transponders design and performance optimization. Harmonic transponders harness RF signal at the fundamental frequency, which may be ambient RF power from a commercial band or come from specialized harmonic radar. After converting it into the second harmonic, transponders send it out to sniffer or harmonic radar for information interpretation. Chapter 6 proposes a new architecture of harmonic transponder by inserting a diplexer to reduce antenna number. A closed-form model for analyzing diode behaviors in frequency conversion of the harmonic transponders is developed, which further helps identify suitable diode candidates for transponder design. Based on measured results, the conversion loss of the proposed fully passive harmonic transponder is reduced by selecting proper diode SMS7630 in this work and optimizing transponder antennas. Chapter 7 presents the readout distance enhancement of harmonic transponders by using diode SMS7621 in this work and low-temperature operations. Theoretical analyses, together with far-field measurement verification, are provided. Finally, Chapter 8 offers a general conclusion and discussion on future works.

TABLE OF CONTENTS

LIST OF TABLES

LIST OF FIGURES

LIST OF SYMBOLS AND ABBREVIATIONS

WPT	Wireless Power Transfer
RF	Radiofrequency
DTV	Digital TV
PCE	Power Conversion Efficiency
IoT	Internet of Things
CL	Conversion Loss
ADS	Advanced Design System
OCFD	Off-Center-Fed Dipole
MPPT	Maximum Power Point Tracking
FOCVA	Fractional Open-Circuit Voltage Approximation
Op amps	Operational Amplifiers
VCO	Voltage-Controlled Oscillator
ANFR	National Frequency Agency of France
DT	Downtown
UT	Uptown
IC	Industry Canada
FCC	Federal Communications Commission
DSP	Digital Signal Processor
VNA	Vector Network Analyzer
IL	Insertion Loss
KCL	Kirchhoff Circuit Laws
EG	Efficiency Gain

PIFA	Planar Inverted-F Antenna
IFA	Inverted F Antenna
TEG	Thermo-Electric Generator
5G	Fifth Generation
WRC	World Radiocommunication Conference
FoM	Figure of Merit
RFID	Radiofrequency Identification
CW	Continuous Wave

LIST OF APPENDICES

CHAPTER 1   INTRODUCTION

1.1 Motivation and Objectives

Billions of Internet of Things (IoT) sensors will be implemented globally for a huge number of applications, ranging from automated manufacturing to smart city. They are critical to increase operational efficiency, lower costs, monitor structure conditions, enhance traffic safety, and optimize public transportation. Powering these IoT sensors cannot rely on traditional measures, like dry batteries and wires, which will inevitably add more burden to our vulnerable environment and cost issue as well as application inconvenience. As a result of excessive green gas emissions, humankind is witnessing severe climate change, such as arctic ice melting, more frequent bush fires, and hurricanes. Therefore, a transformative powering solution for these IoT sensors is urgently needed.

Ambient radiofrequency (RF) energy is pervasive in urban and suburban regions as well as industrial production and campus areas. It may come from digital TV (DTV) broadcasting towers, cellular base stations, and Wi-Fi access points. It should be noted that some ambient RF energy is actually dissipated and wasted in free space if not fully captured by target users. This is, in particular, true for omnidirectional coverage of those RF signals. Thus, ambient RF energy is an ideal "green" energy available for IoT sensors. This thesis research strives to bridge the gap of usage between wasted ambient RF energy and energy-demanding IoT sensors. Such an energy bridge is timely and practical for two reasons:

a) **Energy level.** Although the power density of ambient RF energy is usually low in free space, IoT sensors are becoming less and less power-hungry due to advances in ultra-low-power electronics.

b) **Physical locations.** IoT sensors are often geographically distributed so that they may be installed in difficultly accessible corners and ceilings or even be embedded inside building concretes or human bodies. Thus, conventional powering solutions are obviously not good choices or even impossible in these cases. Whereas, ambient RF energy is also omnipresent in free space and can penetrate nonmetal materials so to reach those IoT sensors easily.

For meeting the higher power demands of some IoT sensors in some cases, a dedicated power station to offer wireless power delivery can be introduced as a supplement besides recycling

ambient RF power. To realize battery-free IoT sensors, this thesis discusses two major techniques: far-field wireless power transfer (WPT) and harmonic backscattering. The primary goal is to enhance circuit/system efficiency or reduce loss at a limited power level for both far-field WPT and harmonic backscattering. Specifically, the objectives of this thesis can be summarized as:

1) Conduct a density mapping of ambient RF energy in our neighborhood to understand how much ambient RF energy is available in free space, which is also a feasibility study of this Ph.D. research topic;

2) Develop analytical models for far-field WPT rectifiers and harmonic transponders;

3) Summarize a selection guide of Schottky diodes for far-field WPT rectifiers and harmonic transponders for higher efficiency performance;

4) Investigate the temperature effects of far-field WPT rectifiers and hybrid energy rectifying platforms based on multi-physical sources;

5) Propose a new architecture of harmonic transponders to achieve low profile and large readout distance;

6) Enhance the readout distance of harmonic transponders through low-temperature operations with the aid of a closed-form analysis model.

1.2 Outline and Contributions of This Thesis

This thesis is organized in the article-based format, containing six original journal papers:

Chapter 1: Introduction

This chapter presents the background information of far-field WPT and harmonic backscattering. Harvesting RF energy through the above two techniques to energize IoT sensors is the primary goal, which is also the main motivation of this Ph.D. thesis.

Chapter 2: Article 1: Recycling Ambient Radiofrequency (RF) Energy: Far-Field Wireless Power Transfer and Harmonic Backscattering

Chapter 2 reviews in-depth two mainstream techniques to recycle ambient RF energy in free space: far-field WPT and harmonic backscattering. The information on available ambient RF energy in both typical urban and suburban areas is measured and presented first, as an essential reference for designing harvesting circuits and systems. Different diode behaviors and frequency conversion mechanisms of the above two techniques are discussed and compared in detail. Circuit optimization suggestions for both far-field WPT and harmonic backscattering are offered. A feasibility study in this chapter shows that far-field WPT and harmonic backscattering techniques are the effective measures to recycle ambient RF energy and then energize battery-free IoT sensors.

Chapter 3: Article 2: Dynamic Ambient RF Energy Mapping of Montreal for Battery-Free IoT Sensor Network Planning

Before designing any circuits and systems for far-field WPT and harmonic backscattering applications, knowing how much RF power is available in free space should be the very first step and is also of great importance. Chapter 3 summarizes an outdoor dynamic measurement of ambient RF power density in the core areas of Montreal for the first time, which can eventually be exploited for possible battery-free IoT sensor network planning. The frequency range of 400 MHz to 2700 MHz is our focus in this work because it covers most of the used commercial RF bands. Measured results indicate that cellular communication and digital TV bands are ideal targets in Downtown and Uptown Montreal, respectively. Also, one separate measurement at a fixed location in Downtown Montreal is conducted on a typical workday to study the effects of human activities on ambient RF power density. Results do not show evident time-variant fluctuations within that workday.

Chapter 4: Article 3: Optimum Temperatures for Enhanced Power Conversion Efficiency (PCE) of Zero Bias Diode-Based Rectifiers

As the core of far-field WPT rectifiers, the nonlinear device has been subject to significant research and improvements recently, especially at a low power level where rectifying efficiency is so limited. The current responsivity, a significant indicator to describe device nonlinearity, is known to be impacted by the operating temperature, as predicted by the well-known Shockley model.

Chapter 3 explores and quantifies the impact of operating temperature in the RF rectification process and also relate existing diodes with their optimum operating temperature range. An analytical method to predict power conversion efficiency (PCE) of rectifiers from approximate milliwatts (mW) down to nanowatts (nW) level is proposed first. It then identifies the optimum operating temperature of rectifiers corresponding to peak PCE. Enhanced PCE results are then validated experimentally on SMS7630 and HSMS-2850-based rectifiers when operating at their optimum temperatures.

Chapter 5: Article 4: Integrated Cooperative Ambient Power Harvester Collecting Ubiquitous Radiofrequency and Kinetic Energy

Chapter 5 reports an integrated cooperative harvester capable of collecting both electromagnetic (principally RF) and kinetic energy simultaneously. One single substrate board is demonstrated to accommodate and integrate an electromagnetic kinetic generator, an F-shaped antenna, and a rectifying circuit, within a compact credit-card size. In this chapter, a closed-form method is proposed to predict the enhanced efficiency performance of the cooperative harvester within a low power range of −50 to −30 dBm. Our analysis highlights the roles of the diode's nonlinear junction resistance and capacitance. Good agreements are observed when comparing the analysis results with harmonic balance simulations by ADS. Finally, measured results verify that the cooperative harvesting mode enables a significant enhancement of the diode's power conversion efficiency (PCE) and also greatly strengthening the resilience of the harvester at the same time.

Chapter 6: Article 5: Diplexer-Based Fully Passive Harmonic Transponder for Sub-6 GHz 5G-Compatible IoT Applications

A novel diplexer-based fully passive transponder is presented in chapter 6, which targets sub-6 GHz 5G-compatible Internet of Things (IoT) applications. To alleviate the antenna design restrictions of traditional transponder with two separate antennas, a new architecture has been proposed with the introduction of a diplexer, which allows transponders to simply employ a dual-band antenna. In this chapter, a dual-band circularly polarized omnidirectional spiral slot antenna, with enhanced bandwidth and gain performance, is designed as the transponder Tx/Rx antenna.

Besides the new architecture, a diode selection criterion is proposed as well. Analytical models are derived, showing relationships between the diode's SPICE parameters and the conversion efficiency or conversion loss (CL) of such diode-based transponders. With the aid of the selection criterion, low-barrier diode SMS7630 is chosen for verification. Measured CL results of the transponder circuitry part show a noticeable improvement over the state-of-the-art works.

Chapter 7: <u>Article 6: Readout Distance Enhancement of Battery-Free Harmonic Transponder</u>

Chapter 7 proposes to enlarge the maximum readout distance of battery-free harmonic transponders through a careful Schottky diode selection and a consideration of low-temperature operations. Diode SMS7621 is identified to deliver lower conversion loss (CL) of harmonic transponders based on a diode selection guide. Moreover, an analytical method for studying temperature effects on transponder CL performance is introduced and derived with satisfactory accuracy. A diplexer inserted in the harmonic transponder design can help reduce antenna number. To mitigate matching difficulties at both fundamental and second-harmonic frequencies, a third-order diplexer is developed to enhance its bandwidth performance. Experimental verification has shown that low-temperature operations can effectively reduce CL of SMS7630-based harmonic transponder, thus increasing its readout distance.

Chapter 8: <u>Conclusion and Future Works</u>

This chapter draws a general conclusion of the entire thesis and highlights some key contributions. Also, some possible extensions of this research topic in the future are suggested at the end.

CHAPTER 2   ARTICLE 1: RECYCLING AMBIENT RADIOFREQUENCY (RF) ENERGY: FAR-FIELD WIRELESS POWER TRANSFER AND HARMONIC BACKSCATTERING

Xiaoqiang Gu, Pascal Burasa, Simon Hemour and Ke Wu

2.1 Introduction

It all started with a spark. Let us rewind back to 1887, in Germany. The days were getting cooler in the garden of the Technische Hochschule in Karlsruhe as Heinrich Rudolf Hertz was setting up the first-ever far-field wireless power transmission with increasingly more power [1]. He was striving to demonstrate the wireless nature of electromagnetic waves and propagation. Moreover, since no high frequency (nearly 100 MHz) voltmeter was available at that time for his experiment, he had to transmit enough power to generate a spark —hundreds of volts!— at the receiver to validate the famous theory of James Clerk Maxwell.

Since this first experimental verification, radiofrequency (RF) wave-based wireless technology has seen rapid developments in many different directions. So far, two primary system functions of wireless technology, namely wireless communication and wireless sensing, have already become the foundations of our modern social and economic life for ubiquitous connectivity, social networking, and environmental awareness [2]. Ambient RF waves quietly flow all around us from radio and digital TV broadcasting towers, cellular stations, Wi-Fi access points to support wireless communication and sensing applications. Besides what is consumed by end-users, a significant portion of ambient RF waves decay in free space and is finally wasted. Therefore, the topic of recycling ambient RF energy whenever and wherever possible has recently emerged and amassed vast attention [3-5]. Ambient RF energy is highly suitable as external ready-to-use power sources for ultra-low-power internet of things (IoT) sensors. In the coming future, IoT sensors will be scattered everywhere in our environment, thus making power cords or battery-based solutions costly and inadequate. Moreover, many IoT sensors, such as temperature and CO_2 monitoring

elements, do not need a continuous operation, thereby suggesting they are less power-hungry. Harnessing ambient RF energy can fundamentally unlock ubiquitous remote sensing's potential as the two dimensions of geographical distribution and power supply/consumption no longer draw obstacles. Hence, despite relatively low power density, omnipresent ambient RF power is an ideal, green power source for ultra-low-power IoT sensors.

2.2 Power Density of Ambient RF Energy in Urban and Suburban Areas

Before jumping into the design process, knowing how much ambient RF energy is available in our daily environment must be the very first step. This will validate the next steps in development. With the roll-out of 5G, more ambient RF power will emerge at higher frequency bands [6]. Nevertheless, the sub-7 GHz frequency band is still the best choice for recycling ambient RF energy in considering its low transmission loss, high-level signal coverage, and abundantly available frequencies. Based on frequency allocation charts, the sub-7 GHz frequency band can be further categorized into seven primary groups, namely DTV, LTE700, GSM/LTE850, LTE1700/2100, GSM/LTE1900, Wi-Fi, and LTE2600 bands. Note that the ambient RF power below the DTV band, such as FM radio, is not included since the recycling circuit/system size will be problematically large for IoT sensor nodes in such low frequencies.

(a)

(b)
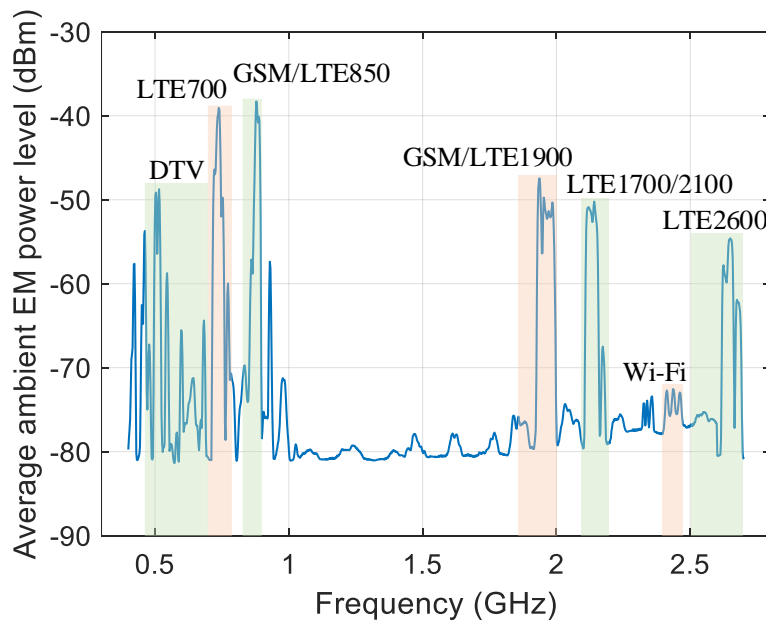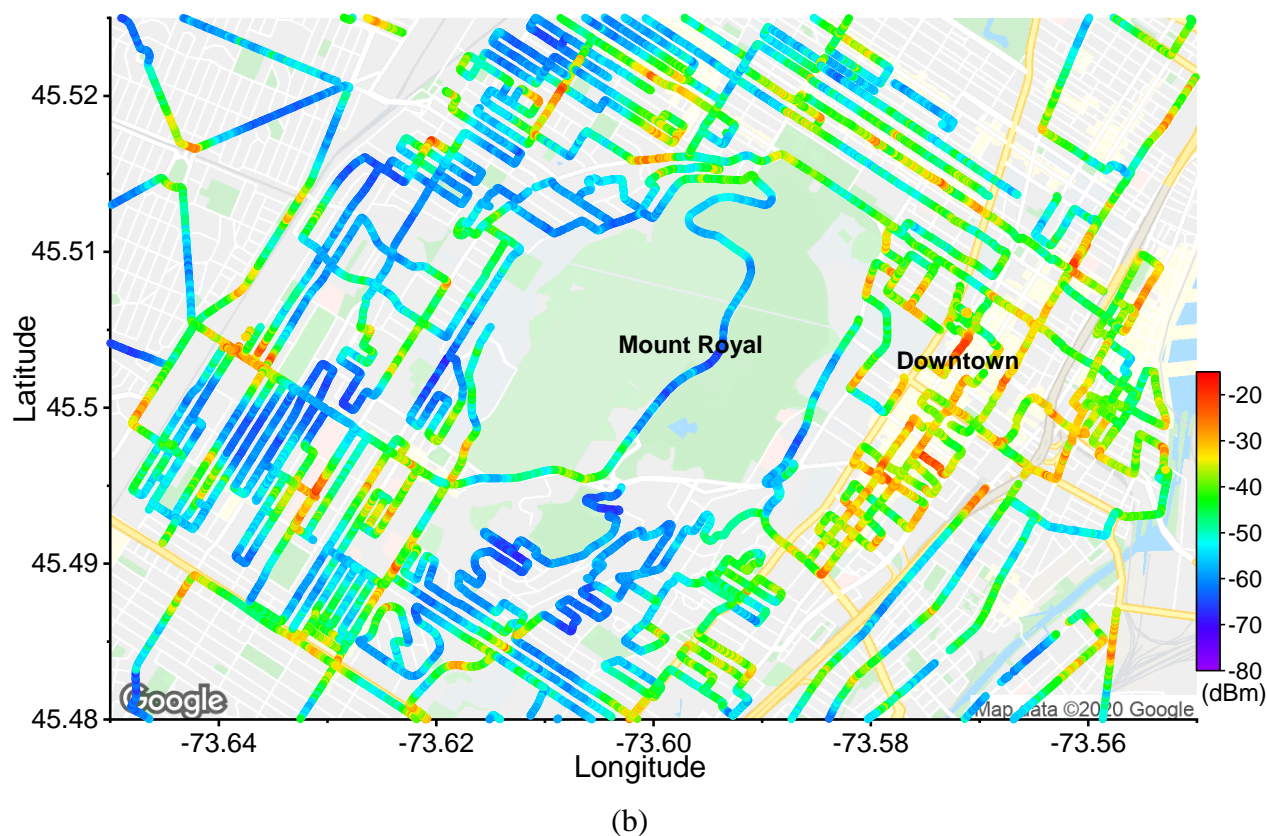
Figure 2.1 (a) Average RF power density in Downtown Montreal across the frequency spectrum of 400 MHz to 2700 MHz. (b) Dynamic measurement results of ambient RF power (GSM/LTE850 band) in core areas of Montreal, Canada.

So far, multiple investigations on ambient RF power density in the sub-7 GHz band were carried out in different cities across the world [7-9]. Such measurements usually target fixed locations close to places involving substantial pedestrian traffics. To cover a larger geographical area and reflecting more representative conditions, the dynamic outdoor mapping of ambient RF energy in the city of Montreal was reported in [10]. Ambient RF power density was measured and evaluated along streets, roads, avenues, and highways—a contrast from previous stationary/fixed-location measurements. Figure 2.1 (a) illustrates the average ambient RF power density levels over the frequency band of interest (400 MHz ~ 2700 MHz) in Downtown Montreal, Canada [10]. Among the above seven sub-7 GHz frequency bands, the GSM/LTE850 band shows the largest average ambient RF power level (−38.29 dBm). Next to the GSM/LTE850 band, the LTE700 band has a comparable average power level of −39.05 dBm. Moreover, the DTV and GSM/LTE1900 bands also have a similar level of average RF power density, slightly higher than −50 dBm. Figure 2.1

(b) presents the dynamic measurement results of ambient RF power density (GSM/LTE850 band) in the core areas of Montreal. It can be clearly observed that Downtown Montreal has a higher overall ambient RF power density than the other areas. The highest recorded power level is about −13 dBm. Based on the above measurement results and discussions, the circuit/system design aiming to recycle ambient RF power should target a power level of −15 dBm and below. The actual amount of power harvesting depends on many factors, including the effective antenna aperture.

2.3 Two Main Techniques: Far-field Wireless Power Transfer (WPT) and Harmonic Backscattering
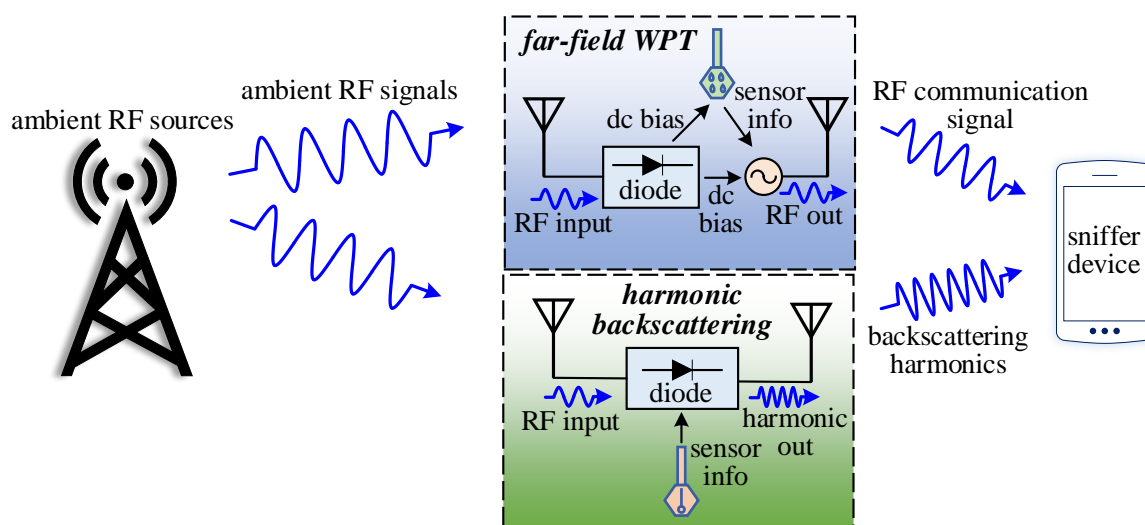
Figure 2.2　Far-field wireless power transfer (WPT) and harmonic backscattering are two mainstream technologies for recycling ambient RF energy in free space.

Currently, recycling ambient RF energy can be mainly realized by two types of techniques: far-field wireless power transfer (WPT) and harmonic backscattering, as shown in Figure 2.2. Ambient RF energy is in both cases collected by the antennas and injected into a nonlinear device for frequency conversion. The primary difference between these two techniques lies in the frequency components after conversion. Far-field WPT converts the RF energy input into dc power, which is then used to drive sensing and communication operation with sniffer devices [11], [12]. By contrast, harmonic backscattering up-converts RF input into higher harmonics, in most cases the second harmonic [13], and directly uploads information to sniffer devices [14], [15].

Both techniques have recently gained increasing attention in the microwave community, which is revealed in Figure 2.3. For example, Figure 2.3 (a) shows the number of papers appearing in two major databases, Web of Science and IEEE Xplore, when the search hits wireless power transfer as author keywords. To further identify works in the particular domain of far-field WPT, the keywords "far-field/RF/radiative" have been introduced to refine results within the initial search outcome. In Figure 2.3 (a), the total number of papers on WPT has been continuously growing since 2010 in both databases. Noticeably, a big jump in papers occurred in the year 2015. Moreover, the far-field WPT papers account for roughly 10 % ~ 15 % of the total number of papers in the research field of WPT. As a new topic, the far-field WPT has become more and more attractive since the last decade and, currently, turns out to be an intriguing, trendy field.

Figure 2.3 (b) presents the search results for "wireless/RF/radiofrequency/microwave backscatter" or "harmonic tag/transponder/backscatter" as author keywords in both databases. The total number of papers in both databases shows an increasing trend since the year 2010, although this number is smaller compared to that of the WPT domain. When further refining the search results by using "harmonic" as a keyword, the number of filtered papers is small without a clear increasing trend, indicating this research topic is relatively new and may hold much potential.
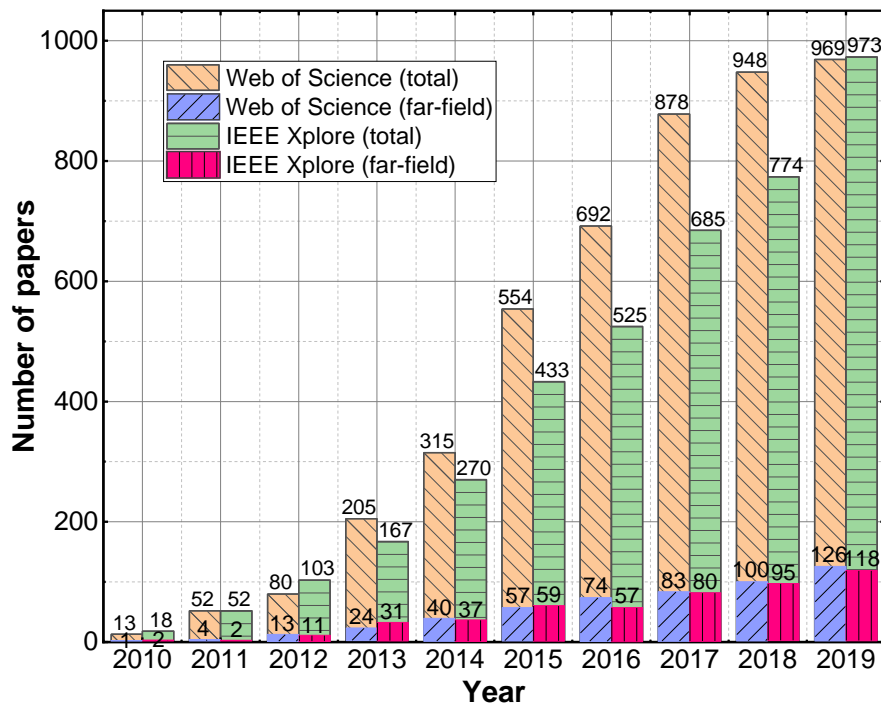
(a)
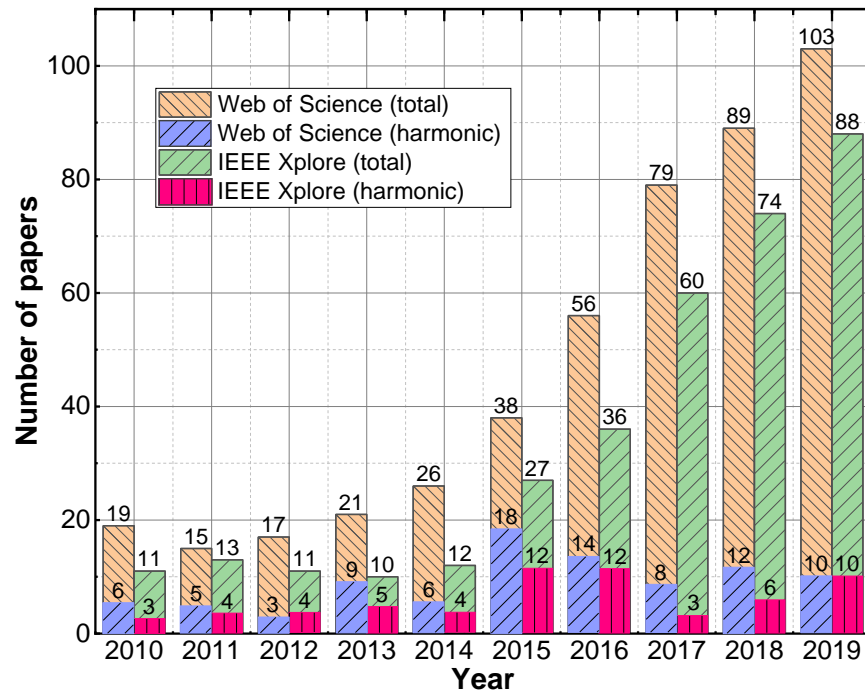
(b)

Figure 2.3 Number of papers in the last decade (2010 ~ 2019) in the research domain of WPT and backscattering. The papers of far-field WPT and harmonic backscattering are further filtered out in the corresponding research fields. Results reveal the outcome of author keywords search in Web of Science and IEEE Xplore. (a) WPT and far-field WPT; (b) Wireless/RF/radiofrequency/microwave backscattering and harmonic backscattering.

Featuring low cost, a well-established fabrication process, and easy accessibility, commercial Schottky diodes working as a nonlinear device for recycling ambient RF energy are still the top choice and will be the focus in this work. Frequency conversion is realized by diode nonlinearity, which indicates that the output signal does not have a linear response to the input. The nonlinearity of Schottky diodes contains two contributors, namely, the junction resistance and junction capacitance. Far-field WPT relies on the nonlinear junction resistance, while harmonic backscattering depends on the nonlinear junction resistance and capacitance simultaneously, which will be discussed in detail later. As mentioned before, the primary difference between far-field WPT and harmonic backscattering lies in how designers select and maximize the target frequency components. As depicted in Figure 2.4, the *I-V* curve of a typical Schottky diode reflects its

nonlinearity. Assuming a sinusoidal RF signal travels through this diode, its output would consist of the fundamental signal, dc component, second harmonic, and other higher harmonics. Getting the most of the dc component and second harmonic at the output ports is the design goal of far-field WPT and harmonic backscattering circuits/systems, respectively. All design efforts are to maximize the outcome of target frequency components; in other words, to suppress the energy outputs at other frequencies.
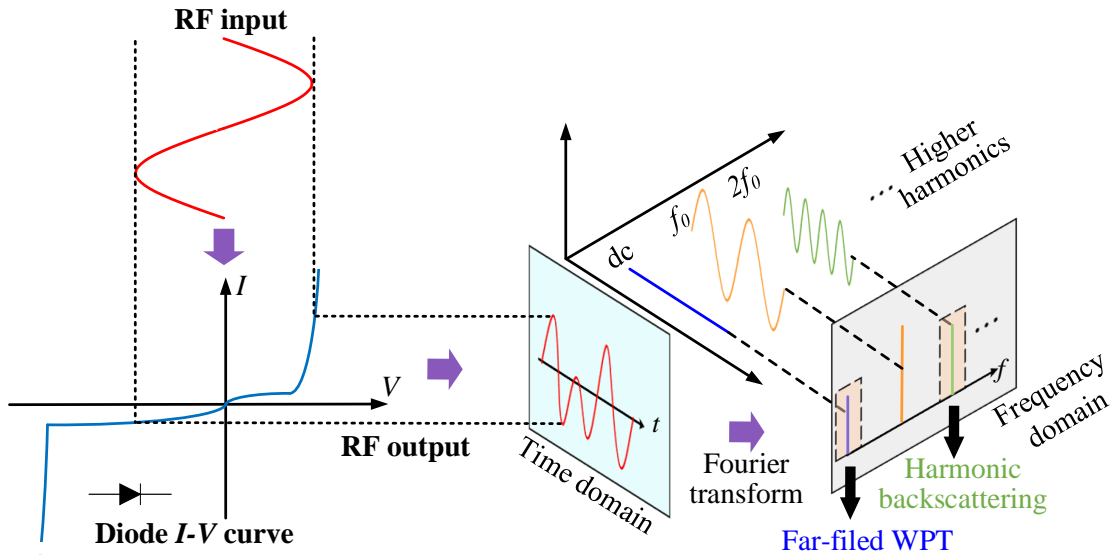
Figure 2.4 Diode nonlinearity would generate all frequency components with a sinusoidal RF input. Far-field WPT and harmonic backscattering circuits/systems maximize the output of dc component and second harmonic, respectively.

Current responsivity $\mathfrak{R}_I$ is often used to quantify the nonlinearity of diodes in RF-to-dc frequency conversion [16]. It is defined as the ratio of dc short-circuit current I_{dc} over RF input power P_{in} [17]:

$$\mathfrak{R}_I = \frac{I_{dc}}{P_{in}} \tag{2.1}$$

When the RF input power is low, which indicates the Schottky diode works in the square law region, the current responsivity $\mathfrak{R}_I$ can be simplified as the quadratic responsivity $\mathfrak{R}_{I0}$. For a Schottky diode, this value can be calculated by its SPICE parameters on the datasheets offered by manufacturers [18]:

$$\mathfrak{R}_{I0} = \frac{q}{2n \cdot k \cdot T} \tag{2.2}$$

where q, n, k, and T are the electron charge, diode ideality factor, Boltzmann constant, and operation temperature (in Kelvin), respectively. The current responsivity of diodes is a significant quantitative indicator associated with the efficiency performance of both far-field WPT and harmonic backscattering.

2.4 Analysis of Diode-Based Far-Field WPT Rectifiers

Considering that the available ambient RF power is relatively low in free space, the circuit topology of far-field WPT rectifiers based on a single diode will lead to higher efficiency. Furthermore, the topologies based on single-shunt and single-series diodes illustrate a negligible difference in rectifying efficiency, despite having different dc paths. Thus, the single-series topology with fewer lumped components is selected for discussion in this work. Figure 2.5 shows the equivalent circuits of single-series rectifier analysis. The Schottky diode is characterized by the well-known Shockley model [19], which consists of nonlinear junction resistance R_j, nonlinear junction capacitance C_j, series resistance R_s, parasitic capacitance C_p and inductance L_p. The equivalent circuit in Figure 2.5 (a) shows a state where the diode absorbs injecting RF power. Inside the diode junction, both nonlinear junction resistance R_j and capacitance C_j convert the fundamental RF signal into other frequency components. However, due to the nature of dc output—it cannot go through junction capacitance C_j—only nonlinear junction resistance R_j contributes to the frequency conversion in far-field WPT rectifiers. The nonlinear junction capacitance C_j is an indirect power dissipator, and the RF input power passing through it is eventually dissipated by the series resistance R_s. After frequency conversion, the diode acts as a dc power source for the load resistance R_l, which is represented by the equivalent circuit in Figure 2.5 (b).
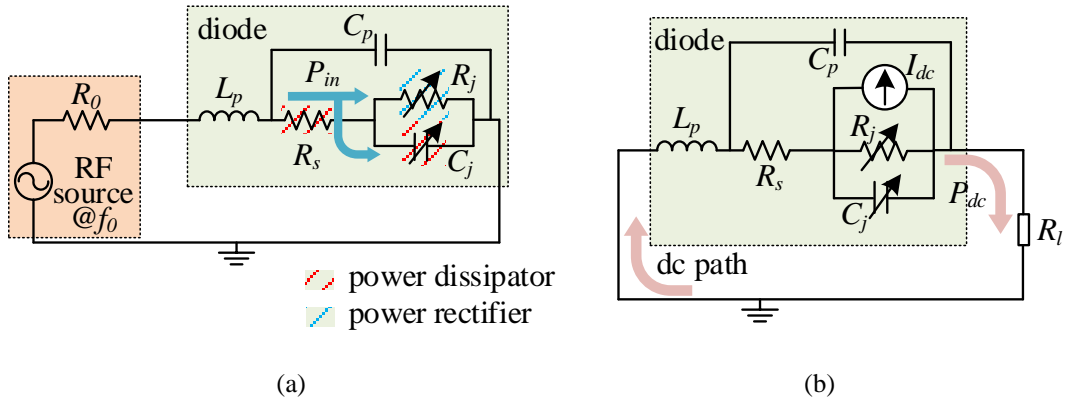
Figure 2.5 Equivalent circuits of diode operations in the rectifier before and after frequency conversion: (a) diode absorbing RF input power and (b) diode serving as a dc power generator.

Based on the equivalent circuit analysis in Figure 2.5, the rectifier efficiency η_{re} can be calculated by [17, 18, 20]:

$$\eta_{re} = \eta_d \cdot \eta_p \cdot \eta_t = \frac{P_{in} \cdot \mathfrak{R}_I^2 \cdot R_j^2}{R_l + R_s + R_j} \cdot \left(\frac{1}{1 + (\omega \cdot C_j)^2 \cdot R_s \cdot R_j}\right)^2 \cdot \frac{R_l}{R_l + R_s + R_j} \tag{2.3}$$

where η_d, η_p, η_t are the rectifying efficiency of the diode junction resistance, parasitic efficiency (due to junction capacitance), and dc power transfer efficiency, respectively. ω is angular frequency. This explicit expression of efficiency prediction is a guideline to optimize the design of far-field WPT rectifiers:

    a.   *Select suitable Schottky diodes;*

    b.   *Enhance input power level P_{in}; and*

    c.   *Optimize load resistance R_l.*

2.4.1 Diode Selection for Far-Field WPT Rectifiers

Based on the efficiency calculation in (2.3), several rules for diode selection can help to quickly identify suitable candidates: preferred diodes are paired with (a) stronger nonlinearity, or in other words, higher current responsivity $\mathfrak{R}_I$; (b) larger nonlinear junction resistance R_j or smaller saturation current I_s; (c) smaller nonlinear junction capacitance C_j and series resistance R_s. Beyond

these simple rules applicable to easy cases, an accurate calculation method or simulation is often required to evaluate diode candidates thoroughly.

Table 2.1 lists popular commercial diodes for recycling ambient RF energy for both far-field WPT and harmonic backscattering applications. The main SPICE parameters and zero bias current responsivity $\Re_{I0}$ of those diodes are also attached for analysis. Regarding the four diodes for far-field WPT rectifiers in Table 2.1, Figure 2.6 presents the rectifying efficiency and dc output voltage results obtained through the harmonic balance simulator of the Advanced Design System (ADS) software. The load resistance R_l for each diode is optimized at a reasonable power level of −20 dBm according to the ambient RF power density study discussed before. The operating frequency is 880 MHz, corresponding to the frequency point with the highest average ambient RF power density in Figure 2.1 (a).

Table 2.1 SPICE parameters and zero bias current responsivity of popular diodes for recycling ambient RF power

Far-field WPT

	HSMS-282x	HSMS-286x	SMS7630	HSMS-285x	HMPS-2820	SMV1430
I_s (A)	2.2e-8	5e-8	5e-6	3e-6	2.2e-8	1e-14
R_s (Ω)	6	6	20	25	8	3.15
n	1.08	1.08	1.05	1.06	1.08	1
C_{j0} (pF)	0.7	0.18	0.14	0.18	0.7	1.11
M	0.5	0.5	0.4	0.5	0.5	0.5
F_c	0.5	0.5	0.5	0.5	0.5	0.5
V_j (V)	0.65	0.65	0.34	0.35	0.65	0.86
B_V (V)	15	7	2	3.8	15	0
I_{BV} (A)	1e-4	1e-5	1e-4	3e-4	1e-4	1e-3
$\Re_{I0}$ (A/W)	18.02	18.02	18.53	18.36	18.02	19.46

harmonic backscattering

Figure 2.6 indicates that HSMS-286x is a better choice for rectifier design since its rectifying efficiency and dc output voltage are the highest among the four diodes in the power range of

interest. Its rectifying efficiency is at least 10 % and 8 % higher than the rest at −30 dBm and −20 dBm, respectively. Noticeably, the dc output voltage of HSMS-286x is close to 0.7 V at −20 dBm. It is more than two times greater than the second-highest at the same power level, referring to SMS7630's approximate 0.3 V. Moreover, the diode HSMS-286x has a breakdown power level of −8 dBm, which is enough for the ambient RF energy recycling applications. It should be noted that the breakdown power level of each diode varies with its load resistance. Thus, a careful evaluation is recommended for each design scenario.
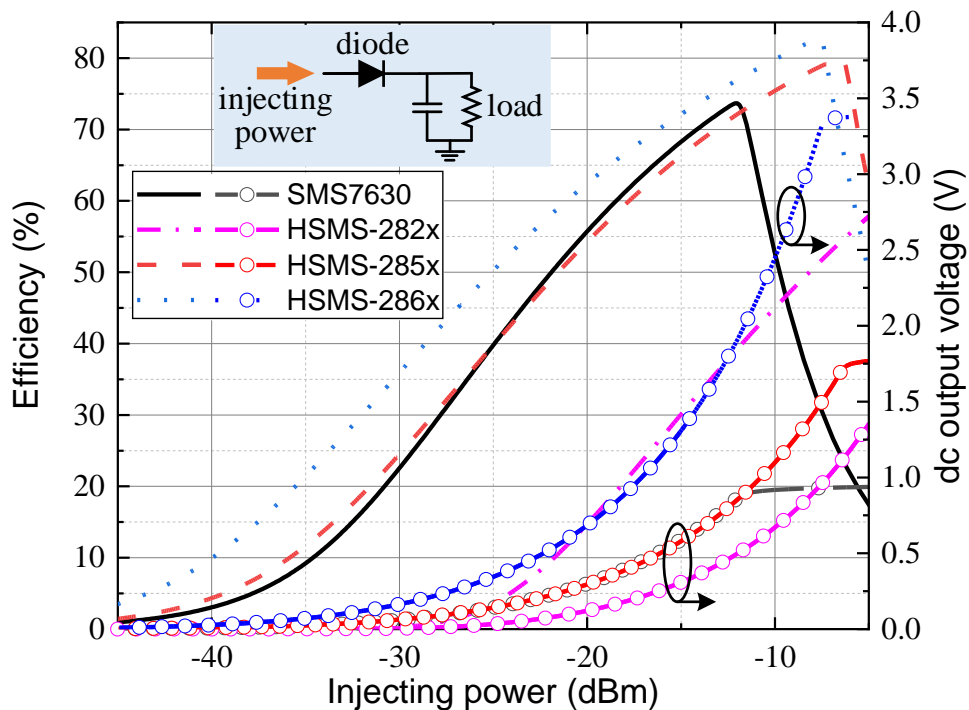
Figure 2.6 Rectifying efficiency and dc output voltage of four selected diodes for far-field WPT rectifiers (Table 2.1) when utilized in a single-series topology. Optimized load resistances for peak efficiency at −20 dBm are 16 kΩ for SMS7630 and HSMS-285x, 75 kΩ for HSMS-286x, and 10 kΩ for HSMS-282x.

Since diodes SMS7630 and HSMS-285x share similar SPICE parameters, as listed in Table 2.1, both diodes present similar responses in rectifying efficiency and dc output voltage, as shown in Figure 2.6. The rectifying efficiency is roughly 24 % and 66 % at −30 dBm and −15 dBm, respectively, for both diodes. The main difference between these two diodes is the breakdown voltage, where HSMS-285x obtains a higher breakdown power level (−6.5 dBm). Thus, its dc output voltage of 1.7 V saturates at a higher level than that of the 0.9 V belonging to SMS7630. As

for the diode HSMS-282x, its rectifying efficiency in the power range of interest is not satisfactory. Nevertheless, with a higher breakdown voltage, HSMS-282x is suitable for high-power rectifier design as rectifying efficiency begins to steadily increase when injecting power exceeds −10 dBm.
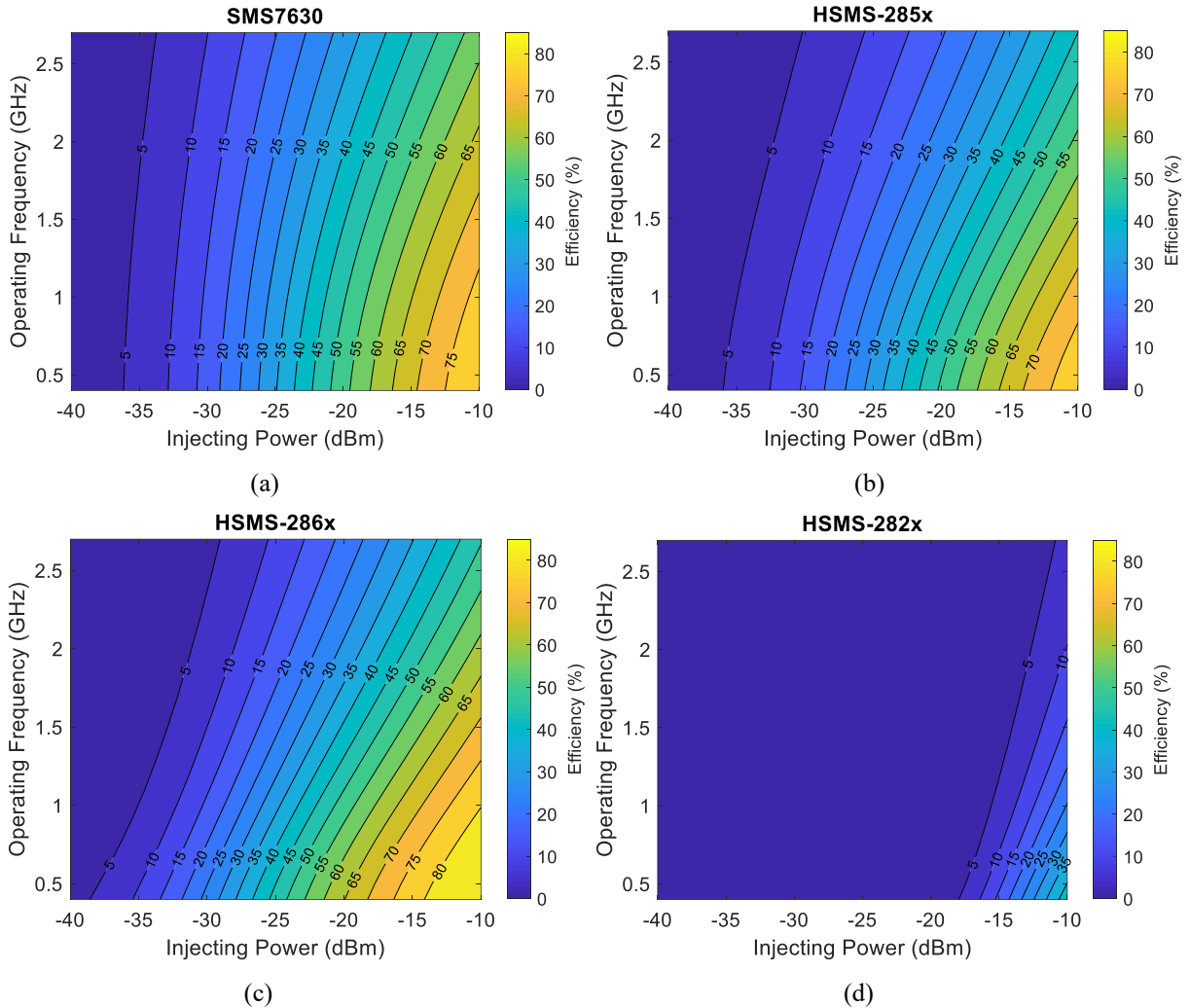
Figure 2.7   Calculated rectifying efficiency of four selected diodes against injecting power (−40 dBm to −10 dBm) and operating frequency (0.4 GHz to 2.7 GHz). Load resistances for each diode are the same as in Figure 2.6. Each subplot contains efficiency contours. (a): SMS7630; (b): HSMS-285x; (c): HSMS-286x; and (d): HSMS-282x.

The operating frequency of diodes also plays a significant role in their rectifying efficiency. Hence, Figure 2.7 attempts to reveal the rectifying efficiency performance of the selected four diodes as a function of injecting power and operating frequency simultaneously. The above results are calculated through the efficiency prediction method reported in [21]. According to the

aforementioned equivalent circuit analysis, as the only contributor to frequency conversion in rectifiers, junction resistance R_j is not frequency-dependent. However, part of the injecting power goes around through the frequency-dependent junction capacitance C_j and are eventually dissipated. Thus, the diode parasitic efficiency due to the junction capacitance C_j varies with operating frequency as seen in Figure 2.7. With a larger C_j, the diode rectifying effiency would decline at a faster rate with an increasing operating frequency. Such a claim can be verified in the comparison between diodes HSMS-286x (C_{j0} = 0.18 pF) and SMS7630 (C_{j0} = 0.14 pF) in Figure 2.7 (a) and (c), respectively. For example, with the input power of −25 dBm, the calculated rectifying efficiency of HSMS-286x is 46.87 % versus 34.65 % of SMS7630 at 400 MHz. When the operating frequency increases to 2700 MHz, the rectifying efficiency of HSMS-286x reduces to 10.95 %, while SMS7630 still obtains an efficiency of 19.77 %. As seen in Figure 2.7 (a) and (b), the diodes SMS7630 and HSMS-285x have similar patterns of rectifying efficiency. Due to a slightly larger junction capacitance C_j, the decreasing rate in rectifying efficiency of HSMS-285x against an increasing operating frequency is larger than that of SMS7630. Figure 2.7 (d) verifies that HSMS-282x is suitable for high-power rectifier applications. Through this investigation, it reveals that SMS7630 is the top choice for far-field WPT rectifier design when the operating frequency goes beyond roughly 1.5 GHz.

2.4.2 **Input Power Enhancement**
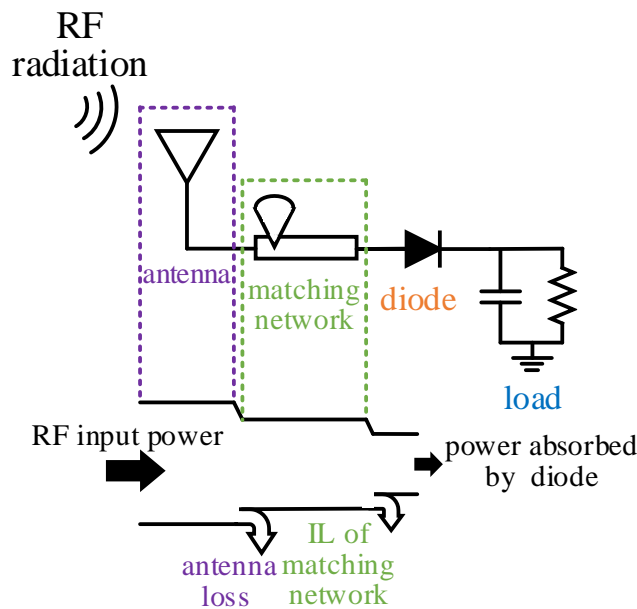
Figure 2.8 Careful design of antenna and matching networks enhances total power absorbed by the diode, finally leading to higher rectifying efficiency.

As shown in Figure 2.6, the rectifying efficiency of diodes ramps up with higher injecting power. Thus, the preceding stages in rectifier design, namely antenna and impedance matching network (Figure 2.8), must be optimized to minimize potential insertion loss. For antenna design, maximizing antenna efficiency entails harnessing the ambient RF energy in free space as much as possible. Multi-band rectennas (rectifying antenna), which can scavenge ambient RF power in multiple bands, are highly desirable [22-25]. As an example, Figure 2.9 (a) illustrates a triple-band rectenna, which covers the frequency bands 0.79 GHz – 0.96 GHz, 1.71 GHz – 2.17 GHz, and 2.5 GHz – 2.69 GHz [22]. Such a triple-band rectenna has already covered major sub-7 GHz communication bands. Besides multi-band rectennas, utilizing an antenna array is a straightforward way to acquire more ambient RF power. It increases the effective antenna aperture since the receiving power of an antenna directly depends on its physical size [26, 27]. However, as the array inevitably occupies more space, it is only suitable when enough room is available for the rectenna. Furthermore, high gain antennas are also preferred in rectenna design to enhance diode rectifying efficiency thanks to a larger input power level. Nevertheless, the broad angular coverage and high gain of a single-element antenna contradict each other. For example, omnidirectional dipole rectennas featuring quasi full spatial coverage are often the first choice to scavenge incoming RF power from various directions. However, the low gains of omnidirectional dipole antennas cannot support an efficient rectifying process inside the rectennas. To overcome this problem, a well-organized scheme of a high-gain antenna array to target ambient RF power in each direction is an intriguing solution shown in Figure 2.9 (b) [28]. Such an idea whereby an array is used to extend the far-field WPT rectifying coverage has been extensively investigated, as it breaks the contradiction of high gain and broad spatial coverage set by one single-element antenna [29-31].
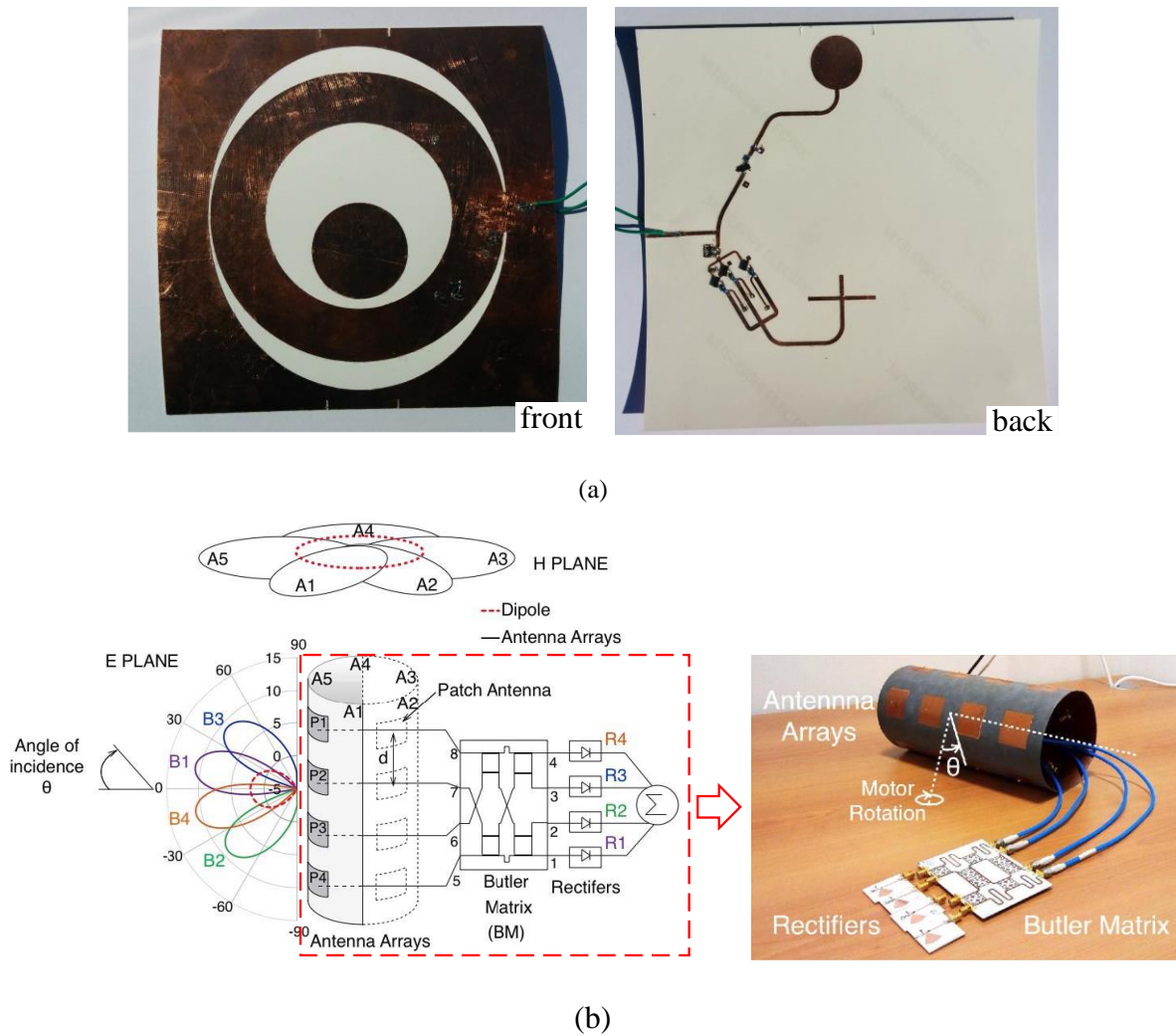
Figure 2.9   (a) Triple-band rectenna reported in [22]. (b) Rectenna with an optimal angular coverage [28].

Besides pervasive ambient RF power, ample vibration, thermal, and solar energy exist in our environment [11]. Cooperatively harvesting two or more of the above energy sources is an efficient way to generate more dc output. Due to different transduction mechanisms, vibration energy is generally converted into low-frequency AC signals first [32]. In contrast, the output of thermal and solar energy conversion is dc power, which does not need any further frequency conversion [33],[34]. Hence, cooperatively collecting from multi-physical sources requires different strategies for power combinations [35]. For hybrid RF and vibration energy harvesting, it is better to inject two power sources into the rectifying diode simultaneously, as seen in Figure 2.10 (a). Measurement results of hybrid energy harvesting show that enhanced total dc output power has

been obtained, compared with the simple superposition of a separate energy harvesting method [36]. By contrast, for thermal/solar energy, combining the rectified dc output power of ambient RF and thermal/solar energy on the load resistance is a more economical way. Figure 2.10 (b) presents an example of a hybrid solar and RF energy rectifier based on flexible substrates [34].

(a)　　　　　　　　　　　　　　　　(b)
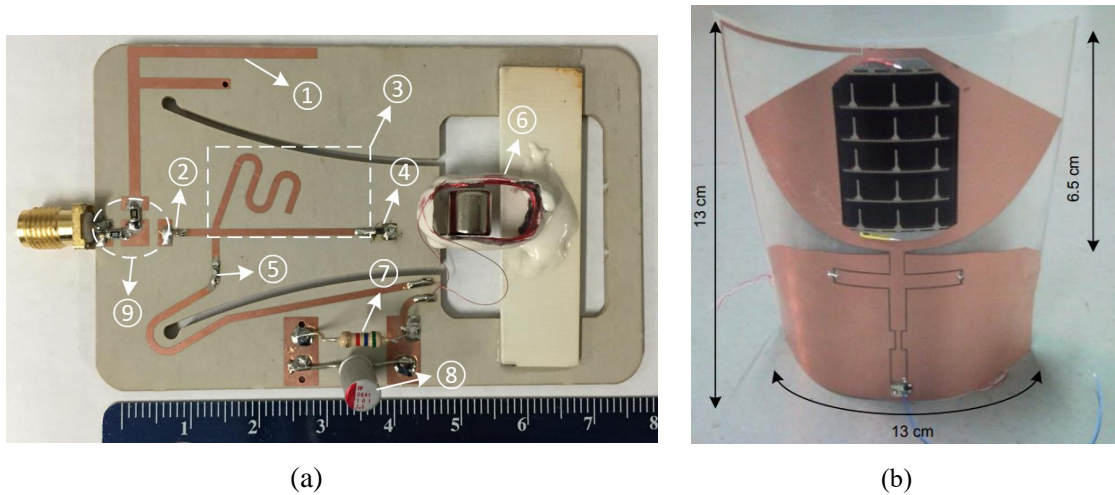
Figure 2.10 (a) Prototypical hybrid RF and vibration energy harvester [37]; (b) Flexible substrate-based hybrid solar and RF energy rectifier [34].

The matching network placed between a receiving antenna and a diode accomplishes impedance transform to maximize power transfer. For a given nonlinear device, the performance of the matching network makes a big difference for the entire rectifying efficiency, as shown in Figure 2.11 (a). Typically, antennas are designed to have a standard 50-Ω impedance. Whereas, Schottky diodes often reflect a high impedance when input power is relatively low. The matching network efficiency η_m can be defined as the power reaching the diode divided by the RF power received by the antenna. And if the Q factor is introduced, η_m can be written as:

$$\eta_m = \frac{1}{1+\frac{Q_r}{Q_m}} = \frac{1}{1+\frac{\sqrt{\frac{R_{high}}{R_{low}}-1}}{Q_m}} \tag{2.4}$$

where Q_m is the Q factor realized by design. Q_r is the required Q factor which is defined by the impedances of antenna R_{low} and diode R_{high} (normally the diode nonlinear junction impedance) in this case. Therefore, if the diode nonlinear junction impedance is higher, it is more challenging to design a high-efficiency/low-loss matching network. It should be noted that η_m is associated

with the ratio of Q_r/Q_m. Based on (2.4), high-impedance antennas can be used to lessen the required Q factor of impedance matching. As one example, a high-impedance and high-Q antenna is reported in [37]. Experimental results show that such an antenna with an impedance of 80 Ω can lead to a 20 % increase in rectifying efficiency compared to a traditional 50-Ω antenna. Another design has demonstrated that with a direct conjugate matching between antenna impedance to diode impedance, the matching network can be eliminated to reduce potential insertion loss [38].

| | (a) | | (b) |
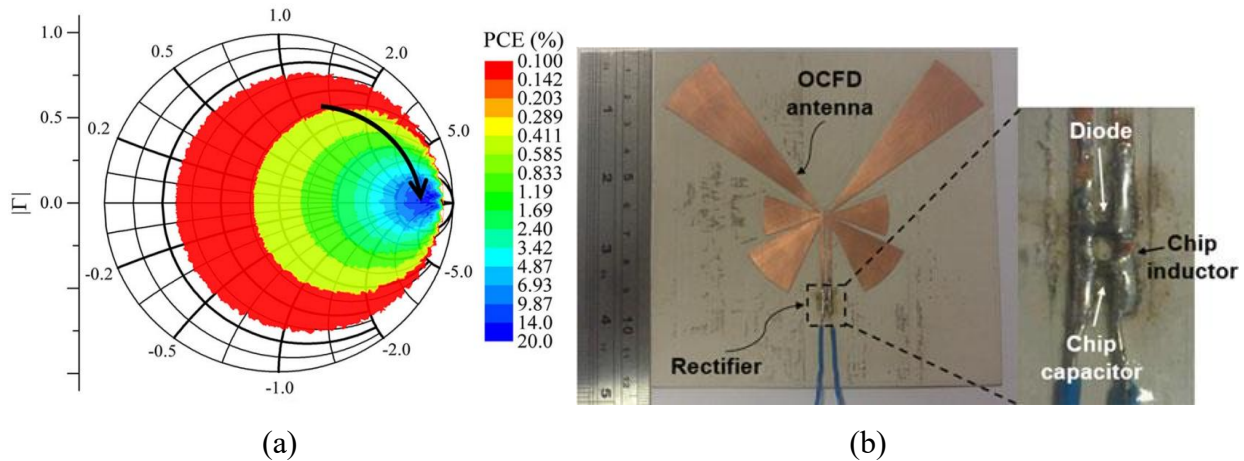
Figure 2.11 (a) Simulated rectifying efficiency corresponding to different matching networks in the Smith chart [39]; (b) High-impedance off-center-fed dipole (OCFD) antenna realizes conjugate matching with diode directly, successfully eliminating the traditional matching network [38].

2.4.3 **Load Resistance Optimization**

The optimal load resistance R_{l_opt} leading to maximum rectifying efficiency can be calculated by setting the derivation of (2.3) to be 0. After some mathematical treatment, R_{l_opt} can be obtained as $R_j + R_s$, which equals to approximately R_j, since R_s is generally much smaller than R_j. Figure 2.12 has displayed diode rectifying efficiency as a function of injecting power and load resistance for diodes SMS7630 and HSMS-286x. The operating frequency is set at 880 MHz. It can be observed that the above calculated optimal load value (R_j) is only valid when the injecting power is relatively low (< -35 dBm). With a stronger injecting power, diodes SMS7630 and HSMS-286x have demonstrated different responses in terms of their optimal load resistance (Figure 2.12). The optimal load resistance of SMS7630 increases. In contrast, with an opposite trend, the optimal load resistance of HSMS-286x continues to decrease at larger injecting power levels.

Optimal load resistance is of paramount importance for maximizing and maintaining the high-efficiency performance of far-field WPT rectifiers. The optimal load resistance depends on injecting RF power, and thus an optimal load tracking method is highly recommended when rectifiers are operating in a large dynamic input power range. The Maximum Power Point Tracking (MPPT) technique is widely used to ensure that optimal load resistance is connected to the rectifiers. For instance, a novel Fractional Open-Circuit Voltage Approximation (FOCVA) method was proposed to obtain the optimal load resistance in [40]. The reported rectifier shows the measured MPPT accuracy over 87 % and a wide working range from −22 dBm to −2 dBm. Another work demonstrating a larger dynamic range from −20 to 20 dBm using the MPPT method is presented in [41]. A measured peak rectifying efficiency reaches 48.19 % with respect to the input power of 0 dBm at 900 MHz.

(a)   (b)
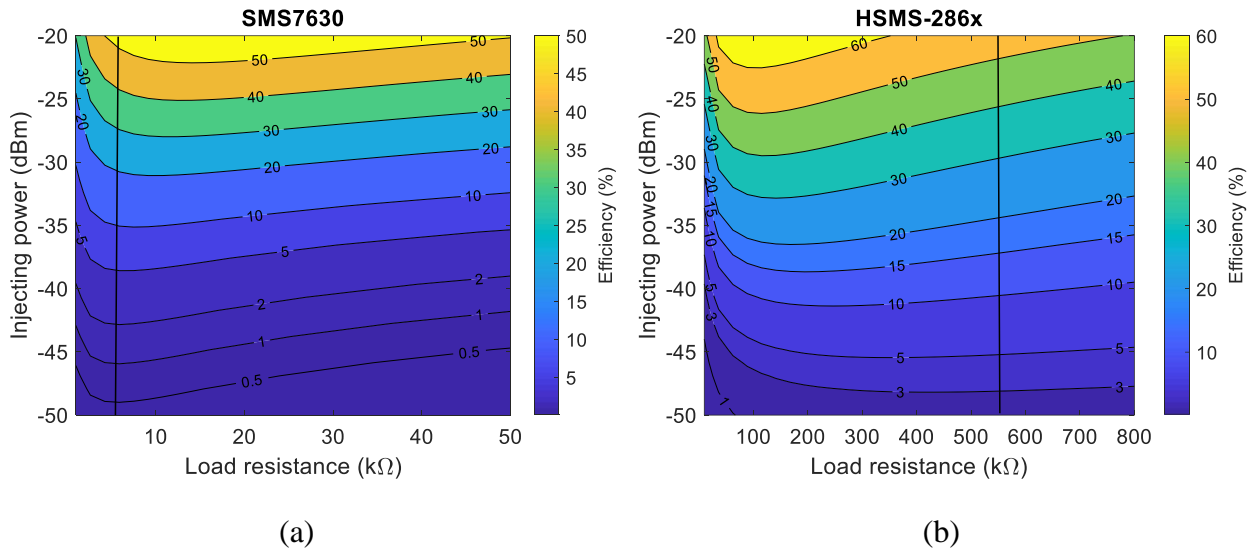
Figure 2.12 Calculated rectifying efficiency as a function of injecting power into diode (−50 dBm to −20 dBm) and load resistance R_l for diode (a) SMS7630 and (b) HSMS-286x. Besides efficiency contours, the vertical line labels the value equivalent to $R_s + R_{j0}$, which is valid for being considered as the optimal load resistance when injecting power is relatively small.

2.5 Analysis of Diode-Based Harmonic Backscattering

When recycling ambient RF power, harmonic backscattering enhances the output of the second-harmonic component. Figure 2.13 (a) presents a typical circuit topology of harmonic backscattering

based on a single Schottky diode [13, 42]. The quarter-wave short-circuited and open-circuited stubs are placed beside the diode to exacerbate the frequency conversion. When the fundamental signal enters the circuit, it sees the open-circuited stub as a short-circuited end due to its carefully designed length. Hence, for the fundamental signal, the equivalent circuit can be simplified in Figure 2.13 (b), where the diode absorbs the ambient RF injecting power. After frequency conversion from the fundamental to the second-harmonic component, the diode can be seen as a power source. At the second-harmonic frequency, the short-circuited stub stays as a short-circuited end. The equivalent circuit in Figure 2.13 (c) clearly explains the situation of diode acting as a second-harmonic power source. Based on this equivalent circuit analysis, the conversion efficiency from the fundamental to second-harmonic frequency can be derived as [13]:

$$\eta_c = \frac{P_{in}}{2} \cdot \left(\frac{\Re_{I0}^2}{4} + \frac{(\omega C_{j0} M R_{j0})^2}{V_j^2} \right) \cdot \text{real} \left(\frac{Z_p^* \cdot Z_p}{Z_p^* + R_s + Z_{out}} \right) \tag{2.5}$$

where $\Re_{I0}$, C_{j0}, R_{j0}, M, and V_j are parameters related to the diode. M and V_j are diode grading coefficient and junction potential, respectively. Z_p and Z_{out} are the source (diode) internal impedance and output impedance, respectively. Like far-field WPT rectifier design, (2.5) can be used as a guideline to enhance total conversion efficiency, in other words, reduce conversion loss, by selecting suitable diode candidates.

(a)

(b)

(c)
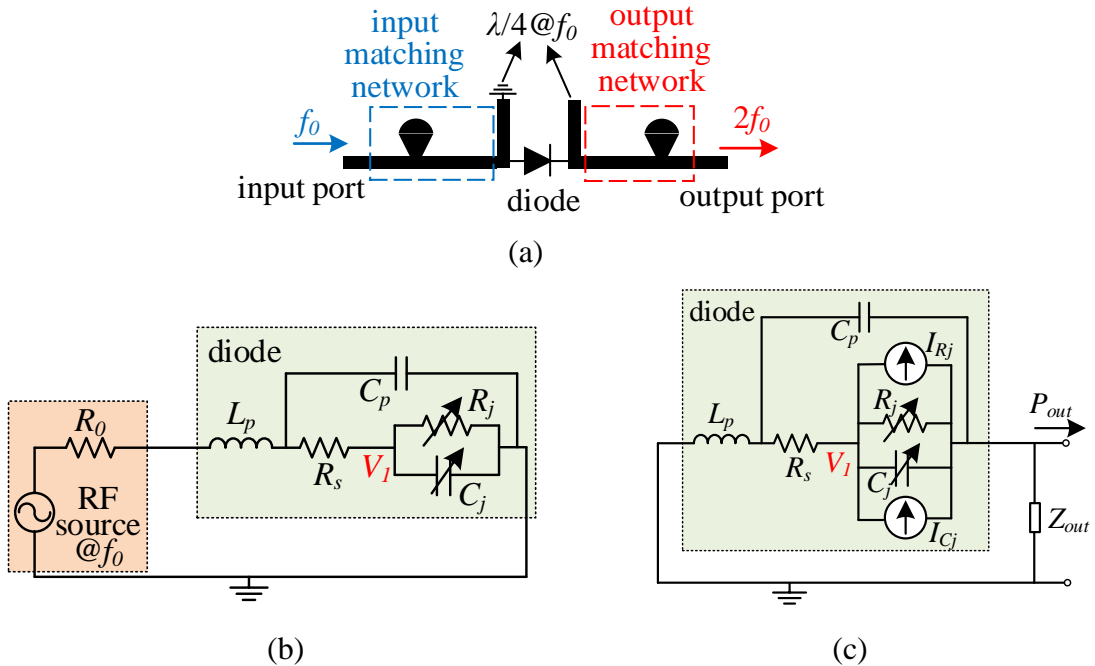
Figure 2.13 (a) Typical circuit topology of harmonic backscattering. (b) Diode absorbs RF input power injected into the circuit. (c) Diode becomes a second-harmonic power source in the circuit.

2.5.1 **Diode Selection for Harmonic Backscattering**

In Table 2.1, four diodes often used in the circuits design of harmonic backscattering are attached [42], [43]. Conversion loss results based on the ADS harmonic balance simulator are presented in Figure 2.14. The operating frequency is at 880 MHz, which is consistent with the above far-field WPT rectifier analysis. Figure 2.14 shows that SMV1430 (a varactor) is a great choice in circuit design of harmonic backscattering in a relatively low-frequency range. When the injecting power is low (−45 dBm), the conversion loss of SMV1430 is roughly 1.5 dB lower than that of its other counterparts. With the injecting power increasing to −25 dBm, the conversion loss gap between SMV1430 and HMPS-282x remains almost unchanged. Yet, on the other hand, the conversion loss of SMV1430 becomes roughly 5 dB lower than that of SMS7630 and HSMS-285x. Due to similar SPICE parameters, both conversion loss curves of SMS7630 and HSMS-285x share the same trend, similar to the analysis case of far-field WPT rectifiers discussed before.
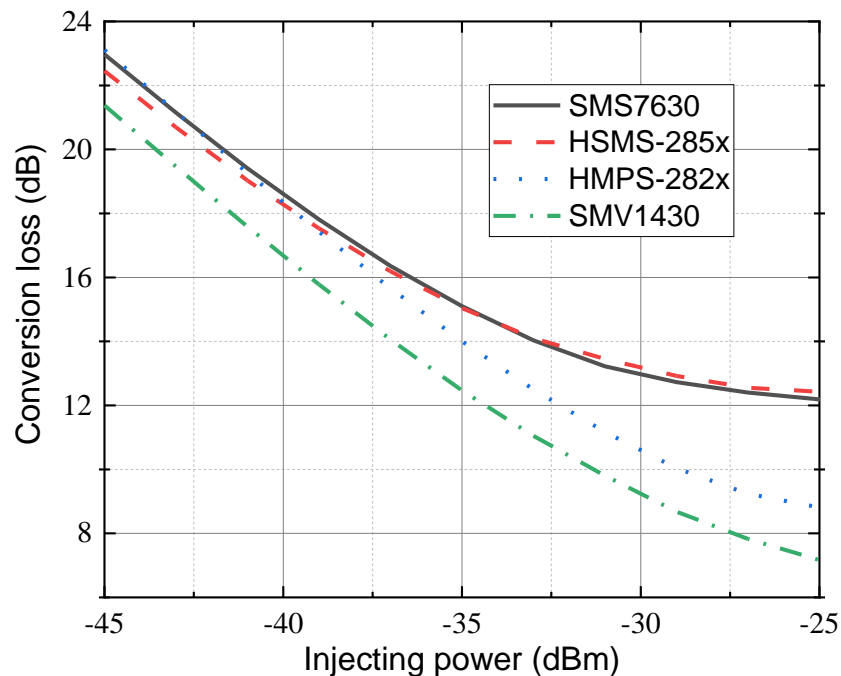
Figure 2.14 Conversion loss results of harmonic backscattering circuits built with four selected diodes (listed in Table 2.1) as a function of injecting power from −45 dBm to −25 dBm.

Across the frequency band of interest (400 MHz to 2700 MHz), the conversion loss performance of harmonic backscattering circuits based on the four selected diodes is investigated. Furthermore, since diodes utilize resistive and capacitive nonlinearity simultaneously in the frequency conversion of harmonic backscattering, contributions due to nonlinear junction resistance and capacitance in the frequency conversion process are also studied. Such investigations are conducted with the aid of an analytical method reported in [13]. The corresponding results are shown in Figure 2.15.

For diodes SMS7630 and HSMS-285x, the influence due to operating frequency on the conversion loss is less significant than in HMPS-282x and SMV1430, which indicates that when operating frequency increases, the conversion loss of HMPS-282x and SMV1430 will degrade. For instance, the conversion loss results of HMPS-282x and SMV1430 are about 7.5 dB at – 30 dBm when the operating frequency is 880 MHz. The results degrade to roughly 25 dB at the same power level if the operating frequency increases to 2400 MHz, which means a 17.5-dB degradation due to frequency increase. Under the same conditions, the conversion loss degradation of SMS7630 and HSMS-285x are roughly 4.5 dB and 6.5 dB, respectively, when the operating frequency changes from 880 MHz to 2400 MHz. Figure 2.15 (f) and (h) can support such a claim, where nonlinear junction capacitance dependent on operating frequency is dominant for diodes HMPS-282x and SMV1430 during the frequency conversion process. Hence, the conversion loss performance of the above two diodes becomes worse than SMS7630 and HSMS-285x with a higher frequency.

At a fixed operating frequency, the conversion loss of HMPS-282x and SMV1430 has smaller variations against injecting power compared to SMS7630 and HSMS-285x. This is due to different mechanisms of resistive and capacitive nonlinearity. During frequency conversion, the diode nonlinear junction resistance has by-products in the form of Joule heating. By contrast, nonlinear junction capacitance is a more efficient choice for frequency conversion without any Joule heating. Therefore, diodes SMS7630 and HSMS-285x, whose both nonlinear junction resistance and capacitance are major contributors in frequency conversion (see Figure 2.15 (b) and (d)), sacrifice more energy when the injecting power increases. Based on the above discussion, diodes SMS7630 and HSMS-285x are suitable for high-frequency and relatively high-power design [44]; whereas, diodes HMPS-282x and SMV1430 are good for low-frequency and low-power scenarios [45].

(a)

(b)

(c)

(d)

(e)

(f)

(g)   (h)
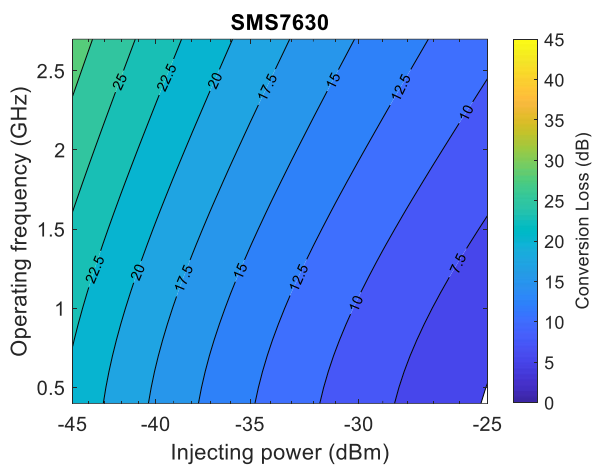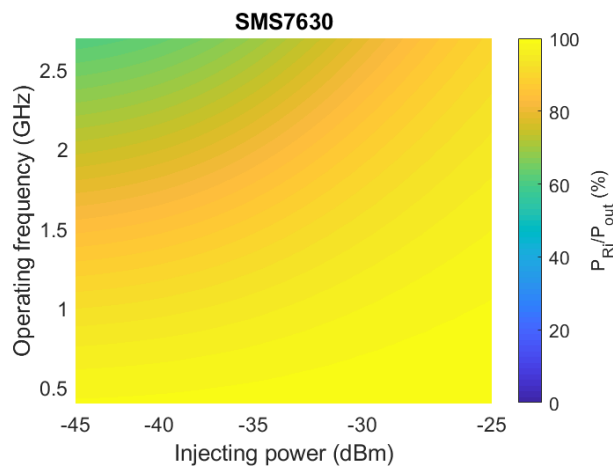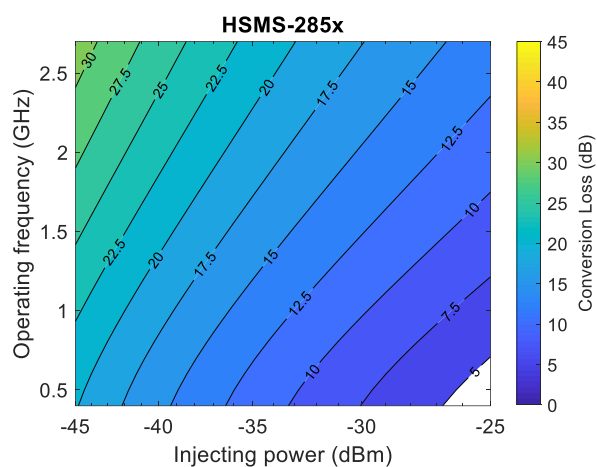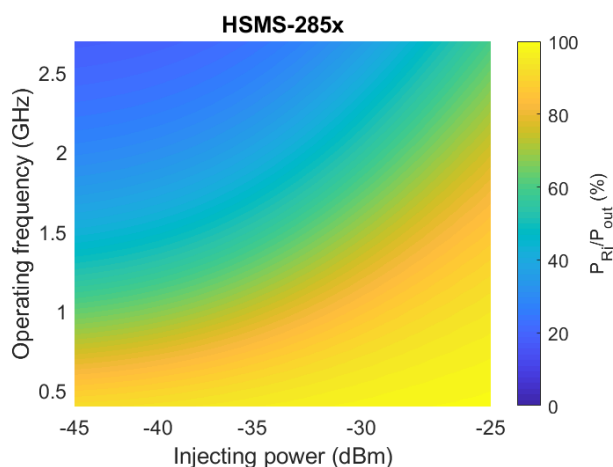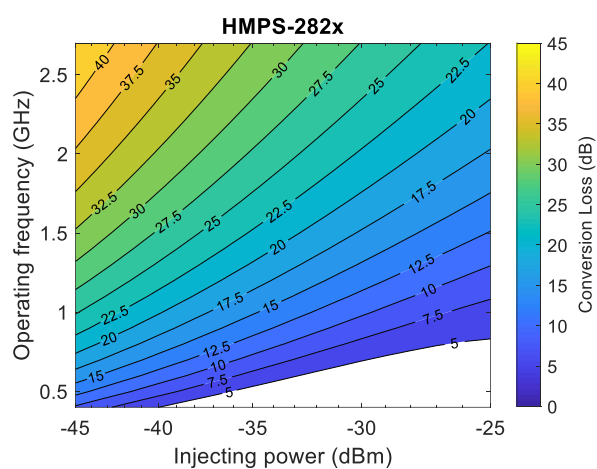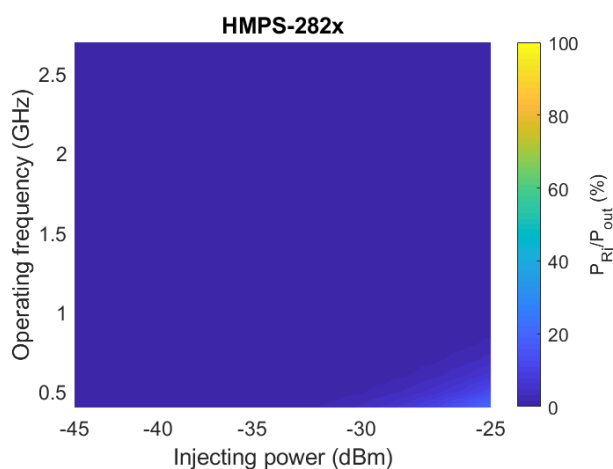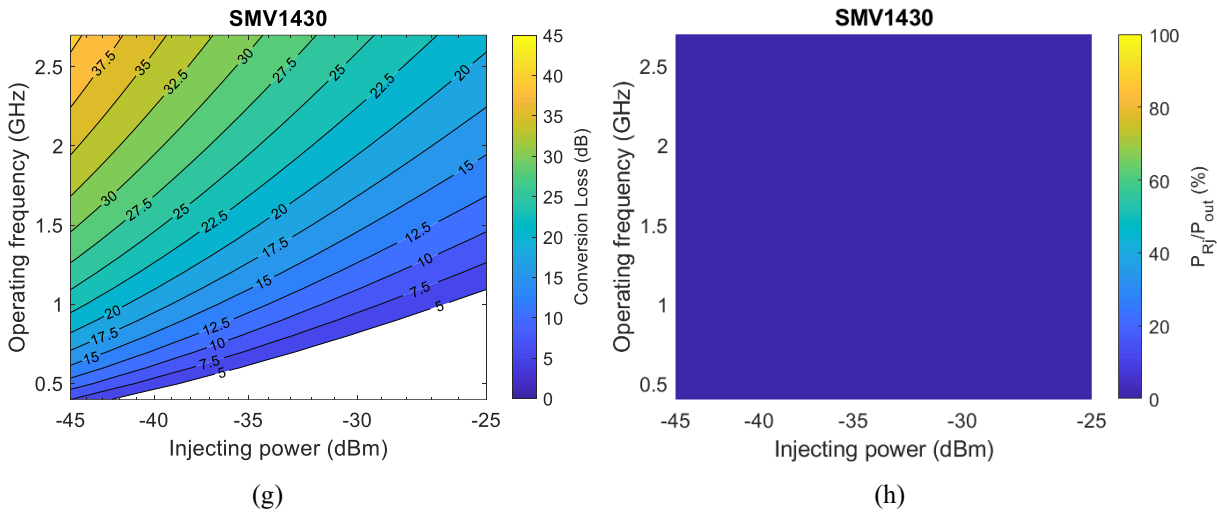
Figure 2.15 Conversion loss and ratio of power due to resistive nonlinearity over total generated second-harmonic power as a function of operating frequency and injecting power: (a)&(b) SMS7630, (c)&(d) HSMS-2850, (e)&(f) HMPS-282x, and (g)&(h) SMV1430. Color bars are consistent for each diode.

2.5.2 **Applications of Harmonic Backscattering**

Harmonic backscattering has been successfully employed to detect insects and amphibians, as shown in Figure 2.16 [46-50]. Such applications usually feature simple loop or dipole antennas loaded with a nonlinear device to significantly reduce the total weight. Direct matching between antennas and nonlinear devices are often implemented in these designs. Impedance tuning elements are sometimes introduced for performance enhancement [51].
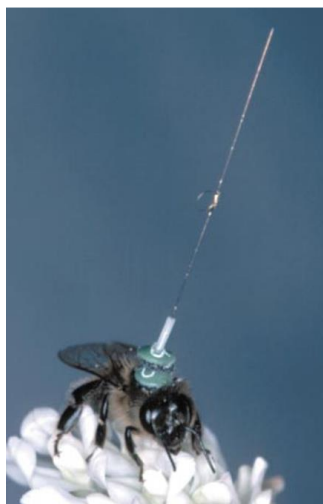
(a)   (b)

Figure 2.16 (a) Harmonic transponder placed on a bee for tracking its flight [46]; (b) Frog wearing a tracking transponder [48].

The above simple detection of insects and amphibians usually does not require complicated transponder/tag circuits. For other scenarios, such as structure fatigue detection, liquid sensing, and temperature sensing, certain information must be loaded into the backscattering signal. Therefore, PCB-based harmonic backscattering circuits should be carefully designed for structure fatigue detection [52], liquid sensing [53], temperature reading [54], and RECCO rescue system [55]. In these cases, useful information is often translated into a frequency shift of the backscattering signal. Sniffer devices then decode the frequency shift and acquire real crack width, liquid, or temperature information. Figure 2.17 has demonstrated two application scenarios for harmonic backscattering to detect structure crack width and liquid volume.

| (a) | (b) |
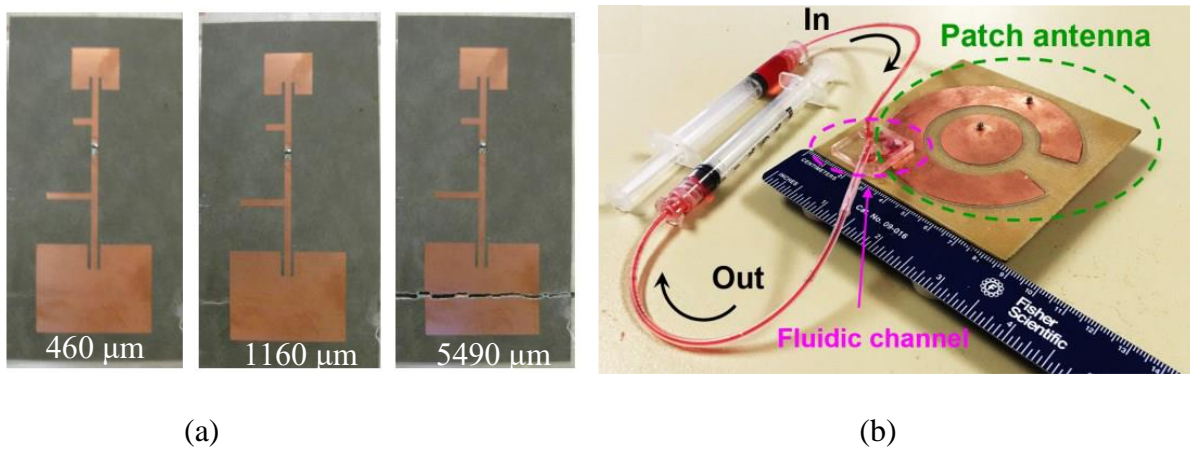
Figure 2.17 Harmonic backscattering applied for (a) crack width [52] and (b) liquid detections [53].

2.6 **Reconfigurability: Single Diode-Based Far-Field WPT and Harmonic Backscattering**

As mentioned before, the primary difference between far-field WPT and harmonic backscattering is picking out the desired frequency component. It is possible to implement both functions based on one single Schottky diode for a reconfigurable and compact design. Figure 2.18 demonstrates such an idea, with both functions integrated on the same substrate using one Schottky diode [56]. A switch connected to the open-circuited stub near the output port is the critical component to

control/select functions of either far-field WPT or harmonic backscattering. For example, if the switch is connected, the harmonic backscattering output is thus short-circuited, and the nonlinear circuit design becomes a far-field WPT rectifier. All dc output is accumulated at the load resistance. Once the switch is disconnected, this design evolves into a circuit for harmonic backscattering. Its circuit topology and equivalent circuit models are the same as those in Figure 2.13. Second-harmonic signals are generated and can reach the output port. Note that most of the circuit space (> 90%) of this reconfigurable design has been shared by both functions of far-field WPT and harmonic backscattering (Figure 2.18 (b)).

(a)

(b)
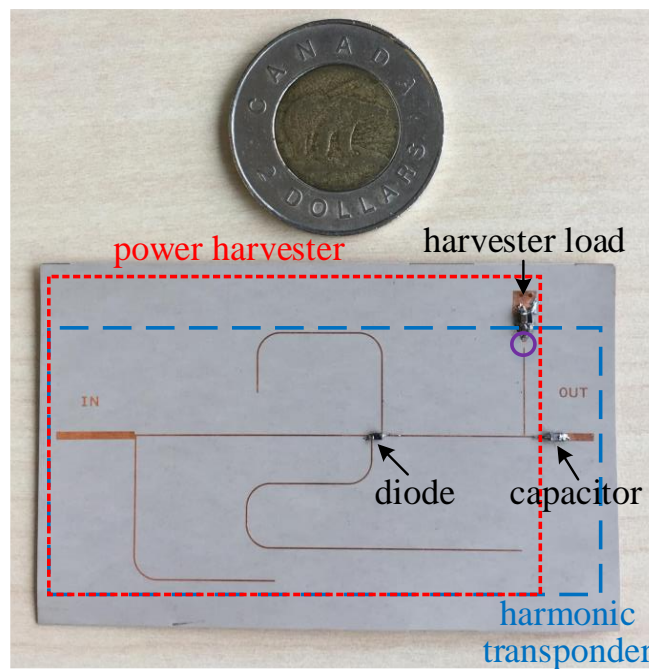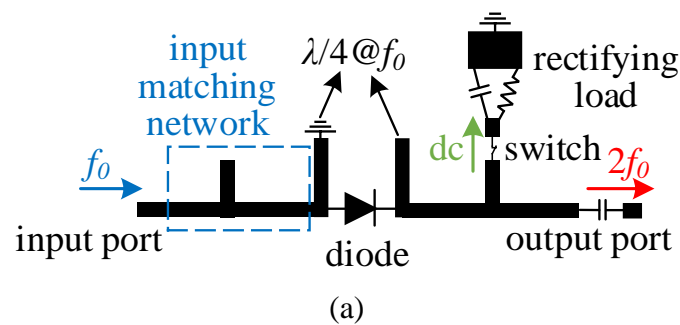
Figure 2.18 Reconfigurable nonlinear circuit for far-field WPT and harmonic backscattering: (a) schematic and (b) prototype.

As a preliminary design, the switch in the prototype is represented by a 0-Ω resistor. A normally-on switch is required in this design to realize function switching between far-field WPT and harmonic backscattering. For a complete design, the initial operation mode will be a far-field WPT rectifier, which enables voltage/energy collection on the load resistance. Once the load has gathered enough energy, it can trigger the switch to disconnect. Therefore, the design enters a harmonic backscattering mode and generates second-harmonic signals, which are further backscattered to sniffer devices. When power across the rectifier load goes below the switching threshold due to consumption, such a reconfigurable design will go back to the far-field WPT rectifier mode to collect power again.

2.7 Outlook
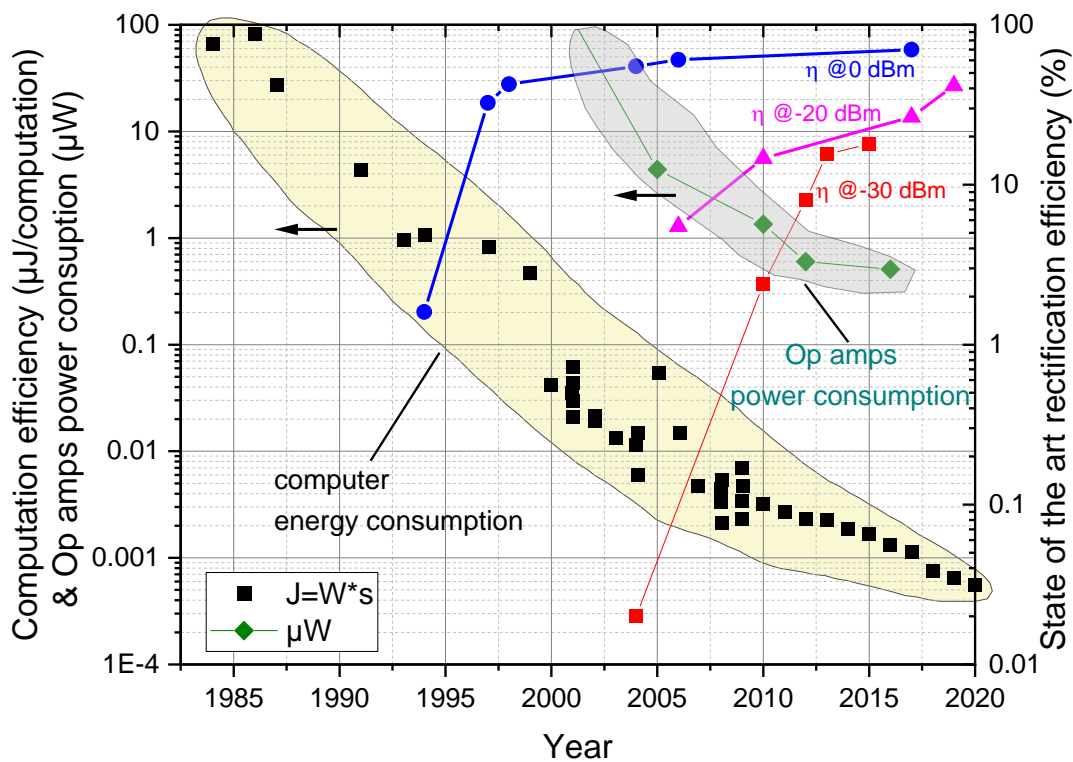
Figure 2.19 Evolution of the peak-output energy efficiency of computation (energy required by each computation) in the last four decades [57-59]. The energy required by the latest ultra-low-power operational amplifiers (Op amps) during one-second operation [60-63]. The rectifying efficiency of the latest far-field WPT works at input power levels of 0 dBm, −20 dBm, and −30 dB [21, 39, 64-71].

The main driving force for any new technology towards maturation are the applications. Over the past several decades, solid-state technology continued to get improved following Moore's law until the turn of the millennium [57]. Although there have been just incremental performance improvements with cutting-edge chip development in the last two decades, the peak-output energy efficiency of computation still doubles every 2.6 years [59]. The latest solid-state technology has enabled computation and operational amplifiers to work in the nanopower range, as shown in Figure 2.19. Meanwhile, the maturation of diode and rectifying design technology continues to drive up the efficiency of far-field WPT, especially in a power range under −20 dBm. Both evolution trends have timely bridged the gap between the low-duty, low-power electronics-based applications and the ambient RF power enabled far-field WPT. Figure 2.19 displays such a historical trend. And more ambient RF powered battery-free applications are poised to emerge in the future.
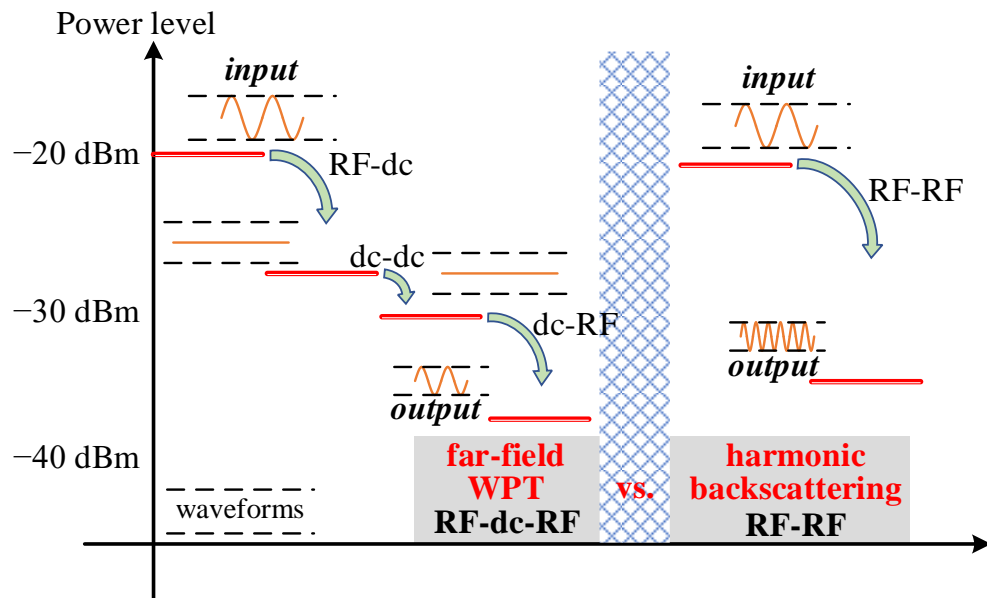
Figure 2.20 Comparisons of power budget and waveform change between far-field WPT and harmonic backscattering used in applications.

As for the harmonic backscattering, this may be a more power-efficient solution for certain applications compared to the far-field WPT. Figure 2.20 presents the differences in power budget and waveform change between far-field WPT and harmonic backscattering used in applications. Far-field WPT converts an incident sinusoidal wave into dc through the rectifying process first. If the input power is −20 dBm, such RF-dc conversion efficiency can reach roughly 20 % [21]. Then,

to enable specific applications, the rectified dc voltage usually needs to be amplified, which requires a dc-dc step-up converter. Based on recent works [72], this dc-dc conversion efficiency is estimated as 50 % at a low-power level. Finally, an integrated voltage-controlled oscillator (VCO) featuring low power and low phase noise is the critical component for realizing communications. The dc-RF conversion efficiency of such VCOs are normally low: 17.5 % is our estimation here [73]. For far-field WPT, the entire process of RF-dc-RF conversion has been shown in Figure 2.20, where the power budget estimation and waveform change are also included. By contrast, the harmonic backscattering shows a relatively simple conversion, i.e., fundamental RF to its second harmonic (RF-RF). Compared to the far-field WPT, the final power loss of harmonic backscattering would be smaller if the input power is −20 dBm [13]. It is worth noting that the power budget shown in Figure 2.20 is a rough estimation, as they depend on specific applications. Far-field WPT can support more complicated tasks at the cost of larger power consumption. Whereas, less power-hungry harmonic backscattering is more suitable to handle simple applications. Indeed, the superior solution will be a proper reconfigurable design with two functions integrated for scavenging ambient RF energy more efficiently.

CHAPTER 3   ARTICLE 2: DYNAMIC AMBIENT RF ENERGY MAPPING OF MONTREAL FOR BATTERY-FREE IOT SENSOR NETWORK PLANNING

Xiaoqiang Gu, Louis Grauwin, David Dousset, Simon Hemour, and Ke Wu

Submitted to the *IEEE Internet of Things Journal*

This work summarizes an outdoor dynamic measurement of ambient radiofrequency (RF) power density in the core areas of Montreal, which can eventually be exploited for possible battery-free IoT sensor network planning. The measurement covers a frequency range of 400 MHz to 2700 MHz. The power density along major streets, roads, and highways is captured and analyzed, which differs from previous stationary measurements. Results indicate that cellular communication bands (GSM/LTE850 and LTE700) are the best choice for RF energy recycling in downtown (populated) areas. In contrast, in suburban areas where cellular communication signals are generally weak, the DTV band is a good choice. Moreover, one separate measurement at a fixed location is conducted on a typical workday to study the effects of foot traffic on ambient RF power density. Results illustrate that no obvious fluctuations are detected during this daytime measurement. With the advance of far-field wireless power transfer and backscattering techniques, ambient RF power-enabled battery-free IoT sensors are feasible and will contribute to the planning and implementation of a smarter, greener city.

3.1 Introduction

Urban development and expansion are the most significant engine of economic growth in modern history. In the 1950s, only 30 % of the global population lived in urban areas. That rate increased to 54 % in 2015 and is projected to reach 66 % in 2050, meaning that close to 7 billion people will live in urban areas in 30 years [74]. However, urban sprawl has been a big concern for many people. Thus, there is an urgent need for smarter and greener cities, which requires transformative solutions to handle potential global environmental and energy crises.

One of the foundations to build a smarter and greener city is the deployment of millions of Internet of Things (IoT) sensors with lower energy consumption for efficient city operation and management [75]. Hence, dry cell batteries or power cord connections for energizing IoT sensors cannot sustain such development. By recycling ambient radiofrequency (RF) energy in cities, battery-free IoT sensors can become a silver bullet for tackling global environmental and energy crises [76]. Two mainstream techniques, namely the far-field wireless power transfer (WPT) and ambient backscattering, can be applied for realizing battery-free IoT sensors. Far-field WPT converts ambient RF power into a dc output, which acts as a power source for IoT sensors [20]. Depending on system topologies and applications, ambient backscattering may have a far-field WPT module for communication [77], or it may simply utilize entirely passive sensor tags [78], [13]. Both techniques rely on the ambient RF energy available in the free space of cities, which is an ideal stable power source for battery-free IoT sensors. As shown in Figure 3.1, primary outdoor ambient RF sources in free space are TV broadcasting towers, cellular base stations, and Wi-Fi access points. In urban and suburban areas, such ambient RF sources are usually pervasive and abundant. To assess the feasibility of recycling ambient RF energy to power an extensive network of IoT sensors, researchers must know the power density of ambient RF energy in free space, which is the first and most paramount work.
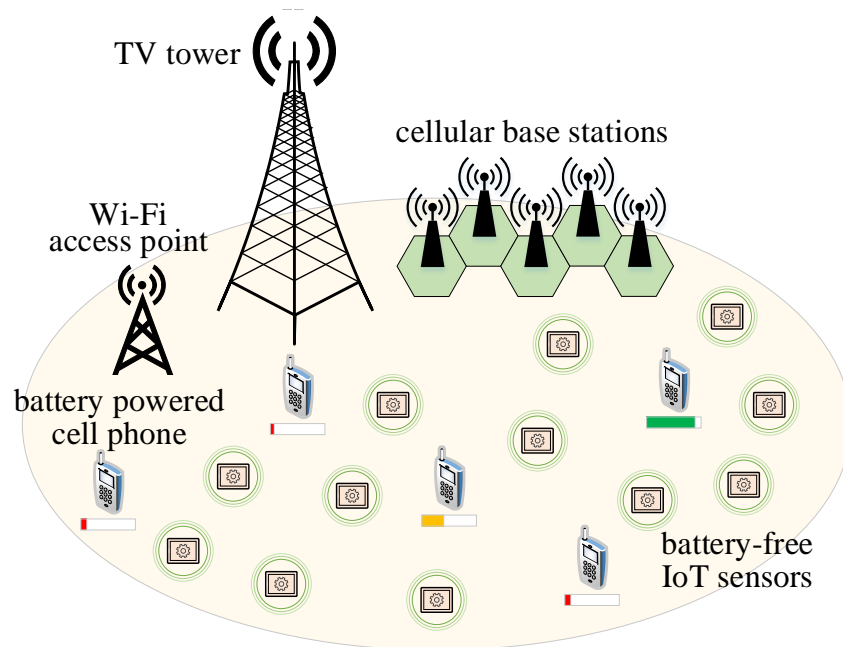
Figure 3.1 Ambient RF power energizing numerous battery-free IoT sensors distributed in cities.

Table 3.1 Measurement results of ambient RF energy density across the world

Testing time & city	No. of testing points	Frequency bands			
		DTV	LTE/GSM700/850/900	LTE/GSM1700/1900	Wi-Fi
2008[*] [79] Eindhoven, Netherlands	–	–	0.1 mW/m^2 ~ 1 mW/m^2 (25 m ~ 100 m)	0.1 mW/m^2 ~ 1 mW/m^2 (25 m ~ 100 m)	10 μW/m^2 (7.05 m) 5 μW/m^2 (8.05 m)
2009 [80] Tokyo, Japan	16	2.3 V/m (500 m) 0.8 V/m (1000 m)	–	0.7 V/m	–
2012 [81] Kyoto, Japan	23	-38 dBm	-25 dBm (500 m)	–	–
2013 [7] London, UK	270	-60.5 dBm/cm^2	-44.4 dBm/cm^2	-40.7 dBm/cm^2	-67.4 dBm/cm^2
2013 [82] Barcelona, Spain	6	–	-52.88 dBm	-62.05 dBm	–
2014 [83] Brasilia, Brazil	4	-30 dBm (1000 m) -25 dBm (close to TV tower)	–	-50 dBm	–
2014[#] [84] Bristol, UK	5	0.0175 nJ/min	0.3023 nJ/min (200 m)	0.0383 nJ/min	0.2129 nJ/min (2 m)
2015[†] [85] Loughborough, UK	5	-81.95 dBm/cm^2	-89.31 dBm/cm^2	-79.54 dBm/cm^2	-93.23 dBm/cm^2
2015 [86] Shunde, China	2	–	-36 dBm	-48 dBm	-65 dBm
2016[‡] [8],[87] Paris, France	20	0.37 V/m (10 m ~ 100 m)	0.34 V/m (10 m ~ 100 m)	0.32 V/m (10 m ~ 100 m)	0.44 V/m (10 m ~ 100 m)
2018[*] [5] Boston, USA	46	3 %	-11.1 dBm, 92 %	5 %	–
2019 [9] Cairo, Egypt	5	-60 dBm (3200 m)	-50 dBm (1000 m)	-45 dBm (1000 m)	–

[*] Part of data extracted from previous measurements in 2001.

[†] Indoor measurements (manufacturing factory).

[*] Measurement was done in 2016. Results indicate percentage times that this channel contains the highest RF energy among all frequency bands.

[#] Indoor measurements (office and residency).

[‡] Data extracted from measurements done by ANFR.

Telecommunication development in the last two decades has been revolutionary, from 2G and 3G to the maturation of 4G and beyond. As of 2020, after initial trials, several countries/regions are soon to kick off 5G services at a large scale [88]. As new cellular base stations are implemented, more frequency bands and denser signals will emerge, which will increase available ambient RF energy in free space. As demonstrated in Figure 3.1, in addition to mobile communication bands, ambient RF power from TV broadcasting and Wi-Fi hotspots are the other two major contributors. So far, multiple ambient RF energy measurements were carried out in different cities across the world, as briefly summarized in Table 3.1 [5, 7-9, 79-87, 89]. For simplicity purposes, Table 3.1 presents four groups of frequency bands, i.e., digital TV (DTV) broadcasting (450 MHz – 650 MHz), lower and higher mobile communication bands (700 MHz – 900 MHz and 1700 MHz – 1900 MHz), and Wi-Fi band (2450 MHz). Most of the measurements have limited testing points, usually fewer than 10. Though in London [7], RF signal levels were tested outside of 270 underground stations, these locations have a potentially higher RF density due to heavy foot traffic, thus, not representing a general case. To verify if RF power levels were set to comply with regulatory exposure limits, the National Frequency Agency of France (ANFR) has conducted wide-range measurements of ambient RF signal levels [87]. Still, each measurement was done at one location targeting specific RF transmitters, thereby making measurement results still geographically discrete.

In this work, an entirely different approach was taken. An outdoor dynamic measurement with a good diversity of geolocations and conditions was carried out on the Island of Montreal. This measurement covers highways, major roads, crowded shopping streets, and ordinary residential streets. RF density is acquired every second during measurements, and the results are visualized and identified on maps with a color bar indicating intensity. Moreover, a daytime measurement at a fixed location in Downtown (DT) Montreal was also conducted to investigate signal density variation on a typical workday. Based on all the measurement results, a detailed discussion on the development of battery-free IoT sensors based on the recycling of ambient RF energy is provided. A feasibility study and outlook of potential applications are also included.

3.2 Ambient RF Frequencies & Methodology

Abundant ambient RF signals exist in the free space of cities across a wide frequency range. In rectifier design, a low frequency may result in a large form factor, while a high frequency would

introduce severe propagation loss between the transmitter and rectifier. Thus, the measurement in this work focuses on a frequency range of 400 MHz to 2700 MHz. Figure 3.2 presents major frequency spectrum segments over this band according to the policy of radio spectrum allocations in Canada. Up and down arrows denote uplink and downlink channels in Figure 3.2, respectively. Moreover, seven frequency bands can be categorized, namely DTV, LTE700, GSM/UMTS/LTE850, UMTS/LTE1700/2100, GSM/UMTS/LTE1900, Wi-Fi, and LTE2600. Since UMTS bands entirely overlap the LTE bands and the LTE service is dominant nowadays, UMTS will be removed when referring frequency bands. For example, GSM/UMTS/LTE850 is simplified to GSM/LTE850 for the remainder of this work. Corresponding to Figure 3.2, Table 3.2 has listed all frequency bands in detail. Note the growing interest beyond 2.7 GHz thanks to the 3.5 GHz band allocation for 5G and to the 6 GHz unlicensed bands for emerging Wi-Fi 6 or 6E. However, they are still in the planning or trial stages, so the measurements would not be considered over those frequency ranges even if 5.8 GHz unlicensed bands are used extensively.

Table 3.2 Ambient RF sources in free space (400 MHz − 2700 MHz)

Band[*]	RF sources	Uplink (MHz)	Downlink (MHz)
	DTV (ch.[#] 14 - 36)	470 ~ 608	
	DTV (ch.[#] 38 - 51)	614 ~ 698	
12	LTE700	699 ~ 716	729 ~ 746
13	LTE700	777 ~ 787	746 ~756
17	LTE700	704 ~ 716	734 ~746
29	LTE700	N/A	717 ~ 728
	GSM850	824.2 ~ 848.8	869.2 ~ 893.8
5	UMTS/LTE850	824 ~ 849	869 ~ 894
4	UMTS/LTE1700/2100	1710 ~ 1755	2110 ~ 2155
66	LTE1700/2100	1710 ~ 1780	2110 ~ 2200
	GSM1900	1850.2 ~ 1909.8	1930.2 ~ 1989.8
2	UMTS/LTE1900	1850 ~ 1910	1930 ~ 1990
	Wi-Fi	2401 ~ 2473	
7	LTE2600	2500 ~ 2570	2620 ~ 2690

[*] LTE bands only   [#] channels in short
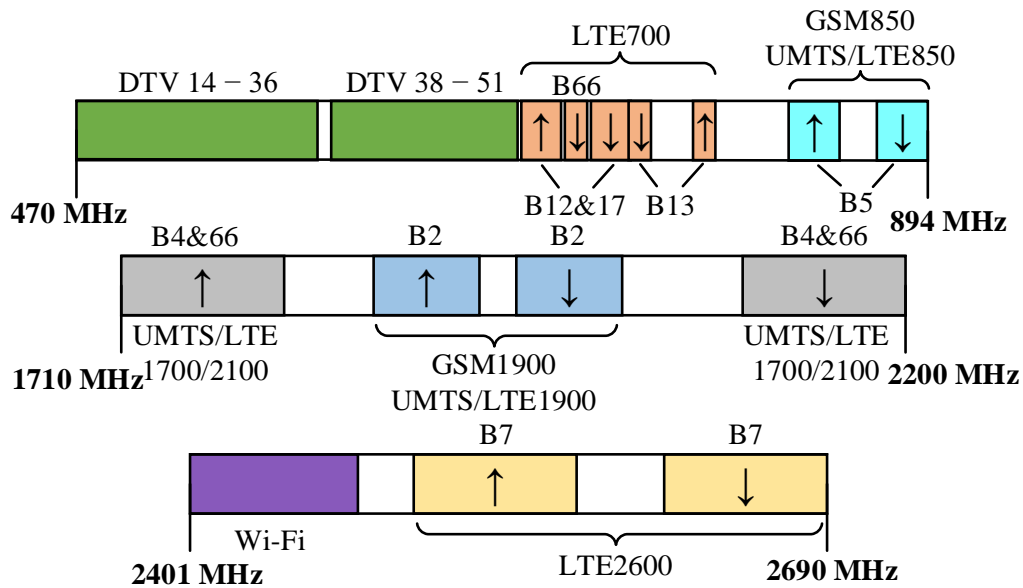
Figure 3.2 Available ambient RF sources in free space (400 MHz to 2700 MHz) according to radio spectrum allocations in Canada. Note that the space in the spectrum segments is not proportional to the actual amount of frequency spectrum occupied.

After identifying the target frequency range (400 MHz to 2700 MHz), preparing and gathering the necessary equipment was the next step for measurements. For correctly receiving ambient RF energy in free space, a wideband omnidirectional antenna N6850A from Keysight was used (Figure 3.3 (a)). It has an operating frequency range of 20 MHz to 6 GHz, which is good enough for our bands of interest. Its radiation patterns at three typical frequencies (500 MHz, 1 GHz, and 3 GHz) taken from the product datasheet are presented in Figure 3.3 (b). Moreover, its average gain over the entire frequency range of interest (400 MHz to 2700 MHz) is uniform, about −1 dBi [90]. Another key equipment to implement this dynamic measurement is a handheld Fieldfox microwave analyzer N9951A, also acquired from Keysight. It can detect and record RF power levels in a frequency range of 300 kHz to 44 GHz, which covers the frequency band of interest for the measurement. It works in a classical spectrum analyzer mode during the measurement. Besides tracking ambient RF energy levels, obtaining and identifying the corresponding geographical locations are as crucial for mapping the measured data. Hence, an external GPS tracker was employed and connected to the Fieldfox microwave analyzer. To avoid the shielding effect of the metallic vehicle roof, both the antenna and GPS tracker are placed outside on the roof of the vehicle

(Figure 3.3 (a)). Such a setup can also minimize any potential interference coming from cell phones or laptops belonging to the testing personnel sitting inside the vehicle.

<div align="center">(a)   (b)</div>
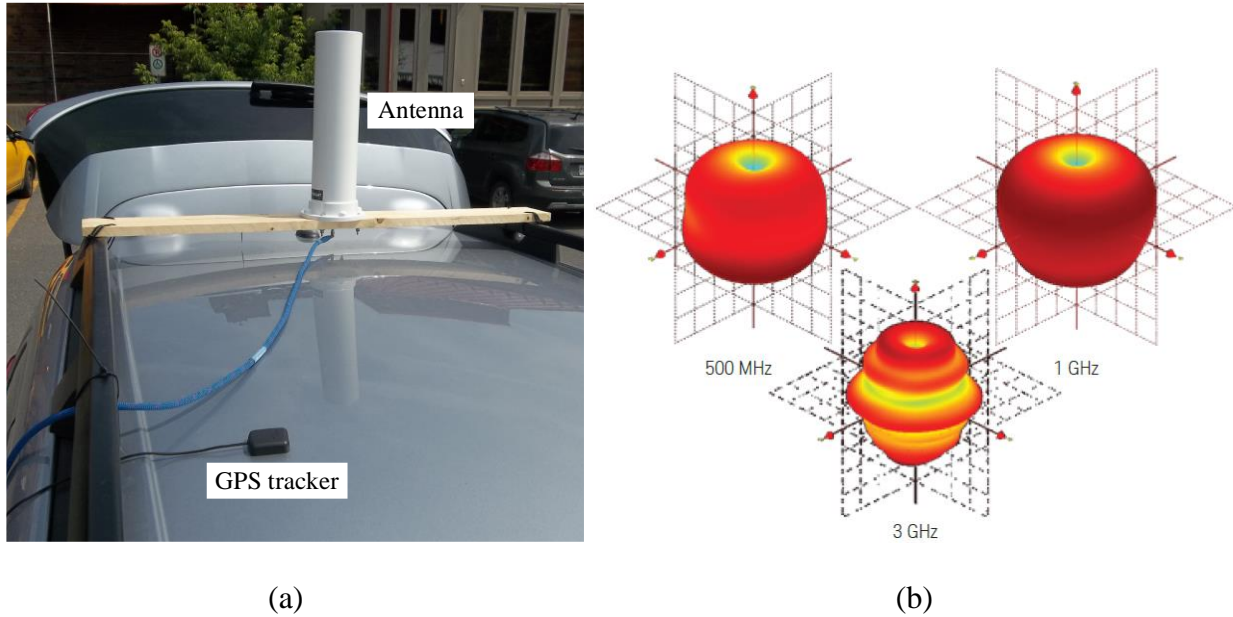
Figure 3.3   (a) Antenna and external GPS tracker are placed on the vehicle roof. (b) Radiation patterns of the antenna at 500 MHz, 1 GHz, and 3 GHz obtained from its datasheet [93].

The complete setup is presented in Figure 3.4. The handheld Fieldfox microwave analyzer is placed inside the vehicle and monitored by the testing personnel. During measurement, our vehicle was at a relatively low speed, about 25 km/h to 30 km/h, to ensure a good RF signal reception. At this speed, the Fieldfox microwave analyzer is set to measure and record ambient RF signal density roughly every second, which is an optimal trade-off between data size and measurement coverage. The testing personnel paused the Fieldfox microwave analyzer each time the vehicle stopped at traffic lights to avoid recording repetitive measurement data. The entire frequency band (400 MHz to 2700 MHz) has been broken down into 1001 points, which translates to a frequency increment of around 2.3 MHz in this measurement. Note that this entire measurement was carried out in the summer season, from July 10, 2019 to August 16, 2019. Also, each set of measurements was conducted under relatively consistent weather circumstances for a fair comparison. In our case, we had either sunny or cloudy days.
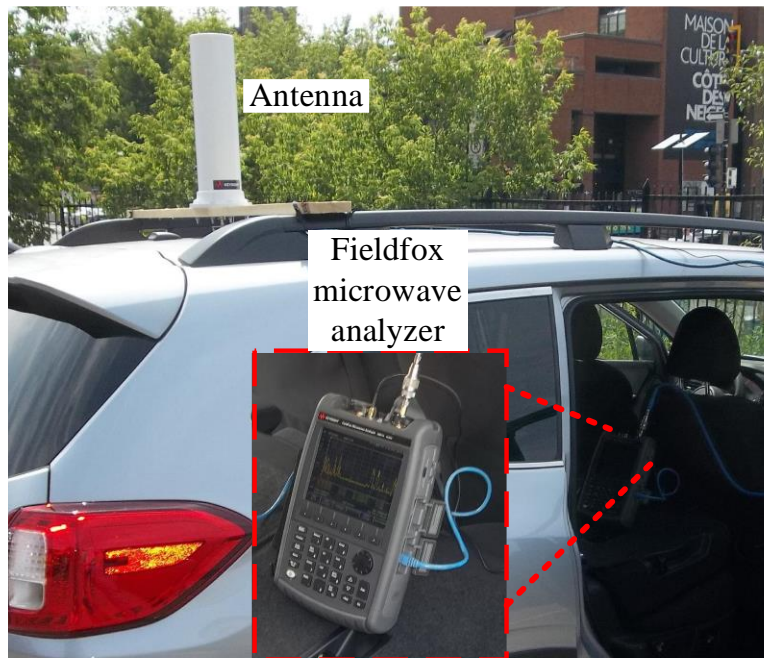
Figure 3.4 Complete setup for the dynamic on-road measurement of ambient RF signal density.

3.3 Results of Dynamic Measurement

3.3.1 RF Power Density in Typical Regions

Usually, RF signal and population density are interrelated or correlated to one another. In this work, the comparisons between DT Montreal and Uptown (UT) Montreal are emphasized. DT Montreal is the most active and populated region of the entire city, with around 100,000 residents and more than 720,000 workers, students, and visitors coming every day [91]. DT Montreal is a region on the east of Mount Royal. Figure 3.5 (a) shows the ambient RF power density of the GSM/LTE850 band in DT Montreal. Figure 3.5 (b) presents the average ambient RF power density levels in DT Montreal, and the GSM/LTE850 band has the highest average RF signal density level (−38.29 dBm) among all seven frequency bands. The LTE700 band has a similar density level of −39.05 dBm. The DTV, GSM/LTE1900, and LTE1700/2100 bands have an RF signal density level of around −50 dBm. The outdoor Wi-Fi signal is only – 75 dBm, much smaller compared to the other frequency bands.
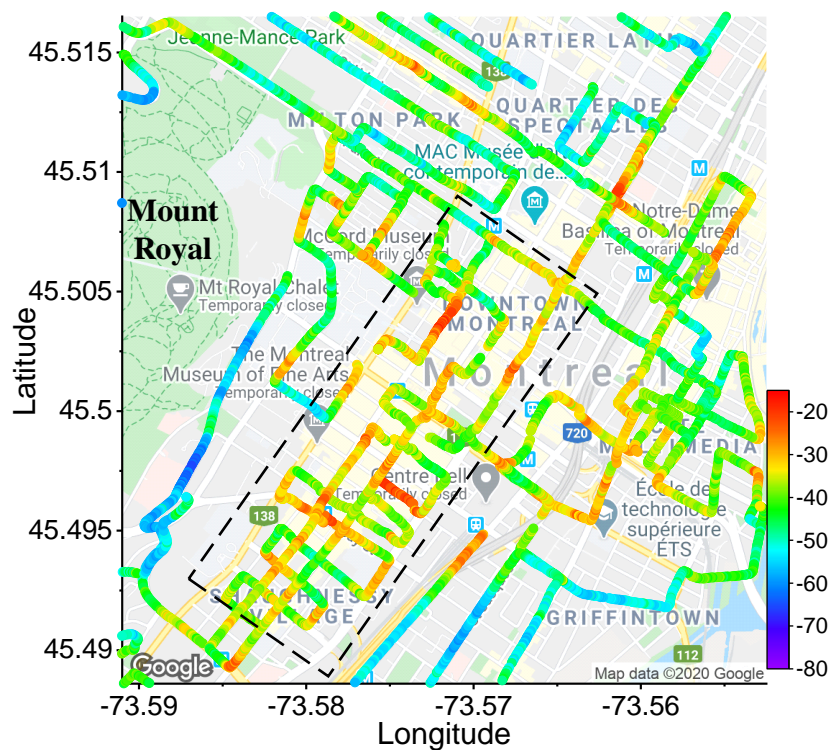
(a)
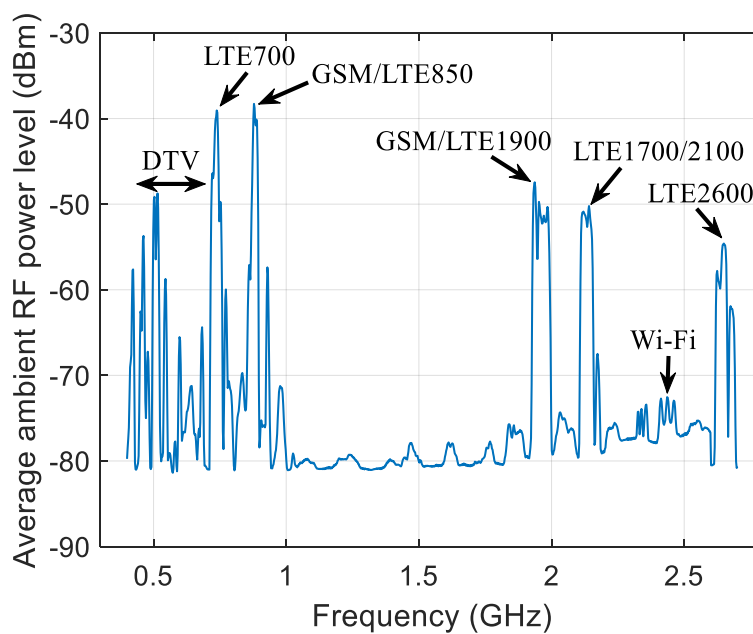
(b)

Figure 3.5 (a) Ambient RF power levels of the GSM/LTE850 band in DT Montreal. (b) Average ambient RF power levels in DT Montreal.

The dashed rectangular box in Figure 3.5 (a) marks the area showing a relatively larger ambient RF power level in DT Montreal. This area corresponds to a more populated region in DT Montreal, with major shopping pedestrian streets. It can be noticed that this area has multiple places with an RF power level higher than −20 dBm. The highest power level recorded in this area is about −13 dBm.

As a comparison, Figure 3.6 (a) and (b) show the mapping results of the GSM/LTE850 band and the average power levels in UT Montreal, respectively. UT Montreal locates on the west side of Mount Royal, as shown in Figure 3.6 (a). Compared to DT Montreal, UT Montreal has a generally lower ambient RF signal density level. In Figure 3.6 (a), two spots labeled by the dashed ellipses demonstrate a higher power level. Both are relatively crowded places where a shopping center and a comprehensive hospital are located. As can be seen in Figure 3.6 (b), the average ambient RF power density of all the cellular communication bands in UT Montreal is roughly 10 ~ 15 dB lower than that of DT Montreal (Figure 3.5 (b)), indicating that communication bands are heavily dependent on active human activities and traffic. Still, the average DTV signal density in UT and DT are at the same level. In UT Montreal, the average DTV signal is the largest, about −51.28 dBm, which is slightly higher than GSM/LTE850 (−51.97 dBm) and LTE700 (−52.53 dBm). The remaining four frequency bands have power density levels of at least 10 dB lower than the above three bands. Since several critical DTV broadcasting towers are on the Mount Royal delivering signals in all directions, both UT and DT Montreal are well covered by DTV signals. The outdoor Wi-Fi signal density is low in both DT and UT Montreal.

Table 3.3 Average ambient RF power density in two types of locations

	Metro stations	Residential areas
DTV	−47.42	−52.11
LTE700	−45.52	−52.59
GSM/LTE850	−45.85	−51.55
LTE1700/2100	−53.57	−60.47
GSM/LTE1900	−53.98	−62.34
Wi-Fi	−71.81	−70.52
LTE2600	−62.86	−70.46
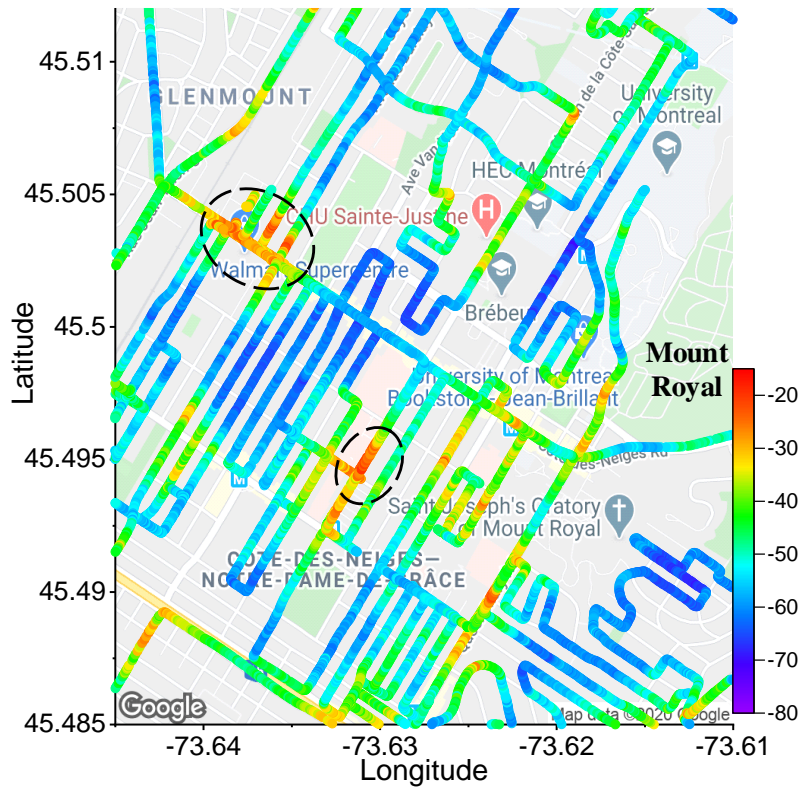
(a)
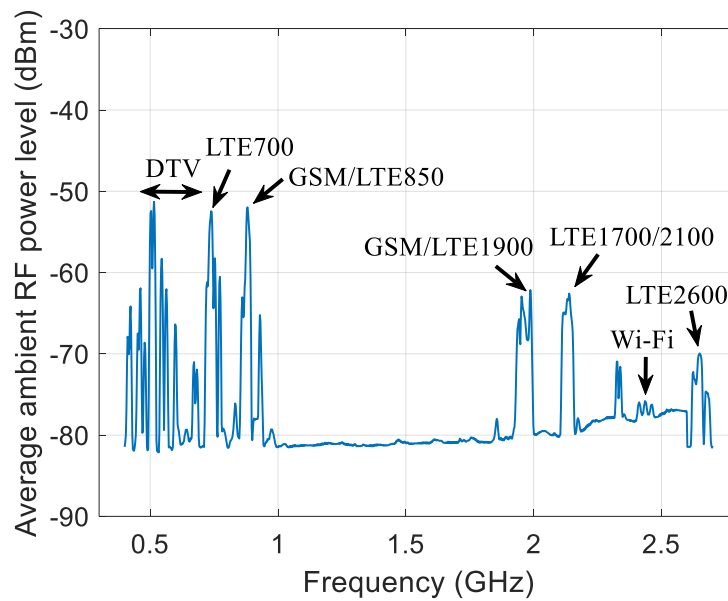
(b)

Figure 3.6 (a) Ambient RF power levels of the GSM/LTE850 band in UT Montreal. (b) Average ambient RF power levels in UT Montreal.

Besides the comparison between the two typical regions on the Island of Montreal, average ambient RF power levels of two more types of places are also highlighted in Table 3.3, namely, metro stations and residential areas. The reported power levels were measured on the streets in front of those locations. The data in Table 3.3 are average power levels of 22 metro stations and 8 typical residential areas, in both UT and DT Montreal. It can be clearly observed that communication bands close to metro stations have larger RF power density. Moreover, the LTE700 and GSM/LTE850 bands have relatively large power density levels near metro stations.

3.3.2 Potential Time Influence
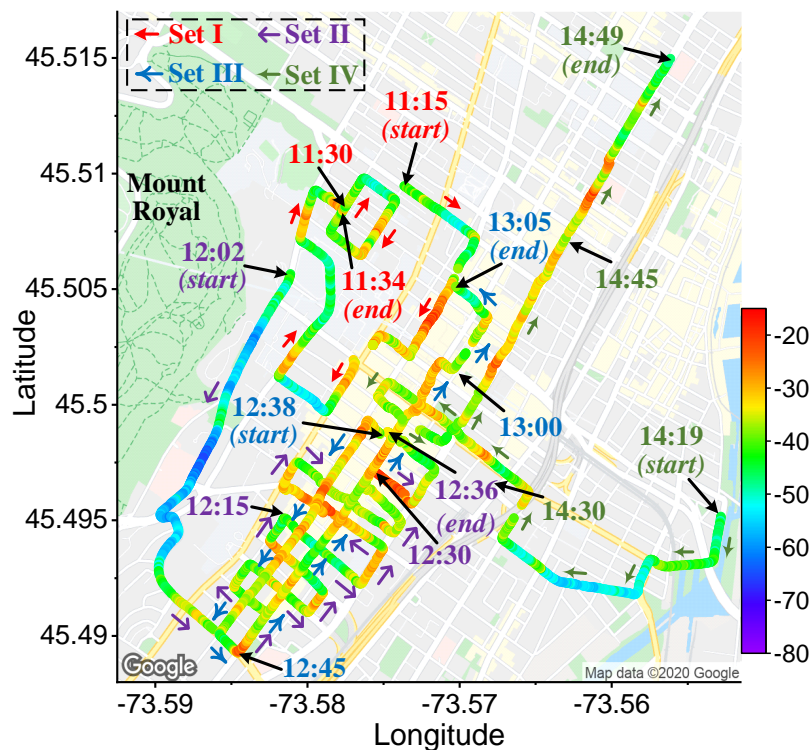
(a)
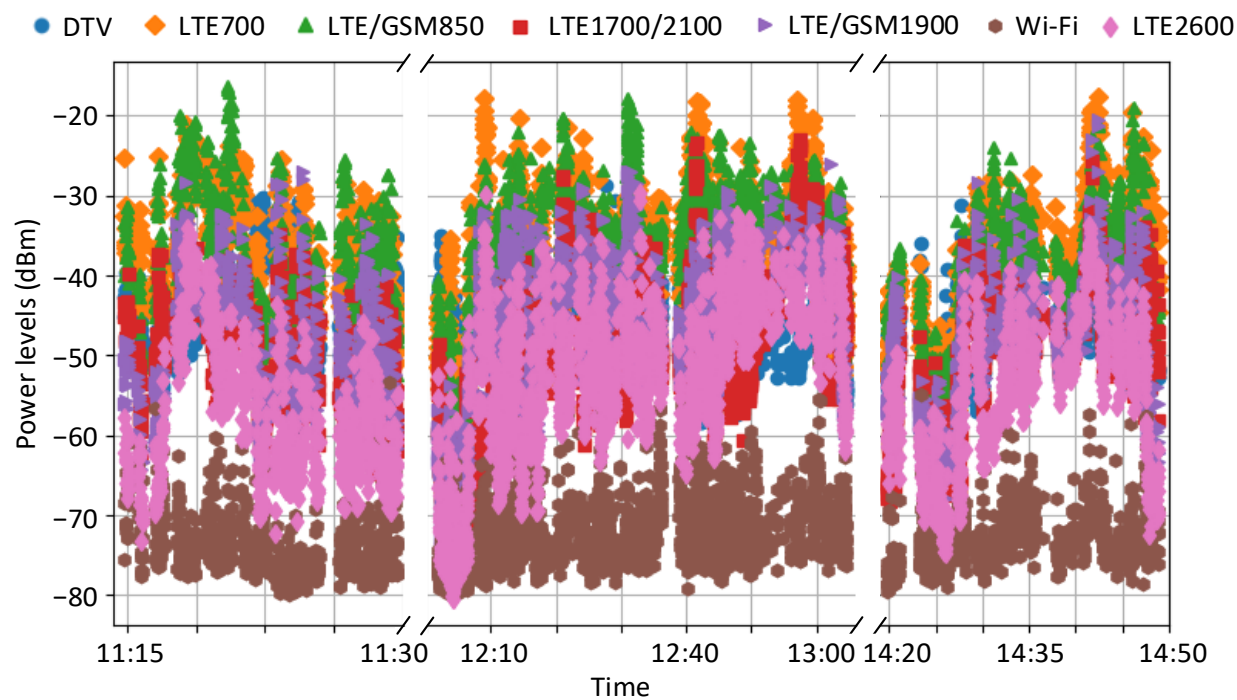
(b)
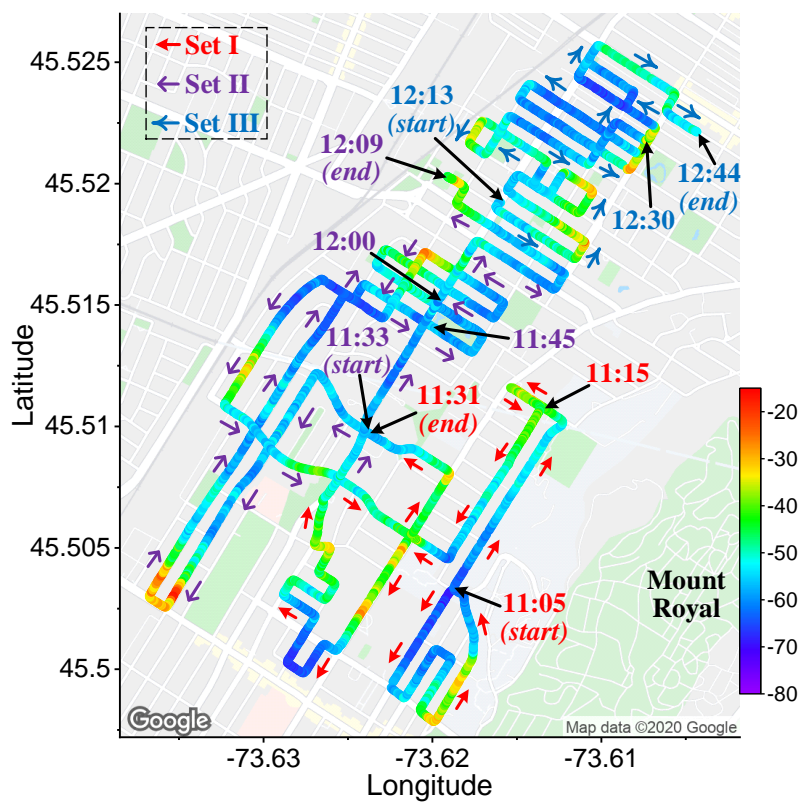
(c)
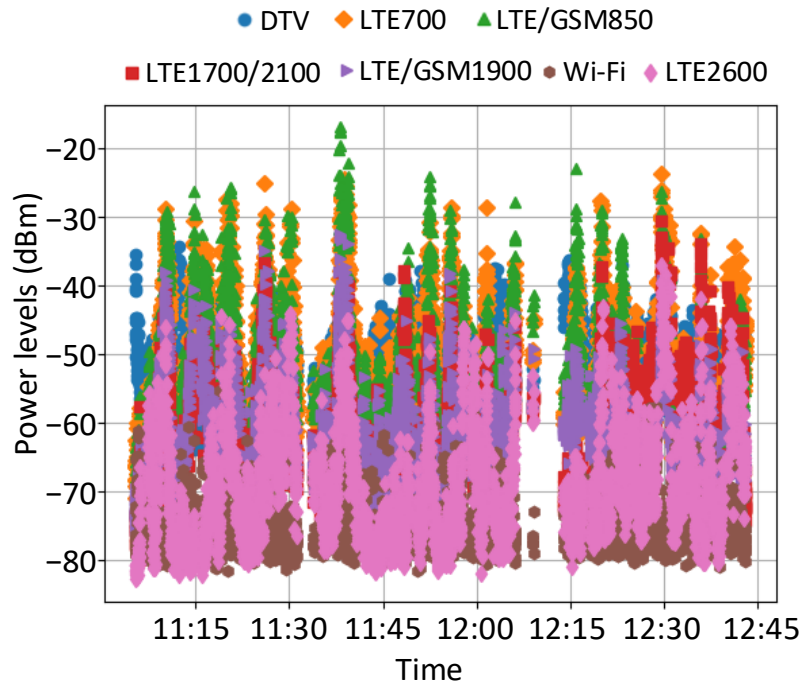
(d)

Figure 3.7 Ambient RF energy mapping of the GMS/LTE850 band with direction and timestamps in typical areas of (a) DT Montreal and (c) UT Montreal. RF power levels of all seven frequency bands of interest at the same geographic locations and time slots: (b) and (d) correspond to (a) and (c), respectively.

Pedestrian traffic may influence the ambient RF power density, which could change power density within a single day. Thus, Section IV will discuss a specific daytime measurement at one typical location in DT Montreal. However, due to workload and cost issues, this dynamic measurement records citywide power density only once for a general case. Although geolocated and timestamped power density levels were obtained, it is still difficult to present all the information simultaneously in this work. Thus, Figure 3.7 (a) and (c) attempt to illustrate ambient RF energy mapping results (GSM/LTE850 band) in typical areas of both DT and UT Montreal, including directions and timestamps. Moreover, within the same time slot, the ambient RF power density of all frequency bands of interest are presented in Figure 3.7 (b) and (d) corresponding to the geographic locations and time in Figure 3.7 (a) and (c).

3.3.3 Different Propagation Mechanism

As discussed before in this section, communication bands are more dependent on human activities. Cellular towers are extensively distributed on the Island of Montreal, especially in DT Montreal, as can be seen in Figure 3.8 (a) [92]. In contrast, the DTV signal comes from centralized high-power broadcasting towers. There are five major DTV towers on the Island of Montreal, as shown in Figure 3.8 (b) [93].

The main differences in ambient RF power density of the GSM/LTE850 band between DT and UT Montreal can be easily understood by the cellular tower map shown in Figure 3.8 (a). The tower density in DT is much higher than in UT Montreal. Different from cellular communications, which feature relatively short-range interaction with towers, the DTV signal is delivered by a few high-power towers. Therefore, those spots close to DTV towers usually have high power density. For example, the measurement results on the road across Mount Royal are much higher than in other places. DTV broadcasting relies on good line-of-sight propagation. Any blocks would dramatically reduce the DTV power levels. The spots DT and UT Montreal showing low DTV power density marked in Figure 3.8 (b) are blocked by DT skyscrapers and the Children's Hospital, respectively.
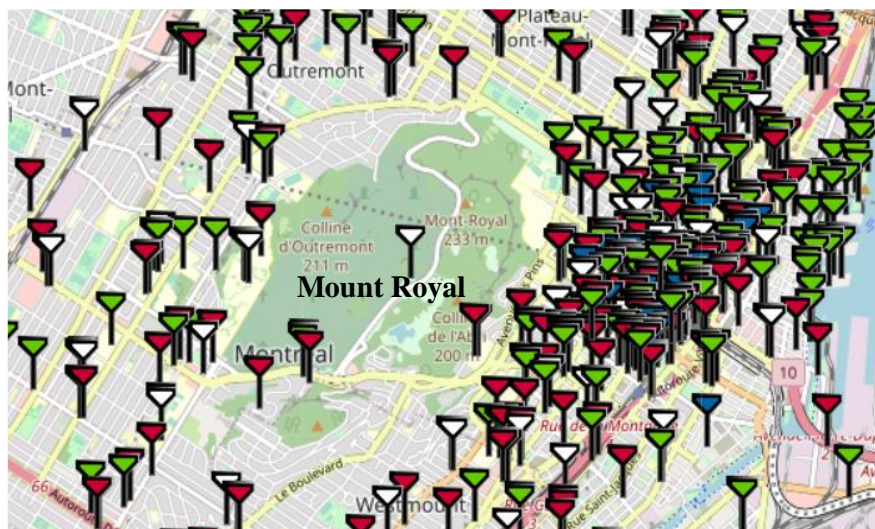
(a)
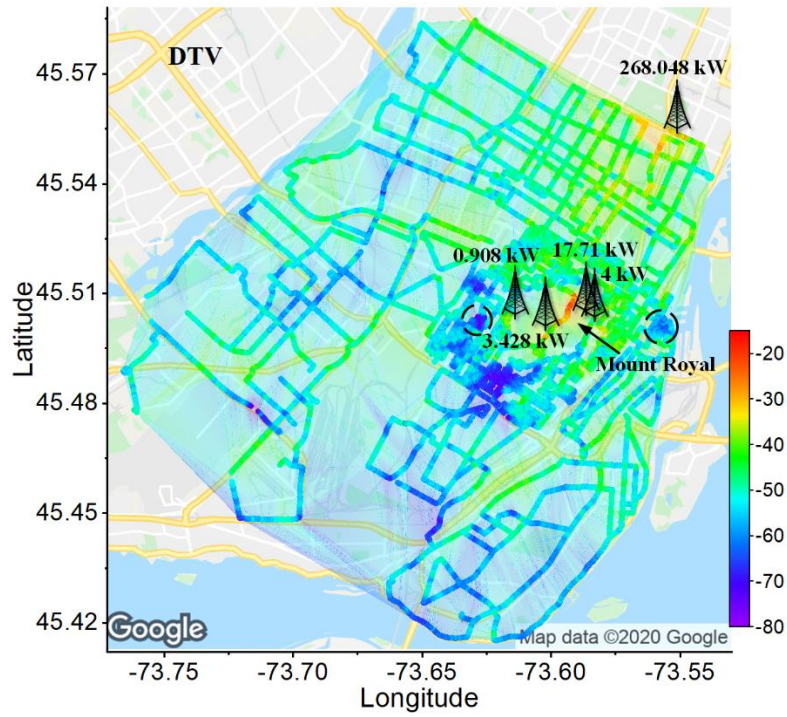
(b)

Figure 3.8   (a) Cellular tower map in Montreal. (b) Ambient DTV signal density mapped in Montreal with the locations of five major DTV broadcasting towers. The effective transmitting power is also attached for each tower. A contour plot based on measured results has been combined in this graph for a prediction of power density in unmeasured areas.

3.4 Results of Stationary Daytime Measurement
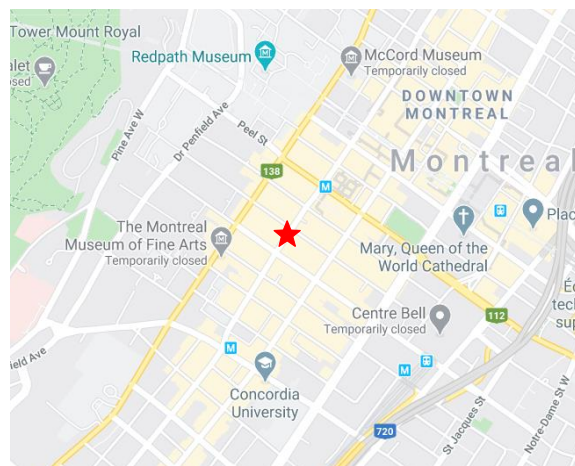
(a)
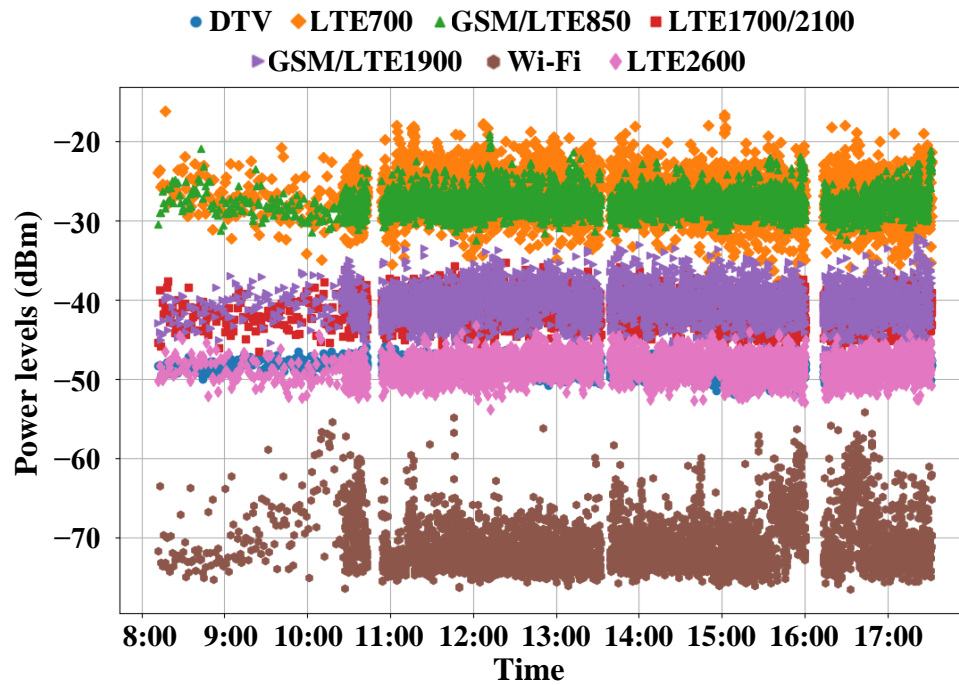
(b)

Figure 3.9 (a) Location of the stationary daytime measurement in DT Montreal. (b) Distribution of measured results along time for the seven frequency bands of interest.

A separate measurement is dedicated to studying the effects of pedestrian traffic on the ambient RF power after finishing all the dynamic outdoor measurements. This measurement was carried out from 8:10 to 17:35 on August 16, 2019 (Friday), at a fixed location in DT Montreal. Figure 3.9 (a) has marked this place. The measurement setup is the same as in Figure 3.4. The vehicle was parked at the curb.

The measured results across the frequency band from 400 MHz to 2700 MHz are presented in Figure 3.9 (b). The measurement was conducted every 1 minute before 10:20, and after it was fastened to every 5 seconds to acquire more data points. Among all the seven frequency bands of interest, the LTE700 and GSM/LTE850 bands have the highest average power density of−28.01 dBm and −28.66 dBm, respectively. However, the results of the GMS/LTE850 band have a more concentrated distribution, with a small variation range from −32 dBm to −25 dBm. In contrast, results of the LTE700 band vary from −35 dBm to −21 dBm. Among the other five frequency bands, the GSM/LTE1900 and LTE1700/2100 also have almost identical average power levels,

which are −40.21 dBm and −41.11 dBm, respectively. Moreover, the distribution range of the above two frequency bands is also similar, in the range of −44 dBm to −37 dBm. DTV band has an average power level of −48.48 dBm. DTV power levels were quite stable throughout the day, as compared to other frequency bands, with most results falling in the range of −50 dBm to −47 dBm. The average power level of the LTE2600 band is about −49.31 dBm, similar to the DTV band. Also, all the results of the LTE2600 band tightly concentrate at the average level. The measured results of Wi-Fi are low, with several large fluctuations in the entire measurement period.

In Figure 3.10, a three-dimensional plot of measured results across the entire frequency band (400 MHz to 2700 MHz) versus time is presented. It can be observed in both Figure 3.9 (b) and Figure 3.10 that no noticeable fluctuations occur in the measured period for all cellular frequency bands. DTV signals also have no significant variations as expected. The overall Wi-Fi power is much lower than the others as the outdoor Wi-Fi signal in this area comes from nearby restaurants or stores. Therefore, this low-power Wi-Fi is more vulnerable to surrounding environments, which explains the variations of Wi-Fi power in the measurement period.
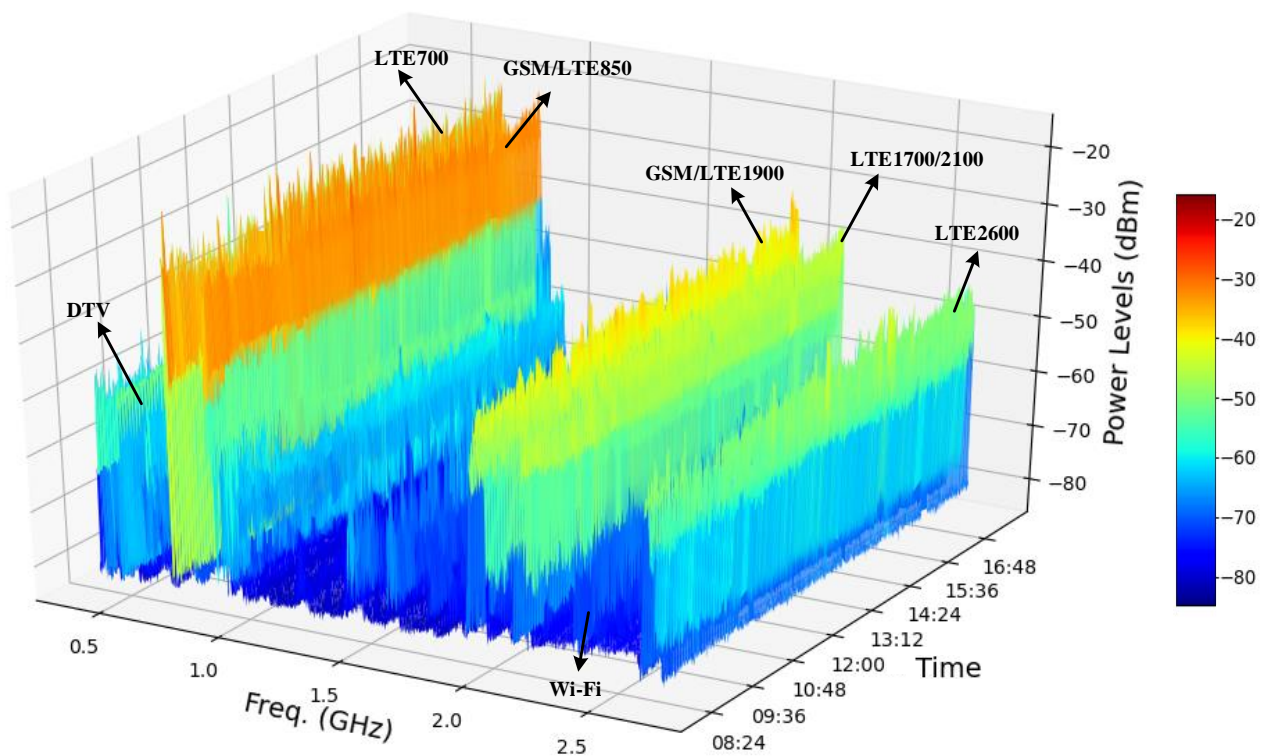
Figure 3.10 Three-dimensional plot of measured ambient RF power levels across the frequency band from 400 MHz to 2700 MHz on a typical workday.

3.5 Feasibility Study of Battery-Free IoT Sensors

As the primary concerns of any applications, safety and interference issues need to be carefully and thoroughly investigated. Battery-free IoT sensors rely on recycling existing RF power in free space; thus, they usually work in a low-power and low-duty-cycle mode. They do not pose a threat to public health in terms of electromagnetic radiation. Such IoT sensors are usually customized and operate in the ISM band to avoid communication interferences. They also have to go through the certification process of Industry Canada (IC), Federal Communications Commission (FCC), or similar national/regional/local regulating body.

Based on the measurement results reported in Section III and IV, several points can be highlighted:

a. The GSM/LTE850 and LTE700 bands have comparable average RF power density in the DT Montreal area. They are at least 10 dB higher than the other frequency bands. Therefore, in DT Montreal, any device trying to recycle ambient RF power should give priority to the GSM/LTE850 and LTE700 bands.

b. In UT Montreal, DTV, GSM/LTE850, and LTE700 bands have similar levels of ambient RF power density. Considering that DTV signal is not dependent on active human activities and thus more stable, the DTV band is the first choice for ambient RF power recycling in this area.

c. The DTV signal comes from a few high-power broadcasting towers, and its transmission follows the line-of-sight propagation. Thus, places near DTV towers and without physical blocks are ideal for implementing battery-free IoT sensors relying on collecting DTV power.

d. Places like the DT area of a city have a high population density and high-rise buildings. Such places usually have excellent coverage of cellular towers, but weak DTV signal reception. Therefore, IoT sensors should target communication bands in DT areas.

e. Streets or buildings near metro stations or similar populated places are promising to deploy IoT sensors.

f. Based on daytime measurement in DT Montreal, no noticeable fluctuations are observed during a typical working day.
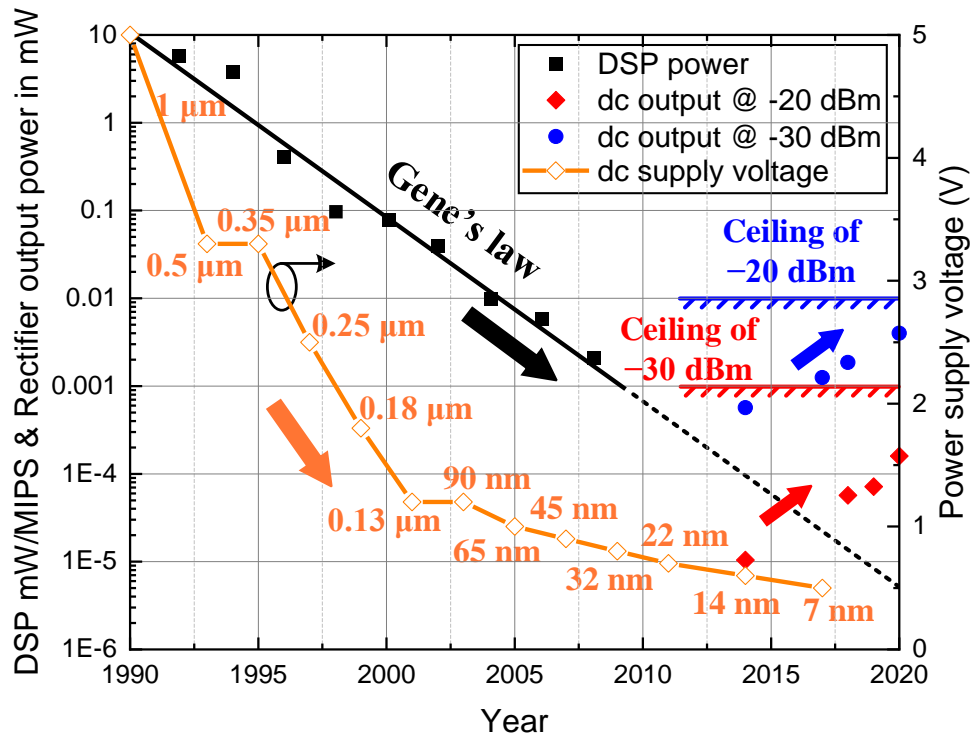
Figure 3.11 Trends of digital signal processor (DSP) power dissipation [94] and dc supply voltage of logic technology [95],[96]. The dashed line is an extrapolation of Gene's Law. The available dc output power of rectifiers when input is −20 dBm and −30 dBm, respectively [21],[28], [38],[97],[98].

Over the years, the power dissipation of electronics reduces continuously. As one example, the power consumption of digital signal processors (DSP) decreases following Gene's Law [94], as shown in Figure 3.11. Moreover, the dc supply voltage is also reducing with the advance of CMOS logic technology [95],[96]. The latest ultra-low-power electronics can work with only 500-mV dc bias. Therefore, IoT sensors are less power-hungry than before, thanks to the above developments.

There are two main techniques to realize battery-free IoT sensors, namely, far-field WPT and backscattering. As shown in Figure 3.11, the recent progress in far-field WPT is encouraging [21],[28],[38],[97],[98]. For example, the latest rectifier demonstrates efficiencies of more than 15% at an input power of −30 dBm and 35% at −20 dBm [21]. Seeing that the available ambient RF power in free space can reach −15 dBm, one experimental demonstration is set up inside our lab, as shown in Figure 3.12 (a) [35]. The multi-function sensor board from Powercast is energized by a 5-stage rectifier harvesting the ambient RF power coming from a signal generator. A 50-mF

supercapacitor acts as the power storage for the sensor board. The required voltage threshold of the sensor board is about 2.7 V, which is equivalent to the rectifier's dc output when the input RF power is about −15 dBm. Once the dc supply reaches 2.7 V, the sensor board is activated to conduct measurements. All obtained environmental parameters are then sent to the access point connected to a laptop. Finally, these parameters are visualized on the laptop screen. Since this sensor board can sense temperature, humidity, light, and external power information, it is a relatively power-hungry device. The minimum input RF power requirement (−15 dBm) can be reduced dramatically by customizing this type of sensor node. Figure 3.12 (b) shows a fully passive harmonic transponder [13]. The transponder responds with second harmonics once it receives a fundamental signal. In our experiments, the input RF power can be as low as −30 dBm, and the communication range can reach 7 m. Such an input power level can also be reduced by choosing a proper diode, and the detection range can be further extended. This type of sensor has been employed to study bees [99], wood frogs [100], and avalanche victim search and rescue [101]. In real applications, ambient RF power is the fundamental signal. Useful information can be transmitted through the second harmonic and sent back to sniffers, such as a user cell phone or other types of gateways.
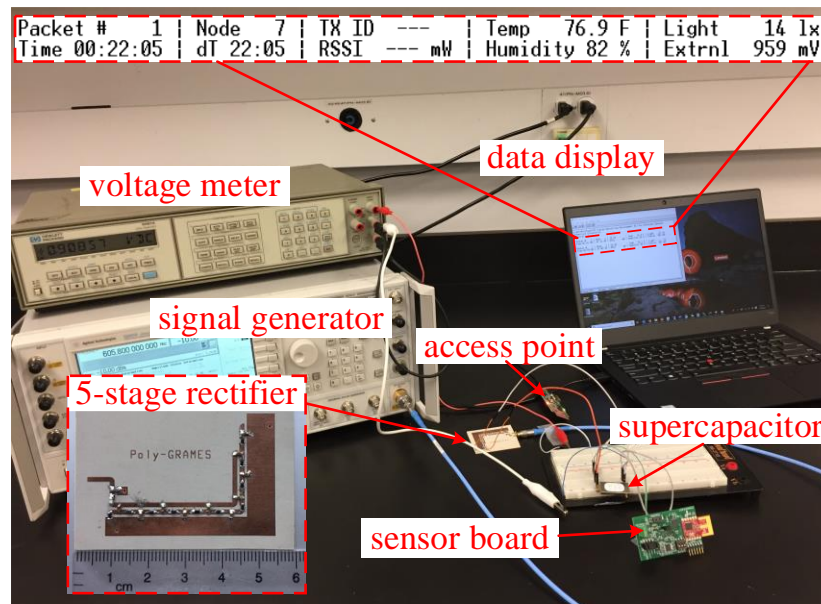
(a)
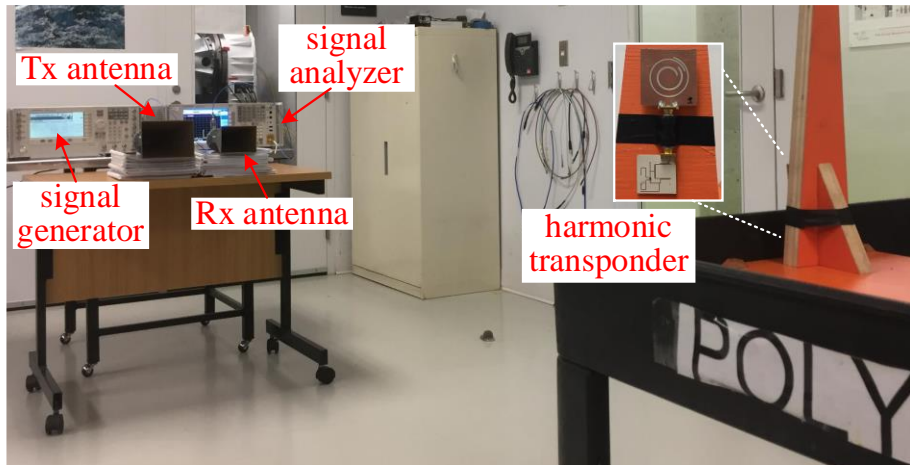
(b)

Figure 3.12 Experimental demonstration of battery-free IoT sensors: (a) far-field wireless power transfer powered multi-function sensor board and (b) fully passive harmonic transponder.

Figure 3.13 Typical battery-free IoT sensor applications powered by ambient RF energy recycling.

Based on the above discussions, battery-free IoT sensors are feasible. Usually, such sensors are highly customized and work in a low-duty cycle. Figure 3.13 demonstrates two typical and feasible

battery-free IoT sensor applications. One is a fatigue sensor on a building to detect any surface cracks. It can be realized by the harmonic backscattering technique [102]. A second sensor could be attached on a bus to measure CO_2 levels along the bus route. The sensor keeps rectifying ambient RF power and triggers measurement when enough power has been collected. The collected information could be shared with local gateways first and finally uploaded to an IoT cloud. Both applications do not require continuous operation. They only conduct measurement and necessary communication when having enough power recycled from ambient RF energy in the environment.

3.6 Conclusion

This work presents an outdoor dynamic measurement in core areas of Montreal, Canada to study the ambient RF power density. Through multiple comparisons, cellular communication bands, specifically the GSM/LTE850 and LTE700 bands, have the highest average power level in DT Montreal. While in UT Montreal, the DTV power is the largest among all the frequency bands. Priorities should be given to those frequency bands with larger ambient power density in corresponding areas when implementing battery-free IoT sensors. Populated places like metro stations or other similar areas with high pedestrian traffic are also good choices for deploying such IoT sensors. The stationary daytime measurement in DT Montreal does not show obvious ambient RF power variations as time progresses on a typical workday.

 The two primary techniques to realize battery-free IoT sensors, far-field WPT and backscattering, can extract low RF power more efficiently nowadays thanks to recent advances. Meanwhile, ultra-low-power electronics are also gathering excellent progress. Battery-free IoT sensors based on recycling ambient RF power are feasible and will play an increasingly critical role in future smarter and greener cities.

3.7 Appendix

Besides the GSM/LTE850 and DTV bands, the entire dynamic mapping results of the three typical bands, namely the LTE700, LTE1700/2100, and Wi-Fi bands, in core areas of city of Montreal have been shown in Figure 3.14. The contour plots have also been generated as a prediction in unmeasured areas and are combined with measured results. Note that contour plots may overestimate RF power density when measurement results are sparse.
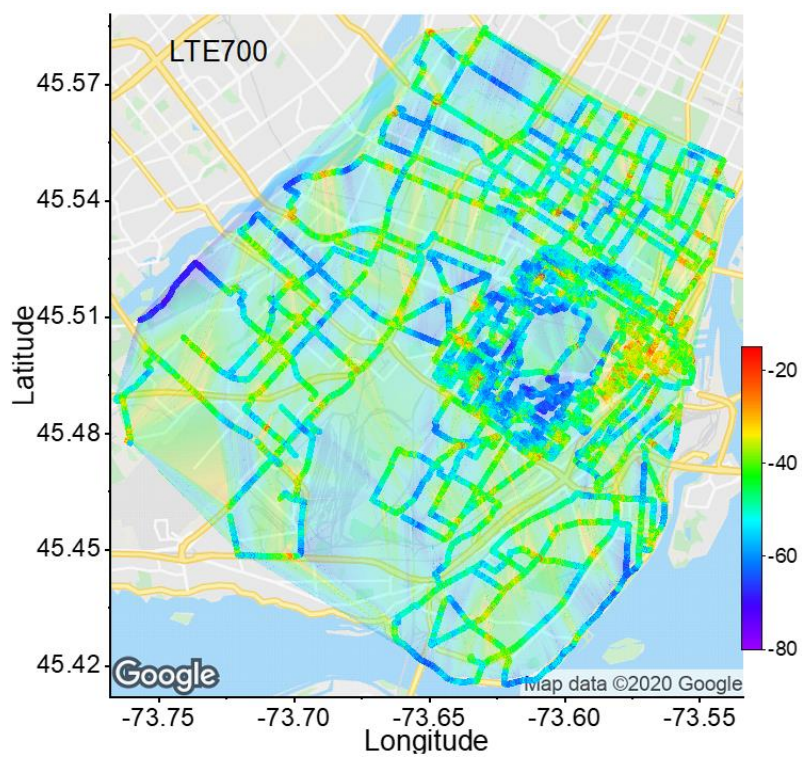
(a)
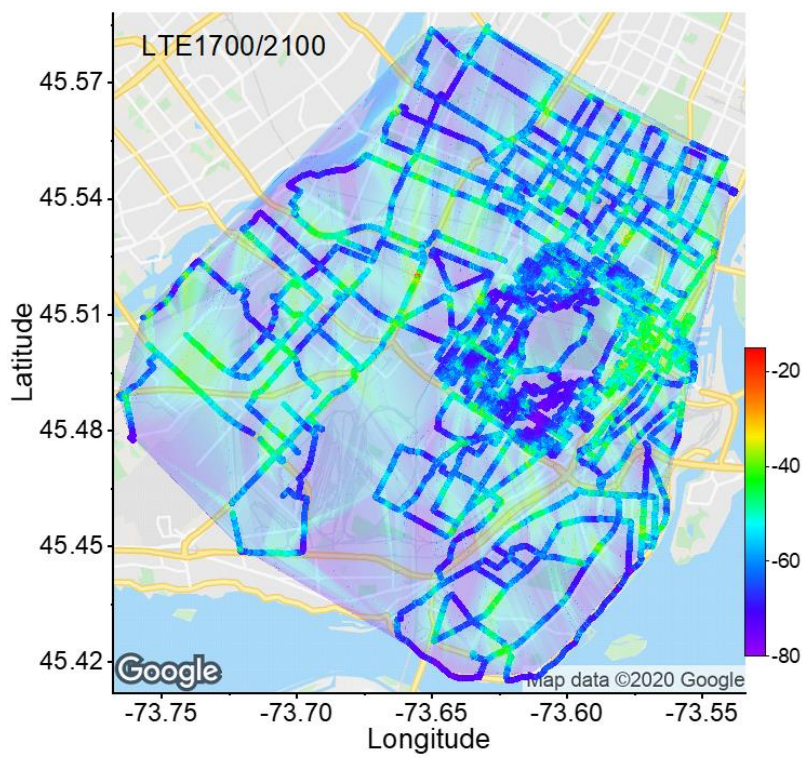
(b)
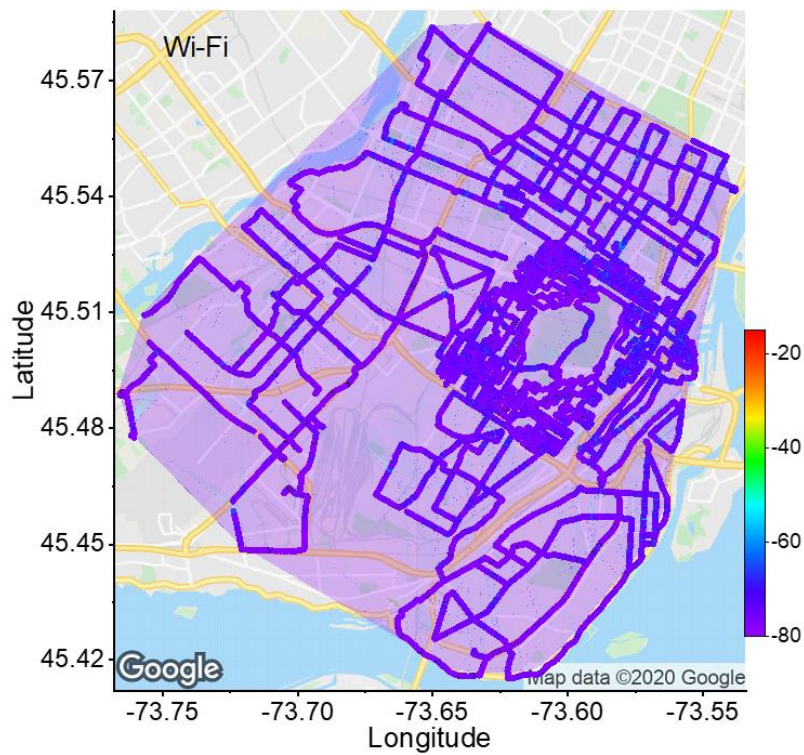
(c)

Figure 3.14 Entire mapping results of ambient RF power in the (a) LTE700 and (b) LTE1700/2100 and (c) Wi-Fi bands in core areas of Montreal. Contour plots have been combined in each graph as a reasonable prediction of RF power density in unmeasured areas.

CHAPTER 4 ARTICLE 3: OPTIMUM TEMPERATURES FOR ENHANCED POWER CONVERSION EFFICIENCY (PCE) OF ZERO BIAS DIODE-BASED RECTIFIERS

Xiaoqiang Gu, Lei Guo, Simon Hemour, and Ke Wu

Ambient power rectifiers are pivotal for batteryless or self-powered Internet of Things architectures and self-sustained communication/sensor platforms. The core of rectifiers, a nonlinear device, has been subject to significant research and improvements recently, especially at a low power level where rectifying efficiency is so limited. Current responsivity (the key rectification parameter describing the nonlinearity) is known to be impacted by the operating temperature, as predicted by William Shockley's law. However, no work has been carried out to quantify the impact of temperature in the RF rectification process, nor to relate existing diodes with their optimum operating temperature range. To address those missing links, this article first develops an analytical method to predict power conversion efficiency (PCE) of rectifiers from approximate milli-watt down to nano-watt level. Next, it identifies the optimum operating temperature of rectifiers corresponding to peak PCE. It also reports that the previous PCE ceiling of 15 % (at an input power level below −30 dBm) can be broken when rectifiers operate at their optimum temperatures. Enhanced PCE results are then validated experimentally on SMS7630 and HSMS-2850-based rectifiers when operating at their optimum temperatures. Noticeably, the SMS7630-based rectifier delivers efficiency of 17.5 % at −30 dBm and 41.7 % at −20 dBm, showing respectively comparable and better PCE than that of tunnel diode-based counterparts at similar power levels. This work also indicates that rectifier design should consider the operating temperature when selecting diodes to maximize rectifying potential.
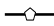
4.1 **Introduction**

The vision to implement wireless power transfer (WPT) can be dated back to more than a century ago [103]. Starting from a conceptual idea, this technology has been going through rapid development, which has already shown a number of successful commercial applications, like charging cell phones and electric toothbrushes. Near-field non-radiative WPT, with either an inductive or magnetic resonance coupling solution, is the key enabling technology behind these applications [104]. As the other type of WPT, namely far-field radiative WPT, has the potential to energize scattered devices simultaneously at a large scale. Nevertheless, as the source power density drops rapidly over the distance, the RF-to-dc rectifying efficiency is low, being the main barrier restraining the far-field radiative WPT from being widely adopted by industry so far [4].

As one of the most significant turning points of WPT, W. C. Brown's work is a milestone of the far-field radiative WPT [31, 105], before which high-power WPT was the main focus [106]. Since then, researchers have continuously concentrated on improving the power conversion efficiency (PCE) of ambient power harvesting techniques. Figure 4.1 lists the measured efficiency results of state-of-the-art works. High-efficiency far-field radiative WPT has already been achieved decades ago in a large input power range (>1 mW), as shown in the right part of Figure 4.1. Whereas, as one of the main goals of the Internet of Things (IoT) technology, developing self-sustained communication/sensor platforms heavily relies on the ambient power harvesting in a much lower input power range. Roughly after the year 2010, more researchers turned to improve the PCE of rectifiers in an input power range below 1 mW. It has become a goal in our WPT community to achieve a higher PCE at a lower input power level. Various effective measures have been taken to improve the PCE of ambient power harvesting. For instance, hybrid energy harvesting was proved to be an effective way to boost the PCE in an ambient power harvesting scenario [35], [33]. As an example, collecting both RF and vibration energy exacerbates a nonlinear process within the diode, thus resulting in an improvement of the diode's PCE [32, 36]. Also, a particular waveform design, such as multi-tone or digitally modulated signals, is an attractive alternative to increase the PCE [107]. Moreover, a specially engineered backward tunnel diode has successfully broken the PCE limitation of conventional Schottky diodes [39]. It still preserves the record of the best PCE at extremely low input power levels. But the fabrication of such tunnel diodes, which are laboratory prototypes, has been challenging and not ready for mass production yet. It also has a limited voltage

swing range since, at a certain voltage range, the current tends to decrease because of the diode bandgap between the p-side valence and the n-side conduction band which move away from each other [17].

Table 4.1 Legend and references in Figure 4.1

Symbol	Year	Diode	Operating frequency (GHz)	Reference
	1982	GaAs	2.45	[31]
	1998	MA40150-119	5.8	[67]
	2002	MA4E1317	2.45	[108]
	2010	SMS7630	2.45	[109]
	2010	SMS7630	1.85	[65]
	2010	SMS7630	2.44	[65]
	2010	HSMS2820	2.45	[110]
	2010	HSMS2860	2.45	[110]
	2014	HSMS2850	1.8	[97]
	2014	HSMS2850	2.1	[97]
	2015	SMS7630	2.15	[111]
	2016	SMS7630	1.9	[3]
	2016	VDI ZBD	1.9	[3]
	2016	Backward tunnel diode	2.4	[39]
	2017	SMS7630	1.85	[38]
	2017	SMS7630	0.85	[66]
	2018	SMS7630	0.9	[98]
	2019	SMS7630	2.4	[28]

By far Schottky diodes, featuring low cost, mature technology, and high commercial accessibility, are still the most commonly used diodes in ambient power harvesting. This work focuses on fully exploiting the potential of Schottky diodes when built in rectifiers to seek possibilities to surpass the tunnel diode in terms of PCE. Prior to any rectifier design, diode modeling is vital as the diode realizing frequency conversion in the circuit is the most important component. Furthermore, the diode modeling helps to better understand diode behaviors and thus provides a guideline on selecting a proper diode for rectifier design.
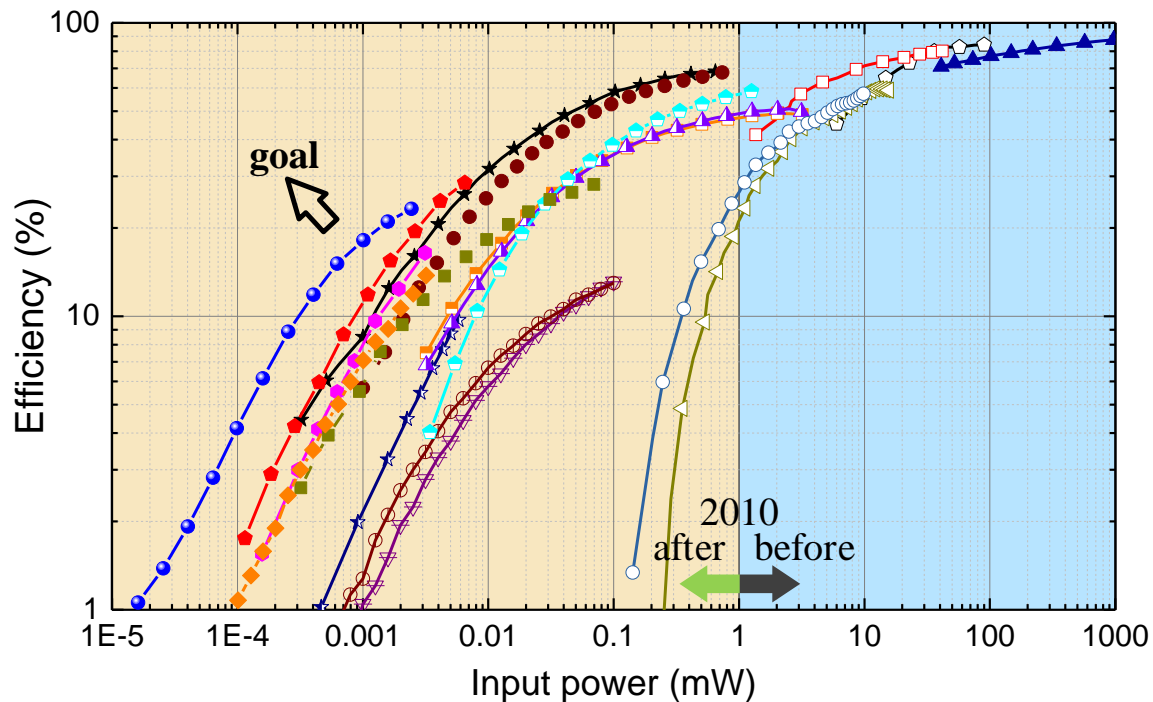
Figure 4.1 Measured efficiency results of state-of-the-art microwave rectifiers. The legend and references are listed in Table 4.1.

There are mainly two different closed-form approaches to model diodes used in rectifiers. The first is time domain-based calculation which was initially introduced in [112]. The diode is analyzed as a perfect switch with ON and OFF states. The diode junction resistance R_j is assumed to be 0 at forward biased status (ON). When reverse biased (OFF) status is created, the diode demonstrates infinite R_j. This method shows a satisfying accuracy at high input power levels (> 0 dBm). Based on this original concept, improvements were reported subsequently in [113], [114]. However, in an ambient power harvesting scenario, the diode cannot be considered as a perfect switch anymore [3]. Therefore, as the other type of closed-form approach, diode modeling based on frequency domain was proposed. It initially comes from the analysis of an RFID transponder, since both devices rely on the diode to realize frequency conversion [115]. During the analysis, one of the most significant steps is to extract each harmonic component from the current (I) – voltage (V) relationship of the diode. This relationship of Schottky diodes is represented by an exponential expression in a low power range, according to the Shockley model [19]. The Taylor series expansion is a simple way to obtain each harmonic component in a low input power range but

shows a limited accuracy [116], [43]. To extend this method to a larger input power range, certain adjustments based on the harmonic balance algorithm have been adopted, which inevitably increases the complexity of the method [3]. The harmonic balance method, as a commercial analysis tool, provides a reliable solution for simulating nonlinear circuits and systems. However, it is not a closed-form solution due to the use of a Fourier transform, which also cannot be easily used on microcontroller-based platforms. Therefore, a simple closed-form method with an extended dynamic range is essential. In this work, an analytical method for the PCE prediction of zero bias diode-based rectifiers is proposed. Diode nonlinear junction capacitance C_j, which is voltage-controlled, has been investigated in detail. The dynamic range with satisfactory PCE prediction can go up to the breakdown point (around -10 dBm) of rectifiers based on diodes SMS7630 and HSMS-2850.

The proposed analytical method offers an opportunity to examine the PCE of rectifiers in various aspects. Among multiple factors associated with the rectifying PCE, the temperature issue has been overlooked for a long time, despite that diode's I-V curves at different temperatures are usually provided on datasheets. Recently, inspired by harmful effects on the p-channel MOSFET voltage multiplier [117], researchers conducted an experimental study to assess the temperature effects on the PCE of Dickson Charge pumps used in energy harvesting rectennas [118]. The temperature variation from 25 °C to 85 °C is reported negative to the PCE at low incident power regimes. However, there is a lack of theoretical analysis presented in [118]. The zero bias current responsivity $\Re_{I0}$ indicating the nonlinearity of a Schottky diode is inversely proportional to the operating temperature T. This implies that a low-temperature operating environment could enhance the PCE of Schottky diode-based rectifiers. With the aid of the proposed analytical method, the thermal responses on the PCE of rectifiers based on zero bias Schottky diodes are investigated in this work. The optimum temperatures for peak PCE at each power level are captured. Further measurement shows that PCE results of rectifiers with optimum load resistors are higher than those with fixed load resistors. Operating at their optimum temperatures, rectifiers based on conventional Schottky diode can outperform tunnel diode at the input power level of –20 dBm. Moreover, this work serves as a reminder that the PCE performance of rectifiers can be optimized by carefully selecting suitable diodes for certain temperature conditions.

4.2 Proposed Method for PCE Prediction

Figure 4.2 (a) presents a classical single Schottky diode-based rectifier. The single-tone RF input source has a magnitude of V_{in} and an internal resistance of R_0. L_p and C_p are packaging parasitic components of the zero bias Schottky diode [19]. The nonlinear junction is characterized by the Shockley model as shown in Figure 4.2 (b), consisting of nonlinear junction resistance R_j, nonlinear junction capacitance C_j and series resistance R_s. A low-pass filtering capacitor C_l is positioned parallel to the load R_l to smooth out AC components over it. V_a, V_b, V_c, and V_d are node voltages and consistent in Figure 4.2 (a) and (b). The packaging parasitic components of the diodes are lossless and their effects can be eliminated by matching networks [114]. Thus, they are removed in deriving the method, but still included in matching network optimization before fabrication. A typical matching network for such a single-series diode-based rectifier is presented in Figure 4.2 (a), consisting of a dc blocking capacitor and a grounded inductor [119]. Moreover, the dc current path has been labeled in the equivalent circuit.
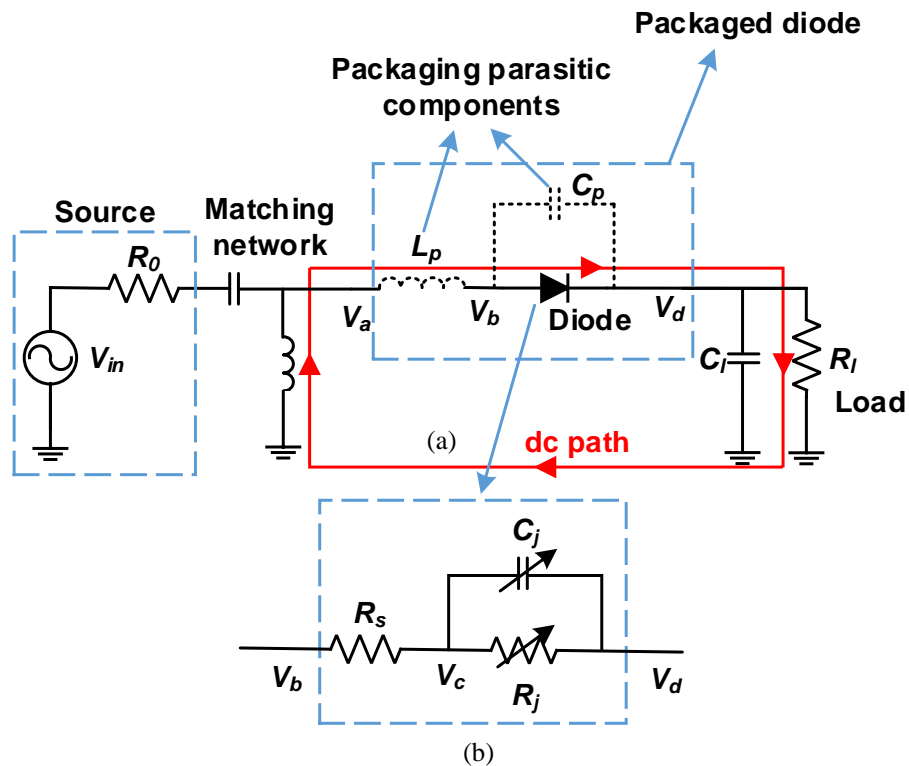
Figure 4.2 (a) Diagram of a classic single Schottky diode-based rectifier. (b) Shockley diode model.

If the power injected into the diode has a sinusoidal waveform with the frequency of f_0, the voltage across the nonlinear junction resistance R_j, having both the fundamental and dc components can be written as:

$$V_{on} = V'cos(2\pi f_0 t) - V_{dc} \tag{4.1}$$

where V' is the voltage magnitude at f_0. Due to the existence of C_l, the fundamental voltage magnitude across the junction V' equals the AC voltage magnitude of node V_c which is defined as V_2. V_{dc} is the generated dc voltage and can be calculated by multiplying the dc current I_{dc} by the total resistance along the dc path:

$$V_{dc} = I_{dc} \cdot (R_l + R_s) \tag{4.2}$$

Then, the Shockley model [19] describing the current passing through the diode can be written as:

$$I_{diode} = I_s \cdot \left[e^{\frac{V_{on}}{n \cdot Vt}} - 1\right] = I_s \cdot [e^{\frac{V_2 cos(2\pi f_0 t) - V_{dc}}{n \cdot Vt}} - 1] \tag{4.3}$$

where I_s is the diode's saturation current; n is the ideality factor; $V_t = k \cdot T/q$ represents the thermal voltage; k is the Boltzmann constant, and q is the electron charge. Operating temperature T is in Kelvin (K). In this analysis, the exponential I-V relationship is adopted to cover the entire power range up to the level where the zero bias diode breaks down. However, according to the sophisticated piecewise SPICE model, this relationship is valid only if V_{on} is within this range [120]:

$$-10 \cdot n \cdot V_t \leq V_{on} \leq n \cdot V_t \cdot \ln\left(\frac{1}{I_s} + 1\right) \tag{4.4}$$
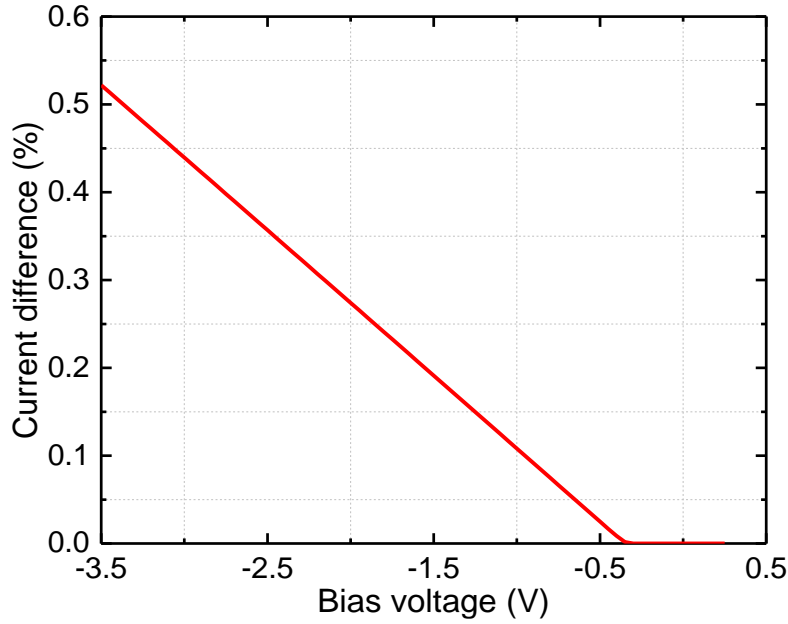
Figure 4.3 Current difference of diode between the piecewise SPICE model and the simple exponential I-V relationship. The range of bias voltage is determined based on the simulated voltage coverage across the diode junction when the diode reaches its breakdown voltage. The selected diode is HSMS-2850 with a load of 9086 Ω and operating frequency is 900 MHz.

Figure 4.3 presents the current difference between using simple exponential I-V equation (4.3) and the piecewise SPICE model, when the diode HSMS-2850 is biased from -3.5 to 0.4 V. The current difference is proved negligible, indicating that the exponential I - V relationship is an approximation with satisfactory accuracy within the power range of interest.

Bessel function [121] separates the diode current into dc and other harmonics efficiently [115]:

$$e^{\frac{V_2 \cos(2\pi f_0 t)}{n \cdot Vt}} = J_0\left(-i\frac{V_2}{n \cdot Vt}\right) + 2\sum_{k=1}^{\infty} i^k J_k\left(-i\frac{V_2}{n \cdot Vt}\right)\cos[k \cdot (2\pi f_0 t)] \tag{4.5}$$

where $J_k(x)$ is the Bessel function of the first kind of order k and i is the imaginary unit.

Then, the dc current component is expressed by:

$$I_{dc} = I_s \cdot \left[J_0\left(-i\frac{V_2}{n \cdot Vt}\right) \cdot e^{\frac{-V_{dc}}{n \cdot Vt}} - 1\right] = I_s \cdot \left[J_0\left(-i\frac{V_2}{n \cdot Vt}\right) \cdot e^{\frac{-I_{dc} \cdot (R_l + R_s)}{n \cdot Vt}} - 1\right] \tag{4.6}$$

Since diode's zero bias junction resistance R_{j0} can be calculated by $n \cdot V_t / I_s$ [16], if we move I_s to the left side, (4.6) can be rewritten as:

$$\frac{I_{dc}}{I_s} = J_0\left(-i\frac{V_2}{n \cdot Vt}\right) \cdot e^{\frac{-I_{dc} \cdot (R_l + R_s)}{I_s \cdot R_{j0}}} - 1 \tag{4.7}$$

Let $G = \frac{(R_l + R_s)}{R_{j0}}$, and moving exponential term to the left, we will have:

$$e^{\frac{I_{dc} \cdot G}{I_s}} \cdot \left(\frac{I_{dc}}{I_s} + 1\right) = J_0\left(-i\frac{V_2}{n \cdot Vt}\right) \tag{4.8}$$

Then, let us multiply both sides by $e^G \cdot G$:

$$e^{\left(\frac{I_{dc}}{I_s} + 1\right) \cdot G} \cdot \left(\frac{I_{dc}}{I_s} + 1\right) \cdot G = J_0\left(-i\frac{V_2}{n \cdot Vt}\right) \cdot e^G \cdot G \tag{4.9}$$

An analytical solution can be obtained by introducing the Lambert W function. Since the right side of (4.9) is always a real value and larger than 0, we can arrive:

$$\left(\frac{I_{dc}}{I_s} + 1\right) \cdot G = W_0\left(G \cdot J_0\left(-i\frac{V_2}{n \cdot Vt}\right) \cdot e^G\right) \tag{4.10}$$

where W_0 is the principal branch of the Lambert W function. After some treatment, we have the expression of I_{dc}:

$$I_{dc} = I_s \cdot \left(\frac{W_0\left(G \cdot J_0\left(-i\frac{V_2}{n \cdot Vt}\right) \cdot e^G\right)}{G} - 1\right) \tag{4.11}$$

The current magnitude at fundamental frequency going through the nonlinear junction resistance is extracted from (4.5) as well:

$$I_2 = I_s \cdot \left[2 \cdot i \cdot J_1\left(-i\frac{V_2}{n \cdot Vt}\right) \cdot e^{\frac{-V_{dc}}{n \cdot Vt}}\right] \tag{4.12}$$

Note that this fundamental current I_2 and the AC voltage across the nonlinear junction resistance V_2 are assumed in-phase. Also, as seen from (4.11) and (4.12), the calculation of fundamental

currents includes only the voltage magnitudes, so the phase information of injecting power can be neglected in the analysis.

As can be observed in Figure 4.2, the RF input power P_{in} at the fundamental frequency is dissipated by the junction P_{R_j} and series resistances P_{R_s}:

$$P_{in} = P_{R_j} + P_{R_s} \tag{4.13}$$

in which $P_{R_j} = \text{real}\left(\frac{V_2 \cdot I_2^*}{2}\right)$. The power consumed by the series resistance P_{R_s} can be calculated by:

$$P_{R_s} = \frac{\left|I_2 + I_{C_j}\right|^2 \cdot R_s}{2} = \frac{|I_2|^2 R_s}{2} + \frac{\left|I_{C_j}\right|^2 R_s}{2} = \frac{|I_2|^2 R_s}{2} + P_{C_j\_R_s} \tag{4.14}$$

where I_{C_j} denotes the current passing through the junction capacitance. Note that I_2 and I_{C_j} have a 90° phase difference. $P_{C_j\_R_s}$ represents the power dissipated by the series resistance due to the current I_{C_j}.

The capacitance value C_j is dependent on the voltage across the junction V_{on}. It can be simplified as the zero bias value C_{j0} in a low input power range (<-30 dBm). This approximation has been verified in our previous work to be accurate, by comparing with commercial ADS harmonic balance simulations and measurements [36]. The reason why this approximation works well can be understood in Figure 4.4, which demonstrates the C-V curve of the diode HSMS-2850. When the magnitude of the injecting signal is relatively small, the voltage swing only covers the region ($C_{j1} \sim C_{j2}$) where both values are very close to C_{j0} (labeled by a pentagram). Nonetheless, with V_{on} increasing, the waveform swings from a low capacitance of value C_{j3} up to a high value C_{j4}, which is the other case shown in Figure 4.4. This suggests that the effective capacitance should be no longer assumed as C_{j0}.

Therefore, to calculate $P_{C_j\_R_s}$, the voltage-controlled nonlinear junction capacitance of Schottky diodes needs to be defined first. In this analysis, the SPICE model of Schottky diodes is developed based on the widely used p-n junction model with diffusion capacitance removed. Thus, the total capacitance C_T in the SPICE model is expressed by [120]:

$$C_T = \begin{cases} C_{j0} \cdot \left(1 - \frac{V_{on}}{V_j}\right)^{-M} & V_{on} \leq Fc \cdot V_j \\ \frac{C_{j0}}{F_1} \cdot \left[1 + F_2 \cdot \left(V_{on} - Fc \cdot V_j\right)\right] & V_{on} > Fc \cdot V_j \end{cases} \tag{4.15}$$

where $F_1 = (1 - Fc)^M$ and $F_2 = \frac{M}{V_j \cdot (1 - Fc)}$. Fc is the forward-bias depletion capacitance coefficient; V_j is the junction potential; and M is the grading coefficient.

According to [122], the current of a voltage-controlled capacitance whose C-V relationship is time-invariant can be expressed as:

$$I_{C_j}(t) = C_T\left(V_{on}(t)\right) \cdot \frac{dV_{on}(t)}{dt} \tag{4.16}$$

Thus, $P_{C_j\_R_s}$ is calculated by:

$$P_{C_j\_R_s} = \frac{1}{T_0} \oint I_{C_j}(t)^2 R_s \, dt = \frac{1}{T_0} \int_0^{T_0} \left(C_T\left(V_{on}(t)\right) \cdot \frac{dV_{on}(t)}{dt}\right)^2 R_s \, dt \tag{4.17}$$

Then, the injecting power P_{in} is obtained by using (4.13) based on (4.14) and (4.17). The dc power is calculated by:

$$P_l = I_{dc}^2 \cdot R_l \tag{4.18}$$

Thus, PCE is defined as:

$$\text{PCE} = \frac{P_l}{P_{in}} \times 100\% \tag{4.19}$$
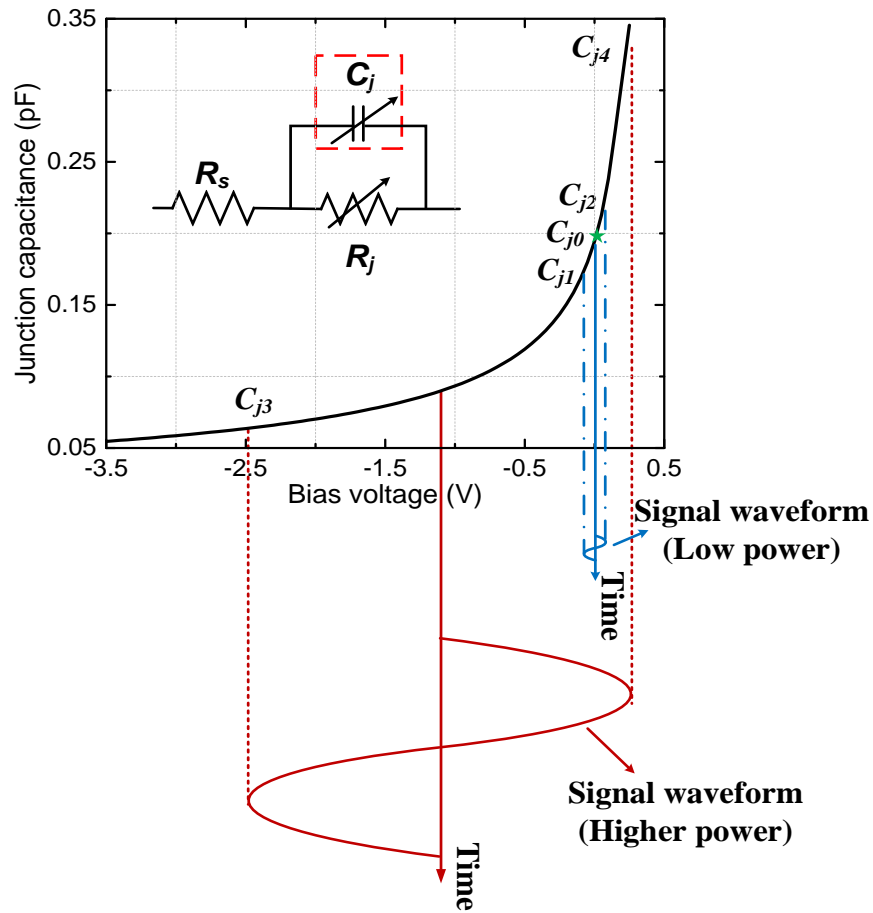
Figure 4.4 Capacitance-voltage (C-V) curve with small and large signal waveform swings covering significantly different capacitance range in comparison.

Table 4.2 Key SPICE parameters

	SMS7630	HSMS-2850
I_s (A)	5e-6	3e-6
R_s (Ω)	20	25
n	1.05	1.06
C_{j0} (pF)	0.14	0.18
M	0.4	0.5
F_c	0.5	0.5
V_j (V)	0.34	0.35

Two most commonly used zero bias Schottky diodes in the low-power rectifier design have been selected for verification, which are SMS7630 and HSMS-2850. Key SPICE parameters of the diodes have been listed in Table 4.2.
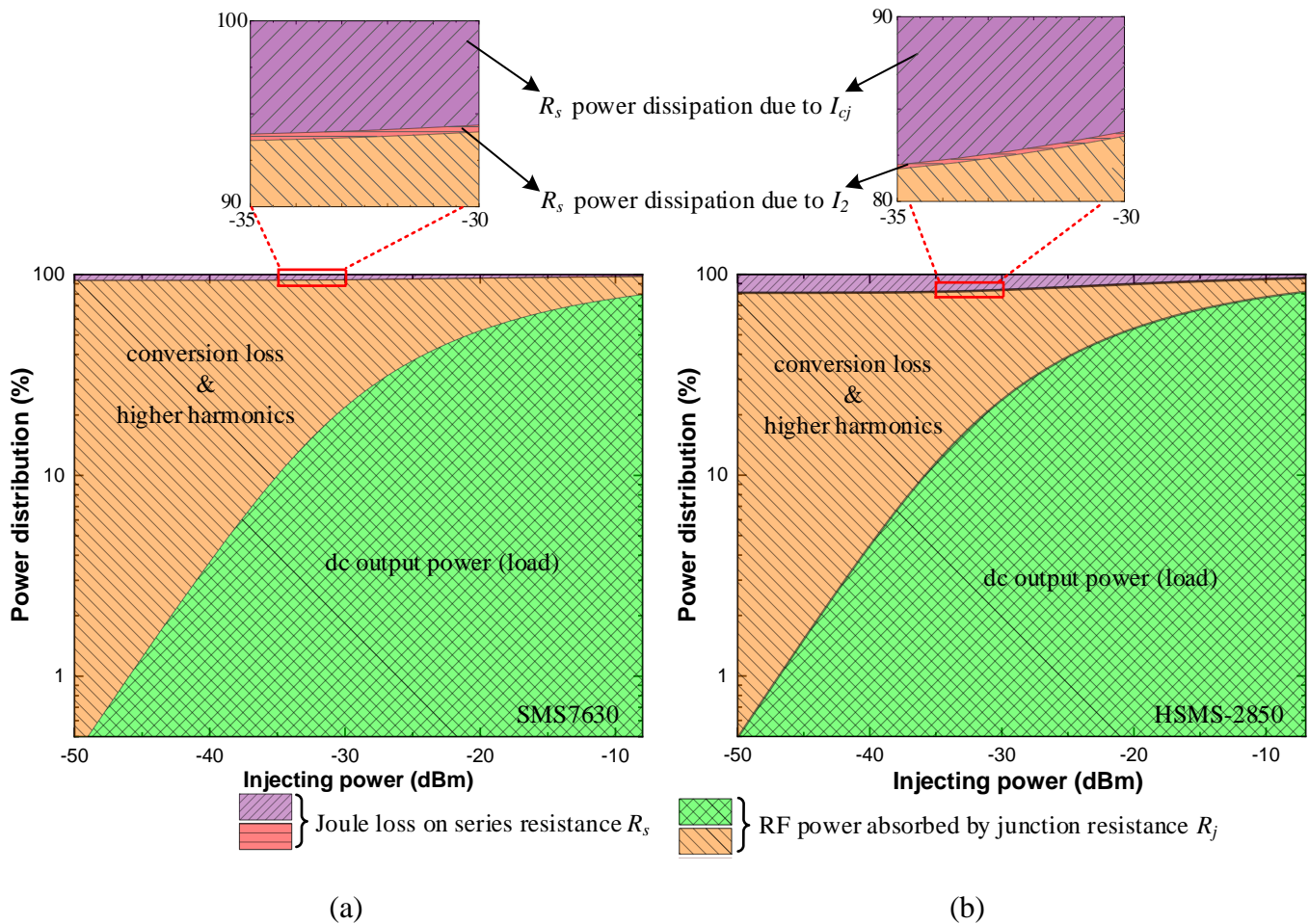
Figure 4.5 Distribution of RF power absorbed by the diode junction against the input power level. (a) SMS7630 and (b) HSMS-2850.

In the demonstration, the operating frequency is 900 MHz, targeting the GSM-900 frequency band. The load resistances of SMS7630 and HSMS-2850 are respectively 5.4 kΩ and 9.1 kΩ, both equal to R_{j0} of the corresponding diodes. The internal resistance of the RF input source R_0 is assumed to be a standard 50 Ω. The distributions of RF input power absorbed by the diode junction are demonstrated in Figure 4.5 (a) and (b) for SMS7630 and HSMS-2850, respectively. The ratio of dc output power increases with a larger input power level. And compared to other losses, power dissipation due to R_s is relatively small for both diodes. Moreover, the ratio of dc power reaching load resistance to the dc power coming out of diode junction can be calculated by $R_l/(R_l + R_s)$. Since R_s is usually much smaller than R_l, the dc power dissipated by R_s is negligible.

Figure 4.6 (a) and (b) present the PCE performance of SMS7630 and HSMS-2850, respectively. For comparison, PCE results based on ADS harmonic balance simulation, low-power model reported in [18], and the proposed method are all demonstrated together. The PCE results obtained from the proposed method have been provided up to the power level where diodes are set to break down. The low-power model using the Taylor expansion only offers satisfactory PCE results when the input power is smaller than −35 dBm. The insets of Figure 4.6 display the PCE results of the three methods in the power range from −30 dBm to −24 dBm. The advantage of our proposed method has been clearly demonstrated. Moreover, the PCE error information of the proposed method with respect to the commercial harmonic balance simulator has been also included in Figure 4.6. Less than a 5 % error has been archived within the power range of interest for both diodes. Our proposed method has presented satisfactory accuracy for PCE prediction in an extended dynamic range.

(a)

(b)
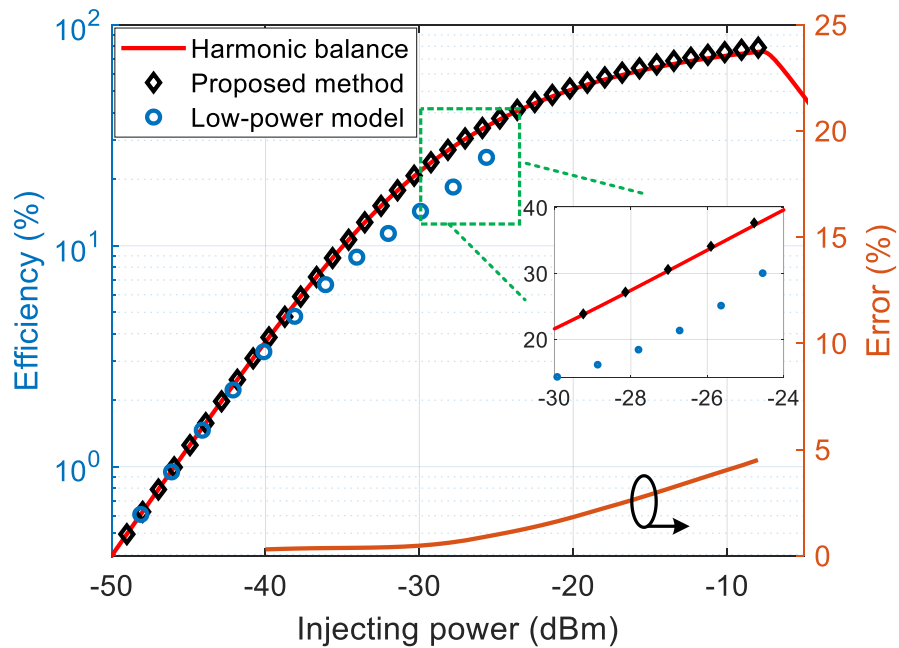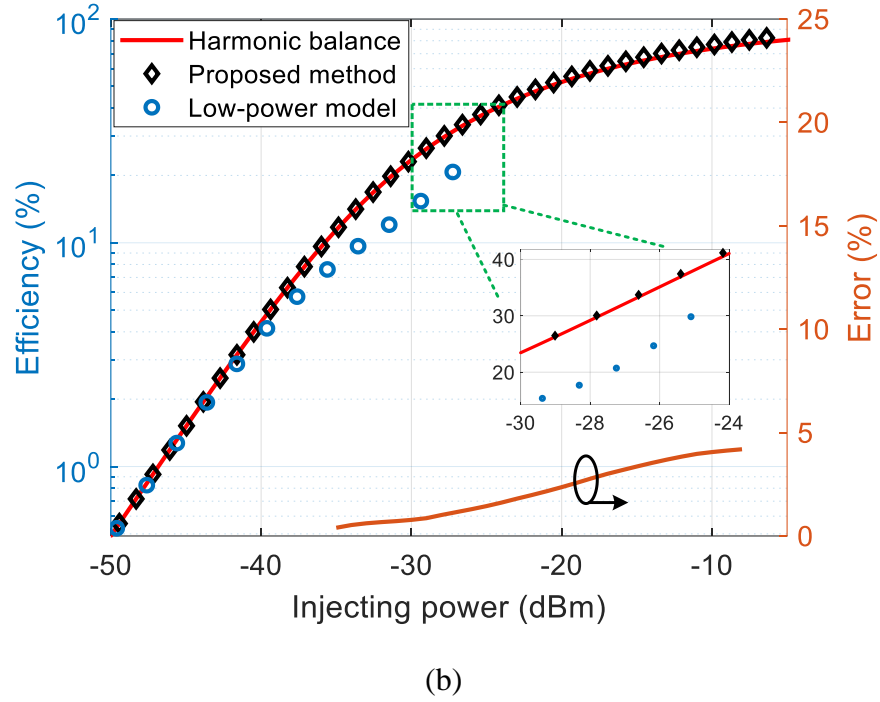
Figure 4.6 Comparison of PCE results based on different models. The calculation error information of the proposed method is also provided, showing superior accuracy performance in an extended dynamic range. (a) SMS7630 and (b) HSMS-2850.

4.3 Thermal Response of Rectifiers

The temperature-dependent parameters of Schottky diodes are I_s, V_j, and C_{j0} [120]. If the operating temperature of the diode is defined as T_{new}, the saturation current $I'_s(T_{new})$ at this temperature is expressed by:

$$I'_s(T_{new}) = I_s \times \left(\frac{T_{new}}{T}\right)^{\frac{Xti}{n}} e^{(1-\frac{T}{T_{new}}) \cdot \frac{Eg \cdot q}{nkT}} \tag{4.20}$$

where Xti and E_g are saturation current temperature exponent and energy gap, respectively. To obtain the temperature-dependent junction potential $V'_j(T_{new})$, the intrinsic carrier concentration $n_i(T_{new})$ has to be defined first [120, 123]:

$$n_i(T_{new}) = 1.45 \times 10^{10} \cdot \left(\frac{T_{new}}{T}\right)^{1.5} \times e^{\left(\frac{1.115 \cdot q}{2kT} - \frac{1.16 - \frac{7.02 \times 10^{-4} \times T_{new}^2}{T_{new} + 1108} \cdot q}{2kT_{new}}\right)} \tag{4.21}$$

Then $V_j'(T_{new})$ is expressed by:

$$V_j'(T_{new}) = V_j \times \frac{T_{new}}{T} + \frac{2kT_{new}}{q} \times ln\left(\frac{n_i(T)}{n_i(T_{new})}\right) \tag{4.22}$$

The temperature-dependent nonlinear junction capacitance $C_{j0}'(T_{new})$ is defined as:

$$C_{j0}'(T_{new}) = C_{j0} \times \left(1 + M \times \left[1 + 4 \times 10^{-4} \times (T_{new} - T) - \frac{V_j'(T_{new})}{V_j}\right]\right) \tag{4.23}$$

Assuming ideal matching conditions and optimum load selected, a simplified overall efficiency expression is reported in our previous work [18]:

$$\eta = \eta_{RFdc} \cdot \eta_p = \frac{P_{in} \cdot \mathfrak{R}_I^2 \cdot R_{j0}^2}{R_L + R_s + R_{j0}} \times \left(\frac{1}{1 + (\omega \cdot C_{j0})^2 \cdot R_s \cdot R_{j0}}\right)^2 \tag{4.24}$$

in which $\mathfrak{R}_I$ is the short-circuit current responsivity and associated with temperature [3]. $\mathfrak{R}_I$ is defined as the ratio of dc output current to the RF input power when the load is short-circuited. Zero bias current responsivity $\mathfrak{R}_{I0} = q/(2n \cdot k \cdot T)$ is a good approximation of $\mathfrak{R}_I$ when the input power of diode is low. When T decreases, I_s becomes smaller, which leads to larger R_{j0} and smaller C_{j0}. But the increase of R_{j0} is in an order of magnitude (Figure 4.7), thus it is the dominant factor to drag down the parasitic efficiency η_p. However, the RF-to-dc conversion efficiency η_{RFdc} becomes larger at a lower temperature due to the increase of $\mathfrak{R}_I$ and R_{j0}. Therefore, the overall efficiency in (4.24) has an optimum operating temperature at a fixed input power level.

Two different cases in terms of the load resistance R_l are investigated through the proposed analytical method in this work. The first one is a rectifier with fixed R_l operating under various temperature conditions. The other is a rectifier with optimum R_l to ensure peak PCE under each temperature condition.

The investigation is based on diodes SMS7630 and HSMS-2850. The operating frequency is 900 MHz. Three input power levels are studied: -20, -30, and -40 dBm. Results obtained by both the proposed method and ADS harmonic balance simulator are included in the comparison.
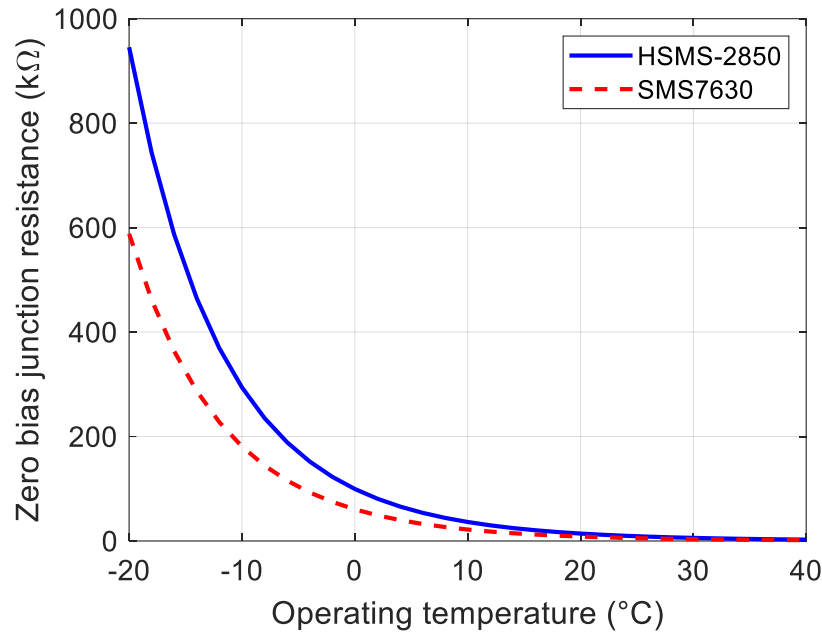
Figure 4.7 Zero bias junction resistances of Schottky diodes vary as a function of operating temperature in a range of −20 °C to +40 °C.

4.3.1 **Fixed Load Resistance**

Figure 4.8 presents the PCE results of rectifiers with fixed load resistances which are set to be 5.4 kΩ and 9.1 kΩ for diodes SMS7630 and HSMS-2850, respectively. The operating temperature range is from −20 °C to +40 °C. As can be clearly seen from the comparison, our proposed method works well in the entire range of interest at various input power levels. Moreover, there exists a temperature at which the rectifier reaches its peak PCE at each input power level, which is consistent with the aforementioned analysis. If this temperature is defined as the optimum temperature, the calculated optimum temperatures of both diode-based rectifiers by the proposed method are summarized in Table 4.3. For both rectifiers, this optimum temperature tends to slightly increase with a larger input power level.
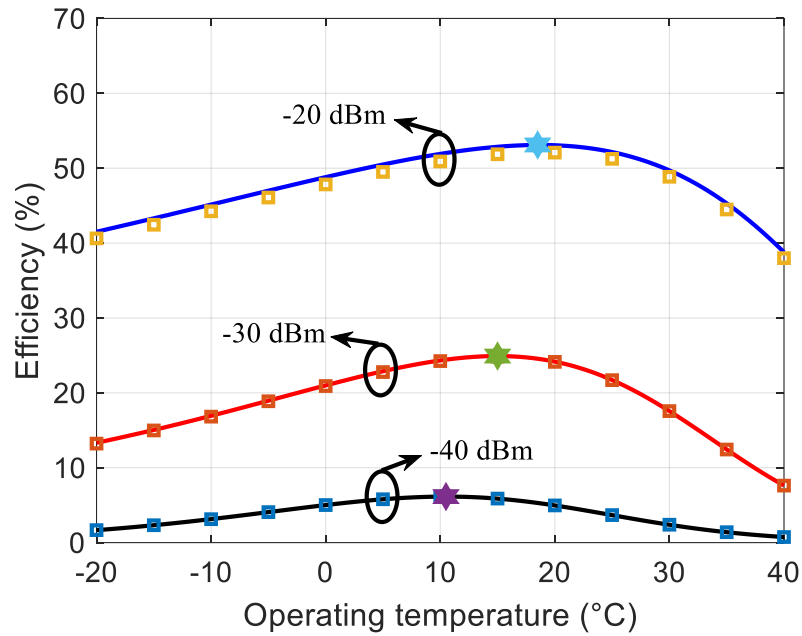
(a)
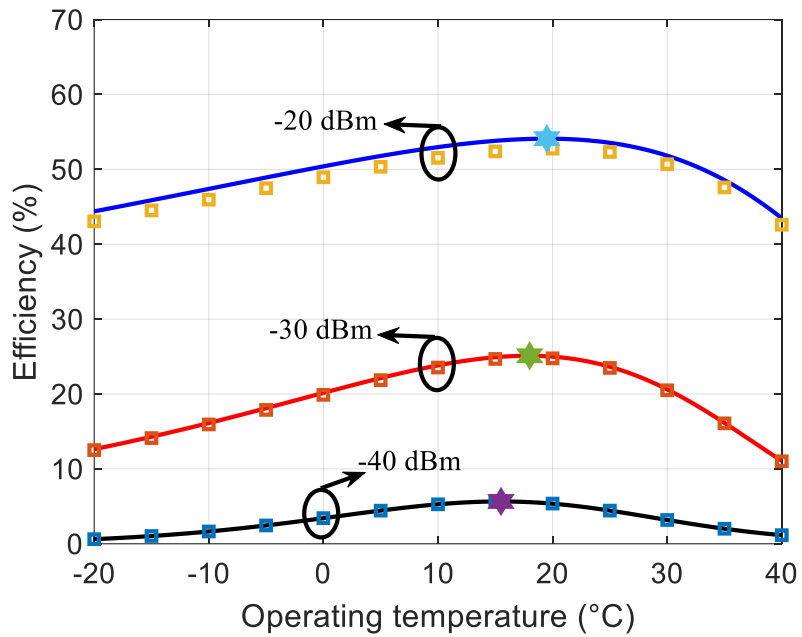
(b)

Figure 4.8 PCE results of rectifiers with fixed R_l versus operating temperatures. (a) SMS7630 and (b) HSMS-2850. Solid line: calculated results based on the proposed method. Square symbols: simulated results by the ADS harmonic balance simulator. Hexagram symbols label calculated the optimum operating temperature at each input power level.

4.3.2 Optimum Load Resistance

(a)

(b)

(c)
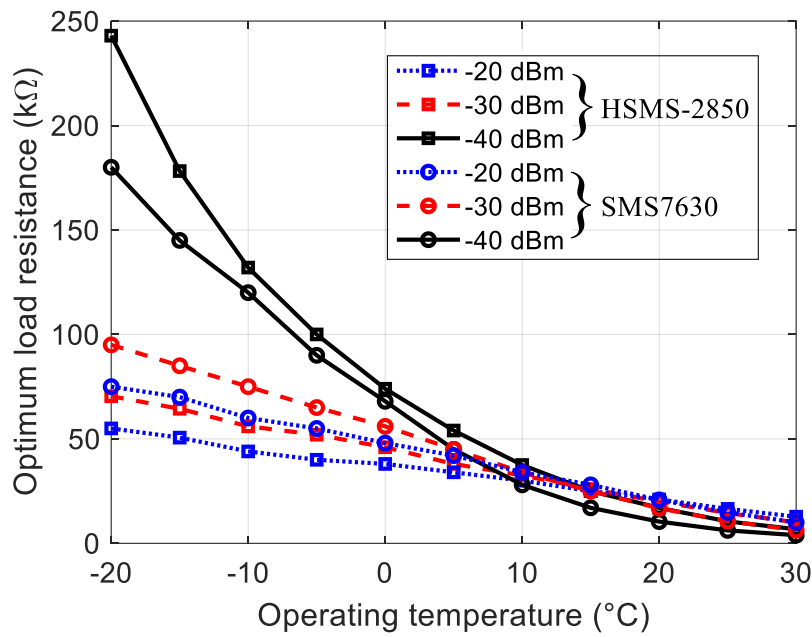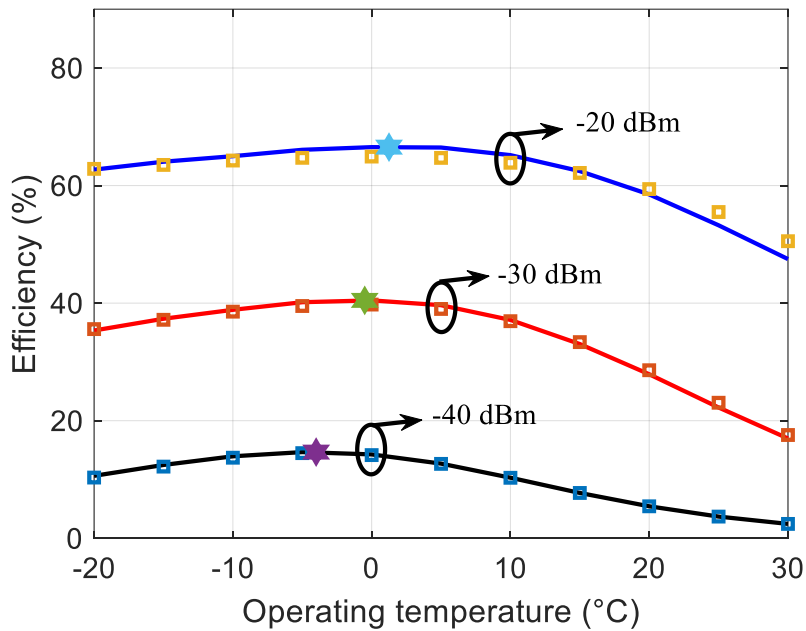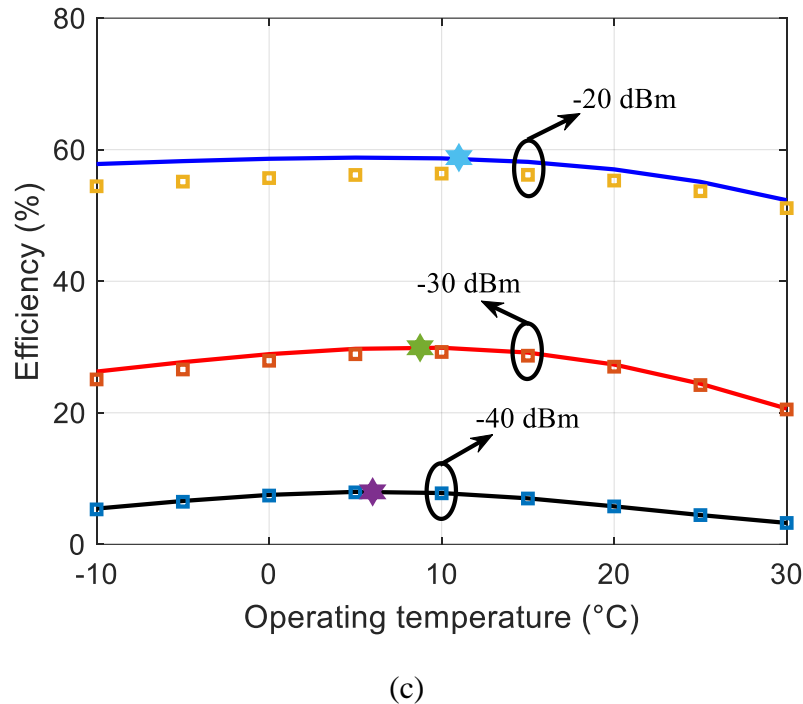
Figure 4.9   (a) Optimum R_l for both diode-based rectifiers at three input power levels versus operating temperatures. PCE results of the rectifiers with optimum R_l as a function of operating temperatures: (b) SMS7630 and (c) HSMS-2850. Line specification is the same as in Figure 4.8.

The proposed analytical method is first applied to attain the optimum load resistances of both diode-based rectifiers at each temperature, which is shown in Figure 4.9 (a). Through a comparison between Figure 4.7 and Figure 4.9 (a), the claim that optimum R_l can be approximated by diode R_{j0} is only valid when the input power is close to being infinitely small. However, the calculation also shows relatively small PCE differences at –40 dBm in both $R_l = R_{j0}$ and optimum R_l values in Figure 4.9 (a). Thus, in a low input power range ($<$–30 dBm), it is still a cost-efficient solution to quickly identify the optimum R_l (equal to R_{j0}). Figure 4.9 (a) also shows that at a low power level (-40 dBm), optimum R_l has the largest variation in the temperature range of interest. With a larger input power level, the variation becomes smaller.

Then, the PCE results of both rectifiers with optimum R_l are calculated and demonstrated in Figure 4.9 (b) and (c). Optimum temperatures are captured which are shifted to a lower temperature range compared to those with fixed R_l. Considering that the optimum temperatures of each rectifier are the main focus, certain changes to the sweeping temperature range of interest are made to keep

optimum temperatures in the middle. For example, the temperature range of HSMS-2850-based rectifier has been set from −10 °C to 30 °C. Table 4.3 also includes calculated optimum temperatures for this case. Similar to the fixed R_l case, the optimum temperatures of rectifiers with optimum R_l tend to increase with a larger input power level. Moreover, optimum R_l keeps the PCE result curve flatter in the entire temperature range compared to the fixed R_l case, indicating that it is a solution to maintain stable PCE under various thermal conditions.

Table 4.3 Calculated optimum temperatures

		SMS7630	HSMS-2850
	−20 dBm	18.5 °C	19.5 °C
Fixed R_l	−30 dBm	15 °C	18 °C
	−40 dBm	10.5 °C	15.5 °C
	−20 dBm	1.25 °C	11 °C
Optimum R_l	−30 dBm	−0.5 °C	8.75 °C
	−40 dBm	−4 °C	6 °C

4.4 **Experimental Verification and Comparison**

Experimental prototypes are built on the substrate of a Rogers RT/duroid 6002 with a 20 mil thickness and 18 μm copper cladding. Since the recommended operating frequency is below 1.5 GHz for diode HSMS-2850, the operating frequency for both rectifiers are designed at 900 MHz. The prototypes are presented in Figure 4.10. The primary design work of rectifiers lies in the optimization of the L matching network at their optimum temperatures based on the previous theoretical analysis. Moreover, filtering low-pass capacitances are carefully placed to maximize dc output across the load through ADS tuning. The impedance of microstrip lines is designed to be 100 Ω with a width of 0.323 mm to reduce the form factor of the entire circuit. At the input port, the width of microstrip line is larger (1 mm) to make SMA connector soldering more convenient and reliable. As our primary goal is to study the temperature response of diode-based rectifiers, both prototypes are designed to be narrow-band. However, it is noted that wide-band operation is possible through optimizing matching networks to cover, for example, digital TV frequency bands.
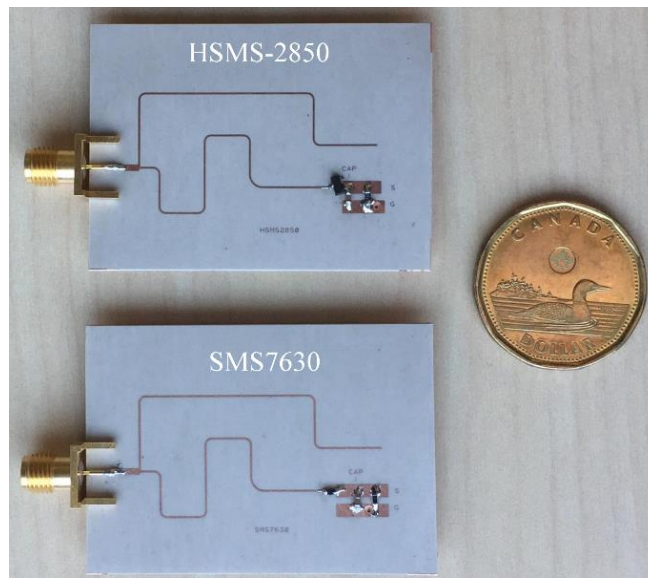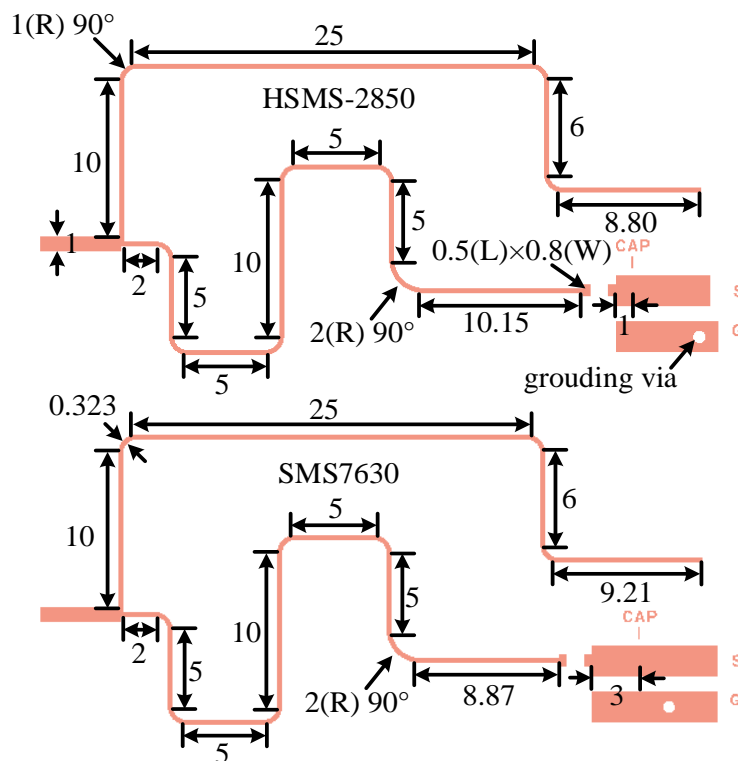
Figure 4.10 (a) Experimental prototypes of rectifiers; (b) Schematics with dimensions in mm. All microstrip curved bends are 90° with a radius of 1 mm except one with a radius of 2 mm which is indicated in graphs. Filtering low-pass capacitances for both designs are the same (0.22 µF).

Measurements were performed with the aid of a TestEquity Model 105 temperature chamber, which offers a temperature range of −40 °C to +130 °C. Figure 4.11 (a) presents the measurement setup in our lab. The multimeter acquires the dc output voltage of the rectifier which is placed inside the chamber. A thermometer is used to monitor the inner temperature for more precise temperature control. The diode nonlinear junction resistance and capacitance change with the temperature variations. The matching conditions of the rectifiers would degrade accordingly, thereby resulting in more mismatch loss. For example, Figure 4.11 (b) shows measured S11 of HSMS-2850-based rectifier at different temperatures. Return loss (−S11) turns out smaller at a lower temperature, and actual power absorbed by the rectifier decreases if the external power supply is constant. To maintain the same level of power injected into the rectifier P_{in} at various temperatures, corresponding adjustments of the external available source power P_{avs} is required to compensate for the mismatch loss. Therefore, a vector network analyzer (VNA) was used in the measurement. Besides its traditional function to obtain S-parameters, it can also offer a continuous wave at a single frequency in CW mode. In this CW mode, VNA conducts no frequency sweeping as only 1 frequency point exists. Then it becomes a signal generator for the rectifier and simultaneously reads the input reflection coefficients that are used for the calculation of input power compensation. Before prototypical experiments, a power meter is connected to the VNA to measure its RF output for calibration purposes. The required external power supply P_{avs} from VNA can be calculated through:

$$P_{avs} = \frac{P_{in}}{1-|S11|^2} \tag{4.25}$$

where S11 is in linear form. As can be seen in Figure 4.11 (b), if a consistent −20 dBm input power P_{in} is desired, the required power supply P_{avs} becomes larger at lower temperatures.
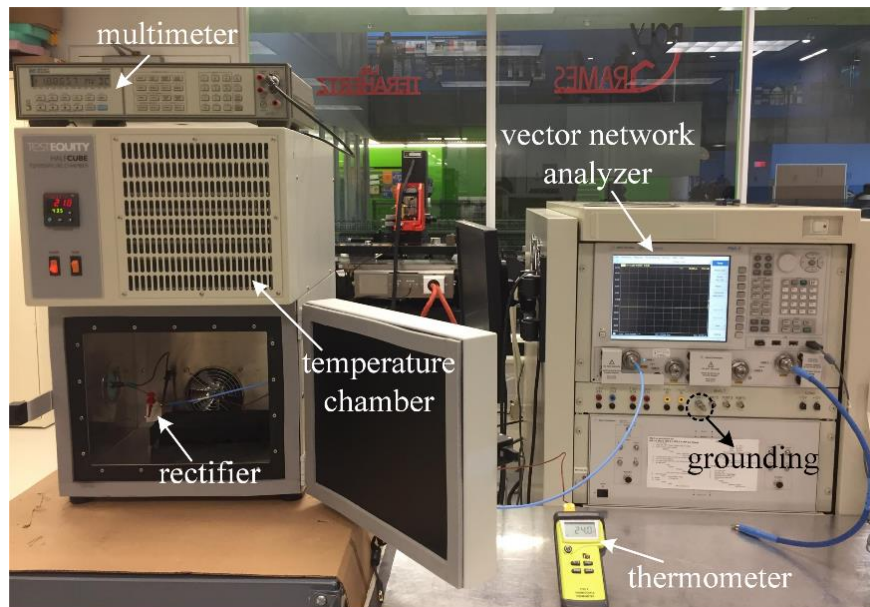
(a)
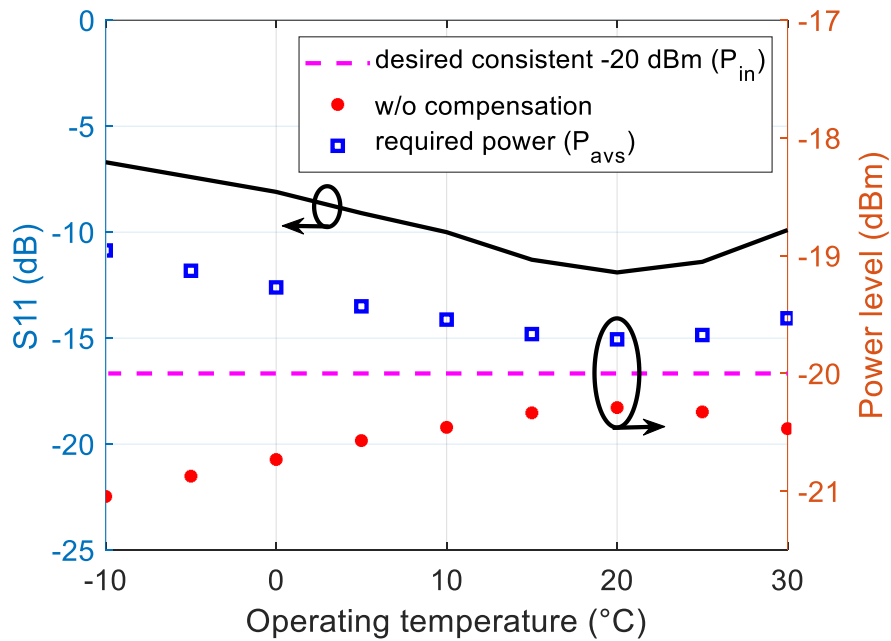
(b)

Figure 4.11 (a) Measurement setup to investigate the dc output power of rectifiers at different temperatures; (b) Measured |S11| and necessary power compensation to keep input power consistent under different temperature circumstances. This plot is extracted from the HSMS-2850-based rectifier with cable loss de-embedded.
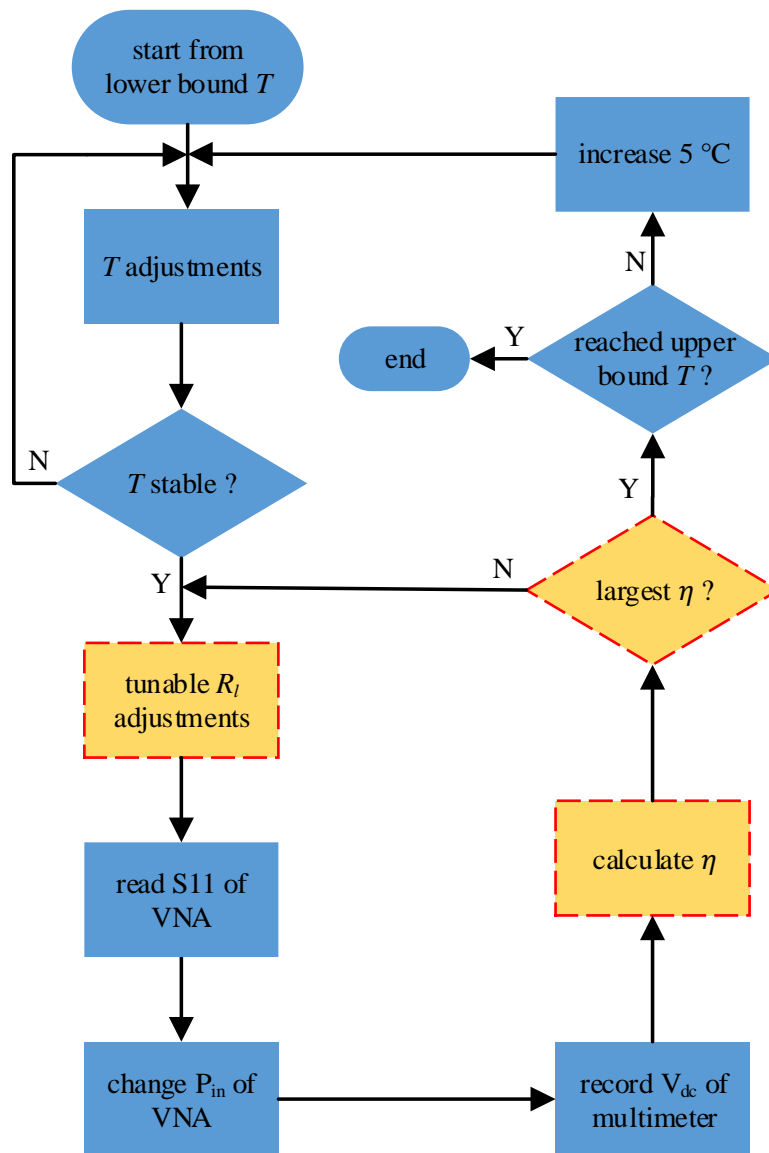
Figure 4.12 Flow chart of measurements. Yellow blocks are steps needed for optimum load measurements.

The major advantage of this setup is that both S11 and dc output voltage measurement can be simultaneously completed, instead of having two separate sets of measurements considering the necessary compensation. It should be noted that one grounding connection to the measurement port of the vector network analyzer is essential, as shown in Figure 4.11 (a), to provide a dc path for the rectifiers. Also, the temperature step was set to 5 °C in order to get enough resolution in the dc output voltage during the measurement. Figure 4.12 presents a flow chart showing each step of measurements.

To verify the proposed method with an extended dynamic range, the rectifiers were measured versus an input power range from −40 dBm to −10 dBm, at a temperature of 22.5 °C. Since the PCE curves of both rectifiers have similar trends and some overlaps at this frequency, the rectifier based on diode HSMS-2850 is taken as an example. The proposed method focuses on diode conversion and loading, so the insertion loss of matching network is estimated by ADS Momentum co-simulation (Figure 4.13 (a)) and then imported for calculation. The insertion loss (*IL*) of the matching network can be described by:

$$IL(dB) = 10 \times log\left(1 + \frac{Q_r}{Q_m}\right) \tag{4.26}$$

in which Q_r is the quality factor of the diode together with the load. Q_m is the quality factor of the realized matching network. Q_r can be calculated by:

$$Q_r = \frac{|X_{in}|}{R_{in}} \tag{4.27}$$

where X_{in} and R_{in} are reactance and resistance looking into the diode together with the load. Simulation results of Q_r with the aid of ADS as a function of input power are also shown in Figure 4.13 (a). Once the matching network is implemented (Q_m is fixed), at a higher RF input power level, Q_r decreases, leading to lower insertion loss.

(a)
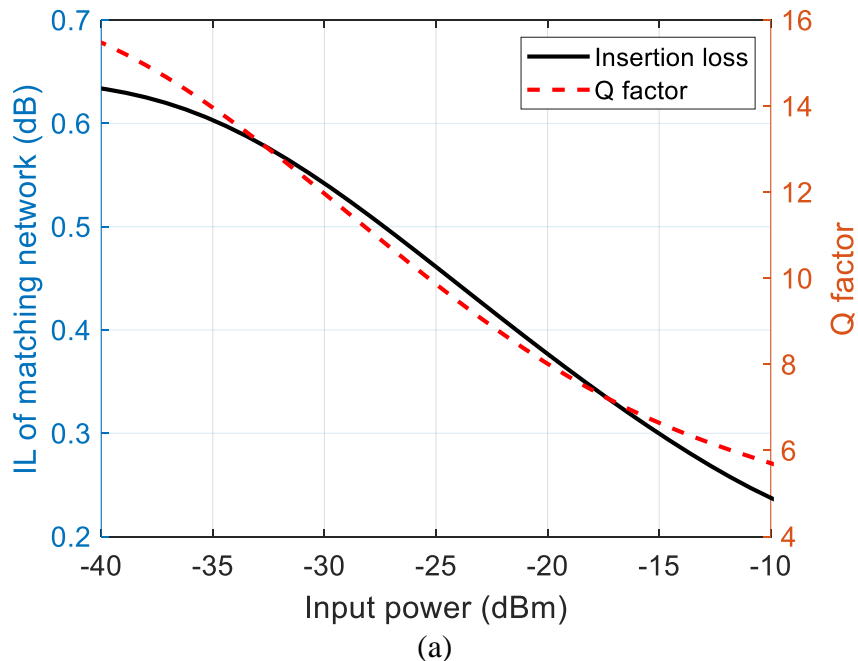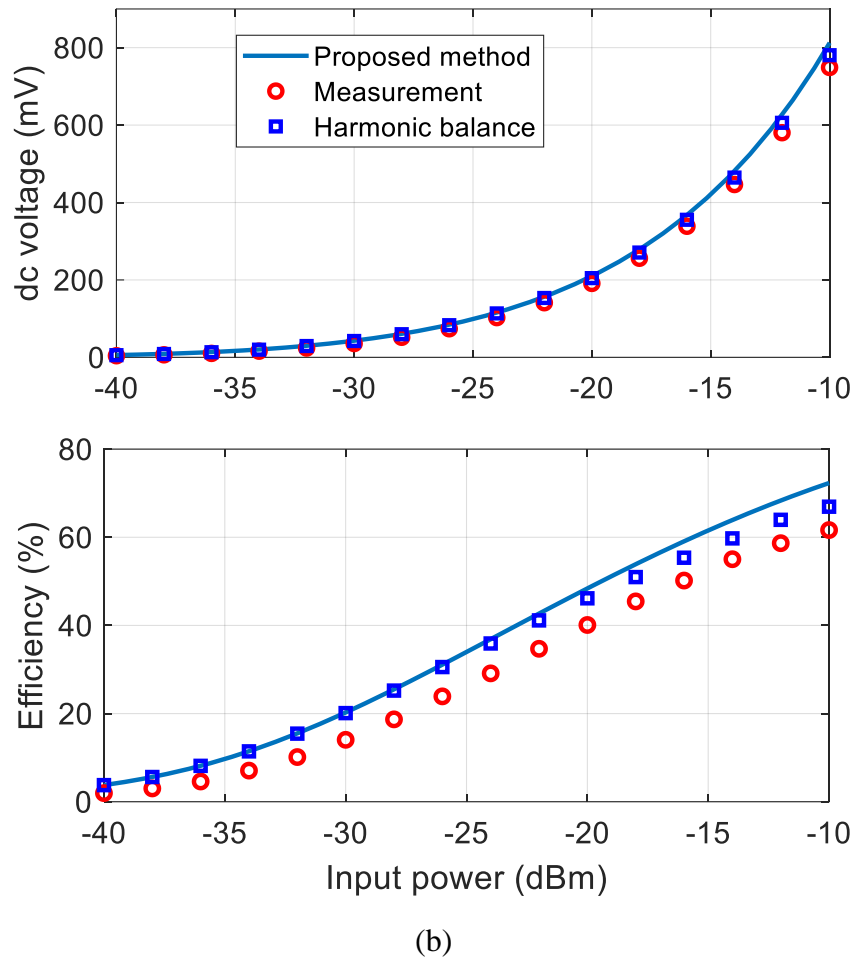
Figure 4.13 (a) Insertion loss of matching network obtained by ADS Momentum co-simulation; (b) Comparison of measured, ADS Momentum co-simulated, and calculated dc output voltage and PCE of HSMS-2850-based rectifier.

The matching network insertion loss of matching network is Figure 4.13 (b) shows a comparison of the measured, ADS Momentum co-simulation, and calculated dc output voltage and PCE results. It can be observed that the three curves of dc output voltage match each other well. Moreover, despite some differences between measured and calculated PCE results, they share a similar trend and agree with each other reasonably well. The above observations demonstrate that the proposed closed-form method can be an effective and powerful tool to analyze and predict the PCE performance of zero bias Schottky diodes-based rectifiers.

4.4.1 **Fixed Load Resistance**
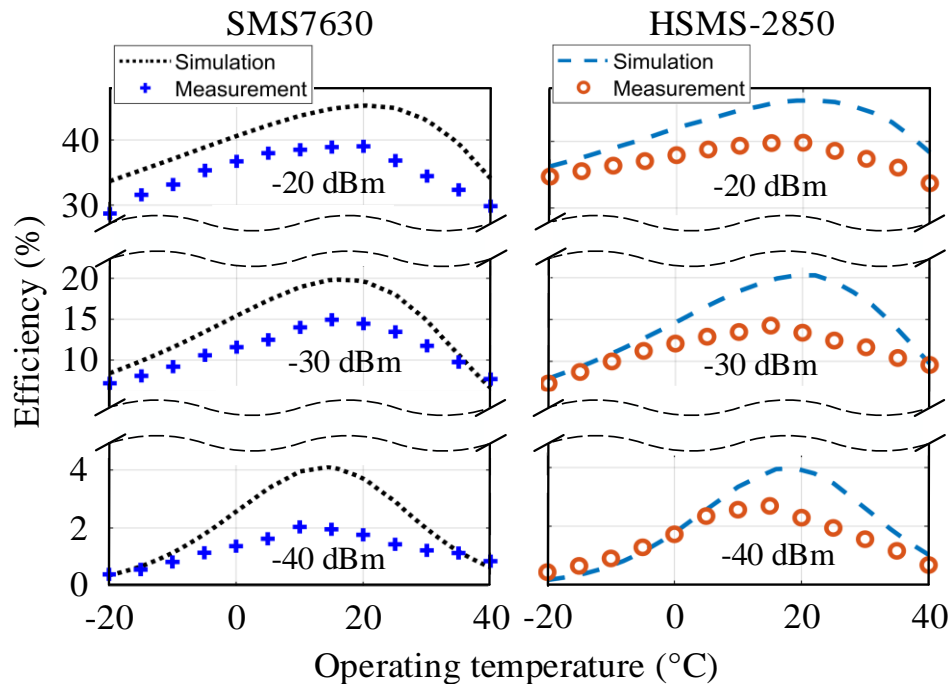
Figure 4.14 Comparisons of measured and simulated PCE results of the rectifiers at different input power levels versus operating temperature. Y ticks are consistent for both.

 The PCE performance of both rectifiers was measured as a function of operating temperatures at three different input power levels: -20, -30, and -40 dBm. In this case, fixed R_l is are chosen for diodes SMS7630 and HSMS-2850-based rectifiers, and they respectively are 5.4 kΩ and 9.1 kΩ. Corresponding measured and simulated results are presented in Figure 4.14. Considering that both the calculated and simulated results are quite close, as shown in Figure 4.8, the calculated results are not included to keep all figures clear and to the point.

Referring to trends in each subplot of Figure 4.14, it can be first observed that the measured results agree reasonably well with simulated ones despite some differences. The microstrip lines with a characteristic impedance of 100 Ω shrink the overall circuity size, but high-impedance lines might introduce more loss in the matching network, resulting in the measured results being smaller than the simulated counterparts. Further improvements of the PCE are still possible. Secondly, for each rectifier, at different power levels, an optimum operating temperature exists as predicted by the theoretical analysis. It should be noted that a few measured results are slightly higher than the

simulated ones, especially when the operating temperature is either quite low or high. A reasonable explanation is that the SPICE parameters of selected diodes for verification do not necessarily have the same values as those that appear on datasheets which are used for simulation.
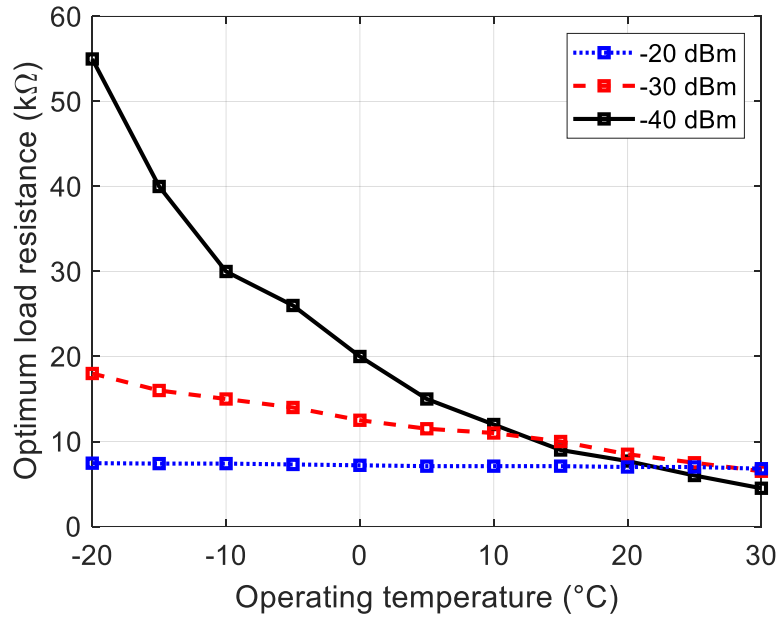
(a)
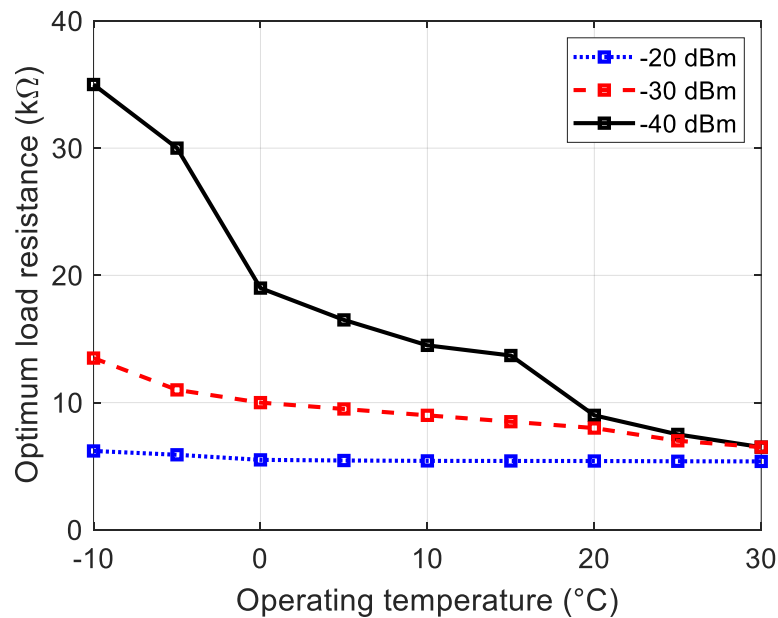
(b)

Figure 4.15 Measured optimum load resistance of rectifiers at different input power levels versus operating temperature. (a) SMS7630, and (b) HSMS-2850.

Thus, when the operating temperature deviates from the optimum one, there are no such dramatic changes in the diode junction resistance and capacitance during the measurement, as predicted by the simulation. This measurement finally displays PCE discrepancies between the optimum and edge temperatures (−20 °C and +40 °C) in measured results are smaller than in their simulated counterparts.

Measured results illustrate that temperature variation plays a significant role in determining the PCE of rectifiers. Table 4.4 summarizes the measured optimum temperatures and PCE improvements over three typical conditions, namely winter (−10 °C), room temperature (25 °C) and summer (+30 °C) times. In other words, it means the PCE of the rectifiers would degrade when the operating temperature shifts away from the optimum value. The PCE improvements at lower input power levels are more obvious. For example, under its optimum temperature of 10 °C, the PCE of the SMS7630 diode-based rectifier has improved by 42 %, 66 %, and 148 % in relation to room temperature, summer, and winter conditions, respectively at −40 dBm.

Furthermore, measured results show that the optimum temperature tends to increase with a larger input power level in the power range of interest for both rectifiers, although such a trend is more obvious in the simulated results due to the measurement's limited resolution. This optimum temperature of rectifiers is closely associated with the diode SPICE parameters as discussed in the previous section. Thus, each type of diode-based rectifiers has its own optimum temperature, and our proposed zero bias Schottky diode-based rectifiers with fixed R_l have optimum temperatures in the range of 10 °C to 20 °C within the power range (Table 4.4).

4.4.2 **Optimum Load Resistance**

To determine the optimum load resistance of the rectifiers, the chip load resistors are first removed, and a manually tunable resistor is used as the loading resistor. The measurement setup is the same as shown in Figure 4.11 (a), except that the replaced tunable load resistor is put outside the chamber. Measurement steps in detail are also addressed in Figure 4.12. At each temperature, the dc output voltage is directly obtained when adjusting the tunable resistor. With this information, PCE is then calculated. Finally, the optimum load resistance corresponds to the highest PCE while sweeping the tunable resistor under the same temperature condition. As the load resistance adjustments are done manually and a following mathematical calculation of PCE is required, this

measurement offers a limited resolution obtaining the optimum load resistance. This explains why the curves in Figure 4.15 are not smooth. Similar to the theoretical prediction, resistance variation is larger at lower input levels. But compared to the theoretical results in Figure 4.9 (a), the measured optimum R_l shows small variations in the same temperature range.
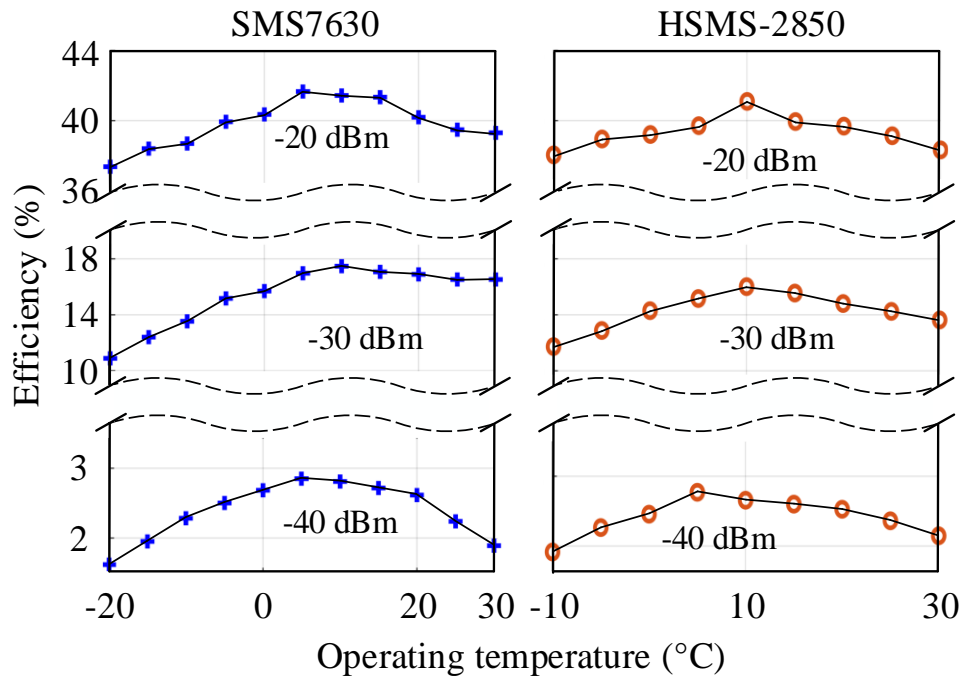
Figure 4.16 Measured PCE results of rectifiers at different input power levels versus operating temperature. Y ticks are consistent for both.

When optimum R_l is reached, the dc output voltage is recorded to obtain the PCE of rectifiers. Results at three input power levels are demonstrated in Figure 4.16. Since the measured optimum R_l is different from the theoretical ones as discussed above, theoretical PCE results are not included for comparison in Figure 4.16. As expected, PCE results with optimum R_l are slightly higher than those in the fixed R_l case shown in Figure 4.14. Moreover, PCE results in the entire temperature range present smaller variations than the previous case. Therefore, PCE improvements at optimum temperatures over the three typical conditions are less obvious compared to the rectifiers with fixed R_l, as shown in Table 4.4. For instance, under its optimum temperature (5 °C), the PCE of the SMS7630 diode-based rectifier has enhanced by 27 %, 51 %, and 25 % in relation to room temperature, summer, and winter conditions, respectively, at −40 dBm. Measured optimum temperatures have been further shifted to a lower range, as listed in Table 4.4.

Table 4.4 Optimum temperature of rectifiers and PCE improvements over three typical conditions

		power level / rectifier	−20 dBm	−30 dBm	−40 dBm
Fixed R_l	Optimum temperature	SMS7630	20 °C	15 °C	10 °C
		HSMS-2850	20 °C	15 °C	15 °C
	PCE improvement at optimum temp. over −10 °C (winter)	SMS7630	18 %	62 %	148 %
		HSMS-2850	9 %	43 %	200 %
	PCE improvement at optimum temp. over 25 °C (room temp.)	SMS7630	6 %	11 %	42 %
		HSMS-2850	3 %	14 %	39 %
	PCE improvement at optimum temp. over +30 °C (summer)	SMS7630	13 %	27 %	66 %
		HSMS-2850	6 %	22 %	73 %
Optimum R_l	Optimum temperature	SMS7630	5 °C	10 °C	5 °C
		HSMS-2850	10 °C	10 °C	5 °C
	PCE improvement at optimum temp. over −10 °C (winter)	SMS7630	8 %	29 %	25 %
		HSMS-2850	8 %	36 %	45 %
	PCE improvement at optimum temp. over 25 °C (room temp.)	SMS7630	6 %	6 %	27 %
		HSMS-2850	5 %	12 %	17 %
	PCE improvement at optimum temp. over +30 °C (summer)	SMS7630	6 %	6 %	51 %
		HSMS-2850	7 %	17 %	29 %

Finally, the peak PCE results of our work have been compared with the selected ones with advanced performance in Figure 4.1, as shown in Figure 4.17. VDI zero bias diode features low junction capacitance; thus it is suitable for high-frequency implementations. However, its high cost is the main barrier blocking widespread use. Cheap Schottky diode-based rectifiers operating at their optimum temperatures present better PCE performance than counterparts built on VDI zero bias diodes. Also, in a low input power range, tunnel diodes that break rectification limitations demonstrate inimitable superiority. However, SMS7630 and HSMS-2850, common off-the-shelf

diodes, set to operate at their optimum temperatures and input power larger than −30 dBm, are believed to have potential to outperform tunnel diodes in terms of power rectification.
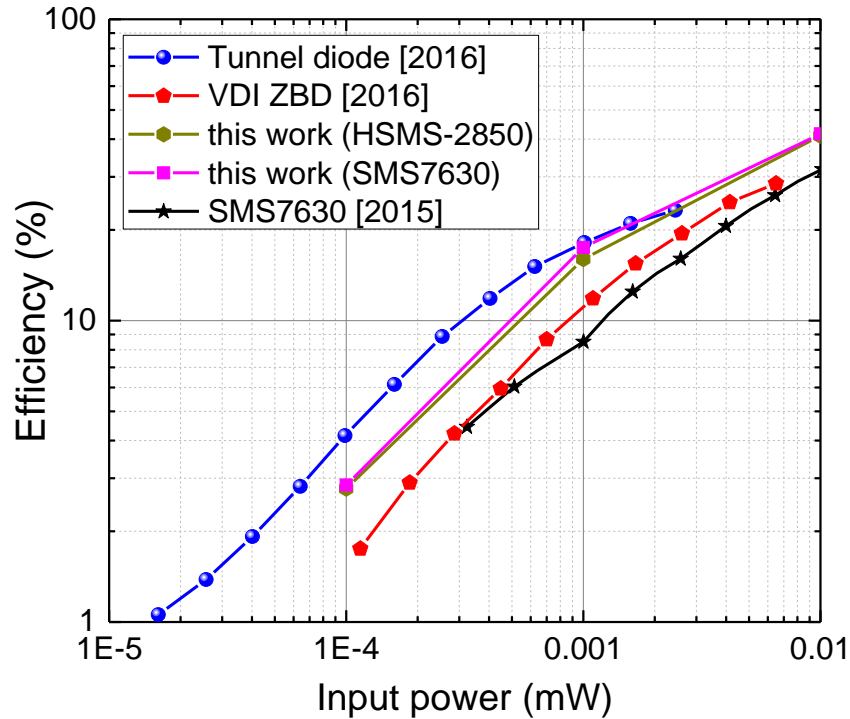
Figure 4.17   Comparison of the measured PCE results with those of selected state-of-the-art rectifiers showing advanced performance in Figure 4.1.

4.5   Conclusion

This work first proposes a closed-form method for PCE prediction for zero bias diode-based rectifiers with an extended dynamic power range of up to −10 dBm approximately. Accuracy has been improved by considering the voltage-controlled junction capacitance at higher input power levels. The proposed method has been validated by both ADS harmonic balance simulation and experiments. With the aid of the powerful method, the thermal effects of two zero bias Schottky diode-based rectifiers are investigated both theoretically and experimentally. Two cases of rectifiers' load resistance are considered: fixed and optimum load resistances. The optimum temperature for each zero bias diode-based rectifier at each power level was captured. And the optimum load resistance condition brings the optimum temperature to a lower range. For instance, the diode HSMS-2850-based rectifier has optimum temperatures of 20 °C, 15 °C, and 15 °C with

the fixed R_l of 9.1 kΩ at −20 dBm, −30 dBm, and −40 dBm, respectively. Whereas, when optimum R_l is applied, the values are reduced to 10 °C, 10 °C, and 5 °C at the same input power levels. This work also demonstrates that noticeable efficiency enhancements can be achieved by considering thermal effects when designing zero bias Schottky diode-based rectifiers. Conventional commercial Schottky diodes can beat expensive VDI zero bias diodes and tunnel diodes by operating at the optimum temperatures when the input power level is beyond −30 dBm. Further improvements are still possible by considering multi-stage matching networks to reduce insertion loss and selecting diodes with lower parasitics.

The conclusion first serves as a reminder that rectifiers should be customized by choosing proper zero bias diodes depending on temperature operations. In fact, as one of the main environmental factors, the operating temperature should be carefully considered when designing nonlinear component-based—not limited to diode-based—devices to ensure its consistent high reliability and great performance.

CHAPTER 5   ARTICLE 4: INTEGRATED COOPERATIVE AMBIENT POWER HARVESTER COLLECTING UBIQUITOUS RADIOFREQUENCY AND KINETIC ENERGY

Xiaoqiang Gu, Simon Hemour, Lei Guo and Ke Wu

An integrated cooperative harvester capable of collecting both electromagnetic (principally RF) and kinetic energy simultaneously is proposed and studied in this work. One single substrate board is demonstrated to accommodate and integrate an electromagnetic kinetic generator, an F-shaped antenna and a rectifying circuit, having a compact credit-card size. Cooperative harvesting mode enables a significant enhancement of the diode's power conversion efficiency (PCE) and also greatly strengthening the resilience of harvester at the same time. Measured results suggest that SMS7630 and HSMS-2850 based cooperative harvesters can increase dc output power by 50% to around 100% when both injecting power sources exhibit below −37 dBm with reference to the total added amount of dc power harvested directly from separate RF and kinetic excitation modes. A closed-form method is proposed and used to predict the enhanced efficiency performance of the cooperative harvester within a low power range of interest (−50 to −30 dBm). Our analysis highlights the roles of the diode's nonlinear junction resistance and capacitance. Good agreements are observed when comparing the analysis results with harmonic balance simulations by ADS. Further, this method is carefully verified by measured results of two different diodes-based harvesters. Measured dc output power rectified from cooperative harvesting mode is reported to be 1.16 and 1.97 times larger with SMS7630 and HSMS-2850, respectively, when both power sources are −40 dBm, compared to the conventional single RF harvesting mode. The proposed cooperative harvester with its strong resilience is highly suitable for ambient power harvesting in an ever-changing environment.

5.1 **Introduction**

Internet of Things (IoT) has been brought more closely to reality thanks to the confluence of popular technologies such as intelligent traffic management system, home automation and wearable health monitoring devices and so on [124]. The implementation of IoT relies heavily on a wide spectrum of networked electronic devices through wireless connectivity. However, it is impractical to power a large number of geographically scattered components with cables, wires and/or batteries, which may present a fundamental hurdle in the realization of IoT systems. In certain applications like powering body implants and embedded structure sensing, the wired power supply is even impossible. Therefore, wireless ambient electromagnetic energy harvesting over legacy RF spectrum or dedicated low-density SAR-complied wireless powering is an attractive and promising alternative for such usually low-duty cycle and low power consumption devices, offering a minimum human intervention [11].

The fact of wireless ambient RF power harvesting in free space is well understood in that it basically provides only very limited energy output [125], thereby resulting in a low power conversion efficiency (PCE) [17]. This crucial issue leads researchers to find more accessible input energy sources so to increase PCE to lift up the final rectified dc output power. Besides electromagnetic RF power, other types of renewable ambient energy, e.g., kinetic, thermal, and solar energy among many others, are actually pervasive and omnipresent in daily life [126]. In the last decade, intensive research interests have been devoted to harvesting these different types of energy sources [127-129]. Although thermoelectric devices and solar cells have been well developed, they technically require large form factors in terms of volume to ensure sufficient amount of energy being converted. Whereas kinetic energy harvester normally has a lightweight and features a higher kinetic-to-electrical PCE of typically 95% [130], compared with thermoelectric materials and solar cells based counterparts. As one of the most commonly attainable and ubiquitous energy sources, kinetic energy is basically a natural target of choice and can be easily converted into electrical energy by electromagnetic, piezoelectric or electrostatic transduction mechanisms [131]. Considering the aforementioned advantages of kinetic energy harvesting, both RF and kinetic energy are being used in this work, but it is also shown that two uncorrelated power sources can be harvested in a *collaborative* manner, in order to generate more dc power output with better efficiency.

The technical issue of how to increase diode's PCE has been a hot topic since the moment when wireless power harvesting technology was born. Recently, different kinds of diodes have been found to be capable of offering stronger nonlinearity, such as spindiodes [18], tunneling diodes [39] and nanodiodes [132]. As a matter of fact, breaking the PCE limitation by improving the diode fabrication process is very challenging in connection with underlying physical principles and material constraints. Whereas adopting a cooperative energy harvesting approach is able to increase diode's PCE dramatically by simply using those off-the-shelf diodes [116]. This is beyond the aforementioned straightforward truth that cooperative energy harvesting obviously brings more input power. Moreover, more power injected into the diode at a low power level shifts operating point to another region with a higher PCE. Thus, cooperative energy harvesting is able to successfully combine both advantages to increase the final dc output power greatly and provide a straightforward resilience of using uncorrelated energy sources. However, the harvester with separate RF and kinetic generator modules in [116], although showing a good performance, normally is impractical for applications in reality because it is too bulky and does not integrate any antenna. Furthermore, it has never been considered that two uncorrelated energy sources operate at frequencies of different orders of magnitude. In previous work [133], the design of an electromagnetic kinetic generator together with its preliminary measurement was presented. In the scope of the present work, a comprehensive theoretical analysis of cooperative harvesting and also a joint measurement using the designed F-shaped antenna in our anechoic chamber are studied and demonstrated.

This paper proposes both theoretical modelling technique and integrated design platform for the analysis and implementation of a simultaneous RF and kinetic energy harvesting. A closed-form analytical method is formulated to examine the PCE enhancement of different Schottky diodes-based harvesters through adopting a cooperative harvesting topology. Harmonic balance simulator is used to verify the method and comparison results show good agreements. Then, one single substrate board mechanically combines an F-shaped antenna, a permanent magnet- and coils-based kinetic generator and a rectifying circuit. Finally, measured results present the PCE improvement of the cooperative harvester over a low power range of interest from -45 dBm to -30 dBm.

5.2 Enhancement of PCE Using Cooperative Harvesting

In [18], the RF-to-dc PCE of a single diode with parasitic loss de-embedded in the circuit is described by:

$$\eta_{RFdc} = P_{in} \cdot \frac{\Re_{I0}^2 \cdot R_{j0}^2}{R_l + R_v} \tag{5.1}$$

in which P_{in} is the input power absorbed by the diode junction, $\Re_{I0}$ is the zero bias current responsivity, R_{j0} is the zero bias differential junction resistance, R_l is the load resistance and R_v is the video resistance. This equation gives a brief glance that PCE is proportional to the input power. The PCE can be theoretically doubled with two identical power sources injecting into the diode junction simultaneously. However, due to the neglect of the parasitic loss for simplification, this method cannot provide a complete picture of the two power injecting case, especially with a large frequency difference.
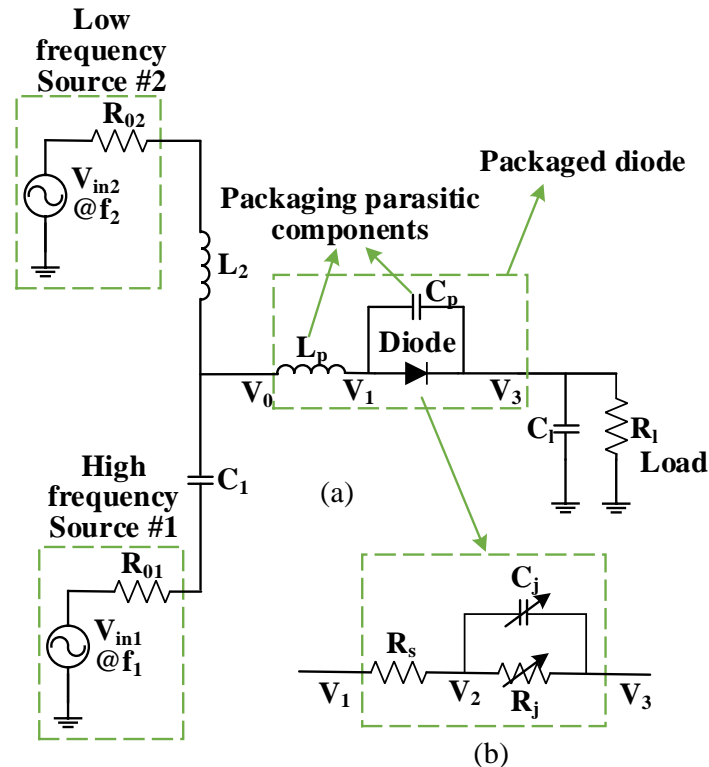
Figure 5.1 (a) Diagram of a single diode based rectifier cooperatively harvesting two sources with high and low frequencies; (b) Shockley diode model. The voltage labels are kept consistent in both (a) and (b).

A comprehensive analysis of the cooperative harvesting topology is presented as follows. Note that the design of a matching network with harmonic terminations is possible to smooth out higher harmonics and maximize the fundamental component [107]. Thus, for the purpose of simplification and also focusing on revealing the PCE performance of diodes, the matching network has been removed in the diagram in Figure 5.1. As can be seen in Figure 5.1 (a), the RF power is labelled as source #1 with high frequency f_1. The electrical signal converted from kinetic energy usually operates at low frequency f_2 (tens or hundreds Hz) and is named as source #2. R_{01} and R_{02} are internal resistances of the RF and kinetic sources, respectively. To prevent interference between those sources operating at different frequencies, one RF choke L_2 and one dc block C_1 are placed in the circuit. L_p and C_p are packaging inductance and capacitance of the diode, respectively. One filtering capacitance C_l is inserted in parallel with load R_l to smooth out the AC voltage across the load. Figure 5.1 (b) shows the classical Shockley model [19] including one series resistance R_s, one nonlinear junction resistance R_j, and one nonlinear junction capacitance C_j.

First of all, both of the input sources are assumed to have sinusoidal waveforms. Let us begin with the diode's Shockley model, the voltage across the nonlinear junction (between V_2 and V_3) has two fundamental components V_{f_1} and V_{f_2} and one dc component V_{dc}. So it has the form of:

$$V_{on} = V_{f_1} + V_{f_2} - V_{dc} = v_{f_1}\cos(2\pi f_1 t) + v_{f_2}\cos(2\pi f_2 t) - v_{dc} \qquad (5.2)$$

where v_{f_1} and v_{f_2} are magnitudes of high- and low-frequency sources, respectively. The dc voltage magnitude is defined as v_{dc} and calculated by dc current times the total resistance in this circuit. The dc current can only reach out to low-frequency source due to the dc block C_1. Hence, the dc voltage is:

$$v_{dc} = i_{dc} \cdot (R_l + R_s + R_{02}) \qquad (5.3)$$

According to [19], the diode's current and voltage relationship (*I-V*) can be written as:

$$I_{diode} = I_s \cdot \left[e^{\frac{V_{on}}{n \cdot Vt}} - 1\right] = I_s \cdot [e^{\frac{v_{f_1}\cos(2\pi f_1 t) + v_{f_2}\cos(2\pi f_2 t) - v_{dc}}{n \cdot Vt}} - 1] \qquad (5.4)$$

in which I_s and n are diode's saturation current and ideality factor, respectively. The thermal voltage V_t is calculated by $k \cdot T/q$, where k, T, and q are Boltzmann constant, operating temperature, and electron charge, respectively. The diode's *I-V* relationship is generally complicated and can be expressed by piecewise equations [120]. So the exponential *I-V* relationship is only valid within a certain voltage range. Through comparing current responses obtained both from the piecewise *I-V* relationship and exponential counterpart, the maximum current error is found to be less than 0.5% when voltage magnitude is smaller than 2 V. Note that SPICE parameters of diode HSMS-2820 is used for this comparison. As the available operational ambient RF power in our lab usually is within −50 to −30 dBm [3], a comparable kinetic power is also kept in the same power range in the following analysis. Based on this assumption, the voltage magnitudes of both sources are basically less than 2 V. Thus, the exponential *I-V* relationship in (5.4) can be considered valid for the analysis within the scope of this work.

The diode current could be easily expanded in terms of separate dc and other harmonics by using Bessel function [115], [121]:

$$e^{\frac{v_{fm}\,cos(2\pi f_m t)}{n \cdot Vt}} = J_0\left(-i\frac{v_{fm}}{n \cdot Vt}\right) + 2\sum_{k=1}^{\infty} i^k J_k\left(-i\frac{v_{fm}}{n \cdot Vt}\right) cos[k \cdot (2\pi f_m t)] \qquad (5.5)$$

where $J_k(x)$ is the Bessel function of first kind of order k and m (1 or 2) decides the high- or low-frequency component, respectively. Thus, the dc current can be expressed as:

$$i_{dc} = I_s \cdot \left[J_0\left(-i\frac{v_{f_1}}{n \cdot Vt}\right) \cdot J_0\left(-i\frac{v_{f_2}}{n \cdot Vt}\right) \cdot e^{\frac{-v_{dc}}{n \cdot Vt}} - 1\right]$$

$$= I_s \cdot \left[J_0\left(-i\frac{v_{f_1}}{n \cdot Vt}\right) \cdot J_0\left(-i\frac{v_{f_2}}{n \cdot Vt}\right) \cdot e^{\frac{-i_{dc} \cdot (R_l + R_s + R_{02})}{n \cdot Vt}} - 1\right] \qquad (5.6)$$

Then, dc current can be obtained by solving (5.6) with the help of a Lambert-W function:

$$i_{dc} = I_s \cdot \left(\frac{W_0\left(G \cdot J_0\left(-i\frac{v_{f_1}}{n \cdot Vt}\right) \cdot J_0\left(-i\frac{v_{f_2}}{n \cdot Vt}\right) \cdot e^G\right)}{G} - 1\right) \qquad (5.7)$$

in which W_n is the *n*th branch of the Lambert-W function and G could be expressed by:

$$G = \frac{(R_l + R_s + R_{02})}{R_{j0}} \tag{5.8}$$

where R_{j0} is the diode's zero bias junction resistance and could be calculated by [16]:

$$R_{j0} = \frac{n \cdot V_t}{I_s} \tag{5.9}$$

The fundamental current through the junction resistance can also be obtained from (5.5). Considering the frequency difference is extremely large, the fundamental currents at each frequency can be formulated below:

$$\boldsymbol{I_{f_1}} = i_{f_1} \cdot cos(2\pi f_1 t) = I_s \cdot \left[2 \cdot i \cdot J_1\left(-i\frac{v_{f_1}}{n \cdot Vt}\right) \cdot J_0\left(-i\frac{v_{f_2}}{n \cdot Vt}\right) \cdot e^{\frac{-v_{dc}}{n \cdot Vt}}\right] \cdot cos(2\pi f_1 t) \tag{5.10a}$$

$$\boldsymbol{I_{f_2}} = i_{f_2} \cdot cos(2\pi f_2 t) = I_s \cdot \left[2 \cdot i \cdot J_1\left(-i\frac{v_{f_2}}{n \cdot Vt}\right) \cdot J_0\left(-i\frac{v_{f_1}}{n \cdot Vt}\right) \cdot e^{\frac{-v_{dc}}{n \cdot Vt}}\right] \cdot cos(2\pi f_2 t) \tag{5.10b}$$

Note that each fundamental current of high- and low-frequency sources is assumed to be in-phase with its corresponding voltage across the nonlinear junction resistance. And only the magnitudes of power sources are used to finally calculate the injecting power sources, as shown in (5.7) and (5.10), resulting in the phase information of each source being neglected in the analysis.

The voltage at V_1 of each fundamental frequency can be expressed by applying Kirchhoff Circuit Laws (KCL):

$$\boldsymbol{V_{1f_m}} = \boldsymbol{V_{f_m}} + \left(\boldsymbol{I_{f_m}} + \boldsymbol{V_{f_m}} \cdot i\omega C_j\right) \cdot R_s \tag{5.11}$$

Next, the voltage magnitude injecting into the packaged diode can be calculated by:

$$\boldsymbol{V_{0f_m}} = \boldsymbol{V_{1f_m}} + \boldsymbol{I_{tf_m}} \cdot i\omega L_p \tag{5.12}$$

in which $\boldsymbol{I_{tf_m}}$ is:

$$\boldsymbol{I_{tf_m}} = \boldsymbol{V_{1f_m}} \cdot i\omega C_p + \boldsymbol{I_{f_m}} + \boldsymbol{V_{f_m}} \cdot i\omega C_j \tag{5.13}$$

Having both injecting voltage and current in place, the injecting power into the diode can be expressed by:

$$P_{inf_m} = real\left(\frac{V_{0f_m} \cdot I^*_{tf_m}}{2}\right) \quad (5.14)$$

Given injecting power V_{f_1} and V_{f_2} could be easily obtained by solving (5.6) and (5.10-5.13). C_j is assumed to be zero bias nonlinear junction capacitance C_{j0} that works well within the low power range of interest. The dc power of the cooperative harvester is:

$$P_{dc} = i^2_{dc} \cdot R_l \quad (5.15)$$

Here, we define PCE of the cooperative harvester with a matching network loss de-embedded as the dc output power over the power injected into the diode:

$$PCE = \frac{P_{dc}}{P_{inf_1}+P_{inf_2}} \times 100\% \quad (5.16)$$

It should be mentioned that single power injecting is actually a simplified model of the two-source case, and can be solved using the same method. To quantitatively analyze the enhancement of PCE, efficiency gain (EG) η_g is defined as dc output power P_{dc_co} through the cooperative harvesting mode over that of a direct summation of seperate RF and kinetic excitation mode $P_{dc\_RF} + P_{dc\_KI}$ [116]:

$$\eta_g = \frac{P_{dc\_co}}{P_{dc\_RF}+P_{dc\_KI}} \times 100\% \quad (5.17)$$

In the calculation of EG, the input power sources of both cooperative and separate harvesting modes are identical, including the power level and operating frequency. Matching networking loss can be studied independently and thus not considered here. Diodes Skyworks SMS7630-079LF, Avago HSMS-2850, and HSMS-2820 with SOT-23 packaging are theoretically investigated through this method. Both SMS7630 and HSMS-2850 are commonly used in low-power rectifier design and share similar features. By contrast, HSMS-2820 is suitable for rectifiers operating at a relatively higher power level which is usually larger than −10 dBm [18]. Compared with HSMS-2820, diodes SMS7630 and HSMS-2850 are low barrier diodes with a much larger saturation current and a smaller nonlinear junction capacitance. Key SPICE and packaging parameters of these diodes are listed in Table 5.1:

Table 5.1 Key SPICE and packaging parameters

Parameters	Units	SMS7630	HSMS-2850	HSMS-2820
I_s	A	5e-6	3e-6	2.2e-8
n		1.05	1.06	1.08
R_s	Ω	20	25	6
C_{j0}	pF	0.14	0.18	0.7
L_p	nH	0.7	2	2
C_p	pF	0.16	0.08	0.08

In the analysis, the frequencies of RF and electrical energy converted from the kinetic power are set to be 1.8 GHz and 100 Hz, respectively. It should be mentioned that the kinetic energy is controllable and the details will be discussed in Section III. For each diode, the load resistor is set to equal to each diode's zero bias junction resistance, which is the optimum value at a low power level. The load resistors used for SMS-7630, HSMS-2850, and HSMS-2820 are 5.40 kΩ, 9.09 kΩ and 1.26 MΩ, respectively. The internal resistance of RF power source is assumed to be 50 Ω. The resistance of coils is the internal resistance of kinetic power source, which is measured to be 2.3 Ω.

Figure 5.2 gives calculated EG curves of the three different diodes based cooperative harvesters against the injecting power and also compares the results obtained from a harmonic balance simulation in ADS. The injecting power of both RF and electrical energy are kept the same and swept from −50 to −30 dBm. As they can be observed in Figure 5.2, results obtained by the proposed analytical method are in agreement with those obtained from ADS within the power range for each diode.

Based on the observation in Figure 5.2, two questions may be raised naturally. (i) What are the main factors determining an increasing or decreasing trend of the EG curve? and (ii) How does each SPICE parameter influence the EG curve? In other words, how the diodes are selected to yield a larger EG? The following theoretical analysis strives to answer the above two questions.

With reference to Figure 5.2, the EG curves of diodes SMS7630 and HSMS-2850 feature a decreasing trend in spite of some differences. But, the EG of diode HSMS-2820 remains at a low

level around 100%, which basically means that the cooperative harvesting mode does not deliver any efficiency enhancement within this power range.
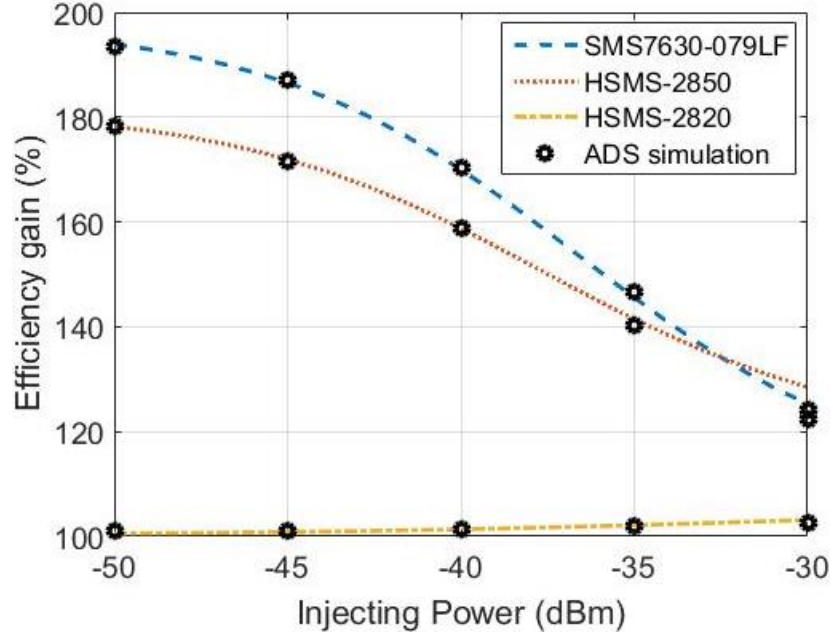
Figure 5.2   Comparison of EG curves of SMS7630, HSMS-2850 and HSMS-2820 based harvesters.

Firstly, to explain the decreasing trend, the formula of EG in (5.17) can be summarized as:

$$\eta_g = \frac{\left(\frac{W_0\left(G\cdot J_0\left(-i\frac{v_{f_1}}{n\cdot Vt}\right)\cdot J_0\left(-i\frac{v_{f_2}}{n\cdot Vt}\right)\cdot e^G\right)}{G}-1\right)^2}{\left(\frac{W_0\left(G_{RF}\cdot J_0\left(-i\frac{v_{RF}}{n\cdot Vt}\right)\cdot e^{G_{RF}}\right)}{G_{RF}}-1\right)^2 + \left(\frac{W_0\left(G\cdot J_0\left(-i\frac{v_{KI}}{n\cdot Vt}\right)\cdot e^G\right)}{G}-1\right)^2} \times 100\% \qquad (5.18)$$

where v_{RF} and v_{KI} are voltage magnitudes injecting into the diode in the single RF and kinetic energy harvesting modes, respectively. Compared with single-source harvesting modes, the cooperative harvesting mode takes into account interactions between the two sources, which is revealed in the calculation of dc output power in (5.7) and fundamental currents in (5.10). Both voltage magnitudes are contained in (5.7) and (5.10). For example, when calculating the fundamental current of a high-frequency source in (10a), the voltage magnitude of a low-frequency source is included. Therefore, once given an injecting power source level, the voltage magnitudes

of single-source (v_{RF}, v_{KI}) are different from those of cooperative harvesting (v_{f_1}, v_{f_2}). The parameter G_{RF} in (5.18) is defined as:

$$G_{RF} = \frac{(R_l + R_s + R_{01})}{R_{j0}} \tag{5.19}$$

According to (5.18), it can be understood that both voltage magnitudes v_{f_1} and v_{f_2} play an important role in determining the EG. This can be explained by (5.20), which describes the calculation of voltage magnitude based on the injecting power, where packaging components are considered to be lossless and removed for simplification. As can be seen from (5.20), when given identical input power (P_{inf_m}), the voltage magnitudes (v_{f_m}) of each power source would be different because of the frequency difference (f_m).

$$P_{inf_m} = i_{f_m} \cdot v_{f_m} + \left(i_{f_m}\right)^2 \cdot R_s + v_{f_m}{}^2 C_{j0}{}^2 (2\pi f_m)^2 R_s \tag{5.20}$$

The cooperative harvesting mode can be considered as an organic combination of two single source harvesting scenarios. Thus, it could be concluded that the following two main factors define the EG of cooperative harvesting mode.

- Voltage magnitude of each input power source (v_{f_1} and v_{f_2}). This reveals the weight of each power source in the rectifying process, which also helps understand which one is the dominant power source.

- PCE performance of the selected diode itself at two different frequencies within this power range. To better understand EG of the cooperative harvesting mode, EG of single source harvesting mode is adopted and defined as the dc output power ratio of doubled and initial injecting power as shown in (5.21).

$$\eta_{g\_single} = \frac{P_{dc_2} \ (P_{in}=2 \ units)}{P_{dc_1} \ (P_{in}=1 \ unit)} \times 100\% \tag{5.21}$$

Since both SMS7630 and HSMS-2850 have similar performance in terms of EG. Let us take SMS7630 as an example. Dashed lines in Figure 5.3 (a) show the EGs of SMS7630 of single RF (high-frequency) and electrical (low-frequency) sources. Obviously, both of them drop with the increase of an injecting power. Here, parameter F_r is defined as the voltage magnitude of low-

frequency source over that of high-frequency source (v_{f_2}/v_{f_1}). In Figure 5.3 (a), voltage magnitude of the low-frequency source is just slightly larger than that of the high-frequency source (F_r is around 1.1). Since both power sources are comparable and their EG curves decrease as a function of the injecting power, the EG curve of the cooperative harvester in Figure 5.2 finally has a decreasing trend within this power range for SMS7630.
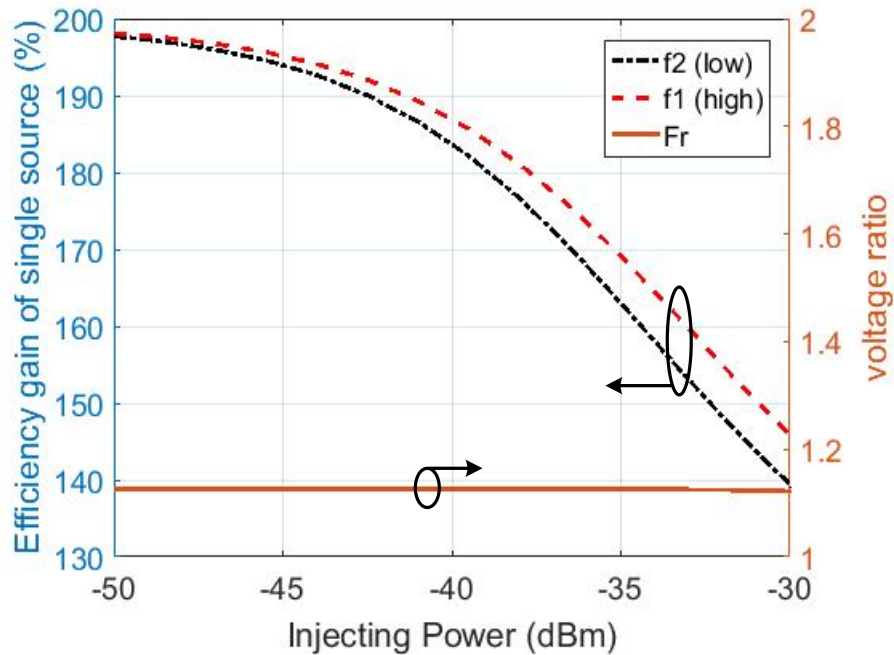
(a)
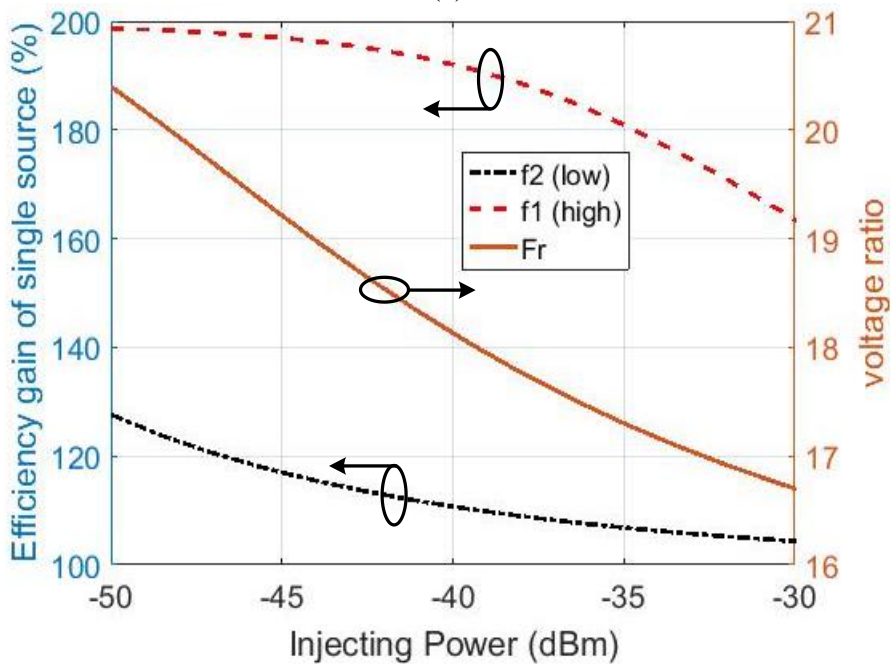
(b)

Figure 5.3 EG curves and voltage magnitude ratios F_r of single low- and high-frequency sources when input power is swept from −50 to −30 dBm. (a) SMS7630 and (b) HSMS-2820.

By contrast, Figure 5.3 (b) shows voltage ratio F_r and EG curves of the single low- and high-frequency sources for SMS-2820. The voltage magnitude of the low-frequency power source is 16 times larger than that of the high-frequency power source. From the power perspective, the dc output power of the low-frequency source is about three orders of magnitude larger than that of the high-frequency. In other words, the contribution of the high-frequency power source is negligible and the cooperative harvesting is actually no longer existing within this power range. Thus, it explains the reason why there is no EG for HSMS-2820 which is indicated in Figure 5.2.

According to (5.20), it is clear that C_{j0} plays a significant role in determining the voltage magnitude. Moreover, saturation current I_s, ideality factor n and series resistance R_s are all involved in the EG calculation. It is essential to understand how each SPICE parameter contributes to the EG of a cooperative harvesting. Due to the complexity of (5.20), no explicit relationship between EG and each SPICE parameter can be obtained. Therefore, numerical analysis of each parameter is individually investigated.
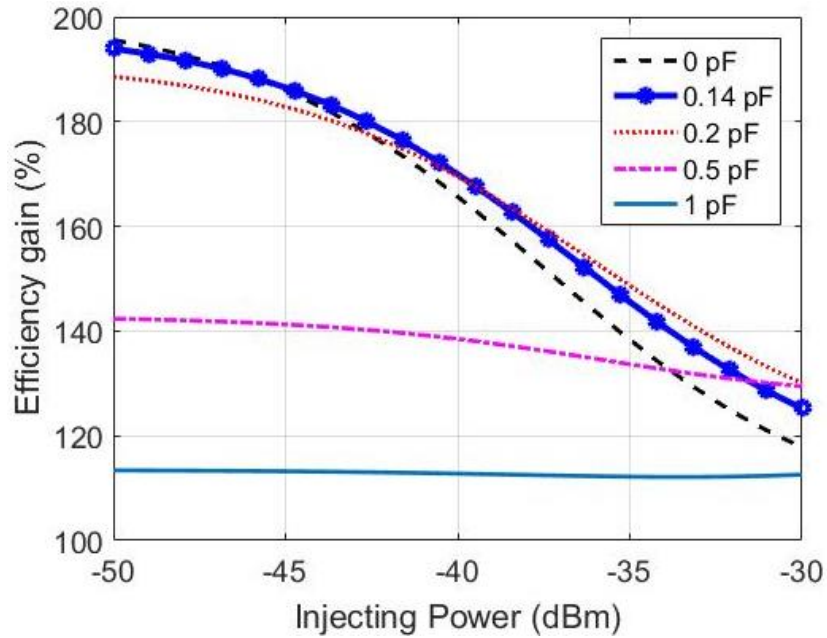
(a)
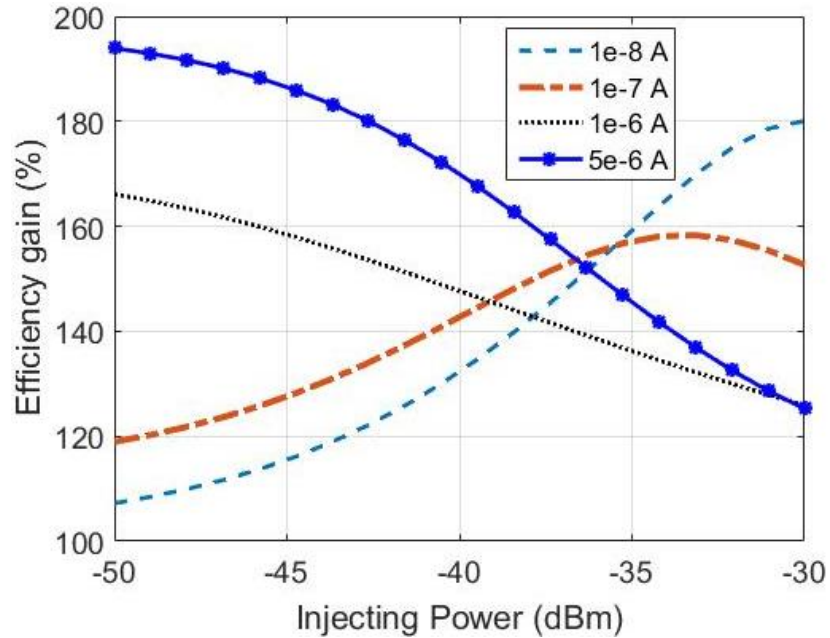
(b)

Figure 5.4 EG curves based on SPICE parameters of SMS7630 as a function of injecting power, for different (a) zero-biased nonlinear junction capacitance C_{j0} and (b) saturation current I_s.

Diode SMS7630 is taken here as an example. Only one parameter is varied with the other remaining parameters unchanged. It should be noted that in both Figure 5.4 and Figure 5.5, blue curves with asterisk symbols represent the EG curves based on real SPICE parameters of SMS7630.

Figure 5.4 (a) shows the EG curves with different C_{j0} of 0 pF, 0.14 pF (default parameter), 0.2 pF, 0.5 pF, and 1 pF. With the increase of C_{j0}, EG decreases to a lower level and drops to around 115% when C_{j0} is 1 pF. As indicated in Figure 5.4 (b), a larger I_s is able to bring a larger EG in a low power range. Since I_s is inversely proportional to the zero bias junction resistance as suggested in (5.9), a larger EG can be resulted from a smaller diode's zero bias junction resistance.

Next, the influence of n and R_s are shown in Figure 5.5 (a) and (b), respectively. When investigated in a reasonable range of both n (1-2) and R_s (1-20 Ω) of those commonly used Schottky diodes, it can be found that n and R_s cannot change the trend of EG curves.

According to the analysis displayed in Figure 5.4 and Figure 5.5, Schottky diodes with smaller zero bias junction capacitance C_{j0} and resistance R_{j0} are desirable in a low power range to obtain a higher EG. It also explains the reason why a rectifier based on HSMS-2820 is not able to boost the

EG. That is just because it has a much larger C_{j0} and R_{j0} than the diode SMS7630, which can be clearly observed in Table 5.1.
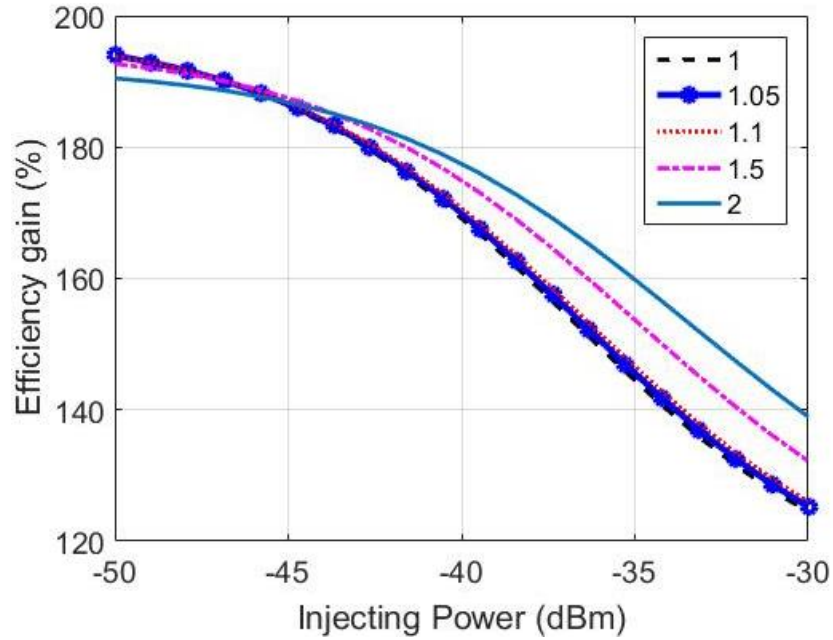
(a)
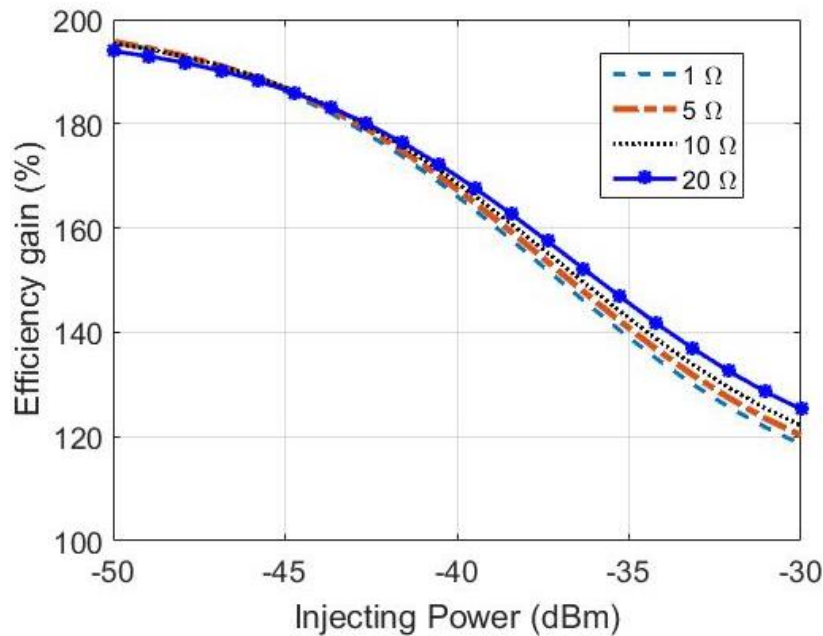
(b)

Figure 5.5 EG curves based on SPICE parameters of SMS7630 as a function of injecting power, for different (a) ideality factor n and (b) series resistance R_s.

5.3 Cooperative Harvester Design

5.3.1 Electromagnetic Kinetic Energy Generator Design

Due to its well-spelled advantages in the literature, a simple topology and low cost, electromagnetic transduction is utilized [133]. Figure 5.6 shows the structure of an electromagnetic kinetic energy generator which contains a permanent magnet and coils. Two arc slots and one rectangular hole are created to obtain an embedded beam on the single substrate [32]. As can be seen from Figure 5.6, the coils are placed on the board and the magnet is glued on tip of the beam. The number of coil turns is 230, which is studied in our previous work [133]. The multi-layer coil has a rectangular shape and its practical size is 16.9 mm × 9.6 mm, which is also indicated in Figure 5.6.

When the substrate board is driven by an external force, the beam together with the permanent magnet would oscillate at its own resonant frequency. In other words, the operating frequencies of the substrate board and the beam are different. Therefore, it creates a relative displacement between the permanent magnet and coils on the board, which generates electrical energy. When the operating frequency matches the beam's resonant frequency, the vibration energy is able to fully transmit to the tip mass (permanent magnet). Typically, for this kind of generator, the resonant frequency can be designed over a range of 30 to 130 Hz by changing the beam length or selecting different substrate or mass weight.
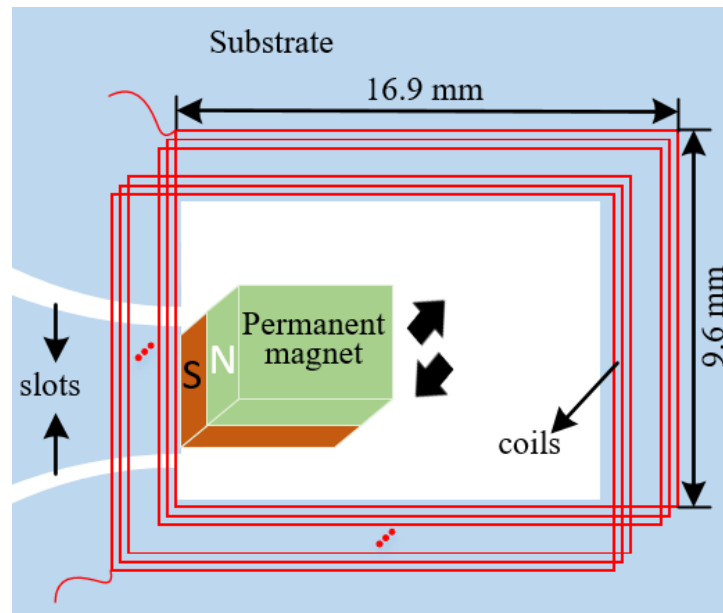
Figure 5.6 Diagram of kinetic energy generator.

5.3.2 **Antenna Design**

Considering the limited space of the board, a compact antenna for collecting RF signal at 1.8 GHz is designed [134]. Figure 5.7 shows the configuration of the proposed antenna which has features of both planar inverted-F antenna (PIFA) and inverted F antenna (IFA).
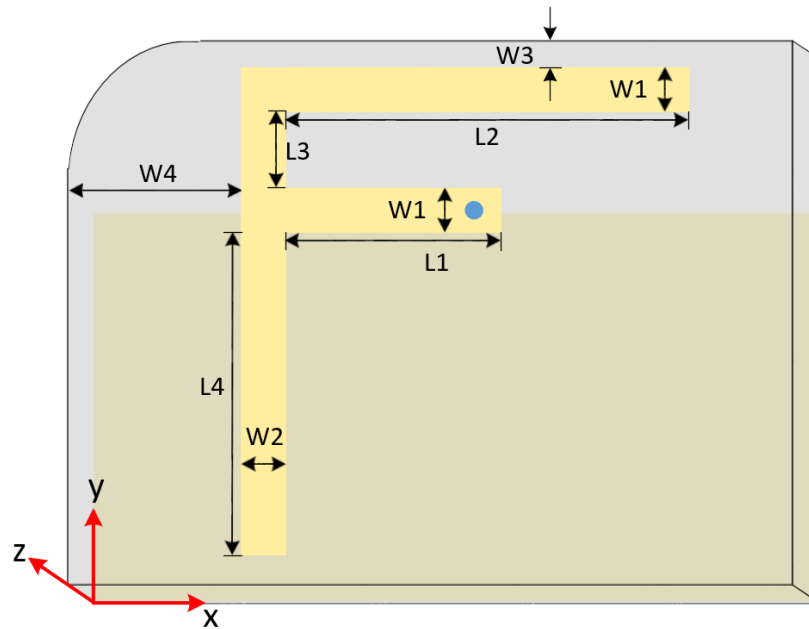
Figure 5.7 Geometry of the F-shaped antenna: W1 = 1.5 , W2 = 1.55 , W3 = 0.5 , W4 = 5 , L1 = 13 , L2 = 25.6 , L3 = 3 and L4 = 15.6 , in mm.

In Figure 5.7, the substrate is Rogers RT/duroid 6002 with a dielectric constant of 2.94 and thickness of 60 mils. The blue circle in Figure 5.7 is a grounding via with a diameter of 0.8 mm. It should be noted that no ground plane is underneath the radiator and the ground plane edge is aligned along the shorter branch of the antenna. All antenna structural parameters are listed in the caption of Figure 5.7.

5.3.3 **Integration of the Cooperative Harvester**

The scheme of the single Schottky diode based integrated cooperative harvester is illustrated in Figure 5.8. The F-shaped antenna is an RF energy receiver. The RF choke prevents high-frequency RF signal from interfering the kinetic generator and a dc block keeps the F-shaped antenna isolated from the low-frequency electrical signal. Diode's cathode is connected to the ground which locates

at the position that magnetic field reaches its first valley to obtain maximum current in the circuit. The dc current flow is indicated in Figure 5.8. The dc current is generated by the diode and goes through the low resistive coils and finally arrives at the load resistor. A large capacitor is connected in parallel with the load resistor to smooth out the AC component over the load. It should be mentioned that all these components are integrated on a single substrate, showing a compact design.
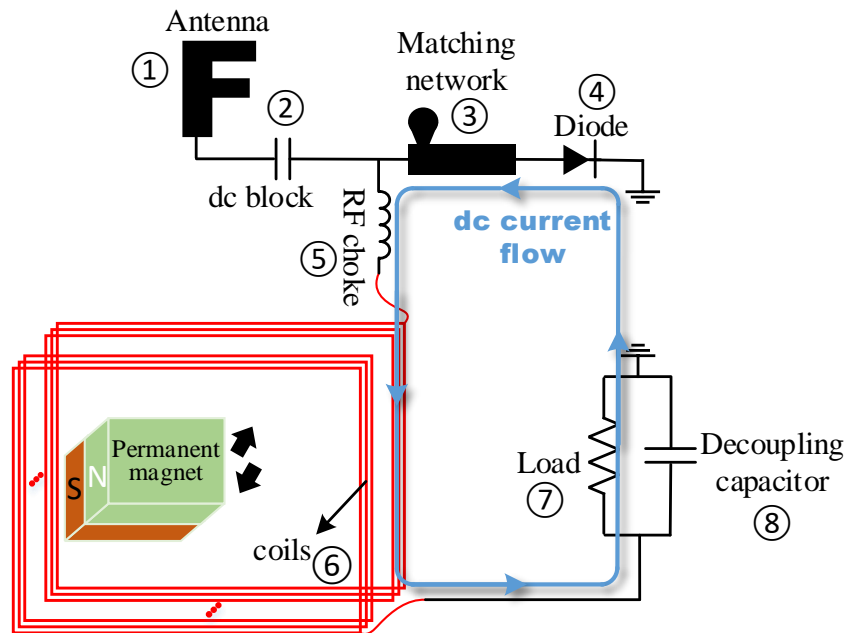
Figure 5.8 Scheme of the proposed cooperative harvester.

5.4 **Prototype and Measured Results**
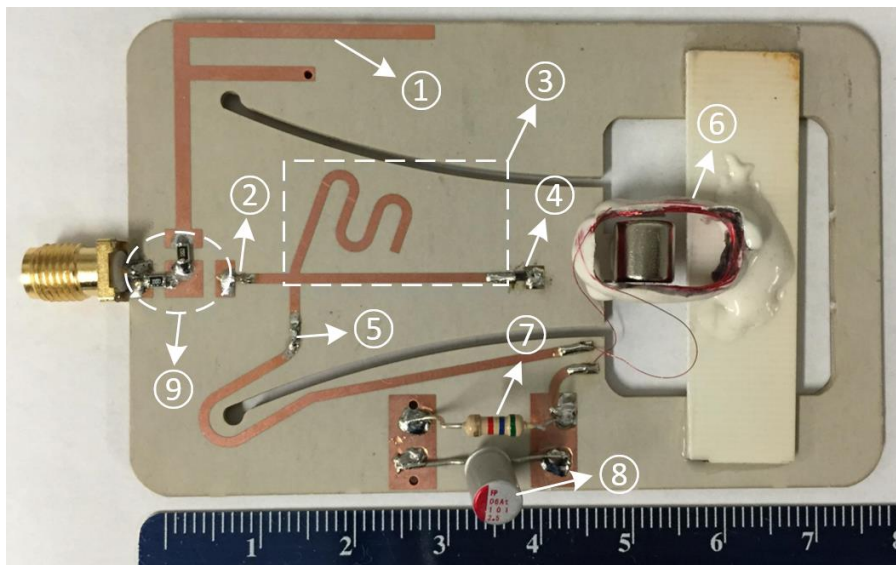
(a)
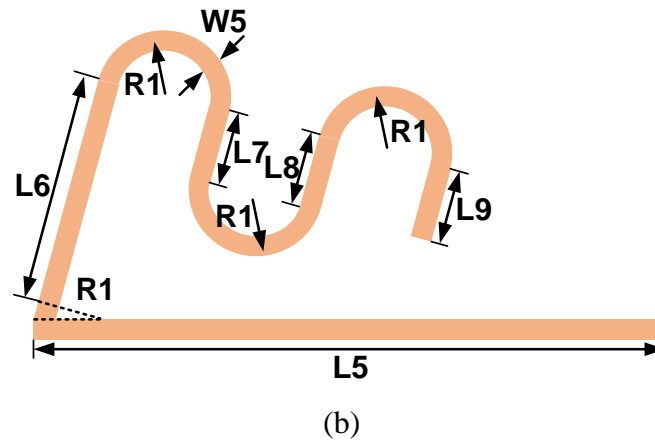
Figure 5.9 (a) Photo of our experimental prototype of the proposed cooperative harvester; (b) The L-matching network with dimensions: L5 = 20.4, L6 = 9.5, L7 = 3.8, L8 = 3.3, L9 = 3.5, R1 = 1.5, W5 = 1, in mm. Note that the microstrip curved bend identified by dashed lines has an angle of 20º while the remaining three are identical with an angle of 180º.

Figure 5.9 (a) shows the experimental prototype of the proposed cooperative harvester. Harvesters based on both diodes of SMS7630 and HSMS-2850 are designed for verification and comparison. It is worth noting that load resistors for both diodes are different. It is 5.6 kΩ for SMS7630 and 9.1 kΩ for HSMS-2850 which are considered to be close to the optimum loadings for each diode in a low power range. The size of the cooperative harvester is 50 mm × 80 mm, comparable to the size of a credit card. The marks of each component in Figure 5.9 (a) are all maintained consistent with those shown in Figure 5.8 except component No. 9. Note that component No. 9 is a square microstrip pad with a characteristic impedance of 50 Ω. Its three sides have different endings, namely SMA connector, F-shaped antenna, and rectifier circuity. Through the following three types of connection by zero-ohm resistors, it can help complete three different measurements which are indicated in Figure 5.10. They are listed as follows:

    (a) Only antenna is connected to the SMA connector. This is to complete antenna performance measurements including S-parameters and radiation pattern measurements.

    (b) Preliminary efficiency performance measurements of the rectifier circuit are conducted with the RF power provided by an external signal generator.

    (c) Finally, ambient RF power in the free space is collected by the antenna and transmitted to the rectifier circuit.
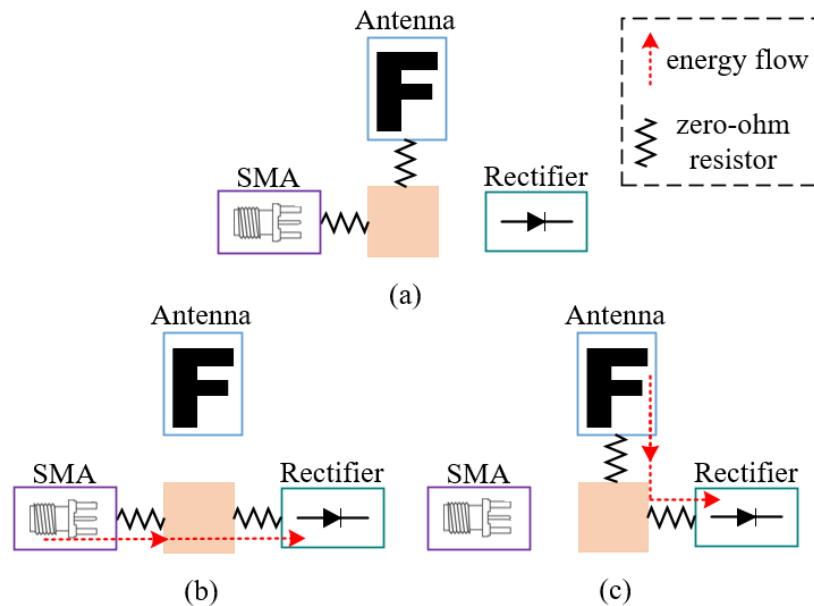
Figure 5.10 Three types of connection for (a) antenna and (b) rectifier performance measurement and (c) cooperative harvesting when the antenna is receiving an external RF energy in the free space.

Figure 5.11 shows the preliminary measurement setup. In this measurement, the RF energy is provided by a signal generator rather than the designed F-shaped antenna. The external vibration is provided by a shaker which is driven by an arbitrary waveform generator. The cooperative harvester is mounted on the shaker. The driver signal is a sinusoidal wave, resulting in the AC output signal of the kinetic generator having a sinusoidal waveform as well, in accordance with the electromagnetic transduction mechanism. Referring to the readings on an AC voltage meter, the kinetic power provided by the generator can be easily captured. As mentioned before, the magnitude and frequency of the driving signal can be changed to control the amount of AC output power coming out of the kinetic generator. The dc voltage meter is used to measure the dc output voltage across the load.

The measurement results are shown in Figure 5.12, with three different excitation modes, namely single kinetic, single RF and cooperative modes. The dc output of cooperative harvesting is labelled as the solid black line. For comparison, the dashed blue line indicates the summation of dc output power from the single kinetic and RF harvesting mode. The dc output power harvested from each individual excitation mode are filled by different patterns for comparison. Due to reduced parasitic

loss from the low-frequency kinetic power harvesting mode, the dc output power is larger than that harvested from RF power, when the injecting power is the same. Such an observation is more obvious in Figure 5.12 (b) for diode HSMS-2850.
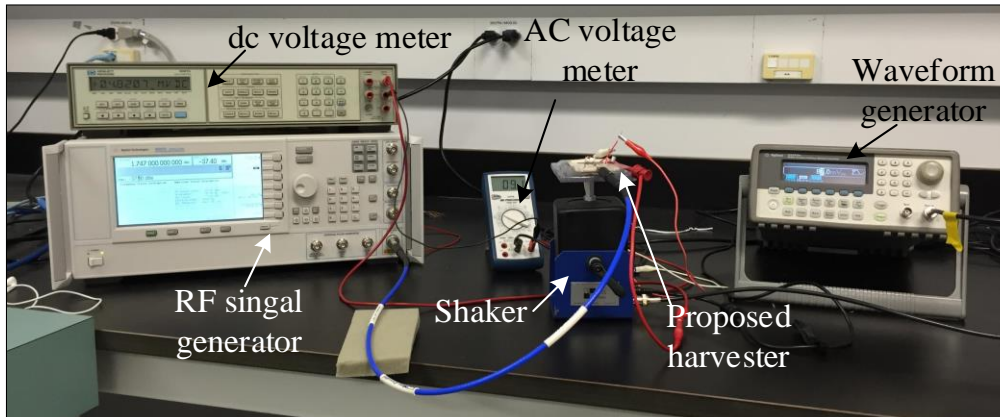
Figure 5.11   Cooperative harvester measurement setup with RF source provided by a signal generator.

For the kinetic energy generation, the operating frequency of this harvester is kept at its resonant frequency which is around 85 Hz. The required kinetic vibration acceleration values are attached under each injecting power level as shown in Figure 5.12. In the cooperative energy harvesting mode, the AC signal converted from the kinetic power is kept the same as the injecting RF power into the diode. Note that in Figure 5.12, the accelerations required for both single kinetic and cooperative energy harvesting are quite close and could be assumed the same.

As can be observed in Figure 5.12 (a), the cooperative harvesting mode based on diode SMS7630 can generate 10.7 nW dc output when both RF and kinetic energy of −40 dBm are injected into the diode. Whereas for the single RF harvesting mode, the same amount of energy (−37 dBm) is provided, the dc output power is only 9.21 nW. Thus the cooperative harvesting is capable of offering 1.16 times larger dc output power than the single RF harvesting when the total injecting power is −37 dBm. The calculated and measured EGs are also compared in Figure 5.12 (a). Both calculated and measured EGs have the same trend, though the measured EG is slightly smaller. For example, when both of the injecting power sources are −40 dBm, the measured and calculated EGs are about 162.45% and 170.13%, respectively. The difference is mainly due to two reasons. One is the inaccuracy of the SPICE parameters on datasheet used for the theoretical EG calculation, as they are average values based on massive measurements. Besides, when operating frequency of the

kinetic generator is close to its inherent resonant frequency, the output AC signal does not have an ideal sinusoidal waveform. However, it is still considered as a sinusoidal wave in the calculation.
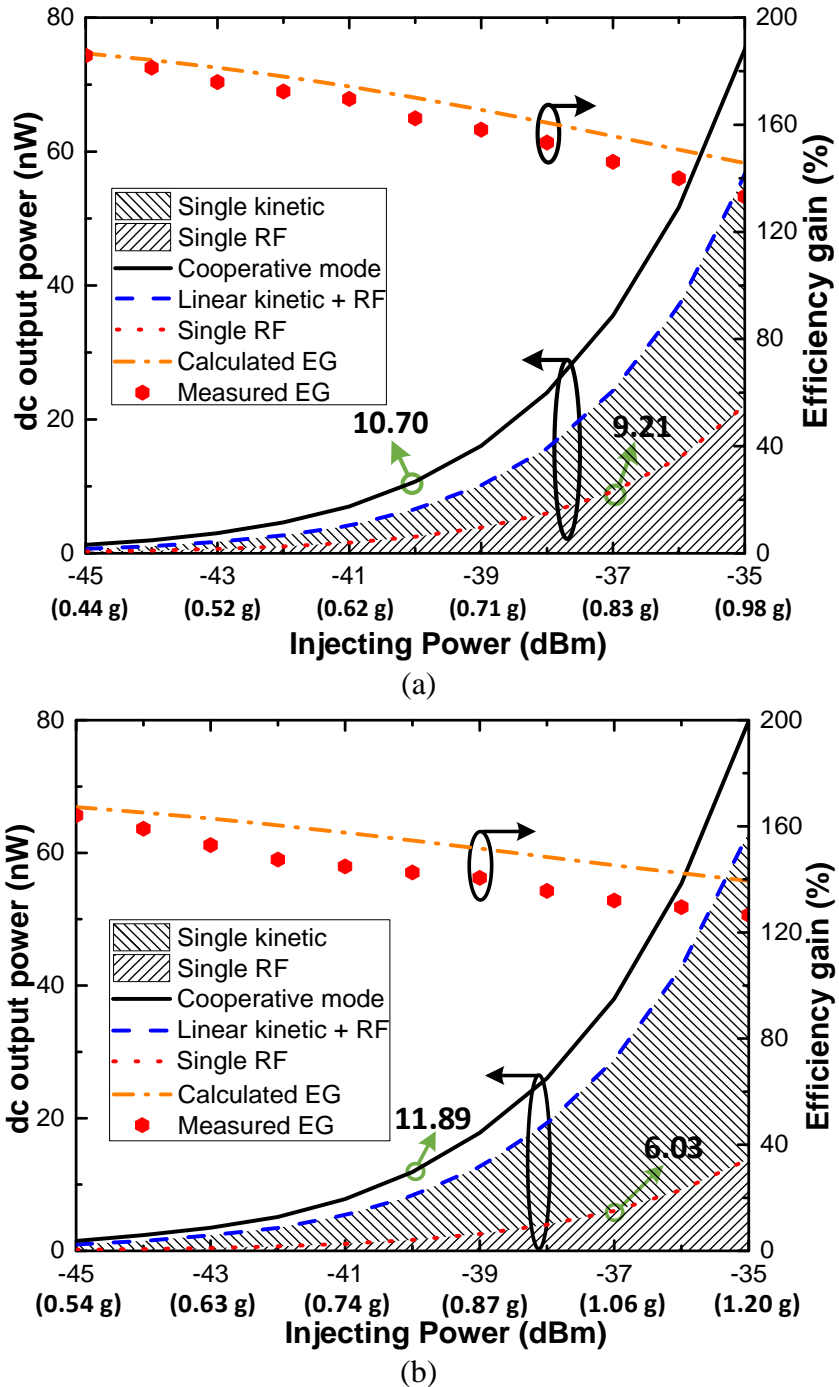
Figure 5.12 Comparison of dc output power rectified from cooperative and single source modes, and comparison of calculated and measured EG as a function of injecting power from −45 to −35 dBm. (a) SMS7630. (b) HSMS-2850.

The measurement data for HSMS-2850 are presented in Figure 5.12 (b), which shows that the cooperative harvesting mode has 11.89 nW dc output power when both injecting power sources are −40 dBm. If the hybrid power is replaced with a pure RF energy and applying single RF harvesting topology, the dc output power is 6.03 nW. Through the comparison, it is shown that the cooperative harvester built on HSMS-2850 can provide 1.97 times larger dc output power than the single RF harvesting mode. The measured EG is about 142.59% when both the power sources are −40 dBm, compared with the calculated result of 154.68%.

Although the cooperative harvester based on SMS7630 has a larger EG, it actually produces less dc output power compared with HSMS-2850 based cooperative harvester. As a matter of fact, SMS7630 is superior in terms of energy harvesting in the microwave frequency band. With a higher junction resistance and capacitance, the PCE of HSMS-2850 based harvester is moderate due to a large parasitic loss at microwave frequency. However, low-frequency energy harvesting has minimized the parasitic loss for both diodes and at the same time, RF-to-dc conversion efficiency becomes dominate [18]. HSMS-2850 with a higher junction resistance takes the advantage and finally delivers a larger dc output power.

Thus, for Schottky diodes with close SPICE parameters and similar features, a careful investigation is essential to finally select one diode with the largest dc output power by applying the cooperative harvesting mode.

One important advantage of the proposed cooperative harvester is its strong resilience. Although it is a combination of RF and kinetic energy harvesting, each harvesting mode is capable of operating separately. With either power source accessible, it has the capacity to offer the dc output with a typical PCE. Whereas the cooperative harvesting is able to provide a higher PCE and a larger dc output power when both RF and kinetic energy are available as shown in Figure 5.12. Therefore, this proposed cooperative harvester has a great potential for different applications in practice. And it is highly suitable to work in an ever-changing environment.

Next, the aforementioned F-shaped antenna performance is measured and both simulated and measured input reflection coefficients are shown in Figure 5.13 (a). The measured results reasonably agree with the simulated ones, with a slight resonant frequency shift. It is worth noting that it is enough for our application although the measured reflection coefficient is around −13 dB

at 1.8 GHz. Measured and simulated normalized radiation pattern of two planes perpendicular to the antenna on board are presented in Figure 5.13 (b) and they match reasonably well. It has a maximum gain = 3.14 dB at operating frequency.

(a)

(*x-z* plane)   (*y-z* plane)

(b)
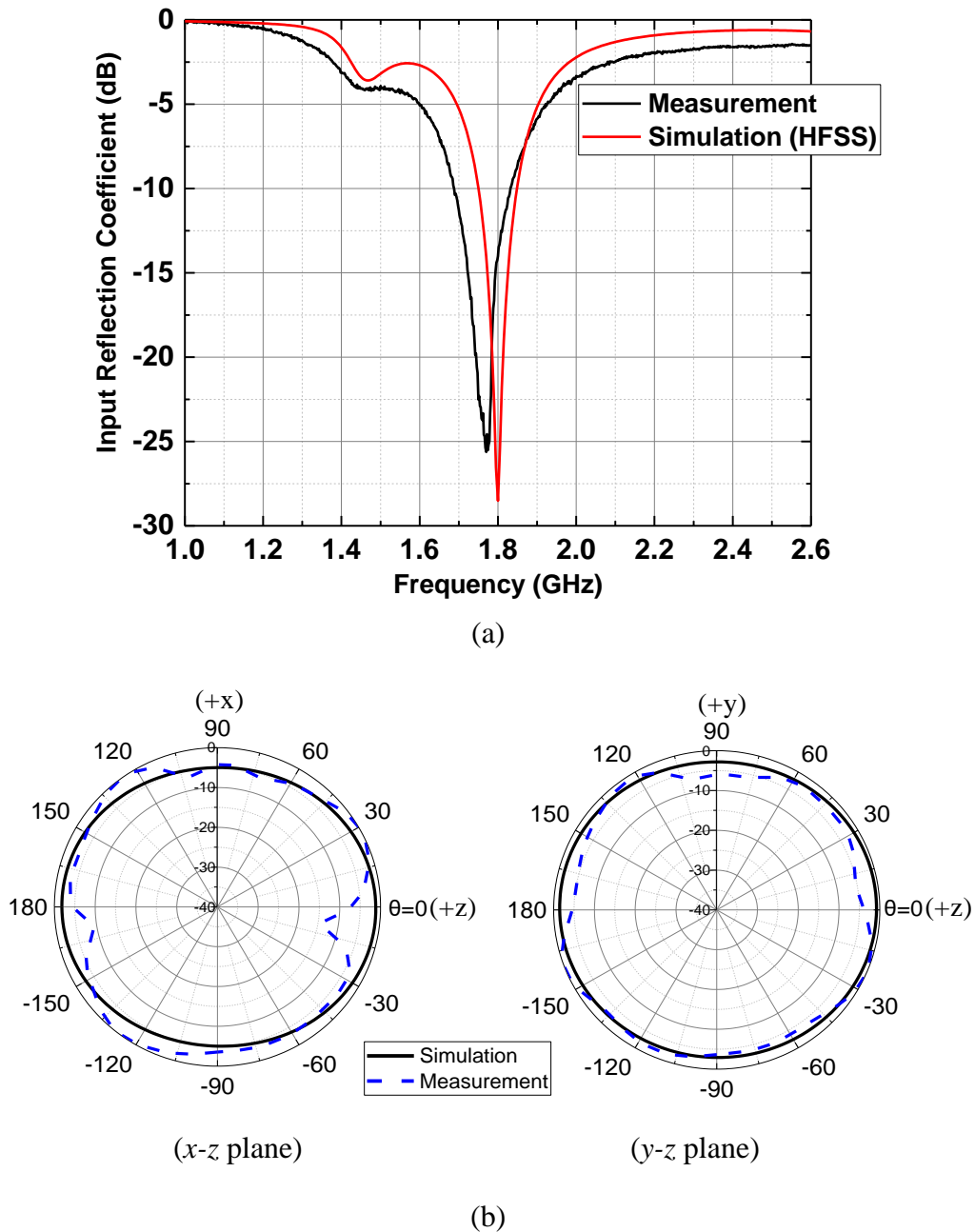
Figure 5.13 Simulated and measured (a) input reflection coefficients and (b) normalized radiation pattern of the proposed F-shaped antenna.

Finally, the measurement is conducted in the anechoic chamber as shown in Figure 5.14, in order to exclude the interference of other existing RF signals. One stubby antenna is connected to a signal generator acting as the RF source in the free space and placed about 3 meters away from the harvester as shown in Figure 5.14 (a). The cooperative harvester is mounted on and driven by the shaker. Also, one tiny accelerometer powered by a portable signal conditioner as shown in Figure 5.14 (b) is attached on the harvester to capture the acceleration information.
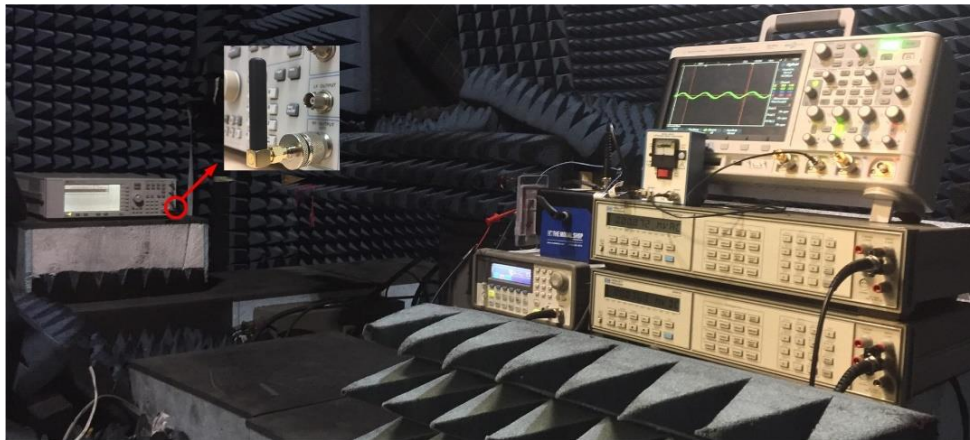
(a)
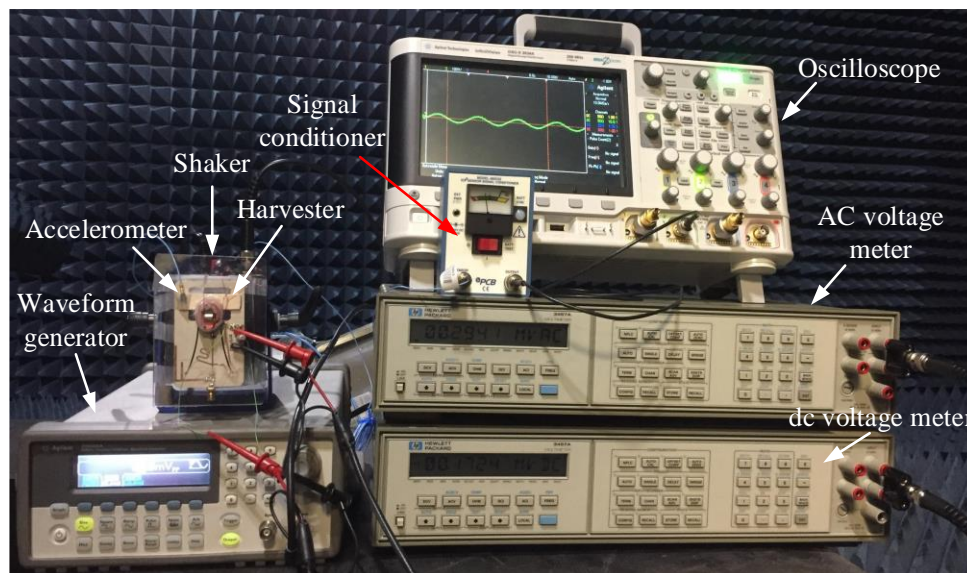
(b)

Figure 5.14 (a) Measurement setup of the cooperative harvester in the anechoic chamber. One stubby antenna is connected to the signal generator as the RF power transmitter. (b) Instruments used for monitoring and data recording.

In the measurement, the RF and kinetic power injecting into the diodes are swept from −45 to −30 dBm. The external kinetic power can be adjusted easily through tuning the magnitude of shaker's driving signal. The vibration frequency is set at the resonance frequency of the mechanical structure (around 85 Hz). Thus, the accelerator is able to obtain the acceleration of the beam as all the vibration energy on the board can be considered successfully transmitted to the permanent magnet. Due to the impedance mismatch between the diode and kinetic generator, more input power is provided to compensate the loss in order to ensure enough low-frequency power is injected into the diode during the measurement. The acceleration data are labelled under each kinetic power level. It should be noted that such a kinetic power level could be easily obtained in daily life. Table 5.2 has listed potential application scenarios in the frequency range of the harvester (30 – 130 Hz). For example, −40 dBm power offered to the SMS7630 based harvester is provided by the vibration of an acceleration of 0.65 g, comparable to that of an operating kitchen blender's casing.

Table 5.2 Potential application scenarios [135], [136]

Vibration Sources	Peak acc. (g)	Peak freq. (Hz)
Working clothes dryer	0.36	121
Kitchen blender casing	0.65	121
Stand fan (low speed)	0.61	100
Door frame just after door closes	0.31	125
Grinding machine	0.36	49

The EGs of SMS7630 and HSMS-2850 are plotted in Figure 5.15 (a) and (b), respectively. As mentioned in (5.17), EG represents a factor that quantifies the efficiency enhancement of the cooperative power harvesting topology over a linear combination of separate power harvesting ones, given identical input power levels. In both graphs, the red lines indicate EG of 150%. It can be observed that the area at the lower left corner surrounded by the red line of SMS7630 is larger than that of HSMS-2850. It means that the diode SMS7630 has a superior rectifying performance in terms of EG in this low power range than HSMS-2850, which verifies the theoretical analysis in Figure 5.2. More specifically, the harvester built on SMS7630 is able to provide an EG of 150% when both injecting power sources are under −38 dBm.

It is also noted that the area surrounded by the red line of HSMS-2850 in Figure 5.15 (b) is slightly shifted from the diagonal line running from lower left hand to upper right hand corner. Since the

EG peaks when voltage magnitudes of both sources are the same as indicated by (5.18), the shift of the peak reveals that the low-frequency electrical signal converted from kinetic source is dominant when both input power sources are equal. It matches the simulated results in Figure 5.12 (b). The peak shift of SMS7630 is not manifested in Figure 5.15 (a). This is reasonable as the kinetic and RF power sources contribute approximately the same to the final dc output power in the cooperative harvesting mode.
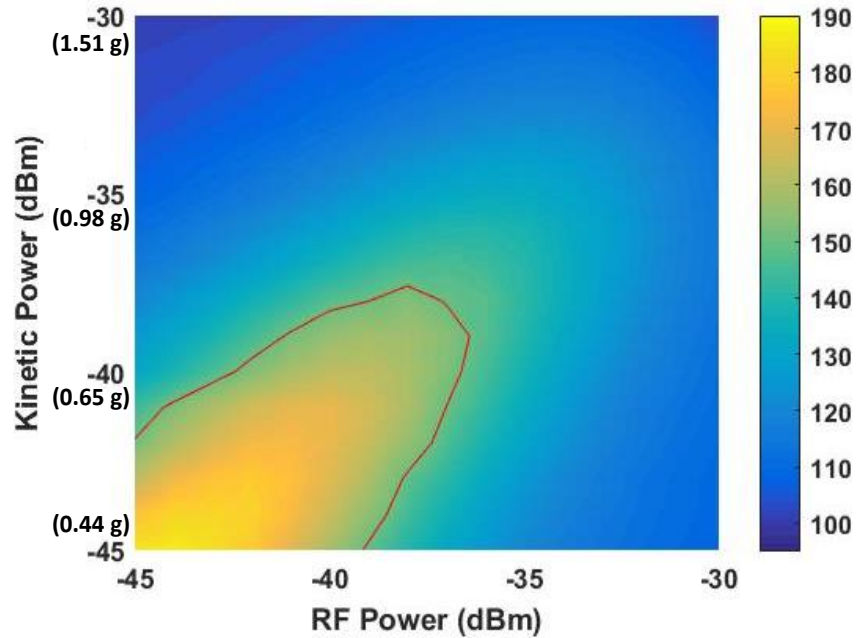
(a)
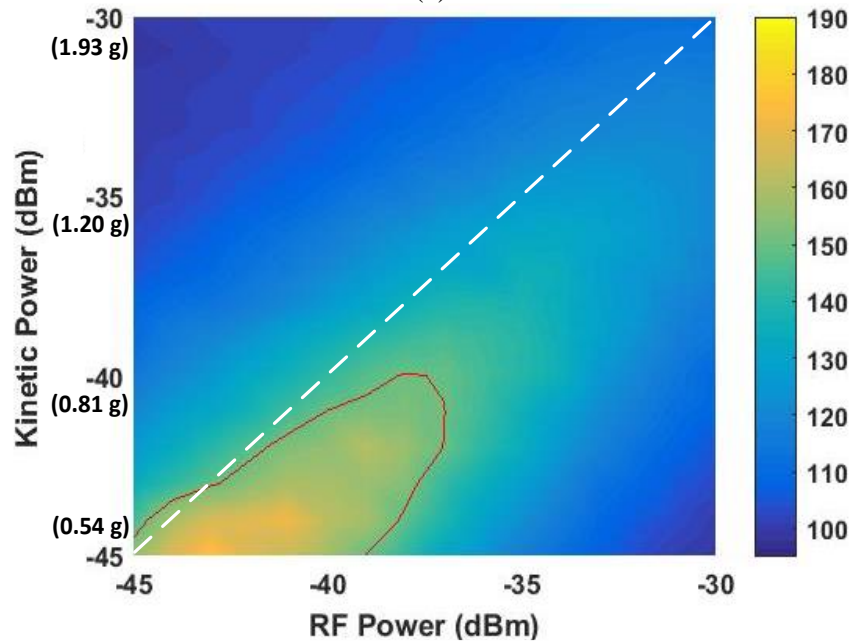
(b)

Figure 5.15 Measured EG distributions with both RF and kinetic power swept from −45 to −30 dBm. (a) SMS7630 and (b) HSMS-2850. The required acceleration information is labelled under each kinetic power level.

Table 5.3 summarizes the comparison of existing different cooperative energy harvesting topologies. The inherent output of thermal and solar energy harvesting is dc power, researchers have successfully taken this advantage to bias the diode to boost diode's RF-to-dc conversion efficiency [137-139]. A possible topology to integrate thermal, solar and RF energy harvesting together is proposed but at the expense of a higher system complexity [139]. Thermal energy harvesting relies on a Thermo-Electric Generator (TEG) which normally requires an efficient cooling system to maintain a good rectifying performance. This makes the integration of harvester more complicated. Solar cells are used to collect light energy in solar energy harvesting. Although featuring a high power density, outdoor sunlight illumination usually has a limited period of time and highly depends on weather conditions. Indoor applications would have trouble when the lights are off at night time. Besides, in such a hybrid cooperative topology, Joule loss on the diode and mismatch loss of the dc source harvested from thermal or solar energy are not included. Thus, a low efficiency gain performance is expected, especially in a low-power harvesting scenario.
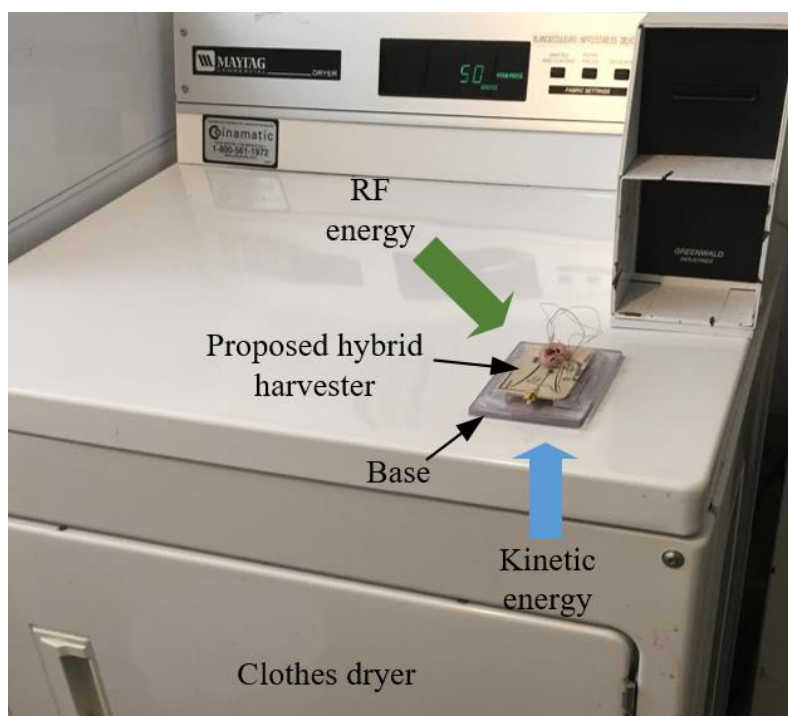
Figure 5.16 Proposed cooperative power harvester is mounted on a working clothes dryer.

Table 5.3 Comparison of the existing different cooperative energy harvesters

	System complexity [30]	Energy availability	Injecting energy	Efficiency Gain	Pros	Cons
(a) Therm. + RF [137]	High	Activity dependent (T)* Continuous (R)	dc (T) High-frequency AC (R)	< 30% **	dc energy biases the diode to increase RF-to-dc conversion efficiency	Requires an efficient heat sink
(b) Sol. + RF [138]	Medium	Daytime (S) Continuous (R)	dc (S) High-frequency AC (R)		Large power density (good illumination), dc energy biases the diode to increase RF-to-dc conversion efficiency	Limited solar energy availability
(c) Therm. + Sol. + RF [139]	High	Activity dependent (T) Daytime (S) Continuous (R)	dc (T) dc (S) High-frequency AC (R)	- ***	Listed in (a) and (b)	Requires an efficient heat sink and limited solar energy availability, isolation between two dc sources, high system complexity
(d) Kinet. + RF this work	**Medium**	**Activity dependent (K) Continuous (R)**	**Low-frequency AC (K) High-frequency AC (R)**	**HSMS-2850 164 % (RF = AC = −45 dBm) SMS7630 186 % (RF = AC = −45 dBm)**	**Output amplification of two AC power sources due to their interactions**	**Relatively larger size and limited power density**

* (T) Thermal energy, (R) RF energy, (S) solar energy, (K) kinetic energy.   ** In a low-power harvesting scenario (<−30 dBm).

*** Measured results from hybrid energy harvesting are not reported.

Unlike the cooperative energy harvesting of one or two dc sources and a high-frequency power source (RF) mentioned above, this work features harvesting two AC energy sources. Through the combination of these two different AC powers and thanks to their interactions, the global efficiency can be increased dramatically. Also, the harvester size is possible to be further minimized by using piezoelectric techniques when harvesting kinetic energy.

Such a cooperative harvester can be easily implemented in daily household environments. Figure 5.16 shows a typical implementation on a working clothes dryer. The kinetic generator converts dryer vibration into AC power and at the same time, the antenna is available to collect cellular energy in the free space. The proposed cooperative harvester is possible to energize low-duty cycle sensors. For example, a tiny CMOS temperature sensor with an ultra-low power consumption has been reported in [31]. The driven energy is only about $1.05 - 65.5$ nW, which is affordable for the proposed cooperative power harvester according to its capacity of the power supply. It is necessary to add the energy storage and power management units including a voltage boost converter to the proposed cooperative harvester, to accomplish energizing such sensors.

5.5 Conclusion

In this paper, a single Schottky diode based cooperative RF and kinetic harvester is proposed and studied theoretically and experimentally. A closed-form analytical method is devised to theoretically analyze the EG performance of the cooperative harvester in a low power range. It shows a good accuracy compared with the results of commercial harmonic balance simulator in ADS. For demonstration, integrated cooperative harvesters built on diodes SMS7630 and HSMS-2850 are designed and tested. When both power sources injecting into the diode are -40 dBm, the measured results show that more than 1.16 and 1.97 times larger dc output power is obtained through the cooperative harvesting mode compared with the single RF harvesting mode for diode SMS7630 and HSMS-2850, respectively. According to the experiments conducted in the anechoic chamber, both diodes based harvesters are capable of increasing dc output power by at least 50 % when both injecting power sources are smaller than -37 dBm, compared with a direct summation of dc power of the single RF and kinetic excitation modes.

CHAPTER 6   ARTICLE 5: DIPLEXER-BASED FULLY PASSIVE HARMONIC TRANSPONDER FOR SUB-6 GHZ 5G-COMPATIBLE IOT APPLICATIONS

Xiaoqiang Gu, Srinaga Nikhil N, Lei Guo, Simon Hemour, and Ke Wu

A novel diplexer-based fully passive transponder is presented in this paper, which targets sub-6 GHz 5G-compatible Internet of Things (IoT) applications. To alleviate the antenna design restrictions of traditional transponder with two separate antennas, a new architecture has been proposed with the introduction of a diplexer, which allows transponder to simply employ a dual-band antenna. In this work, a dual-band circularly polarized omnidirectional spiral slot antenna, with enhanced bandwidth and gain performance, is designed as the transponder Tx/Rx antenna. Besides the new architecture, a diode selection criterion is proposed as well. Analytical models are derived, showing relationships between the diode's SPICE parameters and the conversion efficiency or conversion loss (CL) of such diode-based transponders. With help of the analysis, transponder designers can easily identify diodes to implement transponders with better performance. Under the guidance of the criterion, low-barrier diode SMS7630 is chosen for verification. Measured CL results of the transponder circuitry part show a noticeable improvement over the state-of-the-art works. The complete prototype was tested with radar's transmitting power of 25 dBm, and it presents a maximum read-out distance up to 7 meters when the operating fundamental frequency is 3.5 GHz.

6.1 Introduction

The entire world is about to embrace fifth generation (5G) communication technology by 2020 or so [140]. Recently, a two-hop relay based on an integrated mmWave/sub-6 GHz 5G network has been evaluated, featuring a combination of high data rates and a larger coverage [141]. In an early phase of commercialization, the sub-6 GHz frequency band seems a more practical choice in terms

of reusing all the existing base stations and design expertise/practices. Specifically, the lower part of C band (3.4 − 3.6 GHz) has been allocated as a new IMT band at World Radiocommunication Conference 2015 (WRC-15), making this frequency band a hot topic among the 5G community [142-145]. Also, with a rapid development, the Internet of Things (IoT) technology is no more simply a buzzword of today. The number of IoT devices is forecasted to reach approximately 28 billion by 2021 [146]. Meanwhile, 5G and IoT technologies are not advancing in parallel separately. For example, 5G speeds up expanding and maturity of IoT technology [147]. Thus, 5G-compatible IoT technology is believed to be a new trend, offering new business opportunities for global economic growth and shaping our future life [148].

Wireless sensing, as one of the main applications in the scope of 5G-compatible IoT applications, becomes an ever-challenging task, due to an increasing number of sensor nodes and a combination of heterogeneous networks. Sensing system with desirable features, such as high reliability, low cost, compact size and ultralow power consumption, is highly demanded. Harmonic radar and transponder-based sensing system is an attractive candidate to resolve such dilemmas. This technology was explored more than 50 years ago and has gone through a fast development since then [149]. In this concept, the radar interrogates a transponder at the fundamental frequency f_0. The transponder attached on the target then reflects a higher harmonic, which can be detected by the radar system. Such transponders are realized at the second-harmonic frequency $2f_0$ in most cases [45]. Due to its high robustness to radar clutter interference, harmonic radar and transponder-based sensing system has already been applied in many different scenarios, such as studying bumble bee's foraging range [99], tracking wood frogs [100], RECCO avalanche victim searching system [150], and cracked wall monitoring [102].

For the transponder design, a traditional topology consists of a pair of antennas (one for receiving and the other for transmitting) and a nonlinear device, as shown in Figure 6.1. For the resonant antennas, since the Rx antenna operating at the fundamental frequency f_0 would resonate at the second-harmonic frequency $2f_0$, high isolation between Tx and Rx antennas is highly desired to obtain a good performance. For example, to realize such high isolation, linearly polarized antennas have to be placed orthogonally [151]. However, any specific requirement restricts the freedom of the antenna design.
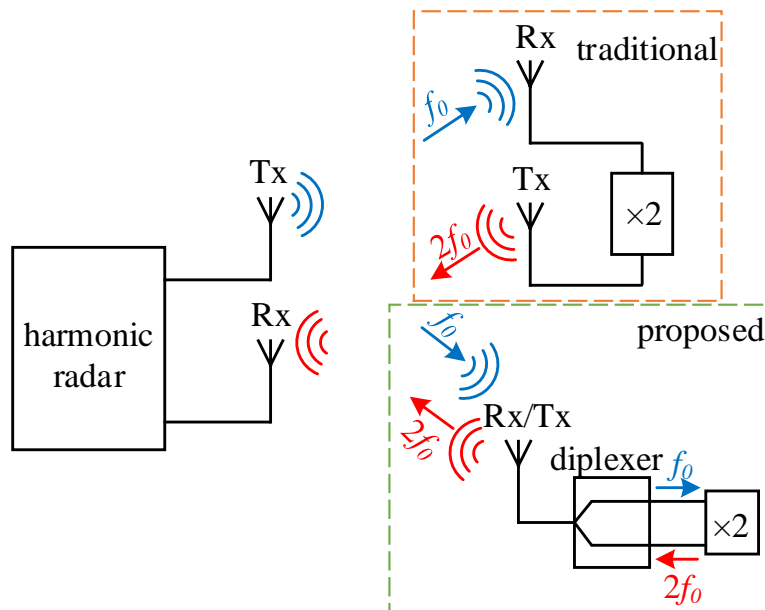
Figure 6.1　Architectural comparison of harmonic radar and transponder system based on traditional and proposed topologies.

In the scope of this work, a novel diplexer-based fully passive harmonic transponder is proposed with its topology presented in Figure 6.1, along with the conventional architecture for comparison. The diplexer to be introduced in the work has pass-bands for both fundamental and second-harmonic frequencies and provides significant isolation between them. This feature relaxes the antennas design with stringent requirements. Thus, the traditional pair of Tx and Rx antennas designed to have a large isolation at the expense of radiation performance can be simplified as a dual-band antenna optimized for improving its radiation performance and bandwidth.

The initial circuit design and preliminary measurement results were demonstrated in our previous work [42]. In this work, analytical models are proposed to establish relationships between the diode's SPICE parameters and transponder conversion loss (CL). Thus, a diode selection criterion is created, which transponder designers can greatly benefit from. Also, the analysis shows the roles of capacitive and resistive nonlinearity in producing second-harmonic power. To implement a complete transponder, a dual-band circularly polarized spiral slot antenna is designed and fabricated to operate as the transponder antenna. Finally, a joint measurement including the harmonic radar and the complete transponder is performed and the results are analyzed carefully.

The integrated fully passive transponder demonstrates an improved CL performance and a noticeable read-out distance of 7 meters at the fundamental frequency of 3.5 GHz.

6.2 Analytical Models of the Harmonic Transponder
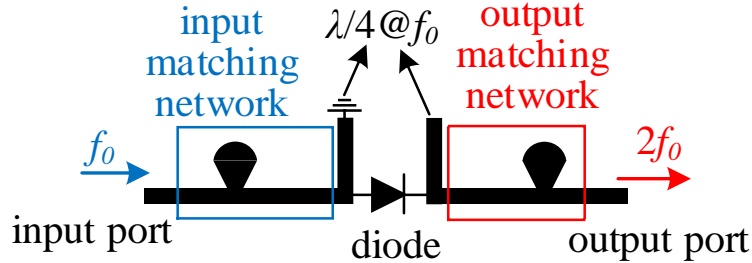
Figure 6.2 Circuit schematic of a typical harmonic transponder (second harmonic generation).

The schematic of a typical harmonic transponder circuitry part utilizing second harmonic generation is presented in Figure 6.2. To exacerbate the nonlinear conversion process in the diode, quarter-wave short-circuited and open-circuited stubs are placed around the diode. At the fundamental frequency f_0, the quarter-wave short-circuited stub operates as open at its input, whereas the quarter-wave open-circuited stub evolves into a short end at its input. Thus, the injected RF signal at f_0 passes through the input matching network and reaches out to the diode input. However, the quarter-wave open-circuited stub at f_0 at the output shorts the fundamental signal. The equivalent circuit of the harmonic transponder at the fundamental frequency f_0 can be described as in Figure 6.3 (a). At the second-harmonic frequency $2f_0$, the short-circuited and open-circuited stubs turn out to be short and open ends, respectively. The diode becomes a second-harmonic energy generator in this case. Due to the stubs and the output matching circuit designed for $2f_0$, maximum second-harmonic power is sensed at the output port. The equivalent circuit depicting the above scenario is presented in Figure 6.3 (b).

Note that the input and output matching networks are removed for simplification. The diode is represented by the Shockley model, consisting of junction resistance R_j, junction capacitance C_j, and series resistance R_s [19]. Parasitic capacitance C_p and inductance L_p are used to model the packaging effect. The fundamental RF source is described by a Thevenin equivalent circuit in Figure 6.3 (a), whereas the diode serving as a second-harmonic source is modeled by a Norton equivalent circuit in Figure 6.3 (b). Also, V_1 is the node voltage as shown in Figure 6.3.
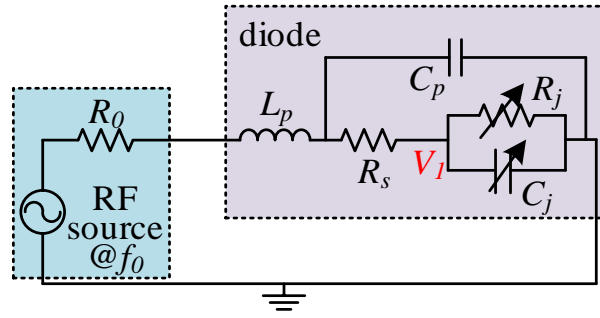
(a)
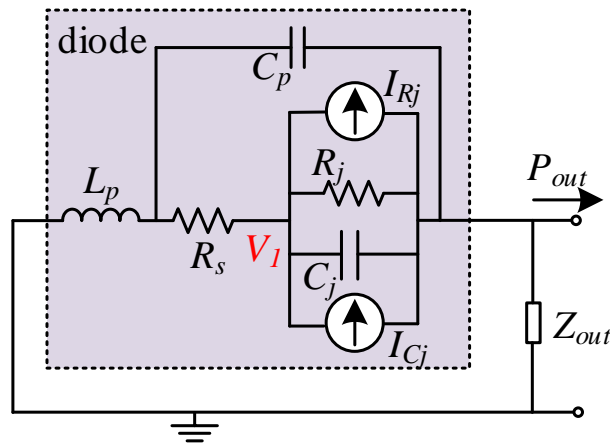
(b)

Figure 6.3   Equivalent circuits describe the harmonic transponder operating at different frequencies. (a) At the fundamental frequency f_0. (b) At the second-harmonic frequency $2f_0$.

6.2.1 Explicit Model A

The injecting fundamental RF signal is assumed to have a cosine waveform with a magnitude of V_0 and angular frequency of ω_0. Therefore, it can be expressed as:

$$V_{in} = V_0 cos(\omega_0 t) \tag{6.1}$$

As shown in Figure 6.3 (a), the voltage across the diode junction can be expressed by:

$$V_{on} = V_1 cos(\omega_0 t) \tag{6.2}$$

The exponential model of describing diode's current I and voltage V is adopted here [36]:

$$I_{diode} = I_s \cdot \left[e^{\frac{V_{on}}{n \cdot Vt}} - 1 \right] = I_s \cdot \left[e^{\frac{V_1 cos(\omega_0 t)}{n \cdot Vt}} - 1 \right] \tag{6.3}$$

where I_s is diode's saturation current and n is the ideality factor. $V_t = k \cdot T/q$ represents the thermal voltage. k, T, and q are the Boltzmann constant, operating temperature (in Kelvin), and electron charge, respectively. This exponential I-V model remains valid in the analysis since the power dealt with by the harmonic transponder is usually small. By using small signal theory, the I-V model can be expanded by the Taylor series around the 0 V bias point [17, 116]:

$$I_{diode} = I_s \cdot \left[\frac{V_{on}}{n \cdot Vt} + \frac{V_{on}^2}{(n \cdot Vt)^2 2!} + \cdots + \frac{V_{on}^n}{(n \cdot Vt)^n n!} + \cdots \right] \tag{6.4}$$

The first two terms can be used for approximation in a low power range. Thus, substituting (6.2) into (6.4), one can obtain the fundamental current and then calculate the absorbed fundamental power level:

$$P_{f0\_A} = \frac{I_s \cdot V_1^2}{2 \cdot n \cdot Vt} \tag{6.5}$$

As can be seen in Figure 6.3 (b), at the second-harmonic frequency $2f_0$, the junction can be considered as a power generator. The second-harmonic current due to the junction resistance can also be extracted based on (6.4):

$$I_{Rj} = \frac{I_s \cdot V_1^2}{4 \cdot (n \cdot Vt)^2} \cdot cos(2\omega_0 t) \tag{6.6}$$

The voltage-controlled junction capacitance is characterized by:

$$C_j(V_{on}) = C_{j0} \cdot \left(1 - \frac{V_{on}}{V_j} \right)^{-M} \tag{6.7}$$

where V_j and M are junction potential and grading coefficient, respectively. C_{j0} is the zero bias junction capacitance. Note that the diffusion capacitance is not considered in the analysis when the diode is forward-biased. Thus, the charge stored in the junction capacitance is:

$$Q_{Cj}(V_{on}) = \int C_j(V_{on}) \, dV_{on} = \frac{C_{j0} \cdot V_j}{M-1} \cdot \left(1 - \frac{V_{on}}{V_j} \right)^{1-M} \tag{6.8}$$

By applying Taylor series to Q_{Cj} and getting the second term as an approximation, the current becomes:

$$I_{Cj} = \frac{d\{Q_{Cj}(V_{on})\}}{dt} \approx \frac{d\left\{\frac{C_{j0} \cdot M}{2V_j} \cdot V_{on}^2\right\}}{dt} \tag{6.9}$$

I_{Cj} is obtained by substituting (6.2) into (6.9):

$$I_{Cj} \approx -\frac{C_{j0} \cdot M \cdot V_1^2 \cdot \omega_0}{2V_j} \cdot sin(2\omega_0 t) \tag{6.10}$$

It can be observed that I_{Rj} and I_{Cj} have a phase difference of 90°. Then, the total current at the second-harmonic frequency $2f_0$ can be written as:

$$I_t = \frac{I_s \cdot V_1^2}{4 \cdot (n \cdot Vt)^2} - i \cdot \frac{C_{j0} \cdot M \cdot V_1^2 \cdot \omega_0}{2V_j} \tag{6.11}$$

Note that I_t is the short-circuited current of the diode source. Before calculating the output current I_{out} through applying the current division rule, the source internal impedance Z_p of the diode needs to be determined first:

$$Z_p = \frac{R_{j0} \cdot \left(i2\omega_0 C_{j0}\right)^{-1}}{R_{j0} + \left(i2\omega_0 C_{j0}\right)^{-1}} \tag{6.12}$$

in which $R_{j0} = nV_t/I_s$ is the zero bias junction resistance. Then I_{out} is obtained by:

$$I_{out} = I_t \cdot \frac{Z_p}{Z_p + R_s + Z_{out}} \tag{6.13}$$

The packaging capacitance and inductance are not included for simplification in this model. Then, the total generated second-harmonic power can be expressed as:

$$P_{2f0\_A} = \text{real}\left(\frac{I_{out}^* \cdot I_{out} \cdot (Z_p + R_s + Z_{out})}{2}\right) \tag{6.14}$$

Thus, the conversion efficiency from fundamental frequency to second-harmonic frequency can be defined as:

$$\eta = \frac{P_{2f0\_A}}{P_{f0\_A}} = \frac{P_{f0\_A}}{2} \cdot \left(\frac{\mathfrak{R}_{I0}^2}{4} + \frac{(\omega_0 C_{j0} M R_{j0})^2}{V_j^2} \right) \cdot \text{real} \left(\frac{Z_p^* \cdot Z_p}{Z_p^* + R_s + Z_{out}} \right) \tag{6.15}$$

where $\mathfrak{R}_{I0}$ is zero bias current responsivity and calculated by $1/(2 \cdot n \cdot Vt)$. Based on (6.15), one knows that to increase the conversion efficiency, a higher input power works like the case of a low power rectifier. $\mathfrak{R}_{I0}$ is usually associated with the inherent nature of junction. Thus, finding a diode with smaller junction potential V_j and series resistance R_s but larger grading coefficient M can enhance the conversion efficiency.

6.2.2 Accurate Model B

Several approximations are made in model A to get an explicit expression (6.15) clearly showing the relationship between key SPICE parameters and the conversion efficiency. To get a more accurate model, modifications in calculating the fundamental input power and the second-harmonic current due to junction resistance R_j are required [44].

The Bessel function can be used to extract each harmonic component of the diode current in (6.3) effectively [115]. Therefore, the fundamental current can be written as:

$$I_{f0} = I_s \cdot \left[2 \cdot i \cdot J_1 \left(-i \frac{V_1}{n \cdot Vt} \right) \right] \cdot cos(\omega_0 t) \tag{6.16}$$

where $J_v(x)$ is the Bessel function of first kind of order v. The injecting current can be obtained by applying the Kirchhoff Circuit Laws (KCL) considering the effect of the packaging components:

$$I_{in} = I_{f0} + V_1 \cdot i\omega_0 C_j + \left(\left(I_{f0} + V_1 \cdot i\omega_0 C_j \right) \cdot R_s + V_1 \right) \cdot i\omega_0 C_p \tag{6.17}$$

Meanwhile, the injecting voltage can be expressed by:

$$V_{in} = V_1 + \left(I_{f0} + V_1 \cdot i\omega_0 C_j \right) \cdot R_s + I_{in} \cdot i\omega_0 L_p \tag{6.18}$$

Hence, the injecting power can be calculated by:

$$P_{f0\_B} = \text{real} \left(\frac{V_{in} \cdot I_{in}^*}{2} \right) \tag{6.19}$$

In the calculation of P_{f0_B}, C_j is simplified to be zero bias value C_{j0} in the power range of interest. Note that there is only one unknown V_1 in (6.19). So, when P_{f0_B} is assigned, V_1 can be easily obtained by solving (6.19). Next, based on (6.3), I_{Rj_B} can be obtained by selecting the component at the second-harmonic frequency $2f_0$:

$$I_{Rj\_B} = I_s \cdot \left[-2 \cdot J_2 \left(-i \frac{V_1}{n \cdot Vt} \right) \right] \cdot \cos(2\omega_0 t) \tag{6.20}$$

Together with I_{Cj} expressed in (6.10), the generated second-harmonic current is:

$$I_{t\_B} = I_s \cdot \left[-2 \cdot J_2 \left(-i \frac{V_1}{n \cdot Vt} \right) \right] - i \cdot \frac{C_{j0} \cdot M \cdot V_1^2 \cdot \omega_0}{2V_j} \tag{6.21}$$

Next, the current coming out of the diode I_{out_B} can be written by:

$$I_{out\_B} = I_{t\_B} \cdot \frac{Z_p}{Z_p + R_s + \frac{(Z_{out} + i2\omega_0 L_p) \cdot (i2\omega_0 C_p)^{-1}}{Z_{out} + i2\omega_0 L_p + (i2\omega_0 C_p)^{-1}}} \cdot \frac{(i2\omega_0 C_p)^{-1}}{Z_{out} + i2\omega_0 L_p + (i2\omega_0 C_p)^{-1}} \tag{6.22}$$

where Z_{out} is the output impedance equal to the complex conjugate of the packaged diode's impedance in order to maximize the power transfer to the output port. Then, the generated second-harmonic power reaching the output can be expressed by:

$$P_{2f0\_B} = \text{real} \left(\frac{I_{out\_B}^* \cdot I_{out\_B} \cdot Z_{out}}{2} \right) \tag{6.23}$$

Thus, the conversion efficiency can be calculated:

$$\eta = \frac{1}{2} \left[I_{Rj\_B}^2 + I_{Cj}^2 \right] \cdot \text{real} \left(\left| \frac{Z_p}{Z_p + R_s + \frac{(Z_{out} + i2\omega_0 L_p) \cdot (i2\omega_0 C_p)^{-1}}{Z_{out} + i2\omega_0 L_p + (i2\omega_0 C_p)^{-1}}} \cdot \frac{(i2\omega_0 C_p)^{-1}}{Z_{out} + i2\omega_0 L_p + (i2\omega_0 C_p)^{-1}} \right|^2 \cdot Z_{out} \right) \tag{6.24}$$

Correspondingly, the CL in dB (a different way expressing the conversion efficiency) then can be easily determined by:

$$CL = P_{f0\_B}(\text{dBm}) - P_{2f0\_B}(\text{dBm}) \tag{6.25}$$

Several commonly used diodes are selected for verifications. Their key SPICE parameters are listed in Table 6.1. Since the calculation starts from the I-V relationship of the selected diode and the input power of the diode is then obtained, the source impedance is not specified in both models. During the verification, the input power is swept from -50 to -30 dBm. Calculated CL results along with simulated results by ADS Harmonic Balance simulator of each diode-based transponder are presented in Figure 6.4. It can be clearly observed that the calculated CL results are in good agreement with the simulated ones by ADS, verifying the great accuracy of the proposed analytical model B. Moreover, diode SMS7630 shows a better CL performance than the others in the power range of interest.

Table 6.1 Key SPICE parameters

Parameters	SMS7630-079LF	HSMS-2850	HMPS-2820	SMV1430
C_{j0} (pF)	0.14	0.18	0.7	1.11
I_s (A)	5e-6	3e-6	2.2e-8	1e-14
R_s (Ω)	20	25	8	3.15
n	1.05	1.06	1.08	1
V_j (V)	0.34	0.35	0.65	0.86
M	0.4	0.5	0.5	0.5
C_p (pF)	0.16	0.08	0.08	0.13
L_p (nH)	0.7	2	2	0.7

[*] Diodes SMS7630 and SMV1430 are from Skyworks. Inc. The remaining two are from Avago Technology.

[**] All diodes are Schottky diodes except a varactor SMV1430.

Good accuracy of model B can help us study the contributions of capacitive nonlinearity C_j and resistive nonlinearity R_j, in terms of generating the second-harmonic power. As can be seen in Figure 6.5 (a), the CL is calculated based on SMS7630, with all parameters kept the same but C_{j0} swept from 0.1 to 1.2 pF and I_s from 0.01 pA to 10 µA. I_s is inversely proportional to R_{j0}, so the variation of R_{j0} is from 2.7 kΩ to 2.7 TΩ. The corresponding values of R_{j0} have been also listed in Figure 6.5 (a) and (b). The power level in this analysis is -30 dBm. Four diode candidates are labeled in this figure based on their C_{j0} and R_{j0} values. Note that it is assumed that SPICE parameters of other diodes are the same as SMS7630 except C_{j0} and R_{j0} in this plotting. This assumption is based on diode's C_{j0} and R_{j0} are two dominant factors determining the CL

performance. By doing so, one can easily know the performance of each diode-based transponder. SMS7630 and HSMS-2850 are clearly better choices. Also, this figure helps to establish a transponder diode selection criterion regarding R_{j0} and C_{j0}, which is higher R_{j0} (lower I_s) and lower C_{j0} are desired. However, considering the potential difficulty of matching network design due to an extremely high R_{j0}, it is almost impossible to use diodes which locate in the left bottom corner of Figure 6.5 (a). Together with the conclusions based on model A regarding V_j, R_s, and M, a complete diode selection criterion has been successfully established.
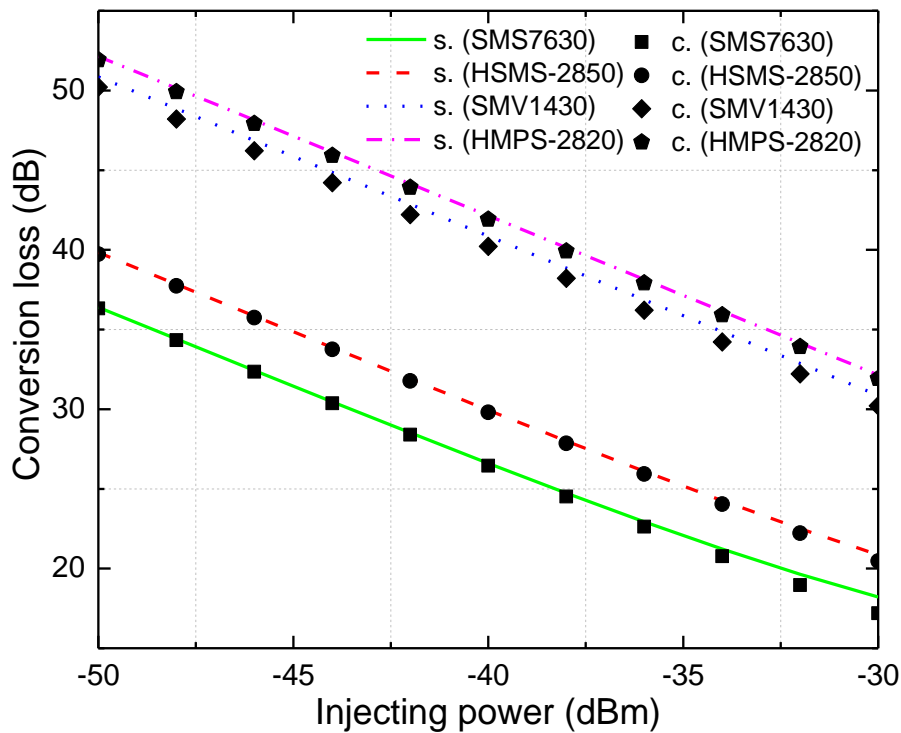
Figure 6.4 Comparison of calculated and simulated CL performance of four typical selected diodes-based transponders, when the injecting power is in a range of −50 to −30 dBm. The diodes are SMS7630, HSMS-2850, SMV1430, and HMPS-2820.

Also, the ratio of power due to resistive nonlinearity over total generated second-harmonic power can be calculated by:

$$\text{Ratio} = \frac{I_{Rj}^2}{I_{Cj}^2 + I_{Rj}^2} \tag{6.26}$$
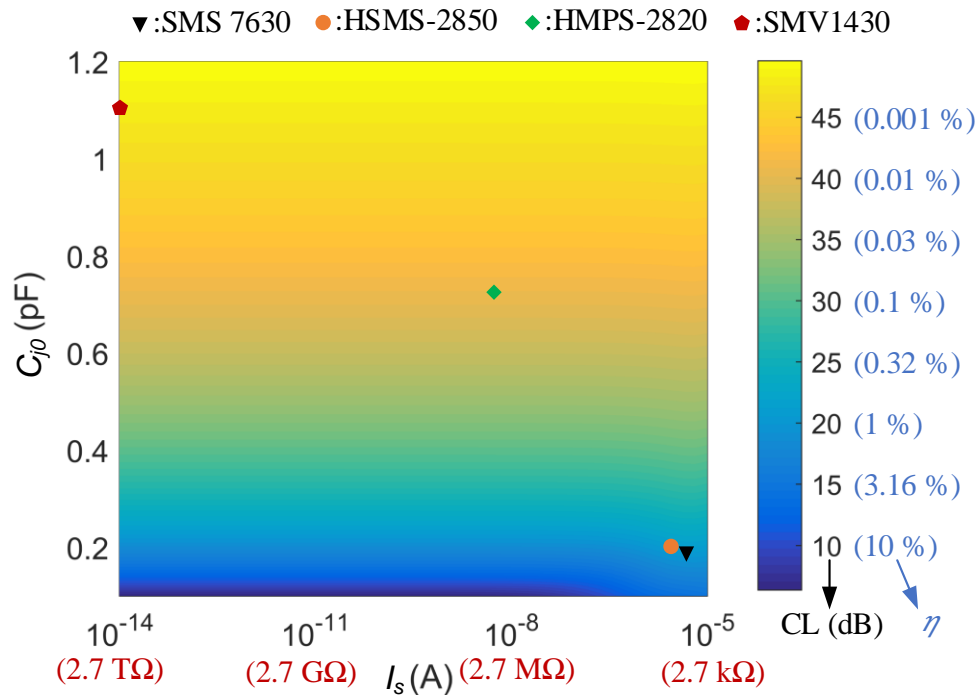
(a)
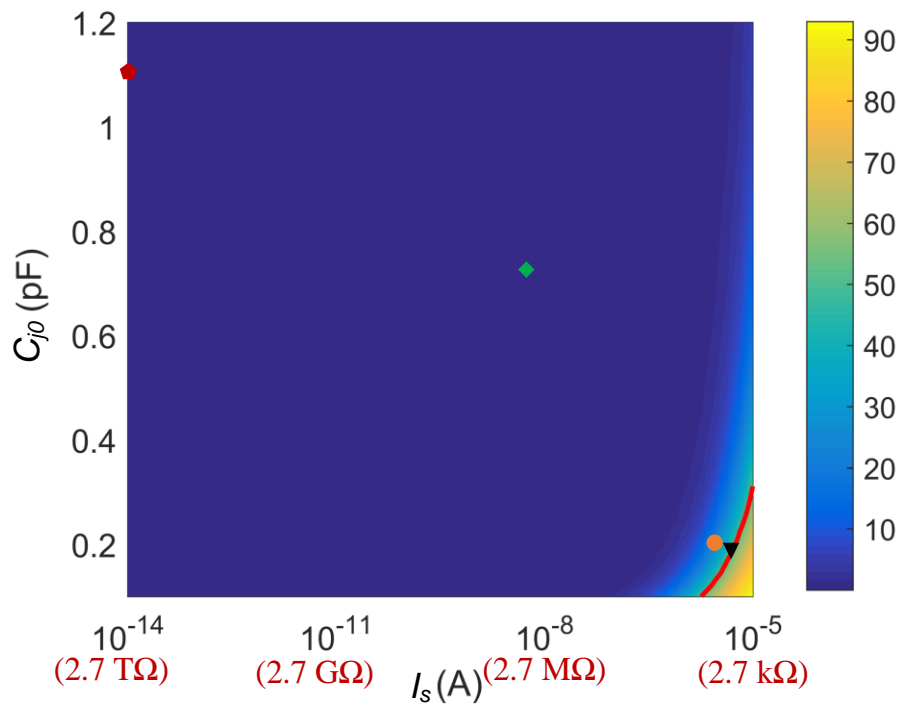
(b)
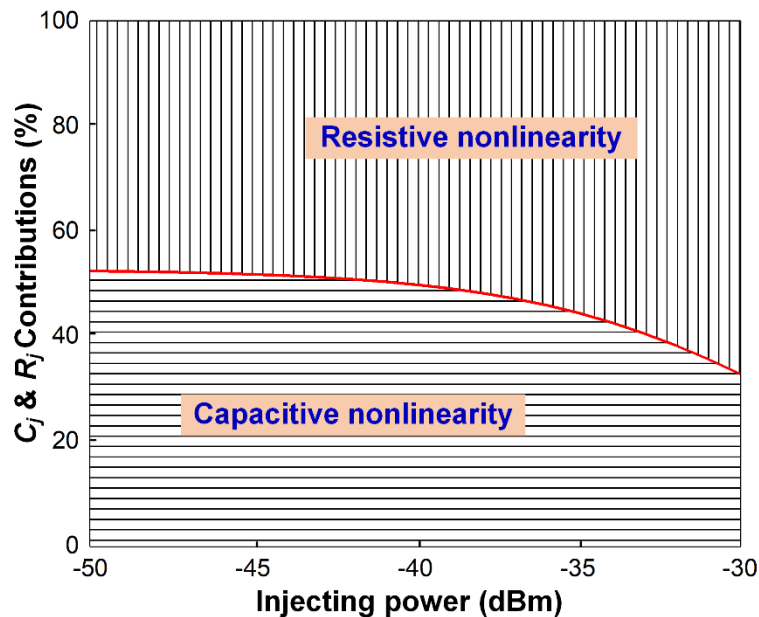
(c)

Figure 6.5 (a) Calculated CL results when sweeping C_{j0} and I_s (R_{j0}). Four diode candidates are labeled according to their C_{j0} and I_s (R_{j0}). (b) Calculated ratio of power due to resistive nonlinearity over total generated second-harmonic power, when sweeping C_{j0} and I_s (R_{j0}). (c) Contribution of C_j and R_j of diode SMS7630 versus injecting power from -50 to -30 dBm.

This ratio is plotted in Figure 6.5 (b). The red line denotes 50%, which means C_j and R_j contribute equally to the generation of the second-harmonic power. The location of diode SMS7630 is close to the red line. Also, if a better-performed diode can be found as mentioned before, its capacitive nonlinearity will be dominant in second-harmonic power generation.

Among the four candidates, the best diode SMS7630 is selected to investigate the contributions of C_j and R_j in terms of different power levels. As shown in Figure 6.5 (c), R_j becomes more dominant with the increase of the injecting power.

The nonlinearity of diodes is commonly used in frequency conversion. Another popular application scenario is applying diodes for rectifier design, which converts RF power into dc power. The conversion mechanism is similar. Thus, a comparison of diode's performance in two different application situations could be meaningful. Figure 6.6 shows the conversion efficiency performance of two diodes-based rectifiers and transponders. SMS7630 behaves better when used

in rectifier while HMPS 2820 better for the transponder. According to it, one knows that for a specific design, a careful selection is essential. Thanks to the criterion addressed in this work and our previous work regarding rectifier diode analysis, it is hoped that transponder and rectifier design can become more convenient.
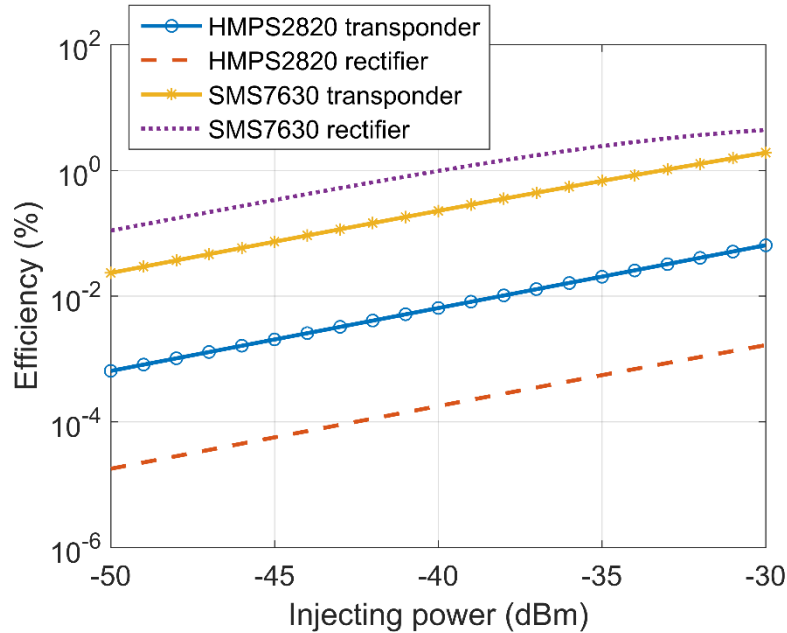
Figure 6.6 Efficiency performance comparison of the same diode-based transponder and rectifier. The selected diodes are HMPS2820 and SMS7630.

6.3 Integrated Design of the Harmonic Transponder

6.3.1 Diplexer Design

As the component offering two pass-bands and high isolation between ports, the diplexer plays a vital role in this circuitry [152]. The fundamental frequency f_0 of the diplexer is 3.5 GHz according to the new IMT allocated by WRC-15. In this diplexer, port 1 connects to the transponder antenna, through which the fundamental signal is injected into the circuit. Due to the strong coupling between ports 1 and 3, the injected fundamental signal reaches port 3. Subsequently, it goes through the transponder circuitry shown in Figure 6.2 and generates second harmonic which reaches port 2. At the second-harmonic frequency $2f_0$, ports 2 and 1 are strong coupled. So, the second harmonic signal reaches port 1 and radiates through the transponder antenna. The smooth signal

transmission also relies on a strong suppression of fundamental and second harmonics between ports 2 and 3, respectively.
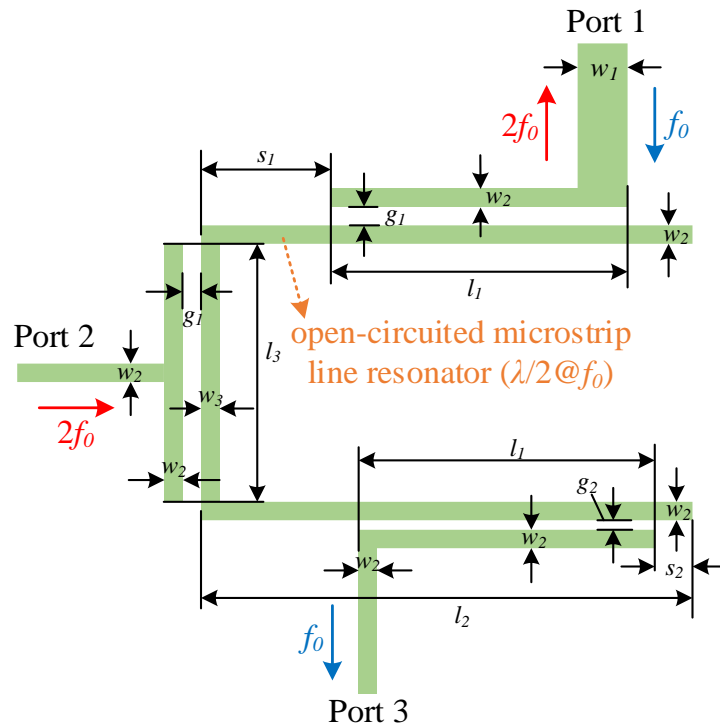
(a)
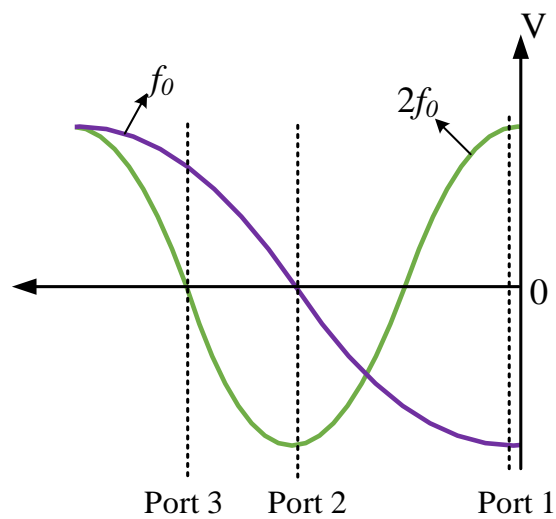
(b)
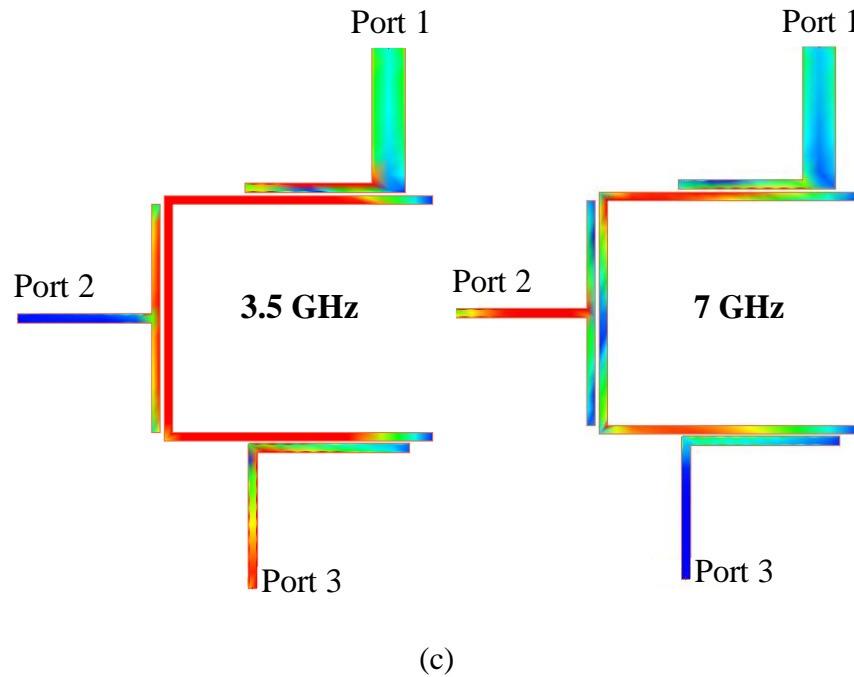
Figure 6.7 (a) Layout of the diplexer. Dimensions: w_1=1.27, w_2=0.323, w_3=0.34, l_1=6, l_2=10, l_3=8.38, g_1=0.127, g_2=0.08, s_1=3, s_2=0.86, in mm. (b) Voltage distribution for an open-circuited microstrip line resonator at the fundamental and second-harmonic frequencies. The locations of each port are labelled along the resonator. (c) Current distributions.

In the middle of the diplexer circuit, a U-shaped half wavelength open-circuited microstrip line resonator at the fundamental frequency f_0 is inserted, as presented in Figure 6.7 (a). The locations of each port around the resonator are crucial to accomplish such a strong coupling and suppression of desired modes simultaneously. Figure 6.7 (b) illustrates the voltage distribution for an open-circuited microstrip line at the fundamental and second-harmonic frequencies, respectively. At the fundamental frequency f_0, it is obviously better for ports 1 and 3 to be placed at the two ends to obtain a strong coupling. Note that the same microstrip line evolves into a λ resonator at the second-harmonic frequency $2f_0$. To ensure a desired strong coupling, port 2 needs to be located in the middle and at the same time port 1 remains at one end. It is observed that during the transmission of the fundamental tone between ports 1 and 3, no power would leak out to port 2. However, port 3 has to be moved to a location where zero voltage occurs on the resonator as shown in Figure 6.7 (b), in order to minimize the leakage of second-harmonic power to port 3. Such a rough analysis enables quickly locating each port around the resonator. The exact dimensions of the diplexer are

obtained through a post-optimization, which are all listed in the caption of Figure 6.7. The current distributions at the fundamental and second-harmonic frequencies are demonstrated in Figure 6.7 (c). The characteristic impedance of microstrip line at port 1 is designed to be 50 Ω, and at ports 2 and 3 to be 100 Ω. The substrate used here is Rogers RT/duroid 6002 with 20 mil thickness and 18 um copper cladding.
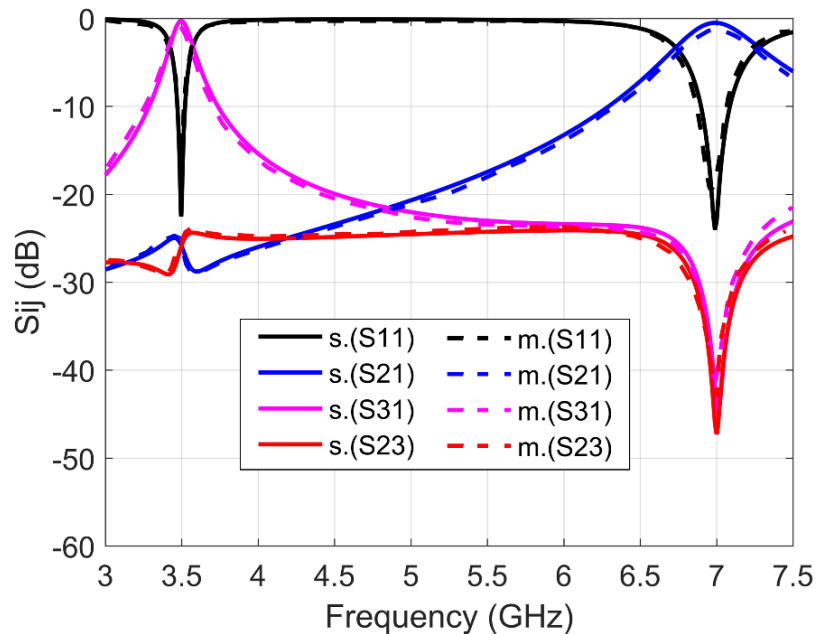
Figure 6.8 Comparison of the measured and simulated S-parameters of the diplexer.

The proposed diplexer is simulated by ADS Momentum microwave simulator. Figure 6.8 presents the comparison of simulated and measured S parameter results, which match well. Although the measurement was conducted using a standard 50 Ω lab setup, the measured results are transformed to a 100 Ω reference for a fair comparison with the simulation results for ports 2 and 3 and presented in Figure 6.8. The results shown are the measured insertion loss values of the pass-bands at the fundamental and second-harmonic frequencies are both less than 1.5 dB, and measured isolation between ports 2 and 3 at both frequencies is over 25 dB.

6.3.2 Circuit Integration

With the aid of the aforementioned analytical models and analysis of multiple diodes for CL performance in section II, the outperforming diode SMS7630-079LF is selected for designing the transponder circuitry. The transponder circuitry integration with the proposed diplexer is presented

in Figure 6.9 (a). The input and output ports shown in Figure 6.2 are respectively connected with the ports 3 and 2 of the diplexer in Figure 6.7 (a). The impedance matching between port 3 and the diode is realized by the input matching network at the fundamental frequency f_0. At the output port, the diode impedance is matched to port 2 by the output matching network at the second-harmonic frequency $2f_0$. The diode impedance is mainly dependent on R_j and C_j as shown in (6.12). Since the selected diode SMS7630 is a low barrier diode, a simple L-matching network is a satisfactory choice in this case.
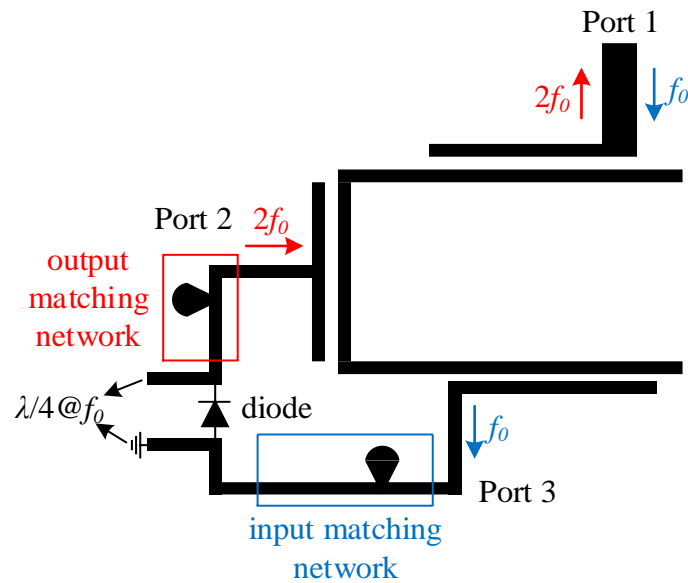
(a)
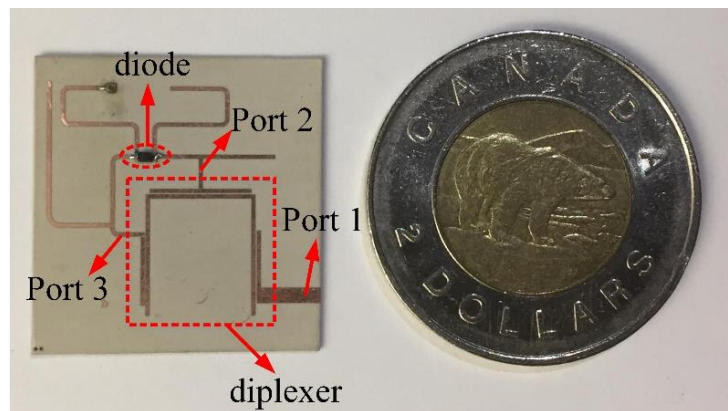
(b)

Figure 6.9   (a) Circuit schematic of the diplexer-based harmonic transponder. (b) Experimental prototype.

In this design, power conversion from the fundamental frequency f_0 to the desired second-harmonic frequency $2f_0$ needs to be maximized. In other words, any other harmonic conversion should be reduced, especially RF-to-dc conversion. Thanks to the gap coupling feature of the diplexer, a conventional capacitor working as the dc block is not necessary at the output port any more. Finally, the fabricated circuity part of the transponder demonstrates a compact and well-rounded design, with the experimental prototype shown in Figure 6.9 (b).

6.3.3 Transponder Antenna Design

The antenna designed to integrate with the harmonic transponder circuitry should satisfy the minimum requirements of the dual-band operation, to receive signal at 3.5 GHz and transmit at 7 GHz. Also, the omnidirectional radiation performance is preferred to increase the spatial coverage [153]. Considering a compact and efficient module, it is better to design the antenna utilizing the same ground plane and feed line of the circuitry. Based on these requirements, slot antennas excited by the feed on the other layer of the substrate is an attractive solution. Circular polarization is chosen for the demonstration and is not limited to it. For our application, the dual-band spiral slot antenna proposed in [154] has been improved in bandwidth by replacing the radius variation after each quarter turn with continuous radius variation and aligning the two spiral slots at different angles.

The design is presented in Figure 6.10, with all the dimensions marked. It has two spiral slots of different radii to operate as a dual-band antenna at 3.5 GHz and 7 GHz. The spiral on the outer perimeter is designed to operate at 3.5 GHz and the inner one at 7 GHz. These two slots are simultaneously excited through a single microstrip line feed placed on the opposite layer of the substrate. Also, the coupling between these two slots significantly improves the bandwidth at both the design frequencies. The spiral slot radius is varied with respect to (6.27) for both slots.

$$r = r_0 + (w + s)N \quad , \quad N = \frac{(\theta - \theta_0)}{2\pi} > 0 \qquad (6.27)$$

where r_0 and θ_0 are the initial radius and initial angle of spiral, w is the width of slot which is constant throughout, s is the spacing between turns, N is the number of turns and θ is the angle of rotation.
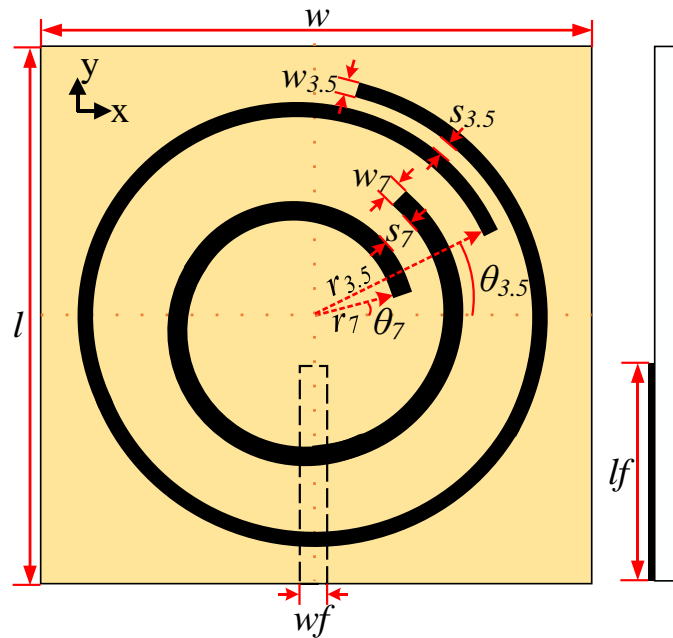
Figure 6.10 Top view and side view of proposed dual-band circularly polarized spiral slot antenna with all dimensions marked: $r_{3.5}$=10.3, $s_{3.5}$=0.57, $w_{3.5}$=0.95, r_7=4.8, s_7=1.6, w_7=1.3, wf=0.67, lf=13.6, w=35 and l=35, in mm; $\theta_{3.5}$=20°, θ_7=10°, $N_{3.5}$= 1.158, N_7=1.10; The substrate is Rogers RT/duroid 6002 of thickness 20 mil, the same one used for the transponder circuitry.

The simulated matching performance of the individual single spiral slots along with that of dual-band spiral slot is presented in Figure 6.11 (a). The improvement in matching performance of the dual-band spiral slot antenna at both the design frequencies is realized by optimizing the coupling between individual spiral slots. The measured results of the proposed dual-band spiral slot antenna agree well with simulated results for both the matching performance and the axial ratio as shown in Figure 6.11 (b). It has a measured −10 dB matching bandwidth of 66% (from 2.9 GHz to 5.8 GHz) at 3.5 GHz and 28% (from 6.3 GHz to 8.4 GHz) at 7 GHz, and a measured axial ratio of 1.56 dB (simulated − 2.1 dB) at 3.5 GHz and 2.3 dB (simulated − 1.5 dB) at 7 GHz.

E- Field variation results of the proposed antenna with time at both frequencies are shown in Figure 6.12. It shows that the E-field varies in a circular pattern, confirming the circular polarization behaviour of the proposed structure at both the design frequencies. It can be observed that the spiral slot with larger radius contributes significantly for radiation at 3.5 GHz, while the inner spiral slot contributes for 7 GHz.
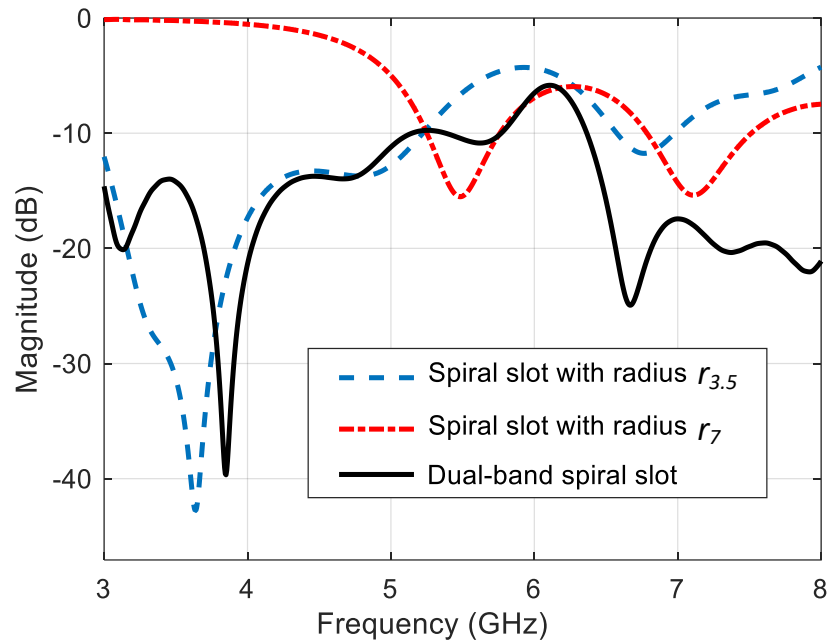
(a)
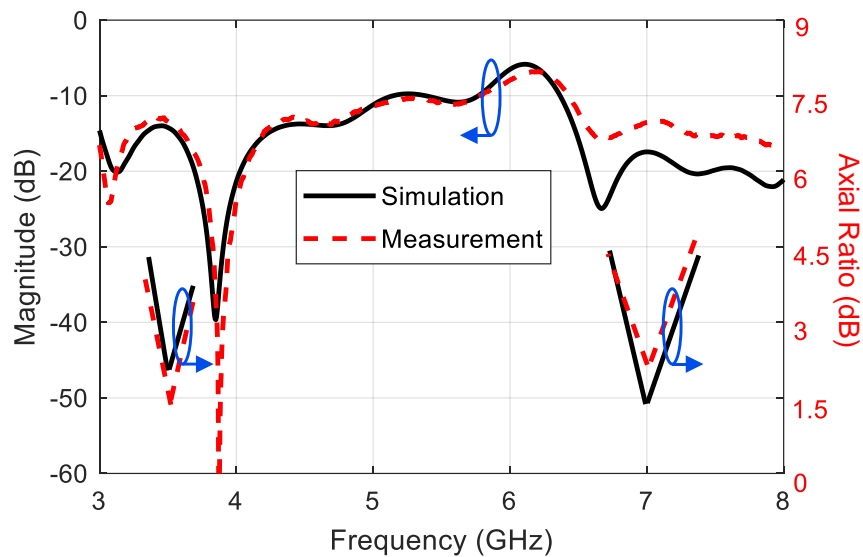
(b)

Figure 6.11 Comparison of (a) matching performance for individual spiral slots along with dual-band spiral antenna and (b) simulated and measured matching and axial ratio performance of dual-band spiral slot antenna.

(a)

(b)
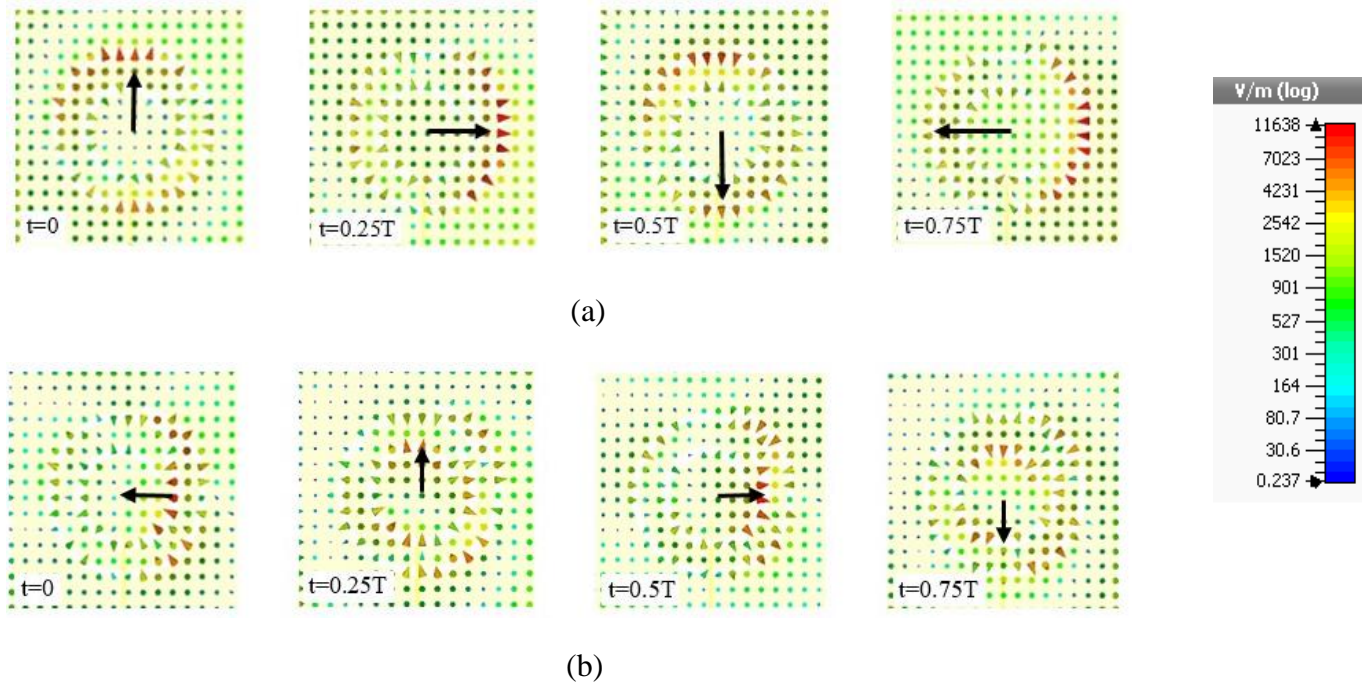
Figure 6.12 E- Field variation with time at (a) 3.5 GHz and (b) 7 GHz.

(a)   (b)
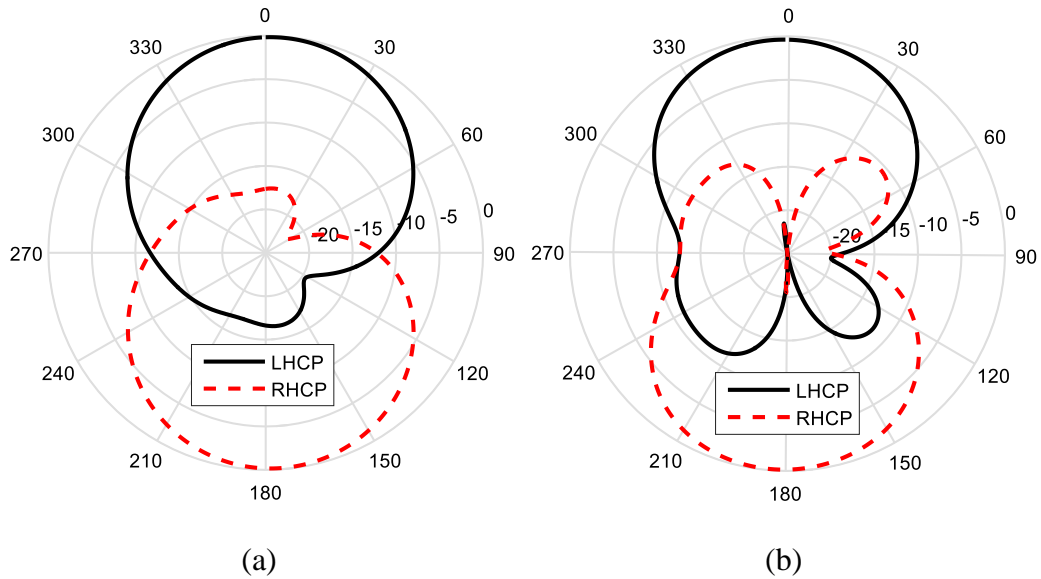
Figure 6.13 Simulated LHCP and RHCP at (a) 3.5 GHz and (b) 7 GHz.

Radiation efficiency of the proposed antenna is 98.5 % at 3.5 GHz and 98.4 % at 7 GHz and has a gain of 4 dB at 3.5 GHz and 3.8 dB at 7 GHz. Simulated radiation pattern for LHCP and RHCP at both the design frequencies are normalized and are shown in Figure 6.13. The radiation pattern is measured with the linearly polarized standard gain horn antenna in XZ plane and YZ plane, at both the frequencies and the normalized results match closely with the simulations, as shown in Figure 6.14.

(a)   (b)
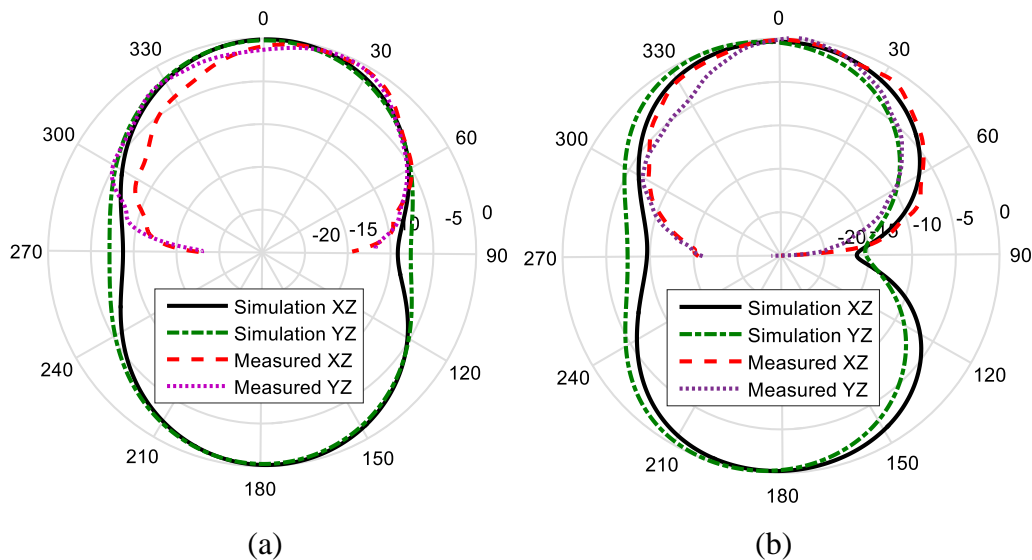
Figure 6.14 Comparison of simulated and measured normalized radiation pattern in XZ and YZ plane at (a) 3.5 GHz and (b) 7 GHz.

6.4 Transponder Measurement and Discussions

As observed from the transponder circuitry in Figure 6.9 (b), there is only one port (port 1) handling both the receiving and transmitting signals. This necessitates the use of a 3 dB hybrid coupler to detect the output second-harmonic power level in measurements. Figure 6.15 (a) shows the block diagram of the measurement setup, including the power transfer at two frequencies. The signal generator connected to port A of the hybrid coupler provides power at the fundamental frequency f_0. Half of this power reaches the transponder. Then, the second-harmonic output generated by the transponder at port C is transferred to port B, where a half of the power arrives at the signal analyzer. This signal analyzer displays the generated second-harmonic power level. The setup realized in the Poly-Grames Research Center is shown in the Figure 6.15 (b).

The measured CL results of this transponder are demonstrated in Figure 6.16, excluding all insertion loss of the coupler and cables. The input power range in the measurement is from -35 to -25 dBm. The simulated results from ADS Harmonic Balance simulator are included in comparison with measured ones, demonstrating a good match between them. Also, the CL results reported by previous related works are presented for comparison [102, 155]. By careful study and utilizing of identified low-barrier diode, the CL performance of the proposed fully passive transponder has been improved greatly compared to previous works.

(a)

(b)
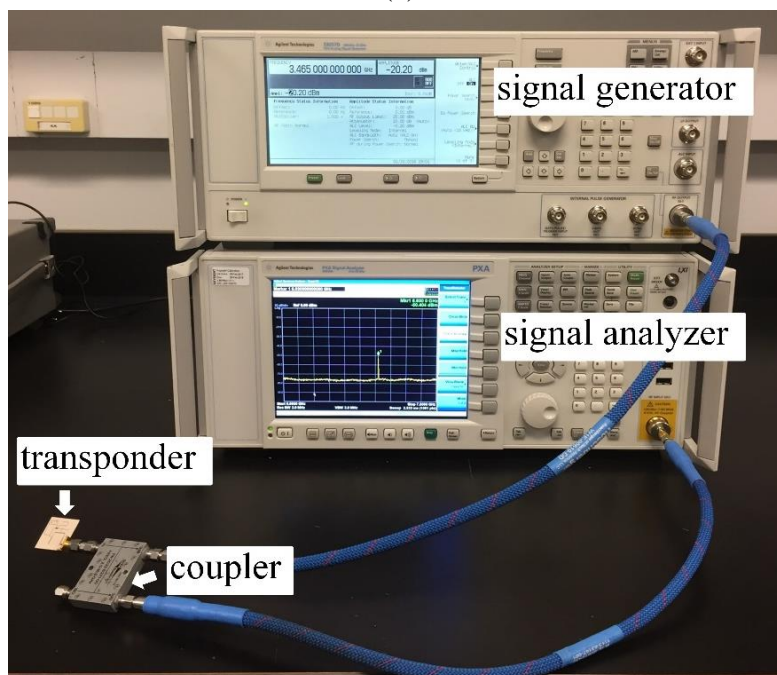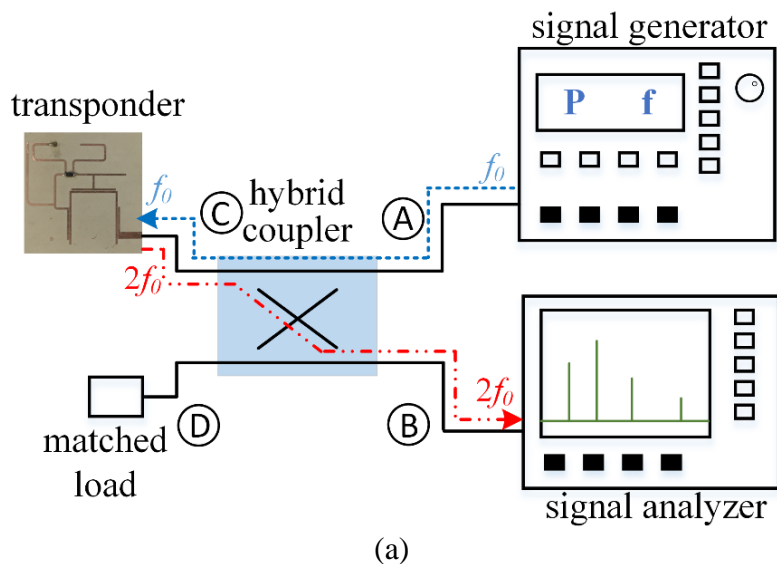
Figure 6.15 Measurement setup. (a) Diagram. (b) Realized setup in the lab.

After this preliminary measurement, a joint measurement of the complete transponder is conducted in the lab. From the building block sizes shown in Figure 6.17 (a), an integrated transponder with dimensions of 60 mm × 35 mm is feasible. The measurement setup to test the complete transponder is presented in Figure 6.17 (b). Both the radar Tx/Rx antennas are horn antennas from ETS-Lindgren, which are model 3160-05 and 3160-06. Note that although the frequency range for model 3160-05 is from 3.95 GHz to 5.85 GHz, it still works properly at 3.5 GHz after verified by S parameters measurements. The radar Tx antenna is connected with a signal generator to radiate fundamental power. And received power by Rx antenna is monitored through a signal analyzer. This describes the setup of the radar side. For the transponder side, the prototype is fixed on a moveable wooden base using tapes as shown in Figure 6.17 (b).
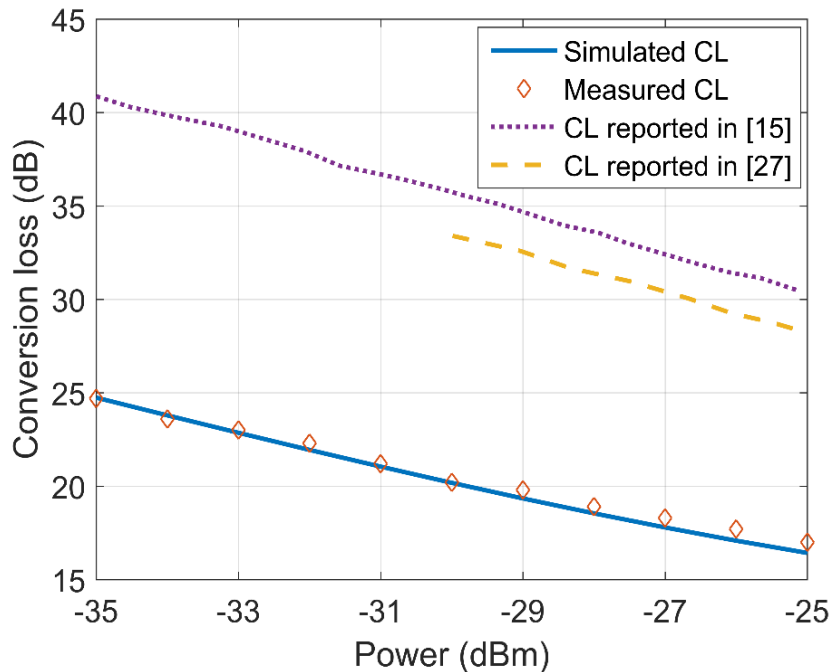
Figure 6.16 Comparison of simulated and measured CL results of the proposed harmonic transponder. Some related results reported recently have also been shown for comparison.

Theoretical link budget analysis (in dB) is based on Friis transmission equation [156], which yields:

$$P_r = P_t + G_{ra}^t + TL_{f_0} + G_{tr}^r - CL + G_{tr}^t + TL_{2f_0} + G_{ra}^r \tag{6.28}$$

where the definitions of parameters included are listed in Table 6.2.

The transmission loss is calculated by:

$$TL = 20 \times lg\left(\frac{\lambda}{4\pi d}\right) \tag{6.29}$$

in which λ is the wavelength and d is the transmission distance.

Table 6.2 Definitions of parameters in (6.28)

Parameters	
P_r	Power received by radar at $2f_0$
P_t	Power transmitted by radar at f_0
G_{ra}^t	Transmitting antenna gain of the radar
TL_{f_0}	Transmission loss in the space at f_0
G_{tr}^r	Receiving antenna gain of the transponder
G_{tr}^t	Transmitting antenna gain of the transponder
TL_{2f_0}	Transmission loss in the space at $2f_0$
G_{ra}^r	Receiving antenna gain of the radar
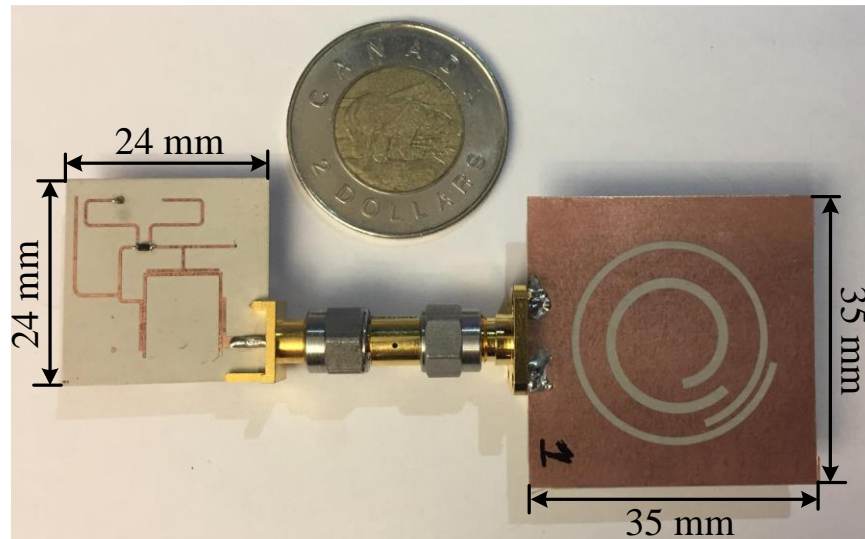
(a)
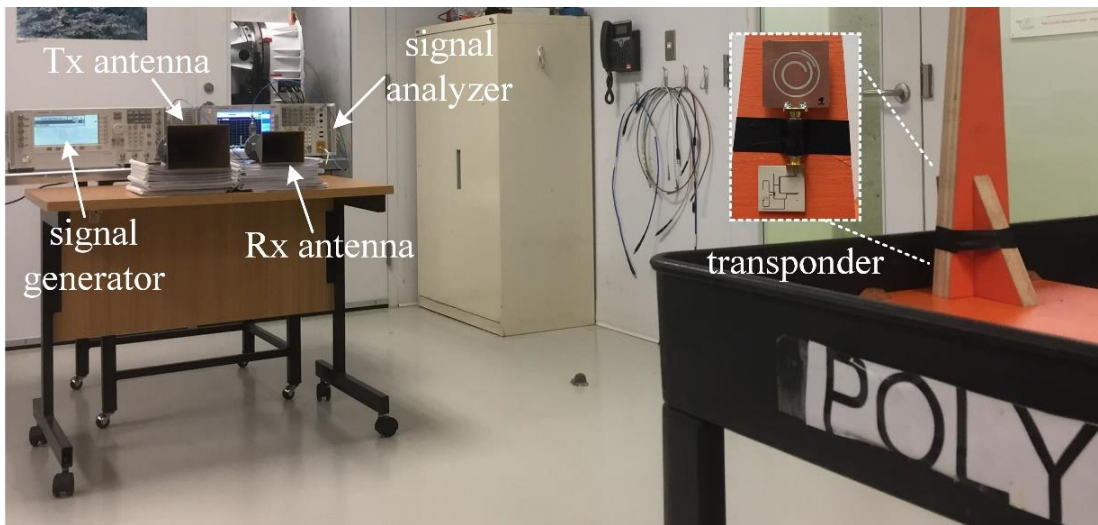
(b)

Figure 6.17 (a) Proposed experimental prototype of the transponder. (b) Measurement setup in the lab.

For measurements, the power level provided by the signal generator is set to be 25 dBm. The gain of the Tx antenna is 16.7 dBi at 3.5 GHz. For the energy detection side, the gain of Rx antenna is 17.1 dBi and the noise floor of the signal analyzer is -100 dBm. The received power by the radar varying distance is presented in Figure 6.18. The testing distance starts from 2 meters which ensures that both horn antennas are operating in the far field. In the measurements, the separate antenna and circuit parts are effectively used to obtain the fundamental power illuminating the transponder antenna and the second-harmonic power transmitted by the same transponder antenna. Thus, these data help establish the power link of the harmonic radar and transponder-based system, showing a global picture of each dissipation part. The above information is included in Figure 6.18. It clearly shows that the loss due to the transponder is low. Also, in the same figure, calculated received results are also presented for comparison. Considering a noise floor of -100 dBm, the maximum read-out distance for this setup is about 7 m.
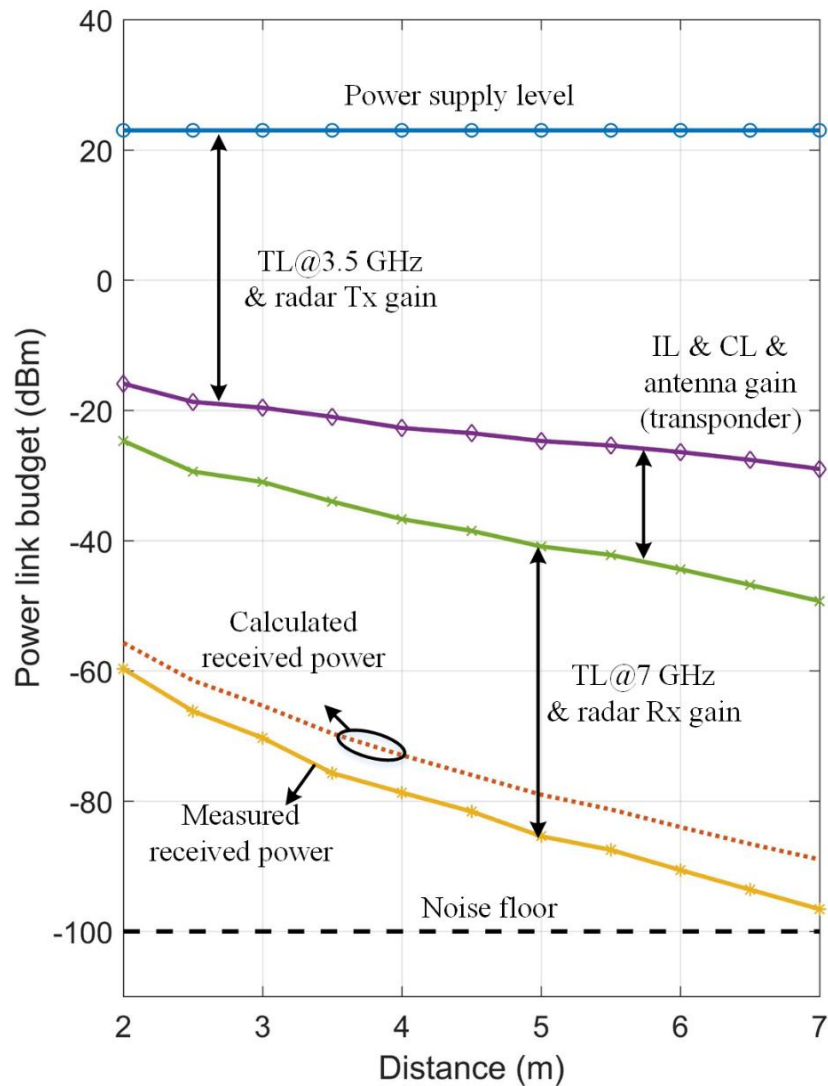
Figure 6.18 Calculated power link and measured received power when the proposed transponder is placed in a distance range from 2 to 7 m.

To figure out a fair way to compare our transponder with other state-of-the-art works, the harmonic radar performance and transmission loss due to different frequencies need to be normalized. Thus, it is assumed that each transponder is tested under the same circumstances, which we assume radar transmits 25 dBm power and both Tx/Rx antennas have a gain of 10 dBi. Although each transponder was measured in a different power range within each work, each covers the same injecting power level into diode of −25 dBm. Thus, during the comparison, the diode's injecting power is assumed to be −25 dBm for each transponder. As shown in Figure 6.19, the operating fundamental frequency is assumed to be 3.5 GHz. Based on the transponder information provided

in each related work, a figure-of-merit of transponder's maximum detection range (FOM_d) can be defined and then calculated:

$$FOM_d = \frac{d_1 + d_2}{2} \tag{6.30}$$

in which

$$d_1 = \frac{c}{f_0 \cdot 4\pi \cdot 10^{\frac{-(P_t + G_{ra}^t + 25 + G_{tr}^r)}{20}}} \tag{6.31a}$$

$$d_2 = \frac{c}{2f_0 \cdot 4\pi \cdot 10^{\frac{-(75 - CL + G_{tr}^t + G_{ra}^r)}{20}}} \tag{6.31b}$$

Note that the calculation of FOM_d also assumes that the antenna gain and CL of each transponder are still the same at 3.5 GHz.
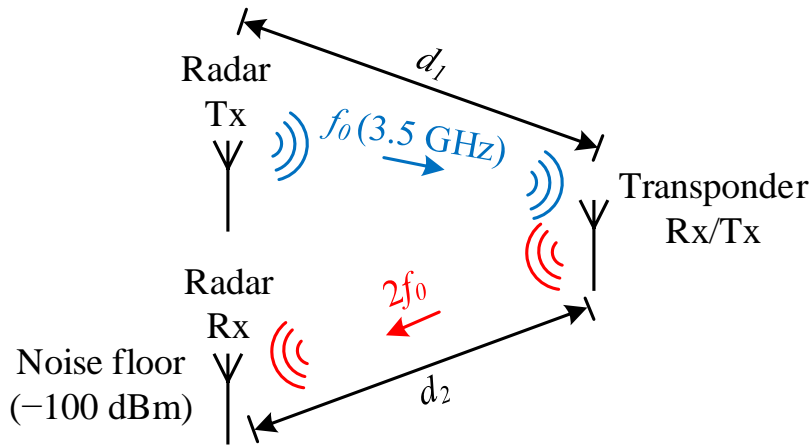
Figure 6.19 Setup diagram for the calculation of FOM_d.

A comparison between this work and other state-of-the-art works is listed in Table 6.3. All of them are fully passive harmonic transponders. Our proposed transponder features more freedom of transponder antenna design, thanks to which a dual-band circularly polarized omnidirectional antenna with enhanced bandwidth performance, higher radiation efficiency and gain are possible. The proposed transponder is able to deliver lower CL, when the input power level is at −25 dBm. Due to the lower CL and higher transponder antenna gains, our proposed transponder prototype shows a noticeable improvement regarding the FOM_d as shown in Table 6.3. The calculation of

FOM_d has several assumptions. For example, all the insertion loss is ignored. The injecting power of transponder is fixed to be -25 dBm. Thus, the FOM_d is larger than the measured read-out distance.

Table 6.3 Comparison between this work and previous related works

work	[102]	[43]	[155]	**this work**
Type	Passive	Passive	Passive	**Passive**
Op. freq. (GHz)	1.2 & 2.4	1 & 2	0.868 & 1.736	**3.5 & 7**
Size (mm^2)	75×65	80×35	200×125	**60×35**
No. of ant.	2	1	2	**1**
Ant. Gain (dBi)	$3.3@f_0$ $3@2f_0$	$1.3@f_0$ $1.7@2f_0$	$1.6@f_0$ $2.6@2f_0$	**$4@f_0$ $3.8@2f_0$**
Polarization	LP	LP	LP	**CP**
CL (dB) @-25 dBm	26.5	19.9	30	**17**
d_1 / d_2 FOM_d (m)	10.0/4.1 7.0	7.9/7.5 7.7	8.2/2.6 5.4	**10.8/13.3 12.0**

6.5 **Conclusion**

This work proposes and presents a novel diplexer-based fully passive transponder. Comparing with traditional architectures with two separate antennas, the proposed transponder allows the antenna design to enjoy more flexibility by adding a diplexer into the circuitry part. Analytical models are proposed to reveal relationships between the diode's SPICE parameters and transponder CL or conversion efficiency. A selection criterion is established and can be used to simplify the transponder design. With the aid of this criterion, the outperforming low-barrier diode SMS7630-079LF is chosen for experimental verification. The proposed transponder shows lower CL of 17 dB at the input power of -25 dBm in the measurement, showing a superior performance compared to the state-of-the-art works. A dual-band circularly polarized omnidirectional spiral slot antenna is designed as the transponder Tx/Rx antenna. The antenna shows improved performance regarding gain and bandwidth. In a measurement of the complete transponder, it is able to reach a read-out

distance range up to 7 meters, when the operating fundamental frequency is 3.5 GHz. This proposed fully passive transponder is believed to have a great potential for sub-6 GHz 5G-compatible IoT applications.

CHAPTER 7 ARTICLE 6: READOUT DISTANCE ENHANCEMENT OF BATTERY-FREE HARMONIC TRANSPONDER

Xiaoqiang Gu, Wentao Lin, Simon Hemour, and Ke Wu

Submitted to the *IEEE Transactions on Microwave Theory and Techniques*

This work proposes to enlarge the maximum readout distance of battery-free harmonic transponders through a careful Schottky diode selection and a consideration of low-temperature operations. Diode SMS7621 is identified to deliver lower conversion loss (CL) of harmonic transponders based on a diode selection guide. Moreover, an analytical method for studying temperature effects on the transponder CL performance is introduced and derived with satisfactory accuracy. A diplexer inserted in the harmonic transponder design can help reduce the antenna number. To mitigate matching difficulties at both fundamental and second-harmonic frequencies, a third-order diplexer is developed to enhance its bandwidth performance. Experimental verification has shown that low-temperature operations can effectively reduce the CL of the SMS7630-based harmonic transponder, thus increasing its readout distance. Specifically, its maximum readout distance at −40 ºC has increased by more than 10 %, from 6.4 m to 7.1 m, compared with that at +40 ºC. A complete harmonic transponder based on SMS7621, with dimensions of 85 mm × 45 mm, has reached a maximum readout distance of 8 m when the fundamental frequency is 3.5 GHz.

7.1 Introduction

Rapid development of the Internet of Things (IoT) has reshaped wireless sensing techniques to meet the requirements of the explosive growth in sensor nodes [157-159]. IoT-based radiofrequency (RF) and wireless sensing starts playing an increasingly critical role in our day-to-day lives, like human activity recognition [160], structural monitoring [161], smart agriculture and farming [162], etc. As one cornerstone of wireless sensing techniques, RF identification (RFID) is a well established and developed technology, already applied in many scenarios [163], [164]. The operating principle that underpins a typical RFID system lies in its transponders receiving RF

signals from an interrogator and sending back signals which carry certain information through modulation. The interrogator then decodes the signals from transponders. The signal transmission is generally arranged at the same frequency. However, this single-frequency-based sensing paradigm brings self-jamming and low clutter rejection problems in the presence of background reflections, such as walls and grounds [165]. Hence, implementing separate frequency bands for uplink and downlink transmissions is an attractive solution. One popular technique is the harmonic radar and transponder-based system [42, 166, 167]. In this case, transponders receive signals at the fundamental frequency (f_0) from a harmonic radar and send harmonics back, in most cases, a second harmonic ($2f_0$) [46]. Therefore, the harmonic radar can easily obtain useful information even in a cluttered environment.
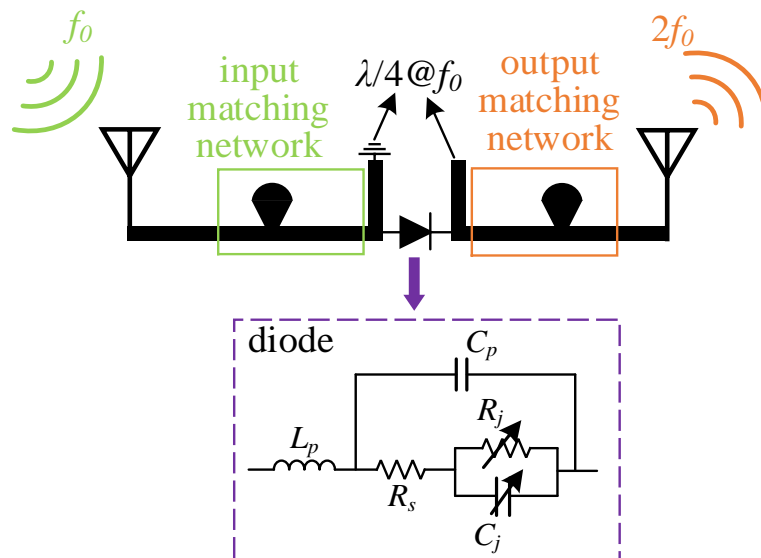
Figure 7.1 Schematic of a harmonic transponder utilizing Schottky diode with its Shockley model attached at the bottom. L_p, C_p, R_s, R_j, and C_j are packaging inductance, packaging capacitance, series resistance, nonlinear junction resistance, and nonlinear junction capacitance, respectively.

In such a harmonic radar and transponder-based wireless sensing system, harmonic transponders are preferred to possess features like small form factor, low cost, no battery, and long readout distance. Most chipless harmonic transponders utilize zero bias diodes to complete the frequency conversion from f_0 to $2f_0$ [15, 168]. Since the diode is the only nonlinear component in the transponder and its conversion loss (CL) accounts for a significant part of the total circuit loss, as shown in Figure 7.1, the selection and analysis of diodes are of great importance. Currently, the

Schottky diodes, which are cheap, technologically mature and highly reliable, are still the most commonly used nonlinear components in harmonic transponder design [151]. However, when considering the numerous Schottky diode candidates on the market, to identify a proper one to achieve lower transponder CL, i.e., a larger readout distance of transponders, is no easy task. Moreover, most device design is assumed for room-temperature operations by default. For passive devices, temperature variations do not bring severe consequences. Whereas, temperature variations are crucial for any Schottky diode or other active components-based devices/systems. For example, the performance of diode-capacitor Dickson charge pumps tends to degrade when operating temperature ramps up from 25 °C to 85 °C [118]. Moreover, for any Schottky diode-based rectifier, there exists an optimum temperature to obtain its peak efficiency at a fixed input power level [21]. As for the research domain of harmonic transponders, no temperature or thermal effects on transponders have been studied yet. Some works have implemented wireless temperature detection based on harmonic transponders with a temperature-dependent filter, but they do not consider the change of diode behaviors against the operating temperatures [169, 170]. Understanding the temperature effects on diode-based harmonic transponders is the first step to optimize the transponder to enlarge its readout distance according to its operating temperature.

This paper presents that Schottky diode-based battery-free harmonic transponders can obtain an enhanced readout distance thanks to a careful diode selection and a thorough understanding of low-temperature operations. In our previous work [13], an analytical method has been developed as a diode selection guide to pick out suitable candidates according to their SPICE parameters for achieving lower CL. Using the diode SMS7630 from Skyworks Inc., the harmonic transponder finally obtains a maximum readout distance of 7 m [13]. In this work, with the aid of this diode selection guide, the diode SMS7621 also from Skyworks has been identified to offer an even better CL performance when used for harmonic transponders. A detailed theoretical analysis is presented, and far-field measurements confirm that an SMS7621-based transponder reaches a maximum readout distance of 8 m. Furthermore, regarding temperature effects on harmonic transponders, our preliminary work has reported that low-temperature operations would reduce the CL of transponders based on the diode SMS7630 [171]. On top of this discovery, transponders based on the SMS7630 and SMS7621 are studied and compared in this work. As discussed above, the SMS7621-based harmonic transponder has lower CL at the same input power level compared to

its SMS7630-based counterpart. However, measurements have shown that the low-temperature operation is more advantageous for the SMS7630-based harmonic transponder. The maximum readout distance of an SMS7630-based transponder has increased by 0.7 m (more than 10 %) at −40 ℃ versus at +40 ℃. Such an advantage thanks to low-temperature operations for battery-free harmonic transponders can find potential opportunities in certain application scenarios, like cold chain storage and transport.

7.2 Diode Selection and Temperature Effects

7.2.1 Diode Selection
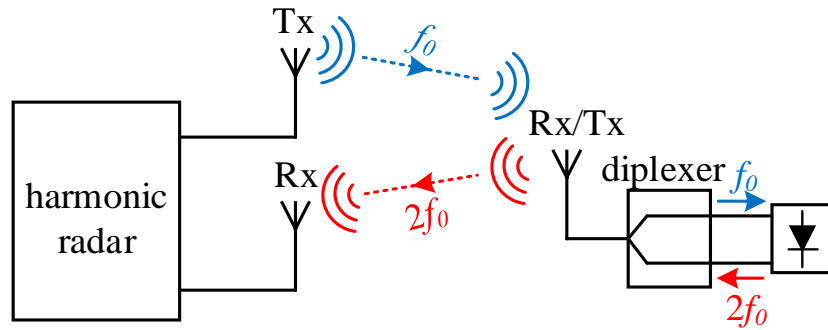
Figure 7.2   Operation principle of harmonic radar and transponder-based sensing system. A diplexer is introduced to reduce the number of transponder antennas.

As can be seen in Figure 7.2, the frequency conversion of harmonic transponders relies solely on the diode. Meanwhile, the total loss of harmonic transponders is heavily dependent on the diode CL, which further determines the transponder readout distance. Hence, the most critical aspect of designing a transponder lies in choosing a suitable diode. The conversion efficiency η of a harmonic transponder from the fundamental power P_{f_0} to the desired second-harmonic power P_{2f_0} can be summarized as [13]:

$$\eta = \frac{P_{2f_0}}{P_{f_0}} = \frac{P_{f_0}}{2} \cdot \left(\frac{\Re_{I0}^2}{4} + \frac{(\omega_0 C_{j0} M R_{j0})^2}{V_j^2} \right) \cdot \text{real}\left(\frac{Z_p^* \cdot Z_p}{Z_p^* + R_s + Z_{out}} \right) \tag{7.1}$$

where $\Re_{I0}$ is the diode zero bias current responsivity and can be calculated by:

$$\mathfrak{R}_{I0} = \frac{q}{2nkT} \tag{7.2}$$

Parameters appearing in both (7.1) and (7.2) are defined and listed in Table 7.1.

Table 7.1 Definitions of parameters in (7.1) and (7.2)

Parameters	Definitions
ω_0	angular frequency
C_{j0}	zero bias nonlinear junction capacitance
M	grading coefficient
R_{j0}	zero bias nonlinear junction resistance
V_j	junction potential
Z_p	impedance of a parallel $R_j \mathbin{//} C_j$ circuit of the diode
Z_{out}	impedance of the output port
q	electron charge
n	ideality factor
k	Boltzmann constant
T	operating temperature (in Kelvin)

For increasing the conversion efficiency η, or in other words, reducing the CL at a particular input power level, deductions can be easily obtained regarding some SPICE parameters according to (7.1). For example, a diode with smaller V_j and R_s but larger M is desired, which is conspicuous. However, for the two most crucial SPICE parameters, I_s (inversely proportional to R_{j0}) and C_{j0}, a more detailed investigation is required. With the aid of our previously proposed method, a diode with smaller I_s and C_{j0} can also mitigate CL [13]. Previously, the SMS7630, popular in low-power energy rectifier designs, has been proved to be a better choice for building a passive harmonic transponder. It improves CL by more than 10 dB compared to the state-of-the-art works at an input power level of −30 dBm [13]. In this work, by comparing SPICE parameters of multiple diodes, SMS7621 has been identified as a candidate that can potentially outperform SMS7630 for transponder design following the above guideline of diode selection. Table 7.2 summarizes key SPICE parameters of both diodes.

Figure 7.3 shows the CL results as a function of the input power of both diodes SMS7630 and SMS7621. The fundamental operating frequency is set at 3.5 GHz. Results from the Advanced Design System (ADS) harmonic balance simulator and calculated results using our proposed method have been shown for comparison. In the same graph, the energy harvesting efficiency

results of both diode-based rectifiers are also displayed. Unlike the frequency conversion of harmonic transponders from f_0 to $2f_0$, energy harvesting converts f_0 into dc, reflecting another aspect of diode nonlinearity. In Figure 7.3, the diode SMS7630 is a better candidate for low-power rectifier design and shows a good performance in the harmonic transponder as well. Whereas, the diode SMS7621, which obviously is not suitable for the rectifier design in this low-power range, decreases the CL roughly by 8~10 dB as compared to SMS7630 if employed in the transponder design within the input power range of interest. The presented theoretical analysis does not consider the insertion loss of a matching network and transmission lines.

Table 7.2 Key SPICE parameters

Parameters	SMS7630-079LF	SMS7621-079LF
C_{j0} (pF)	0.14	0.1
I_s (A)	5E-6	4E-8
R_s (Ω)	20	12
n	1.05	1.05
V_j (V)	0.34	0.51
M	0.4	0.35
C_p (pF)	0.16	0.15
L_p (nH)	0.7	0.7
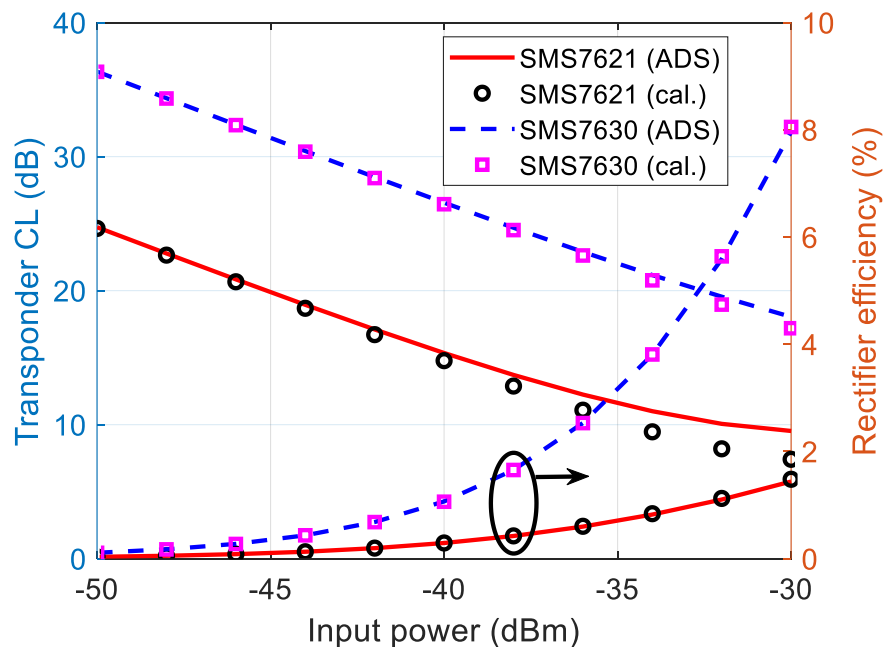
Figure 7.3 Performance comparison of diode SMS7630 and SMS7621 embedded in passive harmonic transponders and low-power rectifiers.

7.2.2 Temperature Effects

Operating temperature (T) has a significant impact on Schottky diodes that rely on thermionic emission [172]. From the SPICE parameter perspective, I_s, V_j, and C_j are three temperature-dependent parameters [120]. If T_r is defined as room temperature (25 °C), the temperature-dependent saturation current $I_s'(T)$ would become:

$$I_s'(T) = I_s \times \left(\frac{T}{T_r}\right)^{\frac{Xti}{n}} e^{(1-\frac{T_r}{T})\cdot\frac{Eg\cdot q}{nkT_r}}$$

(7.3)

where Xti and E_g are the saturation current temperature exponent and energy gap, respectively. The intrinsic carrier concentration $n_i(T)$ needs to be defined in advance in order to obtain the temperature-dependent junction potential $V_j'(T)$ [120], [123]:

$$n_i(T) = 1.45 \times 10^{10} \cdot \left(\frac{T}{300.15}\right)^{1.5} \times e^{\left(\frac{3.7\times10^{-3}\cdot q}{2k} - \frac{1.16-\frac{7.02\times10^{-4}\times T^2}{T+1108}\cdot q}{2kT}\right)}$$

(7.4)

Then, $V_j'(T)$ can be expressed by:

$$V_j'(T) = V_j \times \frac{T}{T_r} + \frac{2kT}{q} \times ln\left(\frac{n_i(T_r)}{n_i(T)}\right)$$

(7.5)

Temperature-dependent nonlinear junction capacitance $C_{j0}'(T)$ is defined as:

$$C_{j0}'(T) = C_{j0} \times \left(1 + M \times \left[1 + 4 \times 10^{-4} \times (T - T_r) - \frac{V_j'(T)}{V_j}\right]\right)$$

(7.6)

The diode SMS7621 is taken as an example to show how its three parameters change as a function of operating temperature from −40 °C to +40 °C, which is presented in Figure 7.4. As can be observed in Figure 7.4 (a), I_s demonstrates a drastic decrease at lower temperatures. The diode zero bias junction resistance $R_{j0} = nkT/qI_s$ is inversely proportional to I_s, and its change has also been attached in the same graph. With a lower operating temperature, R_{j0} would increase to a higher level (about an order of magnitude every 20 degrees). Figure 7.4 (b) illustrates the temperature

response of two other parameters, C_{j0} and V_j, whose variations are relatively minor. C_{j0} becomes smaller and V_j happens to be larger at lower temperatures.
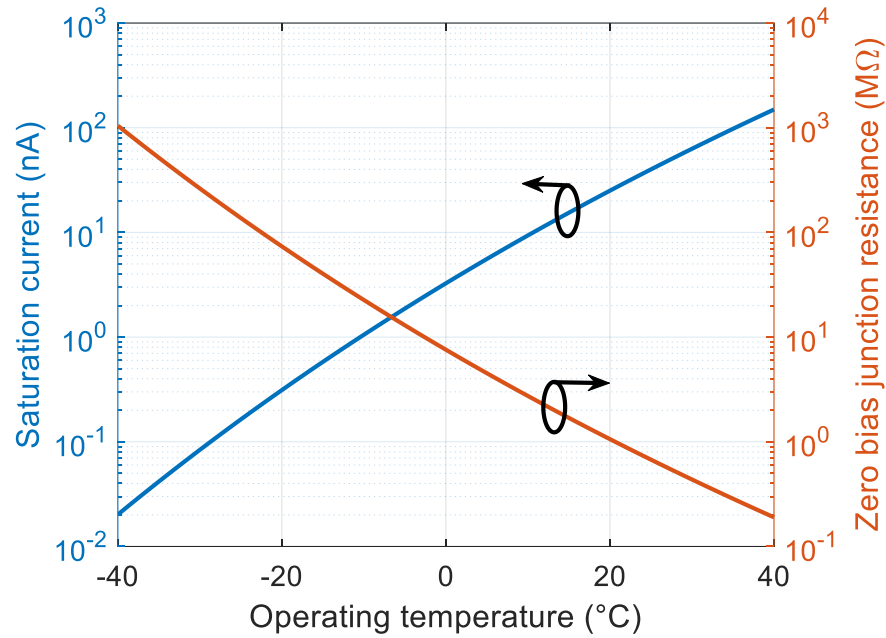
(a)
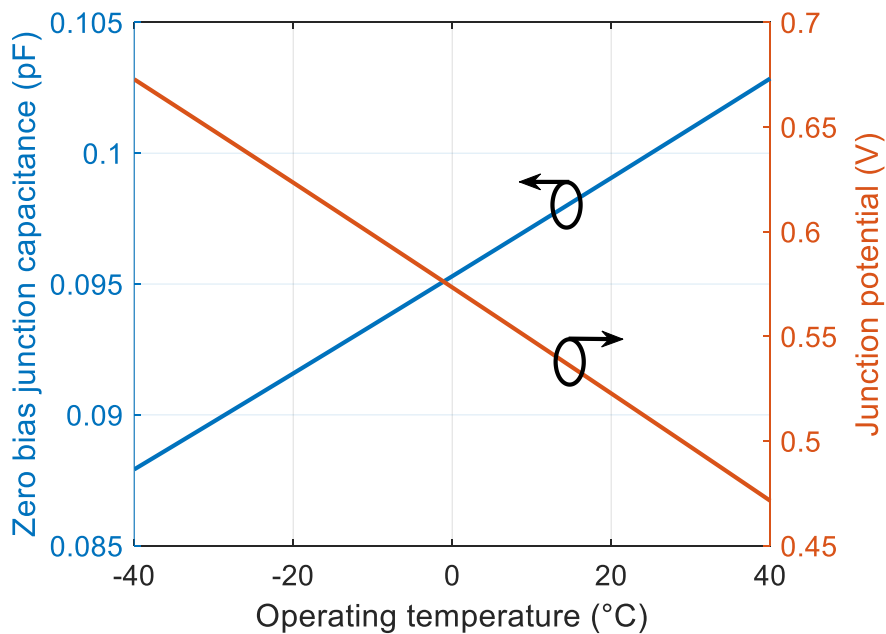
(b)

Figure 7.4   Temperature-dependent SPICE parameters of SMS7621 change as a function of operating temperature. (a) I_s and R_{j0}; (b) C_{j0} and V_j.

As the dominant factors associated with the CL performance of transponders, both diode parameters I_s and C_{j0} decrease at a lower temperature. According to the diode selection guide mentioned above, CL can be lowered at a lower temperature. Thus, both diodes SMS7630 and SMS7621 are selected to study their CL performance under different temperature conditions. By introducing temperature effects into the CL evaluation model, as addressed in [13], the calculated CL results are illustrated in Figure 7.5 (a) as well as the ADS harmonic balance simulation data. The CL reduction due to low-temperature operations is more obvious for the SMS7630-based transponder, which is around 6.5 dB when the operating temperature declines from +40 °C to −40 °C. Whereas, this value is only about 1 dB for the SMS7621-based transponder. Such an observation can be further illustrated by Figure 7.5 (b), which shows the coverage area of operating point for both diode-based transponders with temperature variations. For each transponder, the arrow marks the moving direction of operating points when temperature decreases. It can be clearly seen from Figure 7.5 (b) that the SMS7630-based transponder covers a range with larger CL differences. Its moving direction is along the gradient of the CL change, showing a steep slope. Conversely, the CL response of the SMS7621-based transponder is more stable with a flat slope, as shown in the same graph.

(a)
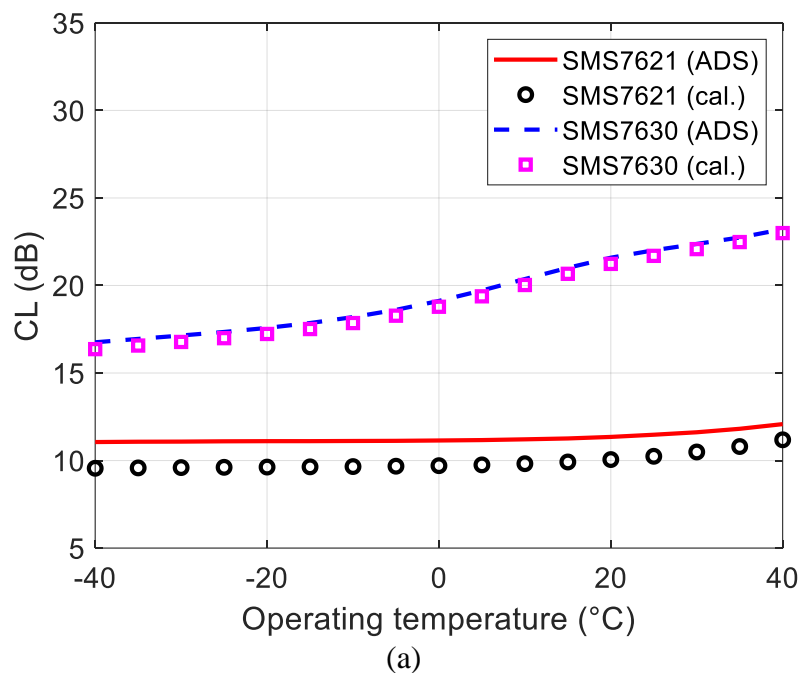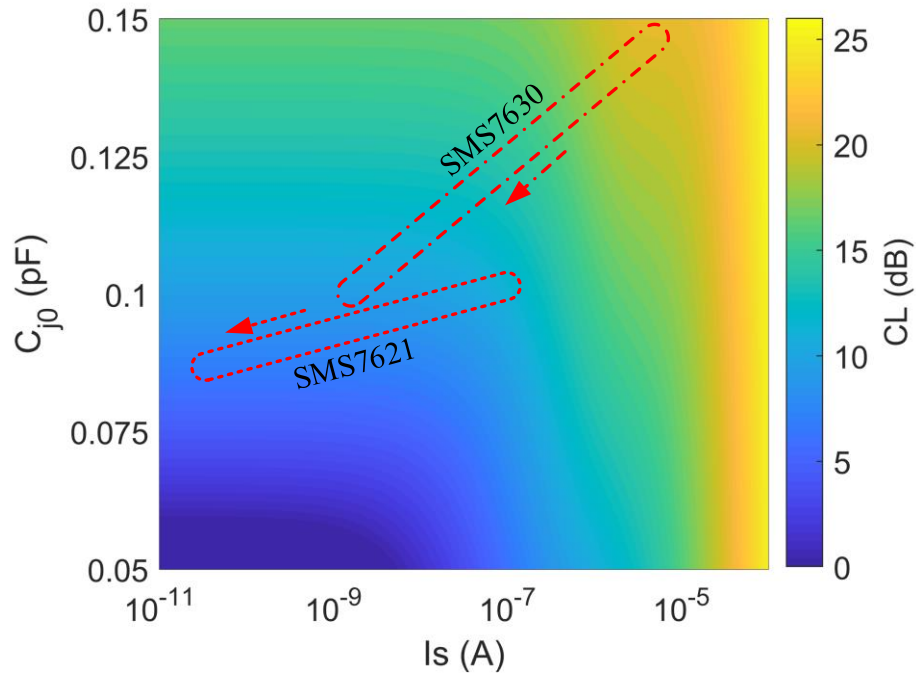
(b)

Figure 7.5 (a) Calculated CL results of both SMS7621- and SMS7630-based harmonic transponders, as well as ADS simulation results in comparison. (b) Coverage area of operating point for both transponders versus temperature variations. For both plots, the input power of transponders is at −35 dBm.

To understand why both Schottky diodes behave differently as a function of operating temperatures, an analytical method is employed to investigate the working principle of diode nonlinearity in the process of frequency conversion. For Schottky diodes, nonlinearity originates from the junction resistance R_j and capacitance C_j, which both contribute to the frequency conversion but presumably in different proportions. Figure 7.6 (a) and (c) present the ratio of converted second-harmonic power due to capacitive nonlinearity (C_j) over the total converted power versus operating temperature (from −40 °C to +40 °C) and injection power (from −50 dBm to −30 dBm) for SMS7621- and SMS7630-based transponders, respectively. Under the same temperature and power conditions, the CL variations as a result of resistive and capacitive nonlinearity for both cases are illustrated in Figure 7.6 (b) and (d).

As can be seen in Figure 7.6 (a), the capacitive nonlinearity of SMS7621 is obviously dominant in frequency conversion. Although a significant increase of CL due to resistive nonlinearity is

captured with decreasing temperatures (Figure 7.6 (b)), such influence on the overall CL responses is almost negligible. Hence, the CL variations as a result of capacitive nonlinearity become our primary focus. In Figure 7.6 (b), the capacitive nonlinearity leads to small reductions in CL. Such a trend eventually results in the CL of SMS7621-based transponder having small variations as a function of operating temperature (Figure 7.5 (a)).

(a)
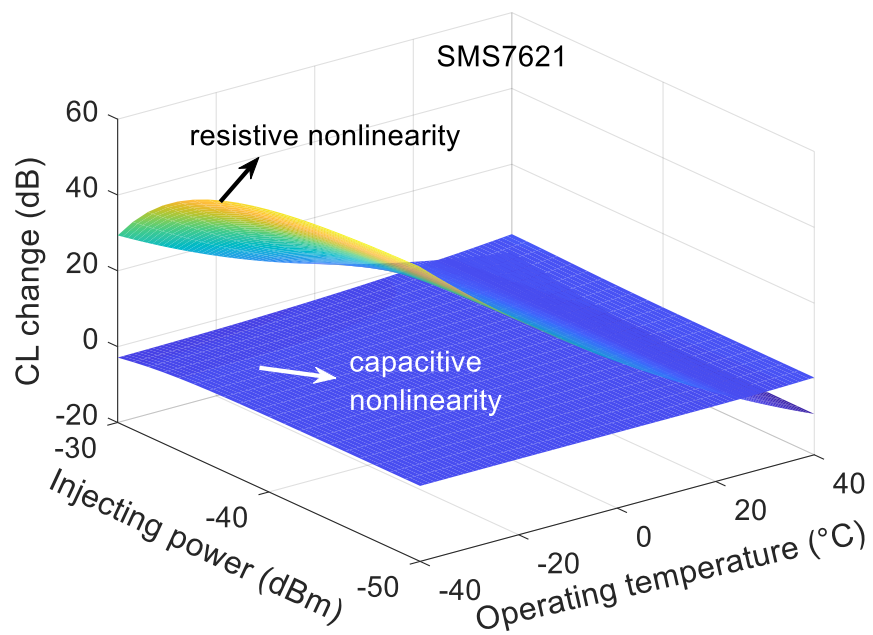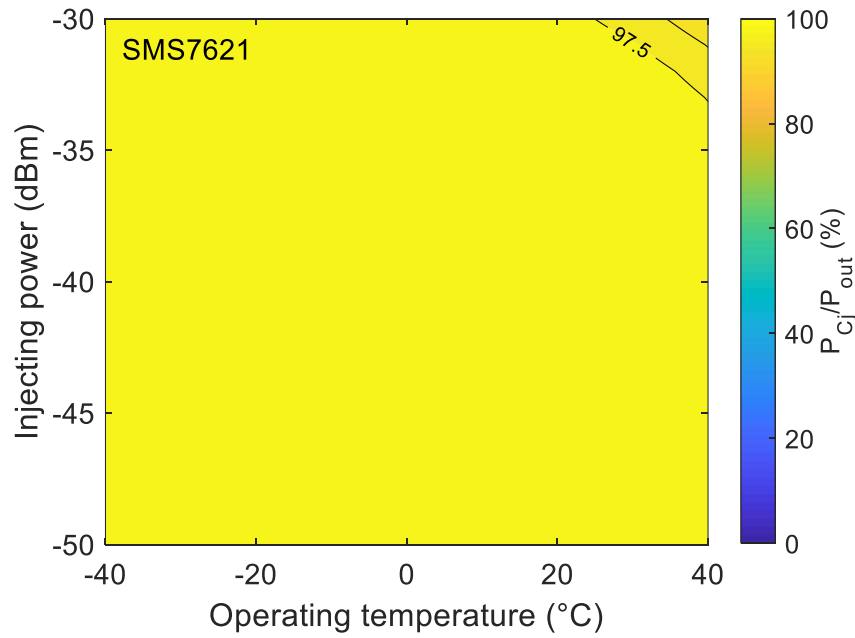
(b)
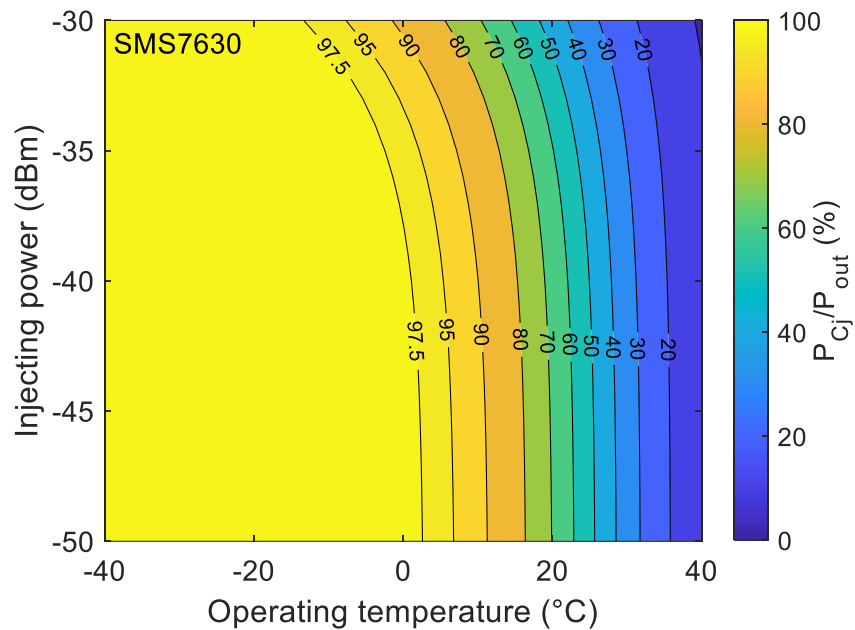
(c)
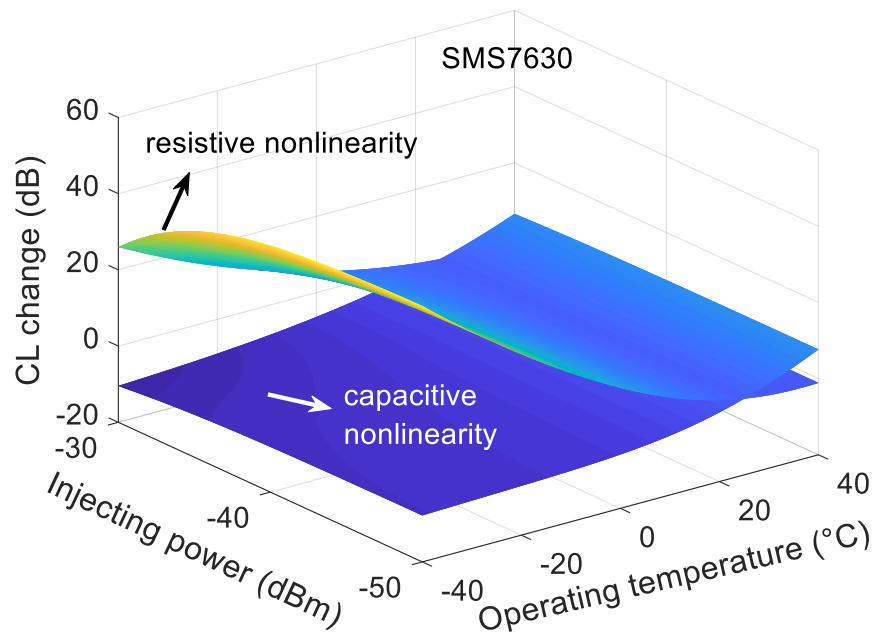
(d)

Figure 7.6 Ratio of second-harmonic power due to capacitive nonlinearity (C_j) over total converted power as a function of operating temperature (−40 °C to +40 °C) and injection power (−50 dBm to −30 dBm): (a) SMS7621-based transponder and (c) SMS7630-based transponder. Colorbar scale has been kept the same for both graphs. CL change due to resistive and capacitive nonlinearity in

the same range: (b) SMS7621-based transponder and (d) SMS7630-based transponder. The reference temperature is at 25 °C (room temperature).

In comparison, both diode capacitive and resistive nonlinearity of the SMS7630 contributes to the frequency conversion, especially when the operating temperature is above 20 °C, as seen in Figure 7.6 (c). Note that the above two types of nonlinearity have opposite responses on the CL changes versus the operating temperature, which is similar to the case of SMS7621, as shown in Figure 7.6 (d). The CL decreases at a fast rate due to the capacitive nonlinearity when the temperature is above 0 °C, whereas the CL ramps up slowly as a result of resistive nonlinearity in the same temperature range. As a combination shown in Figure 7.5 (a), the overall CL of SMS7630-based transponder presents a steep decreasing slope when the operating temperature is above 0 °C. However, when the operating temperature dips below 0 °C, the junction capacitance becomes a dominant contributor to the frequency conversion (Figure 7.6 (c)). Since the CL change rate becomes relatively low against the operating temperature (Figure 7.6 (d)), the overall CL of the SMS7630-based transponder continues to decrease, though with a flatter slope, when the operating temperature is below 0 °C, as shown in Figure 7.5 (a).

Next, Figure 7.7 presents the overall CL of SMS7621- and SMS7630-based transponders against the operating temperature and injecting power. Consistent with the above plots, the input power level is set from −50 dBm to −30 dBm, and the operating temperature is from −40 °C to +40 °C. In this power range, the SMS7621-based transponder has a lower CL, with its maximum under 25 dB. By contrast, the overall CL of SMS7630-based transponder is relatively larger, and its minimum value reaches 11.6 dB. However, when temperature decreases at a fixed input power level, the SMS7621-based transponder demonstrates a smaller CL reduction, which corresponds to the results in Figure 7.5 (a). In comparison, a noticeable CL change due to the temperature variations in the SMS7630-based transponder has been visualized more clearly in Figure 7.6 (b). Such observations are consistent with our above analysis.
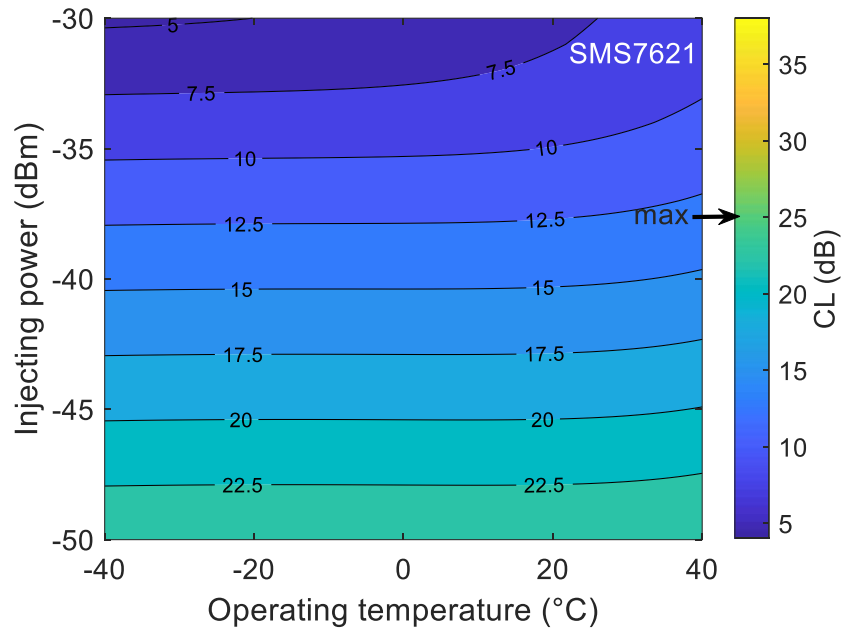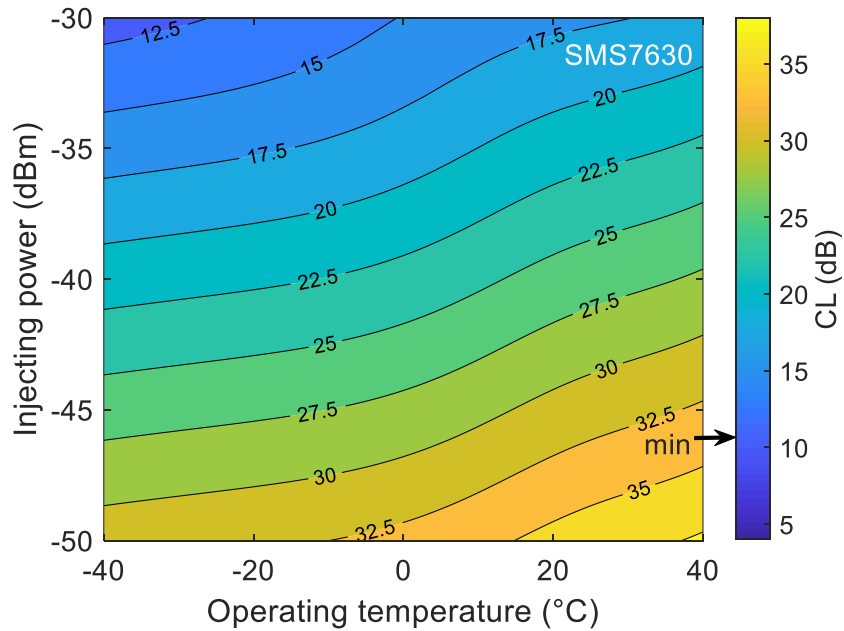
Figure 7.7 2-D mapping of transponder CL versus input power and operating temperature. (a) SMS7621-based transponder; (b) SMS7630-based transponder. Colorbar scale has been kept the same for both graphs.

7.3 Bandwidth Enhancement of Diplexer
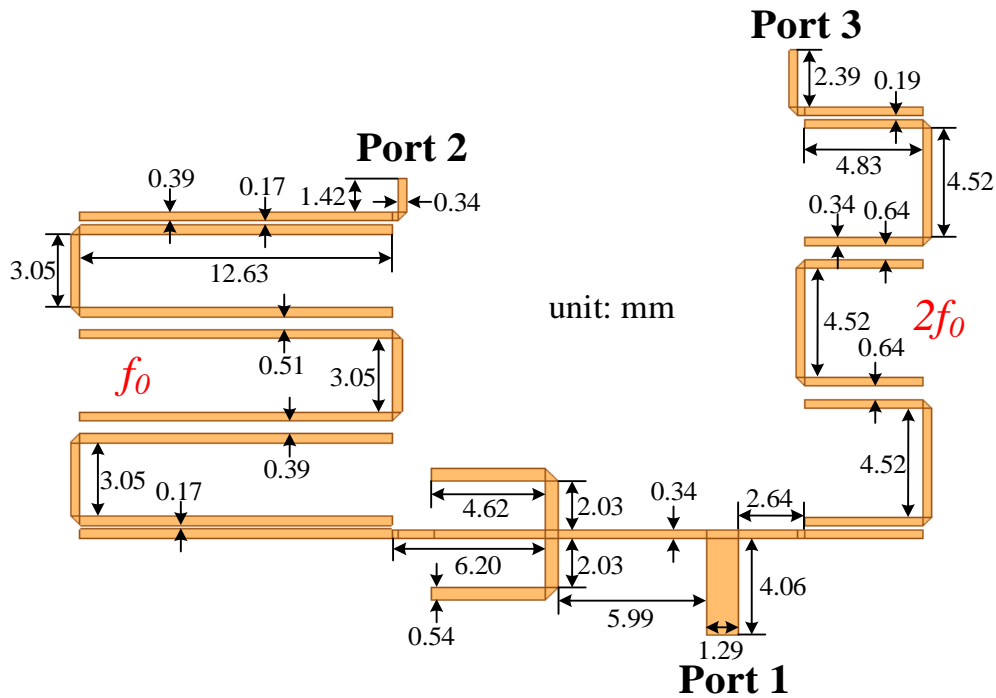
(a)
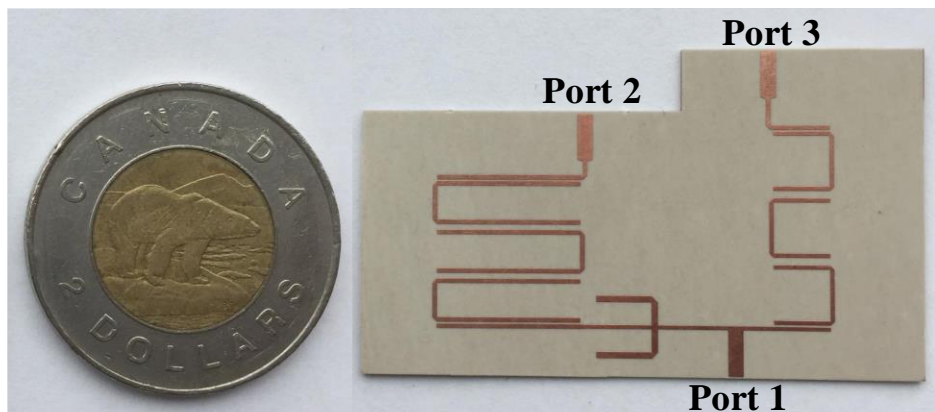
(b)

Figure 7.8 (a) Schematic of the third-order hairpin diplexer with dimensional parameters attached; (b) Photo of the experimental prototype.

For such harmonic transponders, limited bandwidths at f_0 and $2f_0$ would make fabrication error sensitive. For bandwidth enhancement, a third-order diplexer is developed, as shown in Figure 7.8. It contains one input port (port 1) and two output ports, of which port 2 operates at 3.5 GHz, and

port 3 at 7 GHz. Both passbands are designed based on microstrip half-guided-wavelength resonators. To improve the isolation between ports 2 and 3, a balanced stub is placed beside port 1 near the resonate structure of the low passband to mitigate the leakage of the second-harmonic power into port 2. An optimized schematic of this diplexer with physical dimensions attached is presented in Figure 7.8 (a). Figure 7.8 (b) shows a photo of the experimental prototype.
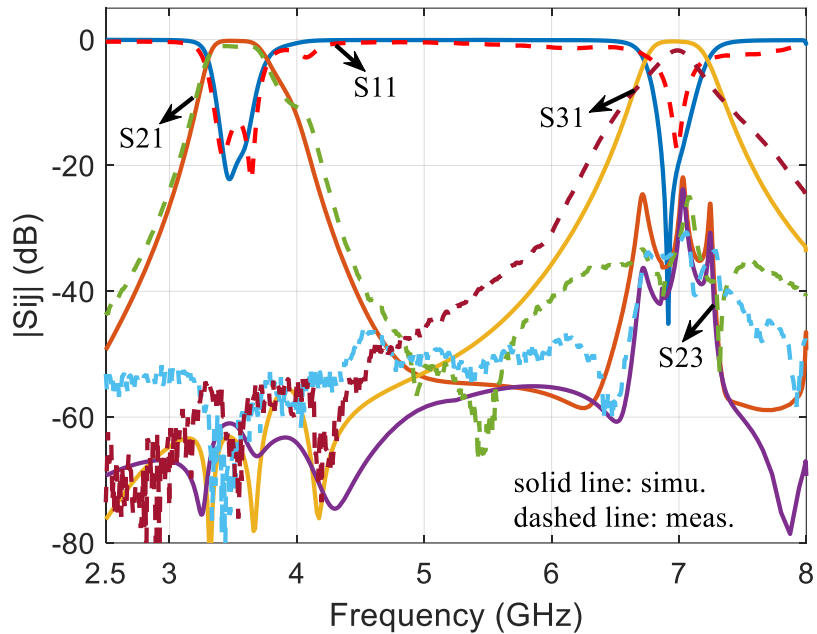
Figure 7.9 Simulated and measured performance of the proposed third-order diplexer.

Both simulated and measured results are demonstrated in Figure 7.9 for comparison. As seen in the graph, the response of the lower and upper channels does not present the same performance compared to the simulation. This is mainly because the physical external couplings are under and over the required coupling strength at f_0 and $2f_0$, respectively, due to fabrication errors. Despite some differences, both bands can effectively transfer more than 90 % energy with no center frequency shifting. Compared to our previous work on the single resonator-based diplexer [42], [13], the proposed third-order hairpin diplexer has extended the 3-dB bandwidth to improve the tolerance of systematic integration with other parts. Specifically, the measured fractional bandwidths of f_0 and $2f_0$ are 12.6 % and 6.1 % for the third-order hairpin diplexer, respectively. By contrast, the respective values for the single resonator-based diplexer are 3.1 % and 4.3 %. Hence, the introduction of this third-order hairpin design has enhanced the bandwidths at f_0 and

$2f_0$ by 306.5 % and 41.9 %, respectively. Moreover, the measured isolation between ports 2 and 3 are at least 24.5 dB in the entire band.

7.4 Measurement Results & Discussion

The substrate used for transponder fabrication is the Rogers RT/duroid 6002 with 0.508-mm thickness and 18-μm copper cladding. A complete harmonic transponder based on the SMS7621 is fabricated with dimensions of 85 mm × 45 mm, as shown in Figure 7.10 (a). It is optimized at room temperature 25 ℃ and contains both the tranponder antenna and circuit. For the transponder antenna, the dual-band spiral slot antenna proposed in our previous related work is utilized here [13]. Its dual-band operation covers both fundamental (3.5 GHz) and second-harmonic frequency (7 GHz) bands in this work and achieves an enhanced bandwidth performance. Also, it has a gain of 4 dBi at 3.5 GHz and 3.8 dBi at 7 GHz. For better fundamental signal reception, this transponder antenna features circularly polarized and omnidirectional operation. Moreover, as shown in Figure 7.10 (b), four prototypal transponders based on diodes SMS7630 and SMS7621 are realized, which are optimized at −40 ℃ and +40 ℃, respectively. Traditional L matching networks with stubs of uniform widths are replaced with radial stubs that can provide broader bandwidth and better fabrication tolerance [173]. Dimensional information related to the matching design has been indicated in Figure 7.10 (c) together with Table 7.3.
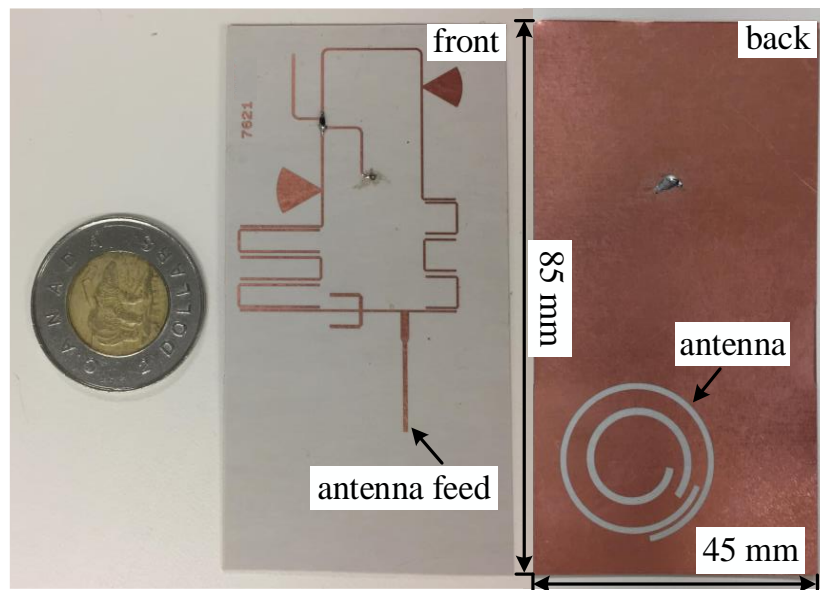
(a)
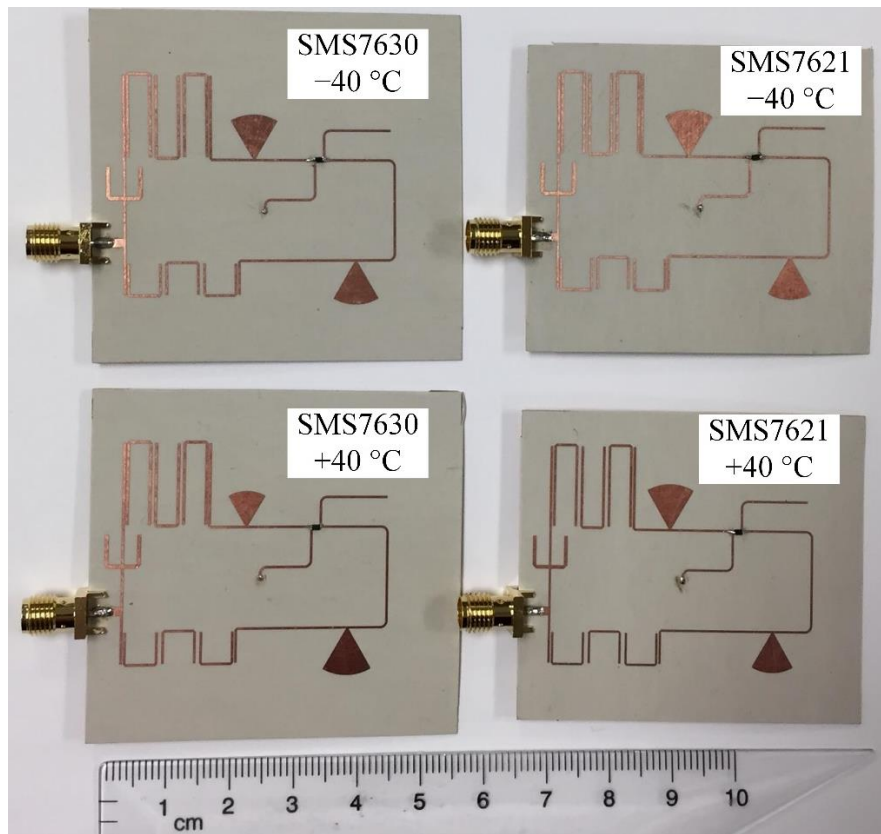
(b)
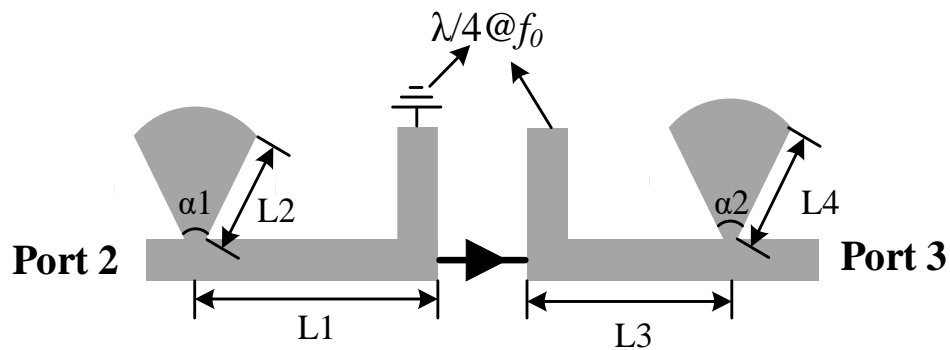
(c)

Figure 7.10 Photographs of experimental prototypes: (a) complete harmonic transponder based on SMS7621 optimized at room temperature (+25 °C); (b) harmonic transponder circuits based on SMS7621 and SMS7630 optimized at −40 °C and +40 °C, respectively. (c) Radial stubs-based matching networks. Dimensions are listed in Table 7.3.

Table 7.3 Dimensions of matching networks in Figure 7.10 (c)

	L1	L2	$\alpha1$	L3	L4	$\alpha2$
SMS7630 (+40 °C)	9.82	5.37	60°	31.38	7.24	60°
SMS7630 (−40 °C)	9.16	6.88	60°	31.93	6.73	60°
SMS7621 (+40 °C)	9.69	7.03	60°	32.04	6.24	60°
SMS7621 (−40 °C)	9.45	7.16	60°	32.07	6.51	60°

Length unit: mm

To investigate temperature effects on the transponder CL under various operating temperature conditions, transponder prototypes in Figure 7.10 (b) are tested with a power compensation solution. Such a solution is introduced to compensate for the mismatch loss at the input port due to diode impedance change at different temperatures. Figure 7.11 presents the measurement setup. A temperature chamber (Model 105) from TestEquity is utilized to offer desired operating temperature conditions in a range of −40 ℃ to +130 ℃. Its internal temperature can be manually set and monitored using the front panel. Still, a thermometer is introduced in the measurement, with its thermocouple placed inside the chamber for a more precise temperature monitoring and control. The external RF power at the fundamental frequency is supplied by a vector network analyzer (VNA), which is crucial for conducting power compensation. Since the operating temperature has a significant influence on diode impedance, as shown in Figure 7.4, the matching conditions would degrade when the operating temperature shifts from our optimization (±40 ℃ in our case). To make sure that constant power injects into the transponder at different operating temperatures, the external power supply has to adjust its RF output dynamically according to the mismatch conditions. Therefore, the VNA plays a crucial role in this measurement. Once it is working in the continuous wave (CW) mode, the VNA can simultaneously read reflection coefficients and output single-frequency RF power. Note that the VNA does not conduct frequency sweeping in the CW mode as only one frequency point exists. In the measurement, the VNA can be adjusted to offer different levels of fundamental RF power to the transponder, thereby compensating for the mismatch loss according to its reflection coefficient. Also, the reflection coefficients at the second-harmonic frequency (7 GHz) are taken down afterward for power

compensation calculation during the post-process. Since the transponder has only one port, a hybrid coupler is necessary to split the input fundamental power and output second-harmonic power. Finally, the generated second-harmonic energy is directed to a signal analyzer, as shown in Figure 7.11. Note that all insertion loss of the cables and hybrid coupler has been de-embedded.
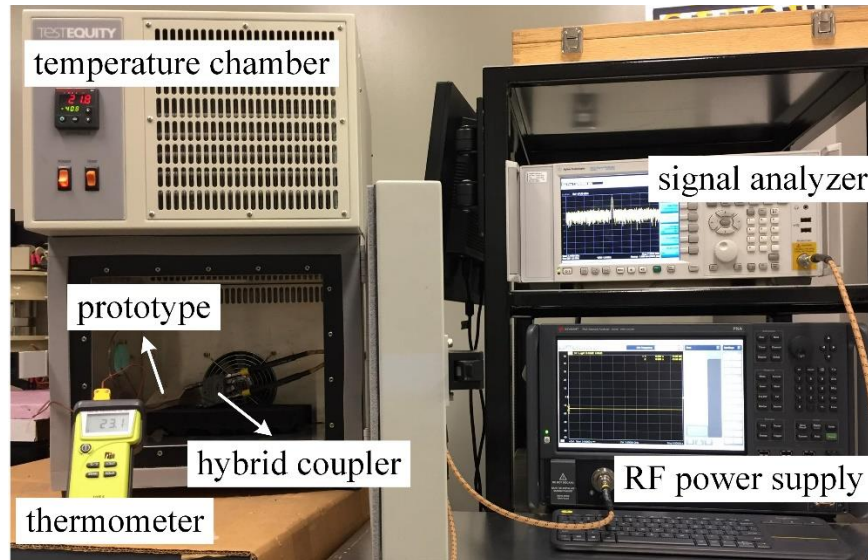
Figure 7.11   Measurement setup for studying the temperature effect on transponder CL performance while the operating temperature changes continuously.

Both transponders based on the SMS7630 and SMS7621 in Figure 7.10 (b) have been tested, with results displayed in Figure 7.12. The EM cosimulation results obtained by the ADS harmonic balance tool are also attached for comparison. The injected power into the transponders at each temperature is kept at −25 dBm after the power compensation. Such a power level is consistent with the received injected power in the far-field testing shown in Figure 7.14. Measurement results in Figure 7.12 for each diode-based transponder match the simulated ones reasonably well, although the measurement results are slightly higher.

Used in transponder design, the SMS7621 is proved to be a better choice than SMS7630 in terms of enhanced CL performance. For example, at the typical room temperature (+25 ℃), the CL of the SMS7621-based transponder is about 14.9 dB. For the SMS7630-based transponder, the value is roughly 19.3 dB, which is 4.2 dB higher. Consistent with the theoretical predictions, measurement results show a larger CL variation in the SMS7630-based transponder than its counterpart. Specifically, the CL result of the transponder based on the SMS7630 is reduced from

20.4 dB at +40 ℃ to 16.5 dB at −40 ℃, indicating a change of 3.9 dB under an 80 ℃ temperature variation. Under the same circumstance, the CL reduction of SMS7621-based transponder is only 1.7 dB, from 15.4 dB at +40 ℃ to 13.7 dB at −40 ℃.
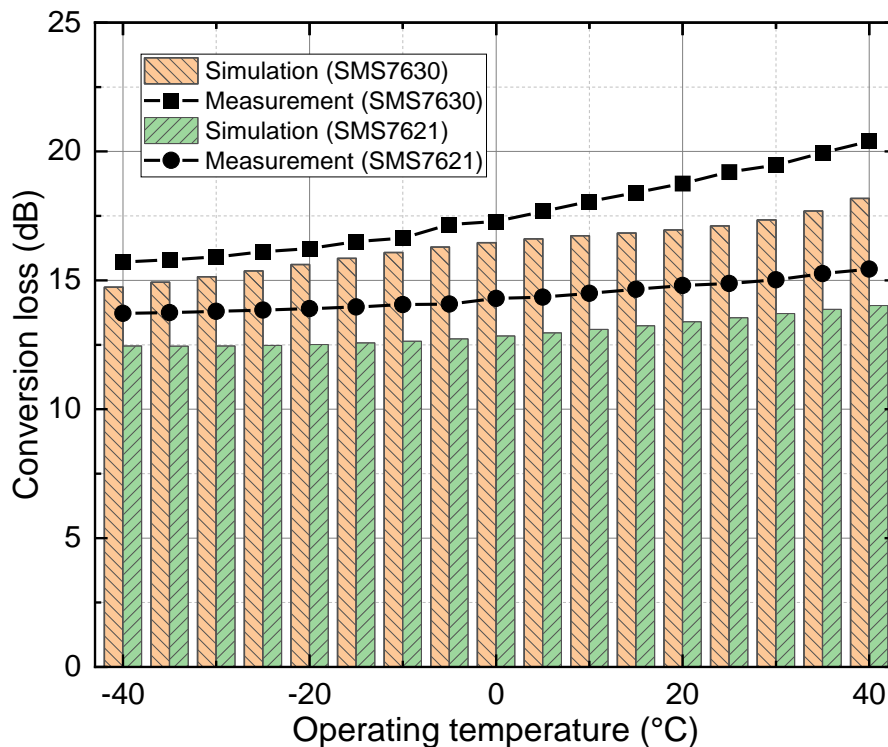
Figure 7.12 Comparison of measured and simulated CL results of transponders based on SMS7630 and SMS7621.

To investigate the readout distance for the above harmonic transponders, far-field testing is necessary. Separate transponder antenna and circuit parts are required to study the temperature effects on the maximum readout distance of transponders. A schematic diagram is presented in Figure 7.13 (a). Two horn antennas from ETS-Lindgren (model 3160-05 and 3160-06) are employed here for radar transmission and reception. Note that the horn antenna model 3160-05 still works well at 3.5 GHz after performing an experimental verification using VNA, although its operating frequency band is 3.95 GHz to 5.85 GHz according to its datasheet. Since any device inside the temperature chamber is shielded from electromagnetic waves, the transponder antenna must be placed outside the chamber for communications, as shown in Figure 7.13 (a). Whereas, the transponder circuit is put inside the chamber and its operating temperature can be adjusted. Corresponding to the schematic diagram, Figure 7.13 (b) demonstrates the real setup in our lab. A

signal generator acts as the fundamental-frequency power supply, and a signal analyzer displays the power levels of the received second-harmonic signal. These two instruments are connected with horn antennas models 3160-05 and 3160-06, respectively, functioning as a simplified basic harmonic radar. As for the transponder side, the transponder antenna is fixed outside the chamber facing the harmonic radar. The transponder circuit is placed inside the chamber. Moreover, a thermometer is also used here for temperature monitoring inside the chamber.
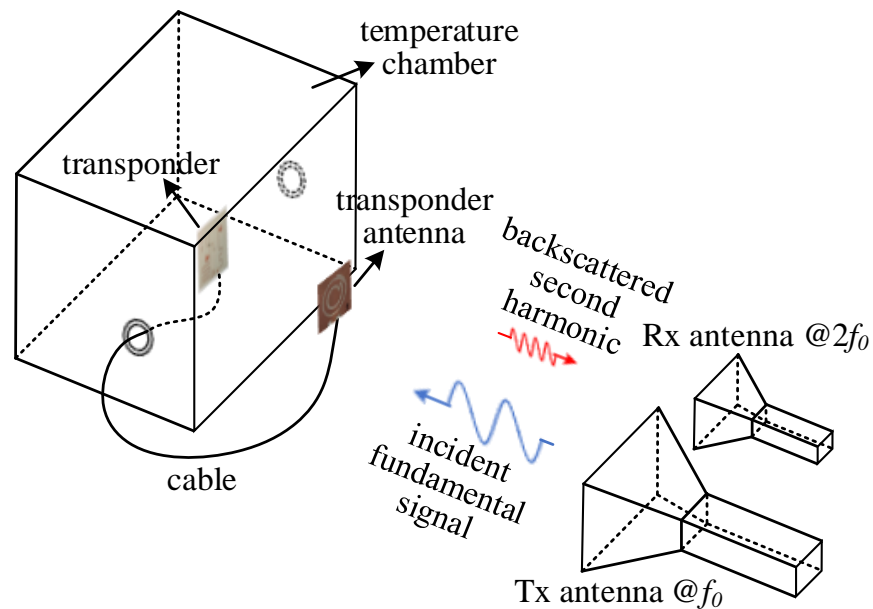
(a)
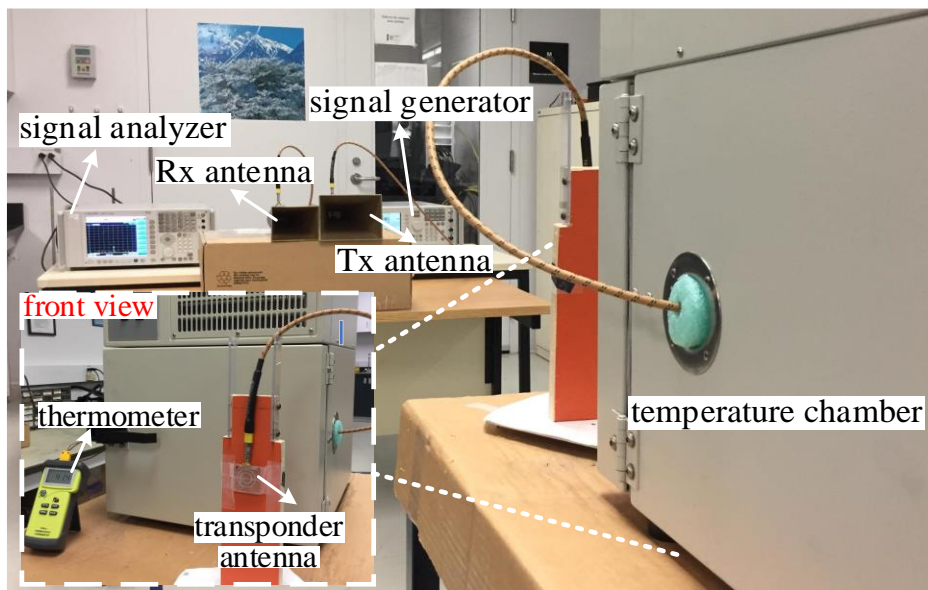
(b)

Figure 7.13 Measurement setup for investigating the enhancement of transponder readout distance due to low-temperature operations: (a) schematic diagram and (b) real setup in our lab.

A link budget analysis is used here to better present and compare results. This link budget calculation (in dB) is based on the Friis transmission equation [156]:

$$P_r = P_t + G_{ra}^t + TL_{f_0} + G_{tr}^r - CL + G_{tr}^t + TL_{2f_0} + G_{ra}^r \qquad (7.7)$$

All parameters in (7.7) have been defined in Table 7.4.

The transmission loss TL is defined as:

$$TL = 20 \times log\left(\frac{\lambda}{4\pi d}\right) \qquad (7.8)$$

where λ is the wavelength of the transmission signal, and d is the transmission distance.

Table 7.4 Definitions of parameters in (7.7)

Parameters	
P_r	Power received by radar @$2f_0$
P_t	Power transmitted by radar @f_0
G_{ra}^t	Gain of the radar Tx antenna
TL_{f_0}	Transmission loss @f_0 in space
G_{tr}^r	Gain of the transponder antenna @f_0
G_{tr}^t	Gain of the transponder antenna @$2f_0$
TL_{2f_0}	Transmission loss @$2f_0$ in space
G_{ra}^r	Gain of the radar Rx antenna

In the measurement, the signal generator, which is the power supply for the harmonic radar, is set to offer a power level of +25 dBm. The noise floor of harmonic radar is −100 dBm. For each harmonic transponder shown in Figure 7.10 (b), individual testing has been carried out with results shown in Figure 7.14. As mentioned above, a cable connection between the transponder antenna (outside the chamber) and the circuit part (inside) is essential. Thus, the transponder loss for the four transponders in Figure 7.14 contains extra cable loss. The complete transponder in Figure 7.10 (a) is measured at the room temperature condition. Unlike the measurement setup of the others,

this complete transponder requires no temperature chamber or cable connection, thereby eliminating extra influence on its maximum readout distance. To acquire link budget information, especially of the received power by transponders, the transponder antenna is effectively used in the measurement. Moreover, transponder loss information is obtained by previous separate circuit measurements. Note that for the complete transponder, the transponder loss data is estimated by measurement results of another SMS7621-based transponder circuit piece at room temperature. Besides the link budget information, the maximum readout distance information of each transponder has been included in Figure 7.14 for comparison.
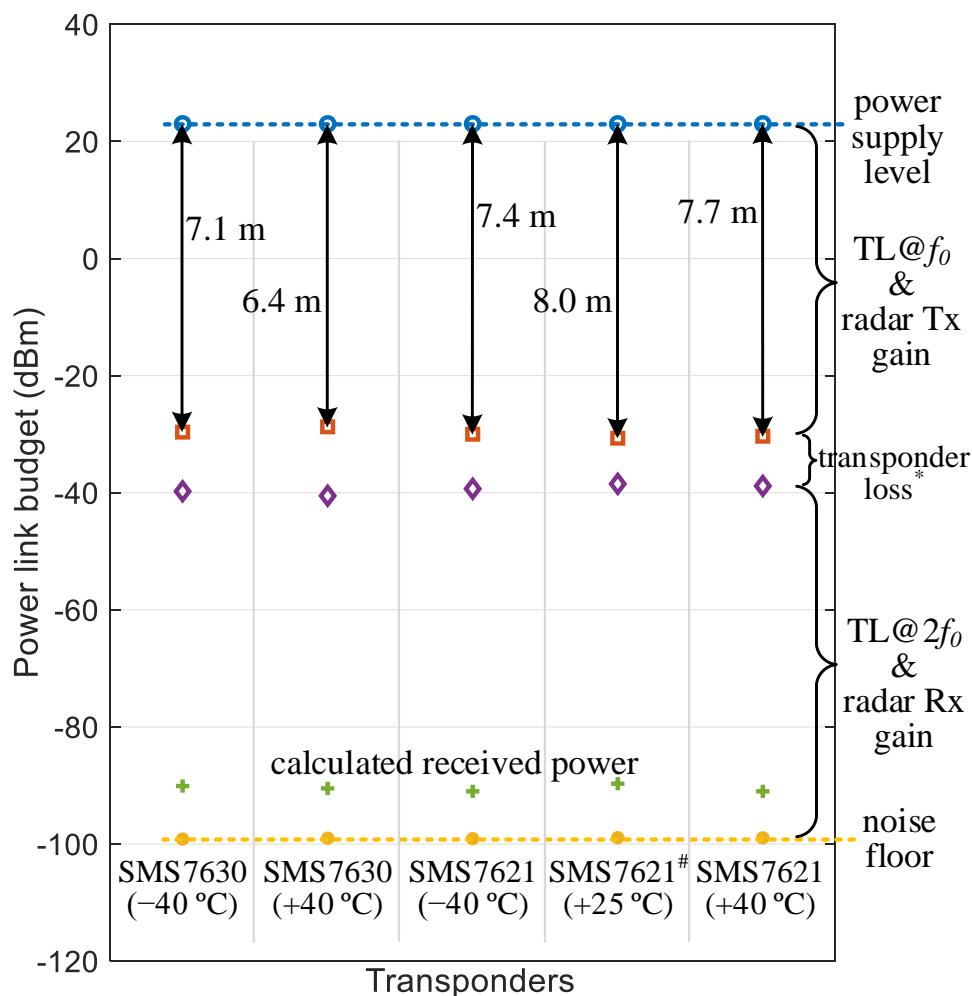
Figure 7.14 Link budget information for each prototypal transponder in Figure 7.10 (a) and (b). * Due to the special treatment in the setup where a cable is necessary, cable loss is included in the transponder loss for transponder circuits in Figure 7.10 (b). # The complete transponder in Figure

7.10 (a) is tested at room temperature without the chamber and cable connections, thereby no extra loss is included.

Since the operating temperature has a larger influence on the transponders built on the SMS7630, this effect has also been reflected in the maximum readout distance. A 0.7-m increase in the maximum readout distance has been observed in the SMS7630-based transponders. In contrast, this value is only 0.3 m for the SMS7621-based counterpart. Due to the cable loss included in the total transponder loss, the measured maximum readout distances of those four transponders with separate pieces have been slightly underestimated. As a complete design, the transponder optimized at room temperature, as shown in Figure 7.10 (a), shows a maximum readout distance of 8.0 m. Such observation indicates that CL enhancement plays a vital role in enlarging the maximum readout distances for battery-free harmonic transponders.

Finally, a comparison between this design and related works has been presented in Table 7.5. A figure-of-merit of the maximum detection distance FOM_d is defined to normalize harmonic transponder performance with different operating frequencies. By using FOM_d, it indicates that all harmonic transponders are tested in the same conditions: harmonic radar transmits fundamental power of +25 dBm; both radar Tx/Rx antennas have the same gain of 10 dBi; injecting power of harmonic transponder is −25 dBm; noise floor is −100 dBm; and fundamental and second-harmonic frequencies are 3.5 GHz and 7 GHz, respectively. Based on these assumptions, FOM_d can be calculated by:

$$\text{FOM}_\text{d} = \frac{d_1 + d_2}{2} = \frac{c}{2 f_0 \cdot 4\pi} \cdot \left(10^{\frac{P_t + G_{ra}^t + 25 + G_{tr}^r}{20}} + \frac{10^{\frac{75 - CL + G_{tr}^t + G_{ra}^r}{20}}}{2} \right) \tag{7.9}$$

where d_1 is the distance between the radar and the harmonic transponder to ensure injecting power into the transponder is −25 dBm. d_2 is the distance when the reflected second harmonic reaches the radar with a power level of −100 dBm (noise floor). FOM_d is a theoretical tool to assess transponder performance and has several assumptions, such as no insertion loss and a fixed injecting power of transponders (−25 dBm). Hence, this value is normally larger than the measured maximum readout distance.

As seen in Table 7.5, the SMS7621-based transponder has achieved a larger maximum readout distance (8 m) than the SMS7630-based counterpart (7 m). The low-temperature operation has enhanced the maximum readout distance for both diodes-based transponders, which is observed to be more obvious for the SMS7630-based transponder. Even with the cable loss included, the SMS7630-based transponder operating at −40 ℃ obtains a slightly larger maximum readout distance than at room temperature.

Table 7.5 Comparison between proposed designs and previous related works

	Op. freq. (GHz)	Size (mm×mm)	Diode	Max readout dist.* (m)	FoM$_d$ (m)
[102]	1.2 & 2.4	75 × 65	HSMS-2850	5.0	7.0
[43]	1 & 2	80 × 35	SMV2019	5.0	7.7
[155]	0.868 & 1.736	200 × 125	HSMS-2850	7.0	5.4
[174]	5.8 & 11.6	21 (dipole)	SMS7630	6.1	6.7
[13]	3.5 & 7	60 × 35	HSMS7630	7.0	12.0
This work	**3.5 & 7**	**85 × 45**	**HSMS7630**	**7.1 (−40 ℃)[#]**	**12.4**
This work	**3.5 & 7**	**85 × 45**	**HSMS7621**	**7.7 (−40 ℃)[#]**	**15.1**
This work	**3.5 & 7**	**85 × 45**	**HSMS7621**	**8.0**	**13.9**

 * Noise floor for each work may vary.

 [#] Transponder loss contains cable loss. The actual values will be larger.

7.5 **Conclusion**

The maximum readout distance of the battery-free harmonic transponders can be enlarged by selecting suitable Schottky diodes and by considering low-temperature operations. Based on a diode selection guide, the Schottky diode SMS7621 is identified for transponder design to reduce CL. Moreover, an analytical method for studying temperature effects on the harmonic transponders have been presented with details in this work. Low-temperature operations are found to be helpful in enhancing the maximum readout distance of such harmonic transponders. Experimental results demonstrate that the SMS7621-based harmonic transponder achieves a maximum readout distance

of 8 m at room temperature, which is 1 m further than that of its SMS7630-based counterpart. Whereas, the low-temperature operation brings less advantage to the SMS7621-based transponder. Its maximum readout distance increased from 7.4 m at +40 ℃ to 7.7 m at −40 ℃, indicating a 0.3-m enhancement due to low-temperature operations. In contrast, this distance enhancement for the SMS7630-transponder is larger (0.7 m or more than 10 %) under the same temperature variations. Such a readout distance enhancement thanks to low-temperature operations can help battery-free harmonic transponder more easily find potential applications in the cold chain storage and transport industry.

CHAPTER 8   CONCLUSION AND FUTURE WORKS

8.1 Conclusion

This Ph.D. thesis proposes, presents and discusses two mainstream techniques to enable battery-free IoT sensors: far-field WPT and harmonic backscattering. Both techniques are compatible with the deployment schemes of recycling ambient RF energy and collecting dedicated wireless RF energy delivery for various application scenarios. Since the available input RF energy is often limited, high-efficiency circuits and systems for both far-field WPT and harmonic backscattering are of significance to energize IoT sensors.

For achieving the above primary goal, this thesis starts with a literature review of far-field WPT and harmonic backscattering techniques. Different frequency conversion mechanisms and related diode behaviors between these two techniques are studied and discussed in Chapter 2. Based on such an in-depth analysis, several measures to enhance the efficiency performance of far-field WPT and harmonic backscattering are proposed and studied. Finally, a possible reconfigurable design integrating far-field WPT and harmonic backscattering features is demonstrated at the end of this chapter.

As a critical step, getting a sense of how much available ambient RF energy exits in our environment is our reference for designing circuits and systems. To this end, Chapter 3 summarizes an outdoor density mapping of ambient RF energy made on Montreal Island, Canada. Different from the previously reported measurements focusing on fixed locations, this dynamic measurement was carried out along streets, roads, avenues, and highways, offering a global picture of ambient RF energy levels in urban and suburban areas for the first time. Measured results indicate that cellular communications bands (GSM/LTE850 and LTE700) have the highest average power level in the DT Montreal, whereas DTV signals are the highest in UT areas. Therefore, for ambient RF energy recycling, cellular communication and DTV bands should be given priorities in DT and UT Montreal areas. A separate stationary measurement in DT Montreal was conducted to study how foot traffics or pedestrians could affect ambient RF power levels. Based on the results, no visible power variations are observed for both cellular communication and DTV bands. Several suggestions regarding ambient RF energy harvesting are then offered, following the discussions on measured results.

For predicting the conversion efficiency of Schottky diodes-based far-field WPT rectifiers, a closed-form model is developed in Chapter 4. It has successfully extended the dynamic power range up to approximately milliwatts (mW) level. Based on this analytical model, the thermal effects of Schottky diodes are introduced to study how operating temperatures influence diode-based rectifiers. Theoretical analysis has predicted that an optimum operating temperature exists for each different diode-based rectifier at a fixed power level. Such a claim is then supported by measurements. Operating at its optimum temperatures, the conventional SMS7630-based rectifier has achieved conversion efficiencies of 17.5 % at −30 dBm and 41.7 % at −20 dBm, respectively.

Due to the limited power density of ambient RF energy in free space, far-field WPT rectifiers are often difficult to deliver satisfactory efficiency performance, due to a positive correlation between conversion efficiency and input power level. Hence, introducing other types of ambient energy sources will be an attractive approach to leverage rectifying efficiency. Based on this idea, Chapter 5 describes an integrated rectifying platform that can collect both ambient RF and vibration energy simultaneously. An analytical method for study such a hybrid harvesting mode is developed first. Enhanced efficiency due to hybrid harvesting is revealed by theoretical analysis. Then, for experimental validation, a hybrid energy harvester with a compact credit-card size is designed. Measured dc output power rectified from hybrid harvesting mode is reported to be 1.16 and 1.97 times larger with diodes SMS7630 and HSMS-2850, respectively, when both RF and vibration energy sources are −40 dBm, compared to the conventional single RF harvesting mode. Besides the efficiency enhancement, this hybrid rectifier also exhibits a strong resilience, which can operate with either one or both ambient power sources.

The remainder of this Ph.D. thesis discusses how to reduce the conversion loss (CL) of harmonic transponders to achieve a larger readout distance. Chapter 6 first proposes a new architecture of fully passive harmonic transponders to reduce circuit profile. The operation principle of harmonic transponder requires receiving fundamental RF energy and transmitting a converted second-harmonic component. Thus, typically two antennas exist in harmonic transponders that oversee fundamental and second-harmonic frequencies, respectively. By introducing a diplexer in the topology, only one dual-band antenna is enough in this case. Besides the topological improvement, one analytical model for analyzing diode behaviors in harmonic transponders is proposed, and equivalent circuits at fundamental and second-harmonic frequencies are also demonstrated. This

model predicts that diode SMS7630 is a suitable diode candidate for harmonic transponder design. CL measurement results verify that the prototypal transponder based on SMS7630 shows a noticeable improvement over the state-of-the-art works. Furthermore, far-field measurements show that this transponder reaches a maximum readout distance of 7 m when the operating frequency is 3.5 GHz.

Chapter 7 reports an improvement over the work in Chapter 6. With the aid of the analytical model, diode SMS7621 has been further identified to potentially outperform SMS7630 in harmonic transponder design after a wide-range search of commercial diodes on the market. To mitigate design difficulties in matching networks at both fundamental and second-harmonic frequencies, a third-order diplexer is developed to enhance its bandwidth performance. Moreover, thermal effects on diode-based harmonic transponders have been included in this work. Analysis indicates that low-temperature operations will enlarge the maximum readout distance of harmonic transponders. Final measurements show that both SMS7630- and SMS7621-based harmonic transponders benefit from low-temperature operations. For example, the maximum readout distance of the SMS7630-based prototype has increased by 0.7 m (> 10 %) at −40 ℃ compared to that at +40 ℃. A complete harmonic transponder based on SMS7621 has reached a maximum readout distance of 8 m at 3.5 GHz.

8.2 **Future Works**

Efforts have been put into this Ph.D. thesis research to realize battery-free IoT sensors through far-field WPT and harmonic backscattering. However, more research works are still required, which can be summarized as below:

➢ During the density mapping of ambient RF energy in Montreal, the signal modulation factor has been neglected. Also, ambient RF energy in different seasons may be different. Since our measurement was carried out during Summer, a season when human activities are considered more active. Hence, similar mapping works in Autumn and Winter can be a good supplement for this set of measurements.

➢ Each diode-based rectifier has an optimum temperature, and outdoor operating temperature varies in a range of −25 ℃ to +30 ℃ in Montreal. So, it is recommended that an intelligent

rectifying system containing multiple diodes can be developed, which can choose the most suitable diode to realize high efficiency rectifying according to real-time operating temperatures.

➢ Multiple ambient energy sources exist in our daily life, such as RF, vibration, thermal and solar energy. A compact hybrid rectifying platform which can collect three or more energy sources will be enough to drive more complicated IoT sensors.

➢ Harmonic transponders only backscatter simple information in this work. However, to deal with diversified applications, a modulation module is highly recommended.

➢ A reconfigurable design that combines both far-field WPT and harmonic backscattering functions will be compatible with more applications. A proper low-power switch and a more compact design can be introduced to enhance the performance of the circuit proposed in Chapter 2.

REFERENCES

[1] J. H. Bryant, "The first century of microwaves-1886 to 1986," *IEEE Trans. Microw. Theory Techn.,* vol. 36, no. 5, pp. 830-858, May 1988.

[2] K. Wu, D. Choudhury, and H. Matsumoto, "Wireless power transmission, technology, and applications," *Proc. IEEE*, vol. 101, no. 6, pp. 1271-1275, Jun. 2013.

[3] C. H. P. Lorenz, S. Hemour, and K. Wu, "Physical mechanism and theoretical foundation of ambient RF power harvesting using zero-bias diodes," *IEEE Trans. Microw. Theory Techn.,* vol. 64, no. 7, pp. 2146-2158, Jul. 2016.

[4] Z. Popovic, "Cut the cord: Low-power far-field wireless powering," *IEEE Microw. Mag.,* vol. 14, no. 2, pp. 55-62, Mar./Apr. 2013.

[5] U. Muncuk, K. Alemdar, J. D. Sarode, and K. R. Chowdhury, "Multiband ambient RF energy harvesting circuit design for enabling batteryless sensors and IoT," *IEEE Internet Things J.*,vol. 5, no. 4, pp. 2700-2714, Aug. 2018.

[6] T. Imai *et al.*, "Development of high frequency band over 6 GHz for 5G mobile communication systems," in *Proc. 9th Eur. Conf. Antennas Propag.*, Lisbon, Portugal, Apr. 2015, pp. 1-4.

[7] M. Pinuela, P. D. Mitcheson, and S. Lucyszyn, "Ambient RF energy harvesting in urban and semi-urban environments," *IEEE Trans. Microw. Theory Techn.,* vol. 61, no. 7, pp. 2715-2726, Jul. 2013.

[8] H. Takhedmit, "Ambient RF power harvesting: Application to remote supply of a batteryless temperature sensor," in *Proc. IEEE Int. Smart Cities Conf.*, Trento, Italy, Sept. 2016, pp. 1-4.

[9] O. M. AbdelGhany, A. G. Sobih, and A. M. El-Tager, "Outdoor RF spectral study available from cell-phone towers in sub-urban areas for ambient RF energy harvesting," *IOP Conf. Ser.: Mater. Sci. Eng.*, vol. 610, p. 012086, 2019.

[10] X. Gu, L. Grauwin, D. Dousset, S. Hemour, and K. Wu, "Dynamic ambient RF energy mapping of Montreal for battery-free IoT sensor network planning," Submitted.

[11] S. Kim *et al.*, "Ambient RF energy-harvesting technologies for self-sustainable standalone wireless sensor platforms," *Proc. IEEE,* vol. 102, no. 11, pp. 1649-1666, Nov. 2014.

[12] J. Kimionis *et al.*, "Zero-power sensors for smart objects: Novel zero-power additively manufactured wireless sensor modules for IoT applications," *IEEE Microw. Mag.*, vol. 19, no. 6, pp. 32-47, Sept./Oct. 2018.

[13] X. Gu, N. N. Srinaga, L. Guo, S. Hemour, and K. Wu, "Diplexer-Based Fully Passive Harmonic Transponder for Sub-6-GHz 5G-Compatible IoT Applications," *IEEE Trans. Microw. Theory Techn.,* vol. 67, no. 5, pp. 1675-1687, May 2019.

[14] T.-H. Lin *et al.*, "On-body long-range wireless backscattering sensing system using inkjet-/3-D-printed flexible ambient rf energy harvesters capable of simultaneous dc and harmonics generation," vol. 65, no. 12, pp. 5389-5400, Dec. 2017.

[15] F. Amato and S. Hemour, "The Harmonic Tunneling Tag: a Dual-Band Approach to Backscattering Communications," in *Proc. IEEE Int. Conf. RFID Technol. Appl.*, Pisa, Italy, Sept. 2019, pp. 244-247.

[16] H. C. Torrey, C. Austin, and S. A. Goudsmit, *Crystal Rectifiers*, New York, NY, USA: McGraw-Hill, 1948.

[17] S. Hemour and K. Wu, "Radio-frequency rectifier for electromagnetic energy harvesting: Development path and future outlook," *Proc. IEEE,* vol. 102, no. 11, pp. 1667-1691, Nov. 2014.

[18] S. Hemour *et al.*, "Towards low-power high-efficiency RF and microwave energy harvesting," *IEEE Trans. Microw. Theory Techn.,* vol. 62, no. 4, pp. 965-976, Apr. 2014.

[19] W. Shockley, "The Theory of p-n Junctions in Semiconductors and p-n Junction Transistors," *Bell Sys. Tech. J.,* vol. 28, no. 3, pp. 435-489, Jul. 1949.

[20] S. Hemour, X. Gu, and K. Wu, "Efficiency of Rectenna," in *Recent Wireless Power Transfer Technologies via Radio Waves,* N. Shinohara, Ed., ed: River Publishers, 2018, pp. 95-132.

[21] X. Gu, L. Guo, S. Hemour, and K. Wu, "Optimum temperatures for enhanced power conversion efficiency (PCE) of zero bias diode-based rectifiers," *IEEE Trans. Microw. Theory Techn.,* to be published.

[22] V. Palazzi *et al.*, "A novel ultra-lightweight multiband rectenna on paper for RF energy harvesting in the next generation LTE bands," *IEEE Trans. Microw. Theory Techn.,* vol. 66, no. 1, pp. 366-379, Jan. 2018.

[23] S. Shen, Y. Zhang, C.-Y. Chiu, and R. Murch, "A Triple-band High-Gain Multibeam Ambient RF Energy Harvesting System Utilizing Hybrid Combining," *IEEE Trans. Ind. Electron.*, vol. 67, no. 11, pp. 9215-9226, Nov. 2020.

[24] C.-Y. Hsu, S.-C. Lin, and Z.-M. Tsai, "Quadband rectifier using resonant matching networks for enhanced harvesting capability," *IEEE Microw. Wireless Compon. Lett.,* vol. 27, no. 7, pp. 669-671, Jul. 2017.

[25] V. Kuhn, C. Lahuec, F. Seguin, and C. Person, "A multi-band stacked RF energy harvester with RF-to-DC efficiency up to 84%," *IEEE Trans. Microw. Theory Techn.,* vol. 63, no. 5, pp. 1768-1778, May 2015.

[26] H. Sun, Y.-X. Guo, M. He, and Z. Zhong, "A dual-band rectenna using broadband Yagi antenna array for ambient RF power harvesting," *IEEE Antennas Wireless Propag. Lett.*, vol. 12, pp. 918-921, Jul. 2013.

[27] U. Olgun, C.-C. Chen, and J. Volakis, "Investigation of rectenna array configurations for enhanced RF power harvesting," *IEEE Antennas Wireless Propag. Lett.*, vol. 10, pp. 262-265, Apr. 2011.

[28] E. Vandelle, T.-P. Vuong, G. Ardila, K. Wu, and S. Hemour, "Harvesting Ambient RF Energy Efficiently With Optimal Angular Coverage," *IEEE Trans. Antennas Propag.,* vol. 67, no. 3, pp. 1862-1873, Mar. 2019.

[29] H. Sun and W. Geyi, "A new rectenna using beamwidth-enhanced antenna array for RF power harvesting applications," *IEEE Antennas Wireless Propag. Lett.,* vol. 16, pp. 1451-1454, Dec. 2016.

[30] Y.-Y. Hu, S. Sun, H. Xu, and H. Sun, "Grid-Array Rectenna With Wide Angle Coverage for Effectively Harvesting RF Energy of Low Power Density," *IEEE Trans. Microw. Theory Techn.,* vol. 67, no. 1, pp. 402-413, Jan. 2019.

[31] W. Brown and J. Triner, "Experimental thin-film, etched-circuit rectenna," in *Proc. IEEE MTT-S Int. Microw. Symp. Dig.,* Dallas, TX, USA, Jun. 1982, pp. 185-187.

[32] X. Gu *et al.*, "Hybridization of Integrated Microwave and Mechanical Power Harvester," *IEEE Access,* vol. 6, pp. 13921-13930, Mar. 2018.

[33] L. Guo, X. Gu, P. Chu, S. Hemour, and K. Wu, "Collaboratively Harvesting Ambient Radiofrequency and Thermal Energy," *IEEE Trans. Ind. Electron.,* vol. 67, no. 5, May 2020.

[34] K. Niotaki, A. Collado, A. Georgiadis, S. Kim, and M. M. Tentzeris, "Solar/electromagnetic energy harvesting and wireless power transmission," *Proc. IEEE,* vol. 102, no. 11, pp. 1712-1722, Nov. 2014.

[35] X. Gu, S. Hemour, and K. Wu, "Enabling Far-Field Ambient Energy Harvesting Through Multi-Physical Sources," in *Proc. Asia-Pac. Microw. Conf.*, Kyoto, Japan, Nov. 2018, pp. 204-206.

[36] X. Gu, S. Hemour, L. Guo, and K. Wu, "Integrated Cooperative Ambient Power Harvester Collecting Ubiquitous Radio Frequency and Kinetic Energy," *IEEE Trans. Microw. Theory Techn.,* vol. 66, no. 9, pp. 4178-4190, Sept. 2018.

[37] N. Shinohara and Y. Zhou, "Development of rectenna with high impedance and high Q antenna," in *Proc. Asia-Pac. Microw. Conf.*, Sendai, Japan, Nov. 2014, pp. 600-602.

[38] C. Song *et al.*, "Matching network elimination in broadband rectennas for high-efficiency wireless power transfer and energy harvesting," *IEEE Trans. Ind. Electron.,* vol. 64, no. 5, pp. 3950-3961, May 2017.

[39] C. H. P. Lorenz *et al.*, "Breaking the Efficiency Barrier for Ambient Microwave Power Harvesting With Heterojunction Backward Tunnel Diodes," *IEEE Trans. Microw. Theory Techn.,* vol. 63, no. 12, pp. 4544-4555, Dec. 2015.

[40] Z. Zeng, J. J. Estrada-López, M. A. Abouzied, and E. Sánchez-Sinencio, "A Reconfigurable Rectifier with Optimal Loading Point Determination for RF Energy Harvesting from-22 dBm to-2 dBm," *IEEE Trans. Circuits Syst. II Exp. Briefs,* vol. 67, no. 1, pp. 87-91, Jan. 2019.

[41] S.-Y. Kim *et al.*, "A-20 to 30 dBm Input Power Range Wireless Power System with a MPPT-based Reconfigurable 48% Efficient RF Energy Harvester and 82% Efficient A4WP Wireless Power Receiver with Open Loop Delay Compensation," *IEEE Trans. Power Electron.,* vol. 34, no. 7, pp. 6803-6817, Jul. 2019.

[42] X. Gu, L. Guo, S. Hemour, and K. Wu, "Novel diplexer-based harmonic transponder for 5G-compatible IoT applications," in *Proc. IEEE MTT-S Wireless Power Transf. Conf.*, Montreal, Canada, Jun. 2018, pp. 1-4.

[43] K. Rasilainen, J. Ilvonen, A. Lehtovuori, J.-M. Hannula, and V. Viikari, "On design and evaluation of harmonic transponders," *IEEE Trans. Antennas Propag.,* vol. 63, no. 1, pp. 15-23, Jan. 2015.

[44] X. Gu, L. Guo, S. Hemour, and K. Wu, "Analysis and Exploitation of Diplexer-based Fully Passive Harmonic Transponder for 5G Applications," in *Proc. IEEE MTT-S Int. Microw. Workshop Ser. 5G Hardw. Syst. Technol.*, Dublin, Ireland, Aug. 2018, pp. 1-3.

[45] K. Rasilainen, J. Ilvonen, J.-M. Hannula, and V. Viikari, "Designing Harmonic Transponders Using Lumped-Component Matching Circuits," *IEEE Antennas Wireless Propag. Lett.,* vol. 16, pp. 246-249, May 2016.

[46] E. A. Capaldi *et al.*, "Ontogeny of orientation flight in the honeybee revealed by harmonic radar," *Nature*, vol. 403, no. 6769, pp. 537-540, Feb. 2000.

[47] A. Lavrenko, B. Litchfield, G. Woodward, and S. Pawson, "Design and evaluation of a compact harmonic transponder for insect tracking," *IEEE Microw. Wireless Compon. Lett.*, vol. 30, no. 4, pp. 445-448, Apr. 2020.

[48] A. Pašukonis, K. B. Beck, M.-T. Fischer, S. Weinlein, S. Stückler, and E. Ringler, "Induced parental care in a poison frog: a tadpole cross-fostering experiment," *J. Exp. Biol.*, vol. 220, no. 21, pp. 3949-3954, Aug. 2017.

[49] T. Langkilde and R. A. Alford, "The tail wags the frog: harmonic radar transponders affect movement behavior in Litoria lesueuri," *J. Herpetol.*, vol. 36, no. 4, pp. 711-715, Dec. 2002.

[50] B. G. Colpitts, and G. Boiteau, "Harmonic radar transceiver design: miniature tags for insect tracking," *IEEE Trans. Antennas Propag.*, vol. 52, no. 11, pp. 2825-2832, Nov. 2004.

[51] R. Brazee, E. Miller, M. Reding, M. Klein, B. Nudd, and H. Zhu, "A transponder for harmonic radar tracking of the black vine weevil in behavioral research," *Trans. Amer. Soc. Agricultural Eng.*, vol. 48, no. 2, pp. 831-838, Feb. 2005.

[52]   C. Cho, X. Yi, D. Li, Y. Wang, and M. Tentzeris, "Passive wireless frequency doubling antenna sensor for strain and crack sensing," *IEEE Sensors J.*, vol. 16, no. 14, pp. 5725-5733, Jul. 2016.

[53]   L. Zhu, M. Farhat, Y.-C. Chen, K. N. Salama, and P.-Y. Chen, "A Compact, Passive Frequency-Hopping Harmonic Sensor Based on a Microfluidic Reconfigurable Dual-Band Antenna," *IEEE Sensors J.*, to be published.

[54]   X. Gu, S. Hemour, and K. Wu, "Remote Temperature Sensing Based on Battery-Free Harmonic Backscattering," in *Proc. IEEE Int. Symp. Antennas Propag. USNC-URSI Radio Sci. Meeting*, Montreal, Canada, Jul. 2020, pp. 1-2.

[55]   S. Zorn, R. Rose, A. Goetz, and R. Weigel, "A novel technique for mobile phone localization for search and rescue applications," in *Proc. IEEE Int. Conf. Indoor Positioning Indoor Navigat.*, Zurich, Switzerland, Sept. 2010, pp. 1-4.

[56]   X. Gu, S. Hemour, and K. Wu, "Reconfigurable Nonlinear Circuit for Wireless Power Harvesting and Backscattering," in *Proc. 49th Eur. Microw. Conf.*, Paris, France, Oct. 2019, pp. 543-546.

[57]   J. Koomey, S. Berard, M. Sanchez, and H. Wong, "Implications of historical trends in the electrical efficiency of computing," *IEEE Ann. History Comput.*, vol. 33, no. 3, pp. 46-54, Mar. 2011.

[58]   J. Koomey and S. Naffziger, "Moore's Law might be slowing down, but not energy efficiency," *IEEE Spectrum*, vol. 52, no. 4, p. 35, Mar. 2015.

[59]   J. Koomey and S. Naffziger, "Energy efficiency of computing: what's next," Accessed on Nov. 28, 2016. [Online]. Available: https://cdn.baseplatform.io/files/base/ebm/electronicdesign/document/2019/03/electronicdesign_10815_energyefficiencyofcomputingwhatsnext.pdf

[60]   Texas Instruments, "LPV511 Micropower, Rail-to-Rail Input and Output Operational Amplifier," LPV511 datasheet, 2005, [Online]. Available: http://www.ti.com/product/LPV511

[61] Touchstone Semiconductor. "TS1002-04 0.8V/0.6µA Rail-to-Rail Dual/Quad Op Amps," TS1002 datasheet, 2010, [Online]. Available: https://www.silabs.com/documents/public/data-sheets/TS1002-04.pdf

[62] Maxim Intgrated. "MAX44264 nanoPower Op Amp in a Tiny 6-Bump WLP," MAX44264 datasheet, 2010, [Online]. Available: https://www.maximintegrated.com/en/products/analog/amplifiers/MAX44264.html

[63] Texas Instruments. "LPV802 Single Channel 450nA Nanopower Operational Amplifier," LPV802 datasheet, 2016, [Online]. Available: http://www.ti.com/product/LPV801

[64] H. Nakamoto *et al.*, "A passive UHF RFID tag LSI with 36.6% efficiency CMOS-only rectifier and current-mode demodulator in 0.35 um FeRAM technology," in *Proc. IEEE Int. Solid-State Circuits Conf. Dig. Tech. Papers*, San Francisco, CA, USA, Feb. 2006, pp. 1201-1210.

[65] C. Meneses Ghiglino, "Ultra-Wideband (UWB) rectenna design for Electromagnetic Energy Harvesting," Masters thesis, Dept. Teoria del Senyali Comun., Escola Tecnica Superior d'Enginyeria de Telecomun. de Barcelona, Catalunya, Spain, 2010.

[66] C. Song, Y. Huang, J. Zhou, and P. Carter, "Improved ultrawideband rectennas using hybrid resistance compression technique," *IEEE Trans. Antennas Propag.,* vol. 65, no. 4, pp. 2057-2062, Apr. 2017.

[67] J. O. McSpadden, L. Fan, and K. Chang, "Design and experiments of a high-conversion-efficiency 5.8-GHz rectenna," *IEEE Trans. Microw. Theory Techn.,* vol. 46, no. 12, pp. 2053-2060, Dec. 1998.

[68] J. O. McSpadden, L. Fan, and K. Chang, "A high conversion efficiency 5.8 GHz rectenna," in *Proc. IEEE MTT-S Int. Microw. Symp. Dig.*, Denver, CO, USA, Jun. 1997, pp. 547-550.

[69] J. O. McSpadden and K. Chang, "A dual polarized circular patch rectifying antenna at 2.45 GHz for microwave power conversion and detection," in *Proc. IEEE MTT-S Int. Microw. Symp. Dig.*, San Diego, CA, USA, May 1994, pp. 1749-1752.

[70] J. A. Hagerty, F. B. Helmbrecht, W. H. McCalpin, R. Zane, and Z. B. Popović, "Recycling ambient microwave energy with broad-band rectenna arrays," *IEEE Trans. Microw. Theory Techn.,* vol. 52, no. 3, pp. 1014-1024, Mar. 2004.

[71]   Y.-J. Ren and K. Chang, "5.8-GHz circularly polarized dual-diode rectenna and rectenna array for microwave power transmission," *IEEE Trans. Microw. Theory Techn.,* vol. 54, no. 4, pp. 1495-1502, Apr. 2006.

[72]   T. Ozaki, T. Hirose, H. Asano, N. Kuroki, and M. Numa, "Fully-integrated high-conversion-ratio dual-output voltage boost converter with MPPT for low-voltage energy harvesting," *IEEE J. Solid-State Circuits*, vol. 51, no. 10, pp. 2398-2407, Oct. 2016.

[73]   C. Li and A. Liscidini, "Class-C PA-VCO Cell for FSK and GFSK Transmitters," *IEEE J. Solid-State Circuits*, vol. 51, no. 7, pp. 1537-1546, Jul. 2016.

[74]   H. Ritchie and M. Roser, "Urbanization," Our World in Data, 2018, [Online]. Available: https://ourworldindata.org/urbanization.

[75]   P. M. Santos *et al.*, "PortoLivingLab: An IoT-based sensing platform for smart cities," *IEEE Internet Things J.,* vol. 5, no. 2, pp. 523-532, Apr. 2018.

[76]   O. B. Akan, O. Cetinkaya, C. Koca, and M. Ozger, "Internet of hybrid energy harvesting things," *IEEE Internet Things J.,* vol. 5, no. 2, pp. 736-746, Apr. 2018.

[77]   V. Liu, A. Parks, V. Talla, S. Gollakota, D. Wetherall, and J. R. Smith, "Ambient backscatter: Wireless communication out of thin air," in *Proc. ACM SIGCOMM*, Hong Kong, China, Aug. 2013, pp. 39-50.

[78]   C. Pérez-Penichet, F. Hermans, A. Varshney, and T. Voigt, "Augmenting IoT networks with backscatter-enabled passive sensor tags," in *Proc. 3rd Workshop Hot Topics Wireless*, New York, NY, USA, Oct. 2016, pp. 23-27.

[79]   H. J. Visser, A. C. Reniers, and J. A. Theeuwes, "Ambient RF energy scavenging: GSM and WLAN power density measurements," in *Proc. Eur. Microw. Conf.*, Amsterdam, Netherlands, Oct. 2008, pp. 721-724.

[80]   Y. Kawahara, K. Tsukada, and T. Asami, "Feasibility and potential application of power scavenging from environmental RF signals," in *Proc. IEEE Antennas Propag. Soc. Int. Symp.*, Charleston, SC, USA, Jun. 2009, pp. 1-4.

[81] S. Kitazawa, H. Ban, and K. Kobayashi, "Energy harvesting from ambient RF sources," in *Proc. IEEE MTT-S Int. Microw. Workshop Series Innovative Wireless Power Transmiss.: Technol., Syst., Appl.*, Kyoto, Japan, May 2012, pp. 39-42.

[82] F. Giuppi, K. Niotaki, A. Collado, and A. Georgiadis, "Challenges in energy harvesting techniques for autonomous self-powered wireless sensors," in *Proc. Eur. Microw. Conf.*, Nuremberg, Germany, Oct. 2013, pp. 854-857.

[83] J. Milanezi, J. P. C. da Costa, and E. P. de Freitas, "Improved radiofrequency energy harvesting based on a rectenna array system and its feasibility evaluation in urban environments," in *Proc. Int. Conf. Renew. Energy Res. Appl.*, Milwaukee, WI, USA, Oct. 2014, pp. 561-565.

[84] K. Mimis, D. Gibbins, S. Dumanli, G. T. Watkins, "Ambient RF energy harvesting trial in domestic settings," *IET Microw., Antennas Propag.,* vol. 9, no. 5, pp. 454-462, Apr. 2015.

[85] E. I. Adegoke, R. Edwards, W. Whittow, and A. Bindel, "RF power density measurements for RF energy harvesting in automobile factories," in *Proc. Loughborough Antennas Propag. Conf.*, Loughborough, UK, Nov. 2015, pp. 1-5.

[86] A. S. Andrenko, X. Lin, and M. Zeng, "Outdoor RF spectral survey: A roadmap for ambient RF energy harvesting," in *Proc. IEEE Region 10 Conf.*, Macao, China, Nov. 2015, pp. 1-4.

[87] ANFR, French Agency for Frequency Management (Agence Nationale des Fréquences). [Online]. Available: http://www.cartoradio.fr/cartoradio/web/

[88] L. Whitney, "5G expands to 378 cities across 34 countries," Feb. 27, 2020. [Online]. Available: https://www.techrepublic.com/article/5g-expands-to-378-cities-across-34-countries/

[89] A. Khemar, A. Kacha, H. Takhedmit, G. Abib, "Design and experiments of a dual-band rectenna for ambient RF energy harvesting in urban environments," *IET Microw., Antennas Propag.,* vol. 12, no. 1, pp. 49-55, Jan. 2018.

[90] "N6850A Broadband Omnidirectional Antenna Data Sheet," Accessed on Dec. 07, 2017, [Online]. Available: https://www.keysight.com/us/en/assets/7018-05040/data-sheets/5992-1237.pdf.

[91] *"Downtown Strategy, Building on Momentum, 2016 Consultation Document,"* [Online]. Available: http://ocpm.qc.ca/sites/ocpm.qc.ca/files/document_consultation/vmvma- 16-026_strategie_centre-ville_final.pdf

[92] Canadian Cellular Towers Map. [Online]. Available: https://www.ertyu.org/steven_nikkel/cancellsites.html

[93] Interactive TV Coverage Browser. [Online]. Available: https://www.tvfool.com/?option=com_wrapper&Itemid=90

[94] G. Frantz, "Digital signal processor trends," *IEEE Micro,* vol. 20, no. 6, pp. 52-59, Nov./Dec. 2000.

[95] M. T. Bohr and I. A. Young, "CMOS scaling trends and beyond," *IEEE Micro,* vol. 37, no. 6, pp. 20-29, Nov./Dec. 2017.

[96] Y.-P. Chen, "Low Power Techniques for Analog Building Blocks of the Ultra Low Power Systems," Ph.D. dissertation, Dept. Elect. Comput. Eng., Univ. Michigan, Ann Arbor, MI, USA, 2016.

[97] Z. Liu, Z. Zhong, and Y.-X. Guo, "High-efficiency triple-band ambient RF energy harvesting for wireless body sensor network," in *Proc. IEEE MTT-S Int. Microw. Workshop Series RF Wireless Technol. Biomed. Healthcare Appl.,* London, UK, Dec. 2014, pp. 1-3.

[98] A. Bakytbekov, T. Q. Nguyen, C. Huynh, K. N. Salama, and A. Shamim, "Fully printed 3D cube-shaped multiband fractal rectenna for ambient RF energy harvesting," *Nano Energy,* vol. 53, pp. 587-595, Nov. 2018.

[99] J. Osborne *et al.*, "A landscape-scale study of bumble bee foraging range and constancy, using harmonic radar," *J. Appl. Ecol.,* vol. 36, no. 4, pp. 519-533, Sept. 1999.

[100] H. M. Aumann and N. W. Emanetoglu, "A wideband harmonic radar for tracking small wood frogs," in *Proc. IEEE Radar Conf.,* Cincinnati, OH, USA, May 2014, pp. 108-111.

[101] A system for locating avalanche victims, [Online]. Available: http://www.recco.com/about

[102] V. Palazzi, F. Alimenti, P. Mezzanotte, G. Orecchini, and L. Roselli, "Zero-power, long-range, ultra low-cost harmonic wireless sensors for massively distributed monitoring of

cracked walls," in *Proc. IEEE MTT-S Int. Microw. Symp.,* Honolulu, HI, USA, Jun. 2017, pp. 1335-1338.

[103] W. Brown, "The history of power transmission by radio waves," *IEEE Trans. Microw. Theory Techn.,* vol. 32, no. 9, pp. 1230-1242, Sep. 1984.

[104] L. Xie, Y. Shi, Y. T. Hou, and A. Lou, "Wireless power transfer and applications to sensor networks," *IEEE Wireless Commun. Mag.,* vol. 20, no. 4, pp. 140-145, Aug. 2013.

[105] W. Brown, "Electronic and mechanical improvement of the receiving terminal of a free-space microwave power transmission system," Raytheon Company, Wayland, MA, USA, Tech. Rep. PT-4964, Aug. 1977, NASA CR-135194.

[106] W. Brown, "The history of the crossed-field amplifier," *IEEE MTT-S Newslett.,* no. 141, pp. 29-40, Fall 1995.

[107] F. Bolos, J. Blanco, A. Collado, and A. Georgiadis, "RF Energy Harvesting From Multi-Tone and Digitally Modulated Signals," *IEEE Trans. Microw. Theory Techn.,* vol. 64, no. 6, pp. 1918-1927, Jun. 2016.

[108] Y.-H. Suh and K. Chang, "A high-efficiency dual-frequency rectenna for 2.45-and 5.8-GHz wireless power transmission," *IEEE Trans. Microw. Theory Techn.,* vol. 50, no. 7, pp. 1784-1789, Jul. 2002.

[109] G. A. Vera, A. Georgiadis, A. Collado, and S. Via, "Design of a 2.45 GHz rectenna for electromagnetic (EM) energy scavenging," in *Proc. IEEE Radio Wireless Symp.,* New Orleans, LA, USA, Jan. 2010, pp. 61-64.

[110] H. Takhedmit *et al.*, "A 2.45-GHz dual-diode RF-to-dc rectifier for rectenna applications," in *Proc. Eur. Microw. Conf.,* Paris, France, Sep. 2010, pp. 37-40.

[111] C. Song, Y. Huang, J. Zhou, J. Zhang, S. Yuan, and P. Carter, "A high-efficiency broadband rectenna for ambient wireless energy harvesting," *IEEE Trans. Antennas Propag.,* vol. 63, no. 8, pp. 3486-3495, Aug. 2015.

[112] T.-W. Yoo and K. Chang, "Theoretical and experimental development of 10 and 35 GHz rectennas," *IEEE Trans. Microw. Theory Techn.,* vol. 40, no. 6, pp. 1259-1266, Jun. 1992.

[113] J. Guo, H. Zhang, and X. Zhu, "Theoretical analysis of RF-DC conversion efficiency for class-F rectifiers," *IEEE Trans. Microw. Theory Techn.,* vol. 62, no. 4, pp. 977-985, Apr. 2014.

[114] J.-h. Ou, S. Y. Zheng, A. S. Andrenko, Y. Li, and H.-Z. Tan, "Novel Time-Domain Schottky Diode Modeling for Microwave Rectifier Designs," *IEEE Trans. Circuits Syst. I, Reg. Papers,* vol. 65, no. 4, pp. 1234-1244, Apr. 2018.

[115] G. De Vita and G. Iannaccone, "Design criteria for the RF section of UHF and microwave passive RFID transponders," *IEEE Trans. Microw. Theory Techn.,* vol. 53, no. 9, pp. 2978-2990, Sep. 2005.

[116] C. Lorenz, S. Hemour, W. Liu, A. Badel, F. Formosa, and K. Wu, "Hybrid power harvesting for increased power conversion efficiency," *IEEE Microw. Wireless Compon. Lett.,* vol. 25, no. 10, pp. 687-689, Oct. 2015.

[117] J.-S. Yuan and Y. Bi, "Process and temperature robust voltage multiplier design for RF energy harvesting," *Microelectron. Reliab.,* vol. 55, no. 1, pp. 107-113, Jam. 2015.

[118] F. G. Della Corte, M. Merenda, G. G. Bellizzi, T. Isernia, and R. Carotenuto, "Temperature Effects on the Efficiency of Dickson Charge Pumps for Radio Frequency Energy Harvesting," *IEEE Access,* vol. 6, pp. 65729-65736, Oct. 2018.

[119] T. Ohira, "Power efficiency and optimum load formulas on RF rectifiers featuring flow-angle equations," *IEICE Electron. Exp.,* vol. 10, no. 11, pp. 1-9, May 2013.

[120] P. Antognetti, G. Massobrio, and G. Massobrio, *Semiconductor Device Modeling With SPICE*. New York, NY, USA:McGraw-Hill, 1998.

[121] M. Abramowitz and I. A. Stegun, *Handbook of Mathematical Functions: With Formulas, Graphs, and Mathematical Tables.* New York, NY, USA: Dover, 1972.

[122] I. Zeltser and S. Ben-Yaakov, "On SPICE Simulation of Voltage-Dependent Capacitors," *IEEE Trans. Power Electron.,* vol. 33, no. 5, pp. 3703-3710, May 2018.

[123] H. Russell Jr, *The SPICE Diode Model.* San Jose, CA, USA: Motorola Inc. Opal Engineering, Aug. 1991.

[124] K. Rose, S. Eldridge, and L. Chapin, "The Internet of Things: An Overview," *Internet Soc. (ISOC),* pp. 1-50, 2015.

[125] A. S. Weddell, M. Magno, G. V. Merrett, D. Brunelli, B. M. Al-Hashimi, and L. Benini, "A Survey of Multi-source Energy Harvesting Systems," in *Proc. DATE*, Mar. 18-22, 2013, pp. 905-908.

[126] F. Yildiz, "Potential Ambient Energy-harvesting Sources and Techniques," *J. Technol. Studies*, vol. 35, no. 1, pp. 40-48. 2009.

[127] M. Freitag, *et al.*, "Dye-sensitized Solar Cells for Efficient Power Generation under Ambient Lighting," *Nat. Photonics,* 2017.

[128] H. Zhang, *et al.*, "Flexible Pyroelectric Generators for Scavenging Ambient Thermal Energy and as Self-powered Thermosensors," *Energy,* vol. 101, pp. 202-210, 2016.

[129] Y. Hou, *et al.*, "Flexible Ionic Diodes for Low-Frequency Mechanical Energy Harvesting," *Adv. Energy Mater.,* vol. 7, 2017.

[130] L. Radovic, Efficiency of Energy Conversion [Online]. Available: http://www.ems.psu.edu/~radovic/Chapter4.pdf.

[131] S. Beeby and N. White, *Energy Harvesting for Autonomous Systems*. Norwood, CA, USA: Artech House, 2010.

[132] A. Sharma, V. Singh, T. L. Bougher, and B. A. Cola, "A Carbon Nanotube Optical Rectenna," *Nat. nanotechnol.,* vol. 10, pp. 1027-1032, Sep. 2015.

[133] X. Gu, S. Hemour, and K. Wu, "Integrated Cooperative Radiofrequency (RF) and Kinetic Energy Harvester," in *Proc. Wireless Power Transf. Conf.,* Taipei, Taiwan, May 2017, pp. 1-3.

[134] A. Rennings, M. Rauf, P. Waldow, and I. Wolff, "A Compact Single/dual-band Printed Inverted-F Type Antenna Structure," *ACES,* New York, Apr. 2004.

[135] S. Roundy, P. K. Wright, and J. Rabaey, "A study of low level vibrations as a power source for wireless sensor nodes," *Comp. Commun.,* vol. 26, no. 11, pp. 1131-1144, Jul. 2003.

[136] M. F. B. Ab Rahman and S. L. Kok, "Investigation of useful ambient vibration sources for the application of energy harvesting," in *Proc. IEEE Student Conf. Res. Develop., 2011,* pp. 391-396.

[137] M. Virili *et al.*, "Performance Improvement of Rectifiers for WPT Exploiting Thermal Energy Harvesting," *Wireless Power Transfer,* vol. 2, no. 1, pp. 22-31, 2015.

[138] K. Niotaki, F. Giuppi, A. Georgiadis, and A. Collado, "Solar/EM Energy Harvester for Autonomous Operation of a Monitoring Sensor Platform," *Wireless Power Transfer,* vol. 1, no. 1, pp. 44-50, 2014.

[139] M. Virili *et al.*, "EH Performance of an Hybrid Energy Harvester for Autonomous Nodes," in *Proc. IEEE Topical Conf. Wireless Sensors and Sensor Netw.,* Jan. 2016, pp. 71-74.

[140] W. Fan *et al.*, "A Step Toward 5G in 2020: Low-cost OTA performance evaluation of massive MIMO base stations," *IEEE Antennas Propag. Mag.,* vol. 59, no.1, pp. 38-47, Feb. 2017.

[141] J. Deng, O. Tirkkonen, R. Freij-Hollanti, T. Chen, and N. Nikaein, "Resource allocation and interference management for opportunistic relaying in integrated mmwave/sub-6 ghz 5g networks," *IEEE Commun. Mag.,* vol. 55, no. 6, pp. 94-101, Jun. 2017.

[142] WRC-15 Press Release. (Nov. 27, 2015). *World Radiocommunication Conference Allocates Spectrum for Future Innovation.* [Online]. Available: http://www.itu.int/net/pressoffice/ press_releases/2015/56.aspx#.W4Xga2iPKUk

[143] Y. Li, Y. Luo, and G. Yang, "12-port 5G massive MIMO antenna array in sub-6GHz mobile handset for LTE bands 42/43/46 applications," *IEEE Access,* vol. 6, pp. 344-354, Oct. 2017.

[144] Y. Zhu, G. Zheng, L. Wang, K.-K. Wong, and L. Zhao, "Content Placement in Cache-Enabled Sub-6 GHz and Millimeter-Wave Multi-antenna Dense Small Cell Networks," *IEEE Trans. Wireless Commun.,* vol. 17, no. 5, 2843-2856, May 2018.

[145] H. Elshaer, M. N. Kulkarni, F. Boccardi, J. G. Andrews, and M. Dohler, "Downlink and uplink cell association with traditional macrocells and millimeter wave small cells," *IEEE Trans. Wireless Commun.,* vol. 15, no. 9, pp. 6244-6258, Jun. 2016.

[146] A. Nordrum, "Popular internet of things forecast of 50 billion devices by 2020 is outdated," *IEEE spectr., [online] Available: https://spectrum.ieee.org/tech-talk/telecom/internet/popular-internet-of-things-forecast-of-50-billion-devices-by-2020-is-outdated.*

[147] L. Lyu, C. Chen, S. Zhu, and X. Guan, "5G Enabled Codesign of Energy-Efficient Transmission and Estimation for Industrial IoT Systems," *IEEE Trans. Ind. Informat.,* vol. 14, no. 6, pp. 2690-2704, Jan. 2018.

[148] N. Saxena, A. Roy, B. J. Sahu, and H. Kim, "Efficient IoT gateway over 5G wireless: A new design with prototype and implementation results," *IEEE Commun. Mag.,* vol. 55, no. 2, pp. 97-105, Feb. 2017.

[149] J. Vogler, D. Maguire, and A. Steinhauer, "DINADE—a new interrogation, navigation and detection system," *Microw. J,* vol. 10, no. 6, pp. 2-6, Apr. 1967.

[150] C. Van Tilburg *et al.*, "Wilderness Medical Society practice guidelines for prevention and management of avalanche and nonavalanche snow burial accidents," *Wildern. Environ. Med.,* vol. 28, no. 1, pp. 23-42, Mar. 2017.

[151] V. Palazzi, F. Alimenti, C. Kalialakis, P. Mezzanotte, A. Georgiadis, and L. Roselli, "Highly Integrable Paper-Based Harmonic Transponder for Low-Power and Long-Range IoT Applications," *IEEE Antennas Wireless Propag. Lett.,* vol. 16, pp. 3196-3199, Nov. 2017.

[152] K. Wang, A. Ghiotto, and K. Wu, "Harmonic feedback-loop oscillator for pulling effect reduction and improved phase noise," in *Proc. IEEE MTT-S Int. Microw. Symp. Dig.*, Tampa, USA, Jun. 2014, pp. 1-4.

[153] E. Vandelle *et al.*, "High gain isotropic rectenna," in *Proc. IEEE MTT-S Wireless Power Transf. Conf.,* Taipei, Taiwan, May 2017, pp. 1-3.

[154] X. Bao and M. Ammann, "Monofilar spiral slot antenna for dual-frequency dual-sense circular polarization," *IEEE Trans. Antennas Propag.,* vol. 59, no. 8, pp 3061-3065, Jun. 2011.

[155] A. Lazaro, R. Villarino, and D. Girbau, "A passive harmonic tag for humidity sensing," *Int. J. Antennas Propag.,* vol. 2014, Jul. 2014, Art. no. 670345.

[156] H. T. Friis, "A note on a simple transmission formula," *Proc. IRE,* vol. 34, no. 5, pp. 254-256, May 1946.

[157] Z. Liu, X. Liu, J. Zhang, and K. Li, "Opportunities and Challenges of Wireless Human Sensing for the Smart IoT World: A Survey," *IEEE Netw.,* vol. 33, no. 5, pp. 104-110, Sept.-Oct. 2019.

[158] H. Shan, J. Peterson III, S. Hathorn, and S. Mohammadi, "The RFID Connection: RFID Technology for Sensing and the Internet of Things," *IEEE Microw. Mag.,* vol. 19, no. 7, pp. 63-79, Nov.-Dec. 2018.

[159] X. Wang, X. Wang, and S. Mao, "RF sensing in the Internet of Things: A general deep learning framework," *IEEE Commun. Mag.,* vol. 56, no. 9, pp. 62-67, Sept. 2018.

[160] V. Bianchi, M. Bassoli, G. Lombardo, P. Fornacciari, M. Mordonini, and I. De Munari, "IoT Wearable Sensor and Deep Learning: an Integrated Approach for Personalized Human Activity Recognition in a Smart Home Environment," *IEEE Internet Things J.,* vol. 6, no. 5, Oct. 2019.

[161] P. Barsocchi, P. Cassara, F. Mavilia, and D. Pellegrini, "Sensing a city's state of health: structural monitoring system by Internet-of-Things wireless sensing devices," *IEEE Consum. Electron. Mag.,* vol. 7, no. 2, pp. 22-31, Mar. 2018.

[162] N. Ahmed, D. De, and I. Hussain, "Internet of Things (IoT) for smart precision agriculture and farming in rural areas," *IEEE Internet Things J.,* vol. 5, no. 6, pp. 4890-4899, Dec. 2018.

[163] X. Jia, Q. Feng, T. Fan, and Q. Lei, "RFID technology and its applications in Internet of Things (IoT)," in *Proc. Int. Conf. Consum. Electron. Commun. Netw.*, Yichang, China, Apr. 2012, pp. 1282-1285.

[164] G. Paolini, D. Masotti, F. Antoniazzi, T. S. Cinotti, and A. Costanzo, "Fall Detection and 3-D Indoor Localization by a Custom RFID Reader Embedded in a Smart e-Health Platform," *IEEE Trans. Microw. Theory Techn.,* vol. 67, no. 12, pp. 5329-5339, Dec. 2019.

[165] S. Mondal and P. Chahal, "A Passive Harmonic RFID Tag and Interrogator Development," *IEEE J. Radio Freq. Identificat.,* vol. 3, no. 2, pp. 98-107, Jun. 2019.

[166] S. Bottigliero, D. Milanesio, M. Saccani, R. Maggiora, A. Viscardi, and M. M. Gallesi, "An innovative harmonic radar prototype for miniaturized lightweight passive tags tracking," in *Proc. IEEE Radar Conf.*, Boston, MA, USA, Apr. 2019, pp. 1-6.

[167] D. Kumar, S. Mondal, S. Karuppuswami, Y. Deng, and P. Chahal, "Harmonic RFID Communication using Conventional UHF System," *IEEE J. Radio Freq. Identificat.,* vol. 3, no. 4, pp. 227-235, Dec. 2019.

[168] B. G. Colpitts and G. Boiteau, "Harmonic radar transceiver design: Miniature tags for insect tracking," *IEEE Trans. Antennas Propag.,* vol. 52, no. 11, pp. 2825-2832, Nov. 2004.

[169] B. Kubina, J. Romeu, C. Mandel, M. Schüßler, and R. Jakoby, "Quasi-chipless wireless temperature sensor based on harmonic radar," *Electron. Lett.*, vol. 50, no. 2, pp. 86-88, Jan. 2014.

[170] M. Schuessler, C. Mandel, B. Kubina, and R. Jakoby, "Realization concepts for chipless wireless temperature sensing," in *Proc. Sensors Meas. Syst. 2014; 17. ITG/GMA Symp.*, Nuremberg, Germany, Jun. 2014, pp. 1-6.

[171] X. Gu, S. Hemour, and K. Wu, "Improving Conversion Loss Performance of Fully Passive Harmonic Transponder at Low Temperature," in *Proc. IEEE MTT-S Wireless Power Transf. Conf.*, London, UK, 2019, pp. 395-398.

[172] C. R. Crowell, "The Richardson constant for thermionic emission in Schottky barrier diodes," *Solid·State Electron.,* vol. 8, no. 4, pp. 395-399, Apr. 1965.

[173] G. Kompa, *Practical Microstrip Design and Applications*. Norwood, MA, USA: Artech House, 2005.

[174] H. Aumann, E. Kus, B. Cline, and N. W. Emanetoglu, "A low-cost harmonic radar for tracking very small tagged amphibians," in *Proc. IEEE Int. Instrum. Meas. Technol. Conf.,* Minneapolis, MN, USA, May 2013, pp. 234-237.

APPENDIX A   LIST OF PUBLICATIONS & AWARDS

1. Invited book chapter:

[BC1]   Simon Hemour, **<u>Xiaoqiang Gu</u>**, and Ke Wu, "Efficiency of Rectenna," in *Recent Wireless Power Transfer Technologies via Radio Waves*, N. Shinohara, Ed., ed: River Publishers, 2018, pp. 95-132.

2. Peer-reviewed journal papers:

2.1 Published papers:

[J1] **<u>Xiaoqiang Gu</u>**, Lei Guo, Simon Hemour, and Ke Wu, "Optimum Temperatures for Enhanced Power Conversion Efficiency (PCE) of Zero Bias Diode-Based Rectifiers," *IEEE Trans. Microw. Theory Techn.*, vol. 68, no. 9, pp. 4040 - 4053, Sept. 2020.

[J2] Lei Guo, **<u>Xiaoqiang Gu</u>**, Peng Chu, Simon Hemour, and Ke Wu, "Collaboratively Harvesting Ambient Radiofrequency and Thermal Energy," *IEEE Trans. Ind. Electron.*, vol. 67. No. 5, pp. 3736 - 3746, May 2020.

[J3] **<u>Xiaoqiang Gu</u>**, Srinaga Nikhil N, Lei Guo, Simon Hemour, and Ke Wu, "Diplexer-Based Fully Passive Harmonic Transponder for Sub-6-GHz 5G-Compatible IoT Applications", *IEEE Trans. Microw. Theory Techn.*, vol. 67, no. 5, pp. 1675 - 1687, May 2019.

[J4] **<u>Xiaoqiang Gu</u>**, Simon Hemour, Lei Guo, and Ke Wu, "Integrated Cooperative Ambient Power Harvester Collecting Ubiquitous Radiofrequency and Kinetic Energy," *IEEE Trans. Microw. Theory Techn.*, vol. 66, no. 9, pp. 4178 - 4190, Sept. 2018. *(MTT-S Newsletter Headline)**

[J5] **<u>Xiaoqiang Gu</u>**, Weiqun Liu, Lei Guo, Simon Hemour, Fabien Formosa, Adrien Badel, and Ke Wu, "Hybridization of Integrated Microwave and Mechanical Power Harvester," *IEEE Access*, vol. 6, pp. 13921-13930, Mar. 2018.

2.2 Submitted papers:

[J6] **<u>Xiaoqiang Gu</u>**, Louis Grauwin, David Dousset, Simon Hemour, and Ke Wu, "Dynamic Ambient RF Energy Mapping of Montreal for Battery-Free IoT Sensor Network Planning," *IEEE Internet Things J.*, submitted.

[J7] **<u>Xiaoqiang Gu</u>**, Pascal Burasa, Simon Hemour and Ke Wu, "Recycling Ambient Radiofrequency (RF) Energy: Far-Field Wireless Power Transfer and Harmonic Backscattering," *IEEE Microw. Mag.,* submitted.

[J8] **<u>Xiaoqiang Gu</u>**, Wentao Lin, Simon Hemour, and Ke Wu, "Readout Distance Enhancement of Battery-Free Harmonic Transponder," *IEEE Trans. Microw. Theory Techn.*, submitted.

3. Conference papers:

[C1] **<u>Xiaoqiang Gu,</u>** Simon Hemour, and Ke Wu, "Wireless Powered Sensors for Battery-Free IoT Through Multi-Stage Rectifier," in *Proc. 33rd URSI GASS,* Rome, Italy, Aug.-Sept. 2020, pp. 1-4. ***(URSI Young Scientist Award)***

[C2] **<u>Xiaoqiang Gu,</u>** Simon Hemour, and Ke Wu, "Conversion Efficiency Sensitivity of Multi-Stage Rectifier Over Temperature," in *Proc. 33rd URSI GASS,* Rome, Italy, Aug.-Sept. 2020, pp. 1-1.

[C3] **Xiaoqiang Gu,** Simon Hemour, and Ke Wu, "Remote Temperature Sensing Based on Battery-Free Harmonic Backscattering," in *Proc. IEEE Int. Symp. Antennas Propag. USNC-URSI Radio Sci. Meeting,* Montreal, Canada, Jul. 2020, pp. 1-2.

[C4] **<u>Xiaoqiang Gu,</u>** Louis Grauwin, David Dousset, Simon Hemour, and Ke Wu, "Ambient Radiofrequency Energy Mapping of Montreal for Far-Field Wireless Power Harvesting," in *Proc. IEEE Int. Symp. Antennas Propag. USNC-URSI Radio Sci. Meeting,* Montreal, Canada, Jul. 2020, pp. 1-2.

[C5] **<u>Xiaoqiang Gu,</u>** Simon Hemour, and Ke Wu, "Low Thermally Activated Schottky Barrier Rectifier: A New Class of Energy Harvester," in *Proc. IEEE Int. RFID Technol. Appl. Conf.*, Pisa, Italy, Sept. 2019, pp. 1- 3. ***(Invited Paper)***

[C6] **Xiaoqiang Gu,** Simon Hemour, and Ke Wu, "Reconfigurable Nonlinear Circuit for Wireless Power Harvesting and Backscattering," in *Proc. 49th Eur. Microw. Conf.,* Paris, France, Sept. 2019, pp. 1-4. *(Student Grant Award)*

[C7] **Xiaoqiang Gu,** Simon Hemour, and Ke Wu, "Improving Conversion Loss Performance of Fully Passive Harmonic Transponder at Low Temperature," in *Proc. IEEE MTT-S Wireless Power Transf. Conf.*, London, UK, Jun. 2019, pp. 1-4.

[C8] **Xiaoqiang Gu,** Erika Vandelle, Gustavo Ardila, Tan Phu Vuong, Ke Wu and Simon Hemour, "Environment-Aware Adaptive Energy Harvester for IoT Applications," in *Proc. IEEE MTT-S Int. Wireless Symp.*, Guangzhou, China, May 2019, pp. 1- 3. *(Invited Paper)*

[C9] **Xiaoqiang Gu**, Simon Hemour, and Ke Wu, "Enabling far-field ambient energy harvesting through multi-physical sources," in *Proc. Asia-Pacific Microw. Conf.*, Kyoto, Japan, Nov. 2018, pp. 1-3. *(Invited Paper)*

[C10] **Xiaoqiang Gu**, Lei Guo, Simon Hemour, and Ke Wu, "Analysis and Exploitation of Diplexer-based Fully Passive Harmonic Transponder for 5G Applications," in *Proc. IEEE MTT-S Int. Microw. Workshop Ser. 5G Hardw. Syst. Techn.*, Dublin, Ireland, Aug. 2018, pp. 1-3. *(Travel Grant Award)*

[C11] **Xiaoqiang Gu**, Lei Guo, Moussa Harouna, Simon Hemour, and Ke Wu, "Accurate Analytical Model for Hybrid Ambient Thermal and RF Energy Harvester," in *Proc. IEEE MTT-S Int. Microw. Symp. Dig.*, Philadelphia, USA, Jun. 2018, pp. 1122-1125.

[C12] **Xiaoqiang Gu**, Lei Guo, Simon Hemour, and Ke Wu, "Novel Diplexer-based Harmonic Transponder for 5G-Compatible IoT Applications," in *Proc. IEEE MTT-S Wireless Power Transf. Conf.*, Montreal, Canada, Jun. 2018, pp. 1-4. *(Best Student Paper Award Finalist)*

[C13] Lei Guo, **Xiaoqiang Gu**, Simon Hemour, and Ke Wu, "Reactive Frequency Downconverter for Low Power Harvesting Applications," in *Proc. IEEE MTT-S Int. Wireless Symp.*, Chengdu, China, May 2018, pp. 1- 4.

[C14] **Xiaoqiang Gu**, Simon Hemour, and Ke Wu, "Integrated Cooperative Radiofrequency (RF) and Kinetic Energy Harvester," in *Proc. IEEE MTT-S Wireless Power Transf. Conf.*, Taipei, Taiwan (R. O. C.), May 2017, pp. 1-3. *(Best Student Paper Award)*

[C15] **Xiaoqiang Gu**, Simon Hemour, and Ke Wu, "Cooperative Radiofrequency (RF) and Piezoelectric Energy Harvesting for Global Efficiency Enhancement," in *Proc. 32nd URSI GASS,* Montreal, Canada, Aug. 2017, pp. 1-1.

4. Awards:

[A1] **URSI GASS Young Scientist Award**, Aug. 2020.

[A2] **2nd Prize** in the Three Minute Thesis contest of Polytechnique Montreal, Jun. 2020.

[A3] **STARaCom Scholarship**, 2020

[A4] **IEEE MTT-S Graduate Fellowship Award**, 2019.

[A5] **Student Grant Award** (Eur. Microw. Conf.), Sept.-Oct. 2019.

[A6] **Travel Grant Award** (IEEE MTT-S IMWS-5G), Aug. 2018.

[A7] **Best Student Paper Finalist** (IEEE MTT-S Wireless Power Transf. Conf.), Jun. 2018.

[A8] **Best Student Paper Award** (IEEE MTT-S Wireless Power Transf. Conf.), May 2017.